January 2011

Isotopic and Elemental Compositions of Stardust and Protosolar Dust Grains in Primitive Meteorites

Maitrayee Bose
Washington University in St. Louis

WASHINGTON UNIVERSITY

Department of Physics

Dissertation Examination Committee:
Thomas J. Bernatowicz, Co-chair
Christine Floss, Co-chair
Charles M. Hohenberg
Martin H. Israel
Frédéric Moynier
Philip Skemer
Ernst Zinner

ISOTOPIC AND ELEMENTAL COMPOSITIONS OF STARDUST AND PROTOSOLAR DUST GRAINS IN PRIMITIVE METEORITES

by

Maitrayee Bose

A dissertation presented to the
Graduate School of Arts and Sciences
of Washington University in
partial fulfillment of the
requirements for the degree
of Doctor of Philosophy

August 2011

Saint Louis, Missouri

ABSTRACT OF THE DISSERTATION

Isotopic and Elemental Compositions of Stardust and Protosolar dust grains in Primitive Meteorites

by

Maitrayee Bose

Doctor of Philosophy in Physics

Washington University in St. Louis, 2011

Professor Thomas J. Bernatowicz, Co-chair

Professor Christine Floss, Co-chair

This dissertation presents the results and implications of the isotopic and elemental analyses of presolar silicate grains from the primitive chondrites, Acfer 094, SAH 97096, and ALHA77307. Oxygen-anomalous, C-anomalous, and N-anomalous grains were identified by O, C, and N isotopic imaging, respectively, using the NanoSIMS 50. Subsequently, the elemental compositions of the grains carrying the anomalous isotopic signatures were acquired in the PHI 700 Auger Nanoprobe. Some silicate grains with unique O isotopic compositions were measured for Si and Fe isotopes.

The isotopic analyses indicate that a majority of the silicate and oxide grains are ^{17}O-rich with solar to sub-solar ^{18}O/^{16}O ratios and come from less than 2.2$M_{\odot}$ Red Giant or Asymptotic Giant Branch stars. The second most abundant fraction of grains show large ^{18}O excesses and come from core collapse supernovae. The next most abundant fraction of grains comes from high metallicity AGB stars of approximately solar mass. A minor fraction of the grains exhibit large excesses in ^{16}O and formed in core collapse supernova ejecta. Grains with extreme ^{17}O excesses are the latest addition to the presolar grain

inventory. These grains may come from binary star systems where one star goes nova.

Numerous presolar SiC and N-anomalous carbonaceous grains were identified in the matrix of ALHA77307. The SiC grains are predominantly mainstream grains and may have condensed in 1–3$M_{\odot}$ AGB stars. The carbonaceous grains may have formed by ion-molecule reactions in the protosolar nebula or interstellar medium. A few carbonaceous grains exhibit ^{13}C-rich compositions; grains with such compositions are rare, which implies that either the fractionation effects that produce C anomalies in opposite directions cancel them out or secondary processing destroyed grains with C anomalies.

The elemental compositions of the silicate grains are predominantly non-stoichiometric (61%), with some grains exhibiting olivine- or pyroxene-like compositions. About 25% of the silicate grains contain Ca and/or Al. Furthermore, most of the presolar silicates are Fe-rich with Fe contents reaching up to about 45 at.% in contrast to equilibrium condensation models, which predict Mg-rich phases such as forsterite and enstatite to form. Although secondary alteration processes have probably modified the compositions of some presolar silicate grains in Acfer 094, the source of the Fe enrichments in most silicate grains is arguably primary. This work has led to the identification of presolar Si-oxide and Mg-oxide grains that had not been observed before. The formation of SiO_2 grains requires non-equilibrium conditions in the outflows of stars.

The abundance of SiC and silicate grains in ALHA77307 is high indicating its pristine characteristics, similar to the CR chondrites QUE 99177 and MET 00426. Although, the number of stardust grains identified in the enstatite chondrite SAH 97096 is low, their identification indicates that such grains were not all destroyed during the

high temperature phase experienced by enstatite chondrites. Finally, silicate grain abundances are much higher than oxide grain abundances in all the three meteorites.

Acknowledgements

First of all, I would like to express my gratitude to **Dr. Christine Floss** and late **Dr. Frank J. Stadermann** for advising me for the past 5 years and keeping track of where my PhD is heading. Thank you, for being extraordinarily patient with everything I've ever written, and for again and again taking your time to explain why things that are right in my head might still be hard to understand for the uninformed reader. Thank you, for answering e-mails almost before I managed to hit 'send', letting me know that it's ok to sometimes say stupid things, and also letting me know when I've managed to do something smart. Thank You, Frank for teaching me to use the instruments and answering the silliest of questions.

Thank you, **Dr. Thomas J. Bernatowicz,** for giving the opportunity to do my PhD thesis under your guidance and making sure that everything was alright with me. Thank you, for reinforcing what I can do, through conversations and advice. I am truly honored to know the first person who saw stardust! Thank you, **Dr. Ernst Zinner,** for teaching me something new, either about science or about places you have traveled to, each time I talk to you. Thank you, **Dr. Kevin Croat** for all your help in improving the dissertation.

Thank you, **Manavi Jadhav** for being the best in-office therapist and being a good friend. I would also like to thank my scientist friends, **Sachiko Amari, Dolly Daftary, Saiti Datta, Sourabh Dube, Jennifer Mabry, Kuljeet Marhas**, **Debajit Saha,** and **Kasey Wagoner**, who motivated me in different times of my graduate student life. Special thanks to a long list of friends and well-wishers who have not been named here. I would also like to thank **Frank Gyngard and Kathryn M. Hynes** for their help and advice. Thank you, **Olga Pravdivtseva** and **Alex Meshik**; you two made the conferences very enjoyable. Thank you, **Tim Smolar** and **Eric Inazaki** for ensuring that the instruments operate at all times. Thank you, **Julia Hamilton**, **Jan Foster**, and **Linda Coffin,** for showering me with care and affection, and ensuring that all secretarial work gets done smoothly.

Thank you, "Bala" **Balakrishnan Chandrasekaran** for enjoying my world of presolar grains! Last, but not the least, thanks 'Bhai', **Soumyonil Bose**, for loving and supporting unconditionally.

Dedicated to Ma & Baba

and

In fond memory of Frank J. Stadermann

Contents

List of Figures

Appendix (List of Tables)

CHAPTER 1

INTRODUCTION AND OVERVIEW

Stardust, most commonly referred to as presolar grains, formed around different stars with distinct masses and initial compositions, and was distributed in the solar nebula prior to its collapse and formation into the solar system. The presolar materials may have remained intact in their pristine state within some asteroid parent bodies. When chunks of asteroids fall to the Earth as meteorites, they are collected and can be studied in the laboratory. Presolar grains can be identified in meteorites by various analytical techniques because they exhibit highly anomalous isotopic compositions in one or more elements.

Presolar grains retain a record of stellar processes and so can be used to retrieve information about the stars. Their isotopic compositions allow identification of the stellar sources as well as provide valuable information on stellar nucleosynthesis, stellar evolution, and chemical evolution of our galaxy. Detailed information on the mechanisms for the formation of presolar grains and the physical conditions in the stellar and protosolar environment can be gathered from microstructural analyses. In addition, presolar grain compositions can tell us about pre-accretionary alteration in the protosolar nebula, aqueous and thermal processing in the meteorite parent bodies, and terrestrial alteration.

1.1. Stellar Evolution

Dust grains form in numerous stellar environments that include Type II supernovae (SNe), novae, Red Giant Branch (RGB) and Asymptotic Giant Branch (AGB) stars. The

evolution of low-mass stars is discussed here because copious amounts of carbonaceous, oxide, and silicate grains have been argued to form in them (e.g., Zinner 2007). See Busso et al. (1999) for a detailed review of AGB star evolution and nucleosynthesis.

Stars, like our Sun, burn H by proton-proton chain reactions to form He at temperatures of about 2×10^7 K, and belong to the main sequence (black line in Figure 1.1). Above this temperature and in the presence of C, N, and O, stars may produce He using these elements as catalysts, via the CNO cycle. The main sequence terminates when the H has been processed into He and nuclear reactions cease in the core. However, burning reactions continue to occur in the shell surrounding the core. Transitioning into the RGB phase for stars with masses of ~$2M_\odot$ (green line in Figure 1.1), the envelope of the star expands, convection currents within the envelope dredge-up *partially processed material* remnant of H burning, and alter the envelope composition. In addition, the core of the Red Giant (RG) star grows in mass, and consequently becomes hotter and denser. Temperatures in the core are high enough to burn He, initially in a violent manner, described as a He flash. Now the three ^{4}He (α particles) may fuse to form ^{12}C. Subsequently, quiescent core He burning occurs and the star enters the AGB phase (Figure 1.1). For a second time, the star expands; the convective envelope deepens, dredging up *completely processed* material remnant of H burning in a process called second dredge-up. The helium burning shell moves radially outward; the region between the He and H burning shells narrows, reaching a situation when the intershell region is unstable and thermal pulses may occur. The star's structure at this phase is composed of an inert CO core surrounded by a He burning shell, followed by a H burning shell on top of the intershell region, and a convective envelope (Figure 1.2a). During thermal pulses,

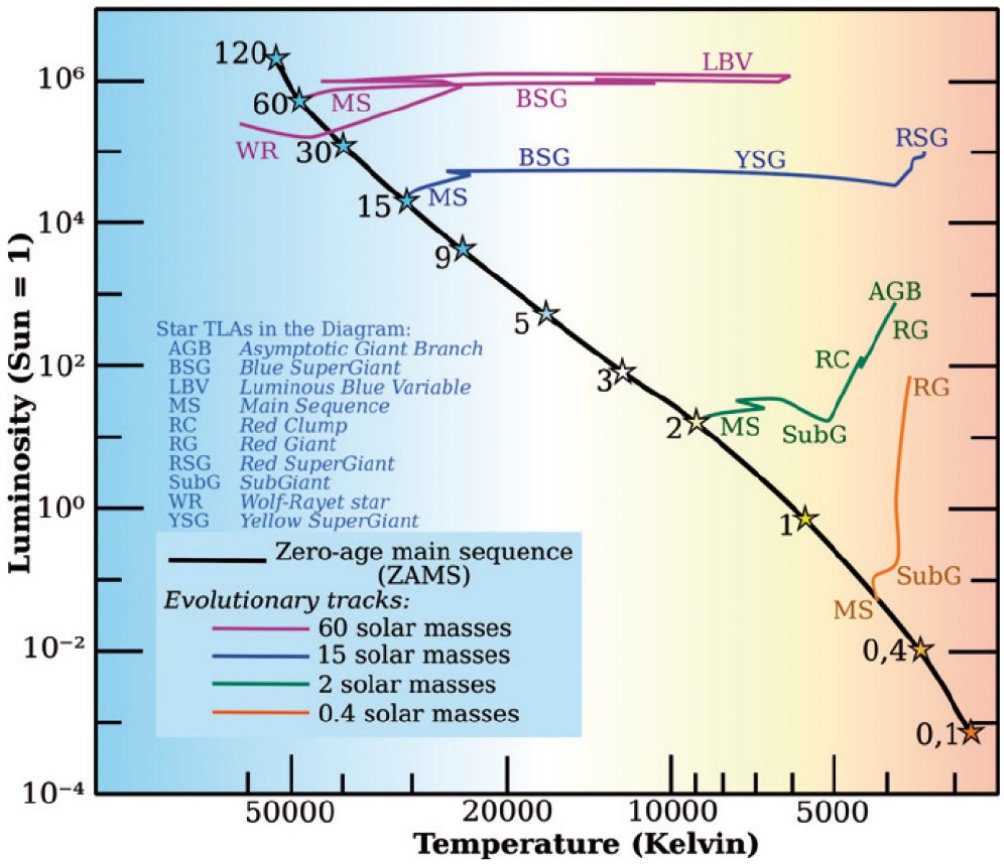

Figure 1.1: The Hertzsprung-Russell diagram shows the relationship between luminosity and effective temperature of stars. The color-coded tracks show stars with different initial masses moving away from the main sequence (black line), as they evolve. See the green line for a 2 solar mass AGB star evolution. Taken from Wikipedia.

the material from the He and H burning shells is mixed dramatically. Because the product of He burning is predominantly ^{12}C, dredge-up of this material, in multiple Third Dredge-Up (TDU) episodes, adds ^{12}C to the envelope, and causes the star to eventually become a C star.

Apart from low-mass stars, Type II or core collapse SNe form dust grains with SiC, graphite, oxide and silicate compositions (e.g., Zinner 2007). Figure 1.2b shows the schematic of the structure of a star of mass greater than ~8$M_{\odot}$. The elements with the highest abundances in each layer are also labeled. Late in the lifetime of such high-mass stars, the core of the star develops an onion-like structure, with heavier and heavier

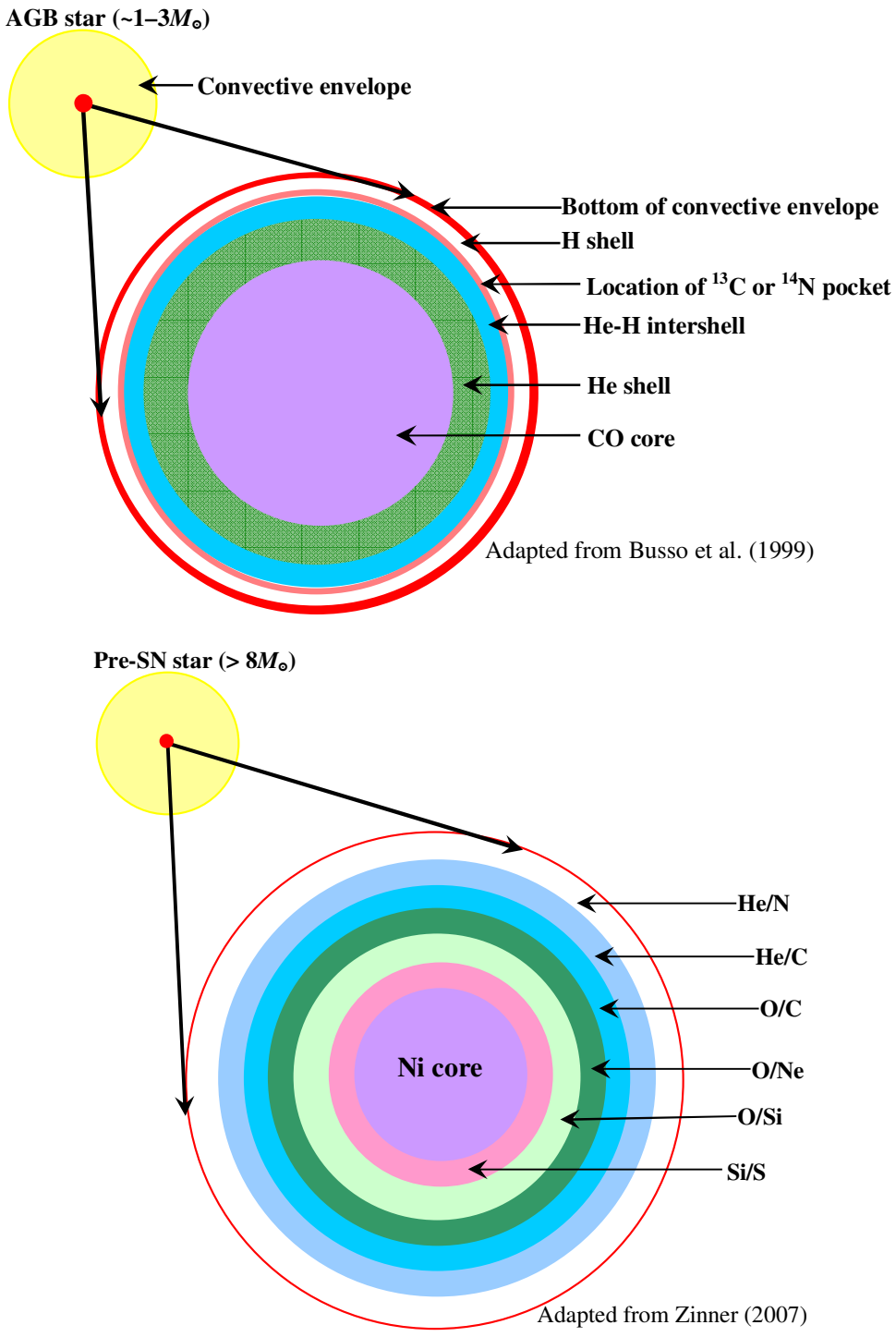

Figure 1.2: Schematic of a (a) low-mass and (b) high-mass star (not to scale).

elements in the deeper layers, ending with an Fe core. Formation of the Fe core makes the star unstable because Fe cannot provide energy through thermonuclear fusion, and the star explodes catastrophically. As a result of the violent explosion, material from different layers with different isotopic and chemical compositions mixes and results in the production of dust grains with unique characteristics.

1.2. Isolation of Presolar Grains: A Historical Perspective

Material from stars at different phases of evolution formed the starting material of our solar system. All elements starting with C are produced in stars by different nucleosynthetic processes (Burbidge et al. 1957; Cameron 1957). Cameron (1962) proposed that the solar system had passed through a phase in its evolution when temperatures were high enough to evaporate and homogenize all solids in the solar system, and signatures of a stellar origin of the elements have been eradicated. However, excesses in ^{129}Xe were observed in the CR meteorite Renazzo, which were attributed to the decay of the extinct radioactive nuclide ^{129}I (Reynolds and Turner 1964). Furthermore, Black and Pepin (1969) observed extreme ^{22}Ne (named Ne-E in stepped heating experiments) excesses in Orgueil that were linked to the decay of ^{22}Na, which is only made in stars. These were the first hints that solar system material had not been completely homogenized as was previously argued.

Numerous associations of the observed anomalies in noble gases, primarily Ne and Xe, were made with stellar nucleosynthetic models because mass dependent fractionation due to physical and chemical processes or *in situ* radioactive decay were only capable of producing anomalies that are few parts in thousand. For example, enrichment in both heavy (H) and light (L) isotopes of Xe was attributed to nuclear processes in a supernova

(SN): Xe-L (^{124,126}Xe) nuclides through proton capture and Xe-H (^{134,136}Xe) nuclides through neutron capture (Manuel et al. 1972; Lewis et al. 1975; Sabu and Manuel 1976). Acid residues from the Murchison meteorite showed excesses in ^{22}Ne, ^{80,82}Kr, and ^{128,130}Xe (named Xe-S); their isotopic patterns exactly matched the predictions for s-process nucleosynthesis and He-shell burning in RG stars (Srinivasan and Anders 1978). In addition to anomalies in noble gases, some of the isotopic anomalies that were discovered involved intermediate elements such as O and Mg (Clayton et al. 1973; Wasserburg et al. 1977) as well as heavy elements, such as Ba and Nd (e.g., McCulloch and Wasserburg 1978). Although the host phase(s) or carrier(s) of the anomalies had not been identified at that time, a high-temperature refractory mineral was expected to carry the anomalies because these minerals had the best chance of survival during the high temperature phase experienced by the solar system.

Searches of the carrier phases of the noble gas anomalies were initiated in various primitive meteorites. Nanodiamonds were found to be the carrier phase of the Xe-HL (Lewis et al. 1987). The phase was first isolated in CV meteorite Allende by dissolving all major minerals in strong acids and generating a colloid to separate nanodiamonds from the coarse-grained oxide grains, followed by oxidation (e.g., Tang and Anders 1988; Amari et al. 1994). Subsequent to this discovery, silicon carbide (SiC) and graphite grains were isolated by density and size separations (Amari et al. 1994). The former phase was found to be the carrier of the Ne-E(H), and the Xe-S anomalies (Bernatowicz et al. 1987), while the latter phase was the carrier of the Ne-E(L) component (Amari et al. 1990). These presolar carbonaceous phases are generally resistant to chemical separation processes making it easier to isolate them compared to presolar silicate grains

(see section 1.4.1).

1.3. Presolar Grain Types: A Review

Numerous nanometer- to micrometer-sized presolar grain types have been isolated in primitive meteorites. Here the isotopic compositions of the major elements present in presolar grains (i.e., C and Si isotopic systems in SiC grains and so on) are discussed. Presolar silicates are the subject of this dissertation and therefore are discussed in section 1.4. Prior to the review about different presolar grains, analytical techniques used to study presolar grains are discussed briefly.

1.3.1. Measurement Techniques

The quest to acquire additional information about presolar grains led to the advent of new chemical and micro-analytical techniques. These techniques are developed and adapted to study presolar grains as aggregates or as individual grains. For example, scanning electron microscopy is used to study the morphology and chemical composition of individual micrometer-sized grains. Elemental compositions of sub-micrometer-sized grains is acquired in the Auger Nanoprobe and is discussed in detail in Chapter 2. Crystallographic information about the grains and internal subgrains is obtained by using Transmission Electron Microscopy (TEM). High-precision isotopic information from grain aggregates is obtained by thermal ionization mass spectrometry and inductively coupled plasma mass spectrometry. However, single grain isotopic analyses are essential because individual grains carry unique nucleosynthetic signatures and can enable a better understanding of the grain formation scenarios. Such analyses are possible by using SIMS instruments including the IMS 3f, IMS 1270, and NanoSIMS 50.

Both NanoSIMS 50 and the next generation NanoSIMS 50L are capable of achieving very high lateral resolution, high sensitivity at high mass resolution, and parallel detection of multiple isotopes. In the NanoSIMS, the lens that focuses the primary ion beam and collects the secondary ions is placed very close to the sample surface (0.5 mm). This small working distance of the focusing lens produces a small primary ion beam and improves spatial resolution, and reduces aberrations in the system. Furthermore, the primary ion beam in the NanoSIMS hits the sample with normal incidence owing to the coaxial design of the ion optics; this results in small beam spots. Normal incidence also results in a low sputter rate. As a result, a higher concentration of primary ions can be implanted in the sample. This increases the ionization efficiency and sensitivity because more secondary ions can be produced for each primary ion. In addition, the secondary ions have a high extraction energy because the samples are held at ±8 keV. The lens in the dynamic transfer optics system is responsible for controlling the primary ion beam and the secondary ion beam while rastering on the sample surface. Finally, the NanoSIMS achieves a high transmission of secondary ions at high mass resolution because of significant improvement in ion optics, in which the secondary ion beam is manipulated via numerous optical lenses. All these attributes have allowed the acquisition of isotopic data from thousands of presolar grains and have played a significant role in the identification of presolar silicate grains.

1.3.2. Nanodiamonds

Nanodiamonds, which are the carriers of Xe isotopic anomalies are ~2-3 nm in diameter on average and are abundant in the matrices of primitive chondrites (up to ~1400 ppm; Anders and Zinner 1993; Ott 1993; Zinner 2007). Nanodiamonds exhibit a

bimodal release pattern with the normal Xe being released at low temperatures, while the Xe-HL component is released at high temperatures (Huss and Lewis 1995). The Xe-HL component is enriched with the light neutron-deficient isotopes ^{124}Xe and ^{126}Xe, as well as with the heavy neutron-rich isotopes ^{134}Xe and ^{136}Xe. Although the Xe release pattern from nanodiamonds measured by stepped combustion show that they have anomalous noble gas compositions, their C isotopic ratios in bulk are close to solar (Russell et al. 1996). While there is isotopic evidence to suggest that at least some meteoritic nanodiamonds are presolar, isotopic evidence for a presolar origin of *individual* grains cannot be obtained because acquiring isotopic data at the sub-nanometer scale is difficult owing to the small number of atoms present in the sample at that spatial scale. As a result, the stellar source(s) of the presolar nanodiamonds remain largely enigmatic.

Based on the anomalous Xe compositions, a SN origin of presolar nanodiamonds has been suggested (Clayton 1989). The high abundances of nanodiamonds in meteoritic matrices suggest a prolific dust source, and because C stars on the AGB are a dominant source of condensed dust, AGB stars have also been suggested to be the source of presolar nanodiamonds (e.g., Jørgensen 1988).

The predominant mechanism proposed for nanodiamond formation is low-pressure condensation similar to chemical vapor deposition in expanding gas ejecta (Clayton et al. 1995; Daulton et al. 1996). Other mechanisms that have been proposed are shock metamorphism by collisions, irradiation-induced transformation, and annealing by intense UV radiation of graphite or carbonaceous grains (Tielens et al. 1987; Nuth and Allen 1992; Ozima and Mochizuki 1993). However, these mechanisms may not be the appropriate route for the formation of nanodiamonds based on isotopic and

microstructural evidence. For example, the $^{12}C/^{13}C$ ratios of graphite grains (Travaglio et al. 1999) and nanodiamonds (Russell et al. 1996) show significant differences, which should not be the case if majority of the nanodiamond population form by transformation of graphite grains.

Although Secondary Ion Mass Spectrometry (SIMS) cannot be employed to study single grains of presolar nanodiamonds, nanodiamonds have been studied using complementary techniques such as Electron Energy Loss Spectroscopy (EELS; e.g., Bernatowicz et al. 1990), TEM (e.g., Daulton et al. 1996), atom-probe tomography (e.g., Stadermann et al. 2011), and aberration corrected Scanning Transmission Electron Microscopy (STEM; Stroud et al. 2011). The application of the EELS technique on nanodiamonds isolated in carbonaceous chondrites, Allende and Murray, indicated that a non-primary element in nanodiamonds is H, which is located on the nanodiamond surfaces, and is enriched in D (Bernatowicz et al. 1990). Atom-probe tomography of single grains of nanodiamonds shows that N atoms are spatially correlated with the presolar nanodiamonds (Stadermann et al. 2011), while STEM of nanodiamond residues in Allende and Murchison contain glassy C, which is probably the carrier of the isotopic anomalies originating in SNe (Stroud et al. 2011).

1.3.3. Silicon Carbide

Silicon carbide is the most well studied presolar phase because of the large grain sizes (> 1 μm), high concentrations of trace elements, and the relative ease of separation (compared to graphite, for instance). Carbon, N, and Si isotopic ratios acquired on individual SiC grains (Figures 1.3 and 1.4) using the SIMS techniques, e.g., IMS 3f and NanoSIMS, have allowed their classification into different populations (Hoppe and Ott

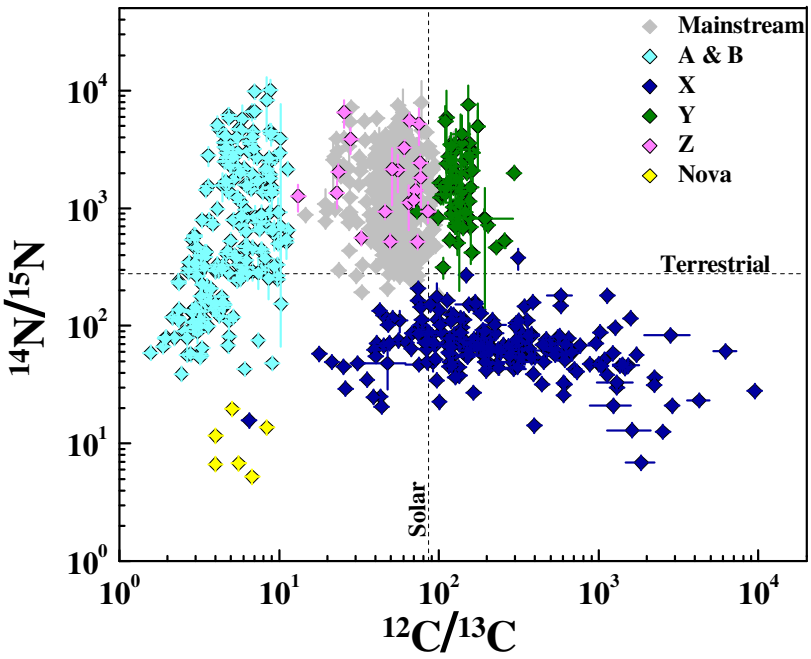

Figure 1.3: Carbon and N isotopic compositions of presolar SiC grains belonging to different populations. Data are from the presolar grain database (www.presolar.wustl.edu/~pgd).

1997a). The likely stellar sources of the diverse SiC grain populations are based on these isotopic systems. Mainstream SiC grains have $^{12}C/^{13}C$ ratios between 10–100 (Figure 1.3); these grains may have condensed in 1–3$M_\odot$ AGB stars (Zinner et al. 1989; Virag et al. 1992; Alexander et al. 1993; Hoppe et al. 1994; Amari et al. 1995a). Hydrogen burning, via the CNO cycle, can produce the ^{13}C and ^{14}N excesses observed in mainstream grains; material exhibiting such signatures is subsequently brought up to the surface by the first or second dredge-up episodes in low-mass stars. Note that the ^{12}C excesses occur by shell He burning and TDU during the Thermally Pulsating (TP)-AGB phase (Busso et al. 1999). The high $^{14}N/^{15}N$ isotopic ratios (up to ~10^4) can be explained by cool bottom processing (CBP) where envelope material is taken to the interior and

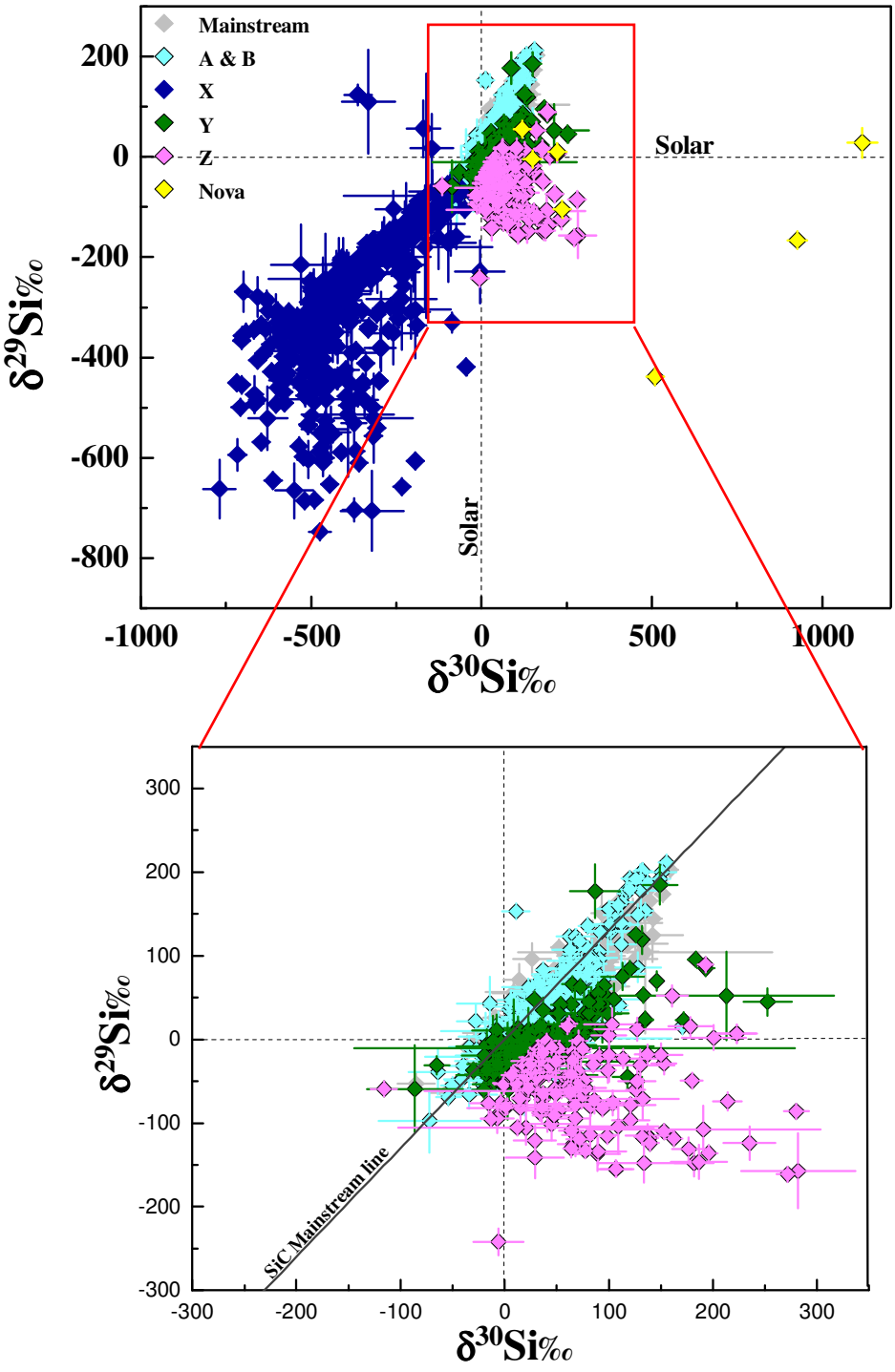

Figure 1.4: Silicon isotopic compositions of presolar SiC grains belonging to different populations are shown in the top figure. The SiC grains in the top figure contained in the red box, except SiC X and nova grains, are shown in the bottom figure. Data are from the presolar grain database (www.presolar.wustl.edu/~pgd).

processed in the regions close to the H-burning shell in AGB stars (Wasserburg et al. 1995; Nollett et al. 2003). In a Si three-isotope plot (Figure 1.4), the mainstream grains fall along a line of slope 1.3, and are characterized by excesses in both ^{29}Si and ^{30}Si, up to ~200‰. However, excesses of only ~20‰ are predicted in ^{29}Si and ^{30}Si by neutron capture in the He shell of low-mass stars (e.g., Zinner 2007). Several explanations have been given for this discrepancy including that the Sun has an "atypical" Si isotopic composition (Alexander and Nittler 1999). A few studies have suggested the evolution of the Si isotopes as different generations of stars produced Si with increasing ^{29}Si/^{28}Si and ^{30}Si/^{28}Si ratios (Gallino et al. 1994; Timmes and Clayton 1996a). Clayton (2003) argued that before the formation of the solar system, our galaxy of high metallicity probably merged with a satellite galaxy of lower-than-solar metallicity to account for the range in Si isotopic ratios in SiC grains. Although all of these aforementioned possibilities have issues associated with them and the galactic merger is the preferred explanation for the Si isotopic compositions of the SiC grains, clear consensus on this problem is still lacking.

Type Y grains have ^{12}C/^{13}C ratios greater than 100 (Figure 1.3) and Si isotopic compositions (Figure 1.4) that lie to the right of the SiC mainstream correlation line (Hoppe et al. 1994; Amari et al. 2001a; Nittler and Alexander 2003). Grains with larger ^{30}Si excesses than Y grains and ^{12}C/^{13}C ratios of less than 100 (Figures 1.3 and 1.4) are classified as SiC Z grains (Alexander 1993; Hoppe et al. 1997b; Nittler and Alexander 2003). Comparison with model predictions indicates that SiC Y grains have an origin in low-to-intermediate mass AGB stars with approximately half the solar metallicity (Amari et al. 2001a), while the Z grains most likely condensed in low-mass and 1/3 solar

metallicity stars (Hoppe et al. 1997b).

Type A and B grains exhibit $^{12}C/^{13}C$ ratios of less than 10 (Figure 1.3) and Si isotopic compositions (Figure 1.4) similar to SiC mainstream grains (Hoppe et al. 1995; Huss et al. 1997; Amari et al. 2001b). Although some SiC A and B grains exhibit $^{14}N/^{15}N$ ratios that are generally similar to those of mainstream grains, a substantial fraction of A and B grains exhibit ^{15}N excesses. Although the sources of these grains are more elusive, J-type C stars and Sakurai objects are suggested as the probable sources of these grains based on the absence and presence of s-process enhancements, respectively (Amari et al. 1995a; Pellin et al. 2000). J-type stars are C-rich stars that show low $^{12}C/^{13}C$ ratios while Sakurai's objects are post-AGB stars that see a very late thermal pulse (Herwig et al. 2004).

Type X SiC grains are characterized by ^{12}C, ^{15}N, (Figure 1.3) and ^{28}Si excesses (Figure 1.4) relative to normal (Amari et al. 1992; Hoppe et al. 1996; Nittler et al. 1996), although a few X grains with ^{12}C depletions exist in the presolar SiC inventory. These studies also showed that ~10–20% of the X grains show ^{44}Ca excesses that come from the decay of short-lived ^{44}Ti, which is produced only in Type II SNe (Timmes et al. 1996b). All these isotopic characteristics indicate an origin of the SiC X grains in SN ejecta. Finally, grains with low $^{12}C/^{13}C$ ratios, low $^{14}N/^{15}N$ ratios, and large ^{30}Si excesses are predicted to form in nova ejecta or in an environment where material from a nova is mixed with solar material (Amari et al. 2001c).

Excesses in ^{6}Li, ^{21}Ne, and ^{126}Xe nuclides in SiC grains have been interpreted as being due to spallation by Galactic cosmic rays (Lewis et al. 1994; Ott et al. 2005; Heck et al. 2008; Gyngard et al. 2009). On the basis of these data, these authors determined the SiC

grain lifetimes in the interstellar medium to be between 10 Myr and 1 Gyr.

Some SiC grains exhibit platy and subhedral morphologies while others are hexagonal or triangular (Amari et al. 1994). Transmission electron microscopy of a large population of SiC grains has shown that grains with cubic and hexagonal structures are the only polytypes (Daulton et al. 2002). These polytypes are the lowest temperature forms of SiC and are consistent with conditions in circumstellar outflows. Crystallographic analyses of SiC mainstream and X grains also revealed that the former are composed of a few crystals, while the latter is made up of many crystals (Hynes et al. 2010). The different crystal sizes indicate their formation under differing stellar conditions. Furthermore, Hynes et al. (2010) found that the X grains contain high concentrations of Mg (probably from the decay of ^{26}Al) as well as numerous subgrains with highly variable Ni/Fe ratios.

1.3.4. Graphite

Graphite grains exhibit $^{12}C/^{13}C$ ratios up to ~10^4 (Figure 1.5) similar to SiC X-grains; a significant fraction of grains also have low $^{12}C/^{13}C$ ratios similar to SiC A and B grains (Amari et al. 1990). Most graphite grains have close to solar N isotopic compositions (Hoppe et al. 1995; Zinner et al. 1995; Jadhav et al. 2006), excluding some low-density grains, which show ^{15}N excesses (Figure 1.5). Normal N isotopic ratios are most likely the result of isotopic equilibration (Jadhav et al. 2006). Note that the chemical separation procedure used to isolate presolar graphite grains led to their classification into low-density (1.67–1.92 g/cm^3) and high-density (2.02–2.30 g/cm^3) grains. The concentrations of trace elements are larger in the former grains.

Some low-density grains have large ^{18}O excesses ($10 < ^{16}O/^{18}O < 499$) that are

uncorrelated with $^{12}C/^{13}C$ ratios; however, numerous ^{18}O-rich grains are close to normal in C isotopic ratios (Amari et al. 1995b; Stadermann et al. 2005; Jadhav et al. 2006). Low-density graphite grains predominantly show ^{28}Si excesses. Large ^{29}Si and ^{30}Si excesses are also observed but are more common in high-density grains. Low-density graphite grains with ^{18}O, ^{12}C, ^{28}Si, and ^{15}N excesses come from SNe (Travaglio et al. 1999). Additional evidence for the SN origin of some graphite grains comes from the presence of of ^{41}Ca and ^{44}Ti (Amari et al. 1996; Nittler et al. 1996). Low-density graphite grains with ^{18}O, ^{12}C, ^{26}Al, $^{29,30}Si$, and ^{15}N excesses probably condense in greater than $20M_{\odot}$ stars that are called Wolf-Rayet stars (Arnould et al. 1997).

Many high-density graphite grains exhibit ^{29}Si and ^{30}Si excesses that are correlated with high $^{12}C/^{13}C$ ratios, which indicate an origin of these grains in low-metallicity AGB stars (Amari et al. 2004, 2005; Jadhav et al. 2006). The presence of ^{44}Ti in a few high-density graphite grains suggests an origin in SN ejecta (Jadhav et al. 2008). However, low $^{12}C/^{13}C$ ratios in the high-density grains are not consistent with a SN origin, and so these authors suggested that born-again AGB stars (like Sakurai's object) are their stellar source. Born-again AGB stars that experience a late He flash are able to explain the low $^{12}C/^{13}C$ ratios and enrichments in s-process elements in the high-density grains.

Most graphite grains are spherical in shape and platy in appearance (Amari et al. 1990). Graphite grain that are argued to have originated in AGB stars (upto ~20 μm in size) exhibit either an onion- or cauliflower-like morphology (Hoppe et al. 1995; Zinner et al. 1995); some are potato shaped (Jadhav et al. 2006). The outer concentric layers of onion-types are well-crystallized C whereas the cores of some grains are composed of nanocrystalline C (Bernatowicz et al. 1991; 1996). Based on these grain structures,

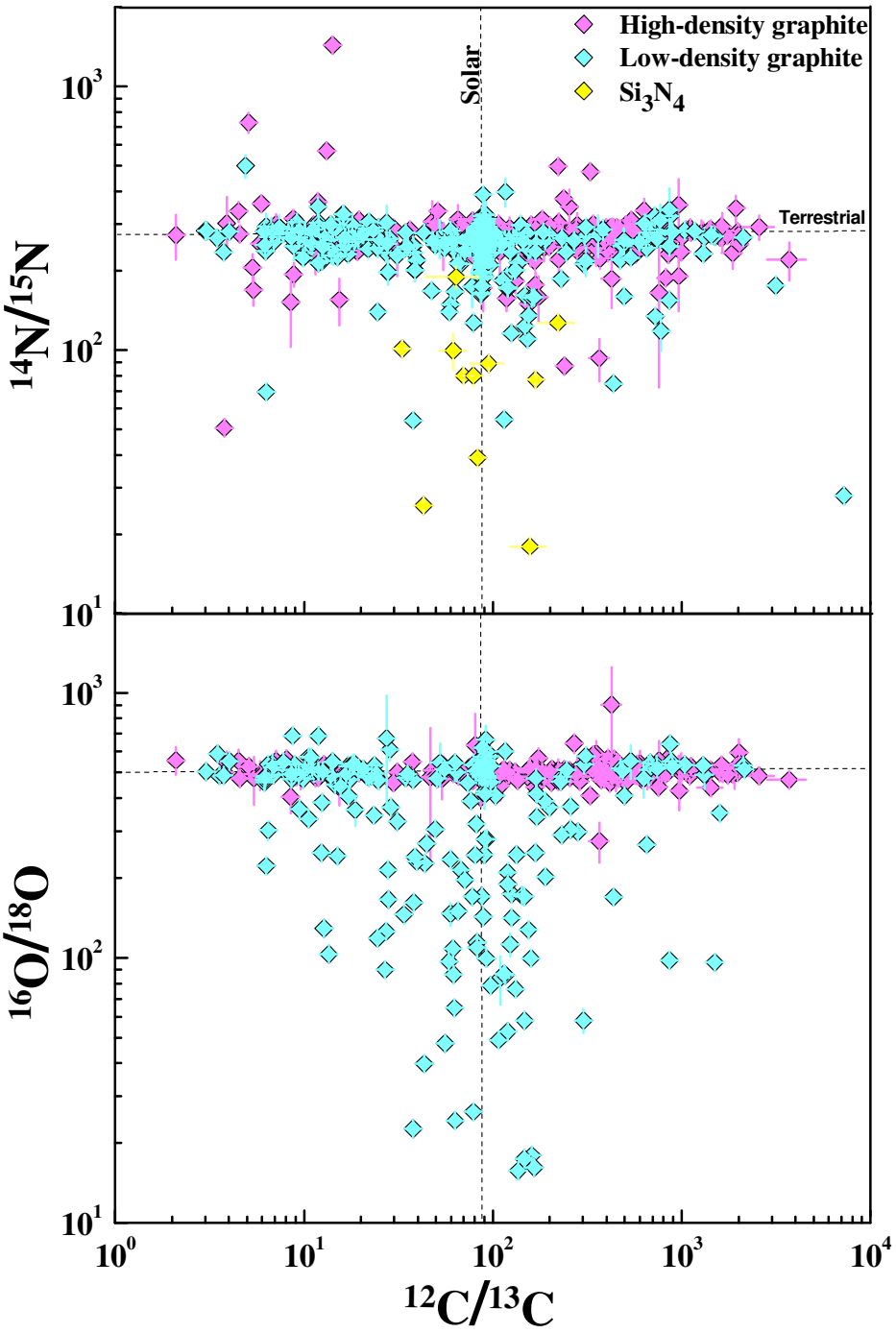

Figure 1.5: Carbon, N, and O isotopic compositions of presolar graphites and Si_3N_4 grains. Data are from the presolar grain database (www.presolar.wustl.edu/~pgd).

Bernatowicz et al. (1996) argued that onion-type graphite grains grew rapidly from supersaturated gas, following heterogeneous nucleation of the cores. Many (Ti,V)C grains are contained within the cores of the grains that form the nucleation sites for the graphite grains (Bernatowicz et al. 1991; 1996). On the other hand, cauliflower-like graphite grains consist of turbostratic graphite sheets that are generally loosely packed; many contain tiny carbide crystals (Bernatowicz et al. 1996). Subgrains within AGB graphite grains contain high concentrations of s-process elements such as Zr, Mo, and Ru (Bernatowicz et al. 1996). Carbides condense before graphite over a wide range of temperatures and pressures; the C/O ratio of the surrounding environment plays a more important role in the condensation of graphite grains compared to the condensation of internal carbides (Bernatowicz et al. 1996). Therefore, based on the condensation curves of these materials as a function of temperature, pressure, and C/O ratio, the conditions under which graphite grains with carbide subgrains can form have been well-constrained (Bernatowicz et al. 1996).

Graphite grains from SNe are less than ~12 μm in size (Croat et al. 2003). These SN graphites have a structure that is intermediate between the onion- and cauliflower-types. Although the SN graphite grains generally do not show subgrains that are carbides of s-process elements such as Mo, Zr, and Ru, they do contain TiC subgrains (Croat et al. 2003). The abundance and compositions of the TiC subgrains vary as a function of the distance from the core to the rim of the graphite grains (Croat et al. 2003). These authors argue that the abundance of TiC subgrains provides us clues regarding the growth rate of graphite grains, while their compositions monitor conditions during the formation of the graphite grains in the SN ejecta.

1.3.5. Oxides

Presolar oxide grains are identified by O isotopic measurements of a large number of single grains obtained from acid residues, using automated ion imaging techniques (e.g., Nittler and Alexander 2003; Gröner and Hoppe 2006; Gyngard et al. 2010). Presolar oxide grains include corundum-Al_2O_3 (Huss et al. 1994; Hutcheon et al. 1994; Nittler et al. 1994, 1997; Choi et al. 1998), spinel-$MgAl_2O_4$ (Choi et al. 1998; Zinner et al. 2003, 2005; Gyngard et al. 2010), hibonite-$CaAl_{12}O_{19}$ (Choi et al. 1999; Nittler et al. 2008), titanium oxide-TiO_2 (Nittler et al. 2008), magnesiowüstite-(Mg,Fe)O (Floss et al. 2008), and Cr-bearing oxide (Nittler et al. 2005; Dauphas et al. 2010; Qin et al. 2011) grains. The O anomalies that have been measured in presolar oxide grains belonging to group 1 agree well with spectroscopic observations of O-rich stars (Harris and Lambert 1984; Harris et al. 1987; Smith and Lambert 1990).

Nittler et al. (1997, 2008) classified the oxide grains into different groups and discussed possible stellar sources based on their O isotopic compositions (Figure 1.6). Group 1 grains with $^{17}O/^{16}O$ ratios greater than solar and $^{18}O/^{16}O$ ratios between ~0.001 and ~0.002 may have formed in the envelopes of low-mass RG or AGB stars (Figure 1.6). Hydrogen burning followed by dredge-up in first (and second for $M > 3M_{\odot}$) dredge-up episode(s) in these stars results in excesses in ^{17}O with respect to ^{16}O (Bothroyd et al. 1994; Boothroyd and Sackmann 1999). Grains with ^{17}O excesses and large ^{18}O depletions ($^{18}O/^{16}O < 0.001$) form group 2 (Figure 1.6). Compositions of group 2 grains can be explained by CBP in low-mass stars (Wasserburg et al. 1995; Nollett et al. 2003). Group 2 oxide grains show evidence for initial ^{26}Al (Nittler et al. 1997; Choi et al. 1998, 1999; Zinner et al. 2005), which is produced in the H-burning shell and is dredged-up during

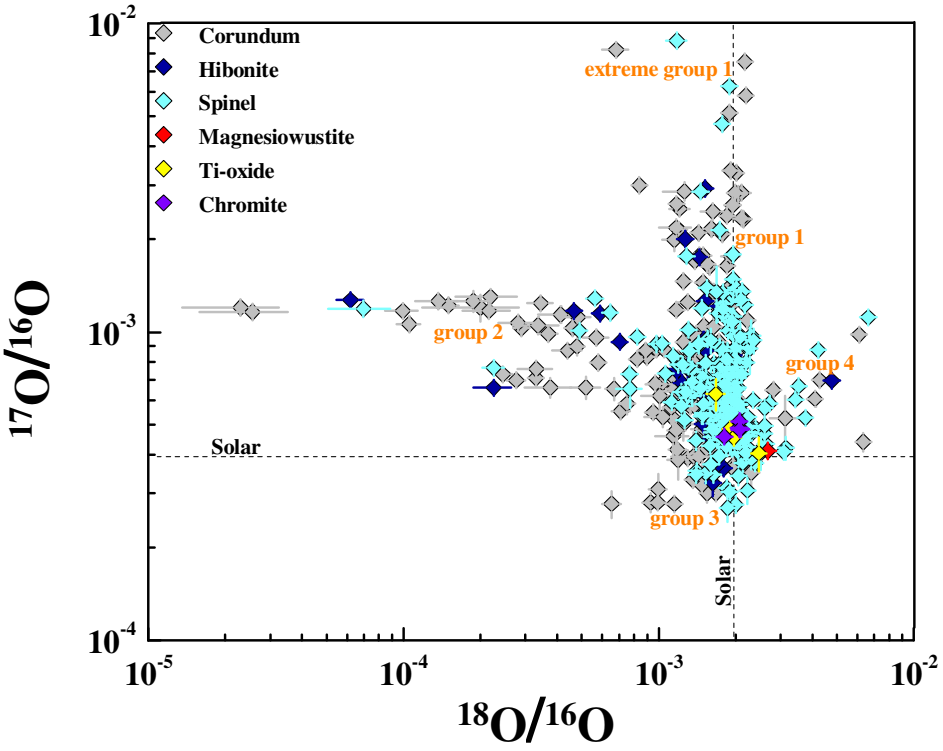

Figure 1.6: Oxygen isotopic compositions of presolar oxide grains belonging to different groups. Data from the presolar grain database (www.presolar.wustl.edu/~pgd).

the TP-AGB phase. Cool Bottom Processing is needed to explain $^{26}Al/^{27}Al$ ratios that are greater than 3×10^{-3} measured in these grains.

Oxide grains exhibiting depletions in both ^{17}O and ^{18}O belong to the group 3. Those that fall on or above the Galactic Chemical Evolution (GCE) line may have formed in lower-than-solar metallicity RG or AGB stars. Those that fall below the GCE are more enigmatic and may form in Type II SNe (Figure 1.6; Nittler et al. 2008). Group 4 grains exhibit excesses in ^{18}O and may or may not show an excess in ^{17}O. These grains condense in either high metallicity stars or SN ejecta (Figure 1.6; Nittler et al. 2008). Some oxide grains are characterized by large ^{17}O excesses ($^{17}O/^{16}O > 0.005$; Figure 1.6) and high $^{25}Mg/^{24}Mg$ ratios. They may have condensed in binary star systems where a

companion star is enriched by material from a nova or an evolved star (Nittler et al. 2008; Gyngard et al. 2010).

A few presolar oxide grains from different groups have been measured for Ti isotopic ratios and they show small excesses in all Ti isotopes relative to ^{48}Ti, in agreement with compositions predicted by AGB models (Choi et al. 1998; Nittler et al. 2008). An exception has been the group 3 spinel grain which shows an excess in ^{44}Ca from the decay of ^{44}Ti (Gyngard et al. 2010). Radiogenic ^{44}Ca originates from the decay of ^{44}Ti in the inner O-rich zones of a Type II SN (Timmes et al. 1996b). In addition, presolar hibonite grains have been analyzed to look for ^{41}K from the decay of ^{41}Ca (Choi et al. 1999; Nittler et al. 2005, 2008; Zinner et al. 2006), which allow us to infer the initial ^{41}Ca/^{40}Ca ratios. The ^{41}Ca/^{40}Ca ratios of the hibonite grains are up to ~2×10^{-4}, similar to that predicted for the envelopes of AGB stars (e.g., Zinner et al. 2006).

Transmission electron microscopy of two presolar Al_2O_3 grains from AGB stars indicates that AGB stars can produce both corundum and amorphous Al_2O_3 grain structures (Stroud et al. 2004). In addition, the absence of subgrains suggests that Al_2O_3 can condense in the absence of TiO_2 seed nuclei. Microstructural analyses of spinels show that O-rich AGB stars can condense single-crystal spinel grains (Zega et al. 2009). Furthermore, single crystals of hibonite can also condense in the SN ejecta, and are structurally similar to hibonite grains formed in AGB stars (Zega et al. 2011). None of the hibonite grains show presence of subgrains.

1.3.6. Other Presolar Phases

The presolar grain list also includes silicon nitride-Si_3N_4 (Nittler et al. 1995) that is found in very low abundance. The C, N, (Figure 1.5) and Si isotopic compositions of

Si_3N_4 grains resemble those of SiC X grains, which imply a SN origin for these grains. Finally, presolar Cr oxides that are typically less than ~200 nm in size have been identified in the meteorite Orgueil (Nittler et al. 2005; Dauphas et al. 2010; Qin et al. 2011). These chromites are the carriers of the ^{54}Cr excesses and most likely come from Type II SNe.

1.4. Silicates

1.4.1. Problems with their Isolation

Individual carbonaceous and oxide grains have been isolated and studied extensively using SIMS techniques, as discussed in section 1.3. However, there are several experimental challenges in isolating and identifying presolar silicates. The chemical dissolution used to separate out almost pure samples of presolar SiC and graphite grains cannot be used to isolate silicate grains. This is because the strong acids (specifically HF) used during the chemical separation process dissolve silicates. In addition, the presolar silicate grains present in the matrix of a meteorite are surrounded by silicate material synthesized in the solar system. Therefore, the identification of presolar silicate grains requires an instrument with high-resolution ion imaging capability along with high sensitivity. The NanoSIMS is ideal for identifying anomalies at the sub-micrometer scale because of the aforementioned (section 1.3.1) attributes. Furthermore, NanoSIMS has the ability to measure 1000s of sub-micrometer grains in a single measurement by rastering the ion beam over a large (e.g., 10×10 μm^2) area. Oxygen isotopic ion imaging of fragments from Interplanetary Dust Particles (IDPs) led to the discovery of presolar silicates (Messenger et al. 2003). Subsequently, measurements on Acfer 094 and NWA

530 led to their identification in meteorites (Nguyen and Zinner 2004; Nagashima et al. 2004; Mostefaoui and Hoppe 2004).

1.4.2. Procedure for Identification

Oxygen ion imaging is performed on samples (see section 1.4.5. for details regarding the samples used in this study) because O is a major element in silicates and is expected to exhibit large isotopic anomalies. A general procedure involved in ion imaging measurements is as follows:

1. A Cs^+ primary beam of ~100 nm beam diameter is rastered over 10×10 or 20×20 μm^2 areas on a sample. Negative secondary ions of O and C isotopes, as well as secondary electrons (Figure 1.7) are measured. For O and C isotopic measurements, the $^{16}O^1H$ interference for ^{17}O and $^{12}C^1H$ interference for ^{13}C requires a careful evaluation during tuning of the instrument. We require mass resolving powers of ~5000 to resolve $^{16}O^1H$ from ^{17}O, and ~3000 to resolve $^{12}C^1H$ from ^{13}C. A mass resolving power of greater than 8000 is easily achievable in the NanoSIMS, and so the hydride peaks are easily resolved.

2. The ion images of $^{12}C^-$, $^{13}C^-$, $^{16}O^-$, $^{17}O^-$, and $^{18}O^-$ are acquired in multi-collection mode with typical dwell times of about 10000–20000 μsec/pixel over 256×256 pixels. The ability to collect isotopic information from the *identical* analysis area, pixel by pixel, is crucial to the identification of presolar silicate grains because the ratio of the ^{16}O counts and $^{17,18}O$ counts can be consequently calculated for individual pixels. This allows us to identify the location of the O anomaly. After the ion images from a given area have been acquired, the measurement is repeated at a new location on the sample in a pre-assigned pattern.

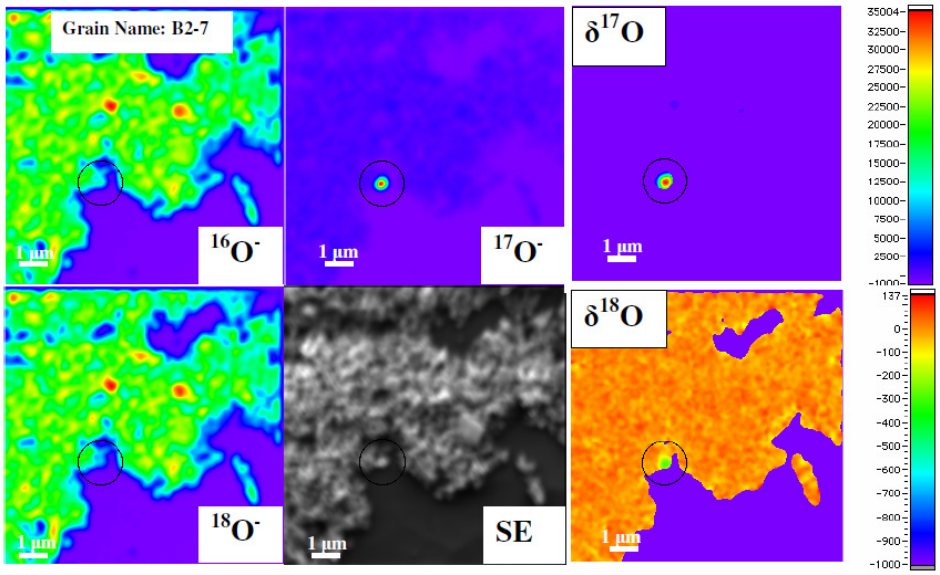

Figure 1.7: Oxygen ion imaging of an area over the mount containing grain size-separates of the EH3 chondrite SAH 97096 revealed an O-anomalous grain, B2-7, which exhibits a ^{17}O excess (~35000‰) and a ^{18}O depletion (~400‰) and is encircled in black. The $^{16,17,18}O^-$ ion images and the $\delta^{17,18}O$ images are in false colors. The $\delta^{i}E/^{j}E$ is defined as $[(^{i}E/^{j}E)_{grain}/ (^{i}E/^{j}E)_{standard} - 1]\times1000‰$, where the element E has the isotopes i and j (reference isotope).

3. The lateral resolution of the ion images is determined by the diameter of the primary beam at the sample, and in order to get a fine ion beam, the use of a low beam current is mandatory. Since the primary beam current that is used in ion imaging is less than 1 pA, multiple images (5–10) of the same area are acquired to reduce statistical errors. Pre-sputtering of the samples prior to analysis is not required for all kinds of samples e.g., grain size-separates need not be presputtered while thin-sections need to be presputtered. Cesium is implanted in the sample during the acquisition of the first image, which enhances secondary ion yield. In cases where there is evidence of a large difference in counts between the first and second ion images, the first ion image can be discarded. While studying thin-sections of meteorites, a high current (~20–30 pA) Cs^+ beam is used to remove the C coating on raster areas slightly larger than the analysis areas in the

thin-section. This pre-sputtering also results in the implantation of Cs^+ in the sample.

4. Ratio images, namely $^{17}O/^{16}O$ and $^{18}O/^{16}O$, and delta images are produced pixel by pixel from the secondary ion images, using the 'NanoSIMS View' imaging software written by Frank J. Stadermann. See Stadermann et al. (2005) for details regarding the post-measurement analyses.

5. We used a number of criteria for the identification of O-anomalous grains. Areas in these ratio images, also termed 'hotspots', that have an O isotopic ratio at least 5σ away from solar or normal ratios ($^{16}O/^{17}O = 2625$; $^{16}O/^{18}O = 499$) and that show the 'hotspot' in at least three consecutive ion images are considered anomalous.

6. A correction for the instrumental mass fractionation is taken into account by doing either an external or an internal calibration. In the former method, isotopic ratios acquired in the unknown sample are compared to an external standard with known isotopic composition. Measurements on the unknown sample and external standard are made under identical conditions. The deviations of isotopic ratios from the standards are then expressed as δ-values, e.g., $\delta^iE/^jE$ is defined as $[(^iE/^jE)_{grain}/ (^iE/^jE)_{standard} - 1]\times1000‰$, where the element E has the isotopes i and j (reference isotope). For normalizing O isotopes, however, internal calibration is performed. In this method, the $^{16}O/^{17}O$ and $^{16}O/^{18}O$ ratios of the anomalous hotspots identified in a 10×10 μm^2 area are corrected by assuming that the O isotopic composition of the bulk matrix is normal or solar.

7. In order to locate C anomalies, $^{12}C/^{13}C$ ratio and delta images are produced. Hotspots with C isotopic anomalies are internally normalized to a solar $^{12}C/^{13}C$ ratio of 89. To identify N anomalies, secondary ions of $^{12}C^{14}N^-$ and $^{12}C^{15}N^-$ are acquired. Nitrogen is not directly measured because it does not form negative ions and its positive secondary ion

yield is extremely low. Comparatively, the CN^- secondary yield is high making it possible to acquire N isotopic compositions. The $^{13}C^{14}N$ interference can be separated from $^{12}C^{15}N^-$ at low mass resolving powers of ~1500. Internal normalization of N-anomalous hotspots identified in ALHA77307 was done by assuming that the composition of the bulk matrix has a $^{14}N/^{15}N$ ratio of 272. Note that this cannot be done for some meteorites that do not exhibit a ratio of 272 in its bulk matrix.

1.4.3. Characterization of Presolar Silicates

Because silicate phases have been discovered rather recently (Nguyen and Zinner 2004; Nagashima et al. 2004; Mostefaoui and Hoppe 2004), little is known about their isotopic compositions, elemental or chemical compositions, and structures. The small sizes of the silicate grains (typically less than 350 nm in size) make it extremely challenging to acquire elemental compositions of the grains. As a result, the traditionally used SEM with an excitation volume of ~1 μm is unsuitable for the characterization of silicate grains. Washington University in St. Louis acquired a PHI 700 Auger Nanoprobe in the year 2006, which can perform elemental measurements at a spatial scale of ~10–20 nm. Elemental compositions and high-resolution elemental maps of the grains can also be obtained by using this novel Auger spectroscopy technique. See Stadermann et al. (2009) for a comprehensive review of the technique.

Subsequent to the identification of O-anomalous grains, the Auger Nanoprobe is used to acquire high-resolution images of the areas analyzed in the NanoSIMS. Alignment of the secondary electron images from the NanoSIMS and the Auger Nanoprobe allows us to locate the grains with O-anomalous compositions. Further information regarding Auger spectroscopy is provided in Chapter 2.

1.4.4. Secondary Alteration Mechanisms

The fine-grained matrix in meteorites where the presolar grains are sited can easily undergo alteration. Modification can occur in the proto nebular cloud or in the asteroid parent body due to the action of water or/and heat. Presolar silicate grains are particularly susceptible to alteration processes, which can bring about subtle changes in their original mineralogy and chemistry. Therefore, evidence of possible alteration of the matrix needs to be taken into account in order to understand presolar silicate grain compositions and to compare the abundances of presolar silicate grains in meteorites belonging to different classes.

Meteorites have been classified into a petrologic sequence from type 1 to type 6 based on their displayed interaction with water and heat (Weisberg et al. 2006). Aqueous alteration can occur in a low-temperature environment producing types 1 and 2; thermal metamorphism in the presence or absence of water produce types 4, 5, and 6 (Huss et al. 2006; Brearley 2006). Meteorites belonging to the type 3 are the most primitive. The alteration mechanisms can result in the formation of secondary phases as well as produce substantial changes in the composition and texture of the meteoritic components. Although evidence for alteration exists in different classes of meteorites, the greatest challenge usually is to distinguish between alteration that might have occurred under different environments i.e., nebular versus parent body. Apart from these space environments, meteorites may have been altered after they fall on Earth. Most meteorites that fall in temperate or tropical areas are destroyed much faster than in either hot (e.g., Sahara) or cold (e.g., Antarctica) deserts because weathering in these environments is slower. In addition, recognizing meteorites in a desert environment is easier because the

dark gray or black fusion crust of meteorites is in stark contrast to the white (ice or snow) or yellowish (sand) surroundings. Meteorites in a hot and dry environment have to withstand large variations in temperature with some degree of interaction with water during the desert's 'wet period', while those found in cold deserts are in contact with ice. Therefore, long residence periods in such environments may lead to the alteration of the meteoritic components (Bland et al. 2006), and consequently may affect presolar silicate grains.

A few indicators have been identified on the basis of which predictions about the presence or absence of presolar silicate material in a given chondrite can be made.

- Matrices that are composed of opaque, fine-grained, and amorphous material are the least altered (Brearley 1993; Scott and Krot 2005).
- The presence of secondary minerals and phyllosilicates provides clues to the degree of aqueous alteration (Jones and Brearley 2006). Aqueous alteration modifies fine-grained matrix components and can certainly destroy presolar silicate grains. Isotopic anomalies in the sub-micrometer-sized presolar grains may also be eliminated via this process.
- The abundance of presolar components correlates strongly with the petrologic type of the host meteorites (Huss and Lewis 1995). These authors showed that the abundance of presolar material decreases systematically with increasing petrologic type. Although presolar nanodiamonds can be found in meteorites up to about type 3.8 (Huss and Lewis 1995), presolar silicate and graphite grains can be found predominantly in type 3.
- A low degree of graphitization observed in the carbonaceous material in the matrices of meteorites can also indicate low levels of thermal metamorphism (Brearley 1999; Bonal et al. 2006).

Based on all the above criteria, the least equilibrated members among the carbonaceous and enstatite chondrites were chosen for presolar silicate grain searches.

1.4.5. Samples in this Study

Acfer 094 and ALHA77307 were chosen for presolar grain searches because they are considered to be among the most pristine chondrites known to date (Brearley 1993; Greshake 1997; Grossman and Brearley 2005). Little is known about the metamorphic history of enstatite chondrites. They display a variety in mineralogical makeup because of a complex thermal and shock histories compared to other chondrite classes. It has been argued that enstatite chondrites have experienced thermal alteration, which may have destroyed or altered the presolar grains in them. Searches in enstatite chondrites can reveal whether presolar grains have survived these complex secondary processes and whether there are chemical differences in the presolar grain populations between carbonaceous and enstatite chondrites. We chose to search for presolar silicate grains in a very pristine enstatite chondrite, SAH 97096 (Weisberg and Prinz 1998).

The diversity in the meteorite classes and environments from where they were collected can help us to understand differences in presolar silicate grain abundances. The meteorites Acfer 094 and ALHA77307 are carbonaceous chondrites; the former is from the Sahara desert while the latter is from Allan Hills, Antarctica. The enstatite chondrite SAH 97096 is another sample from the Sahara desert.

Meteoritic samples used for this thesis include grain size-separates from the meteorites Acfer 094 and SAH 97096, and a thin-section of ALHA77307 acquired from the curatorial facilities at Johnson Space Center (Figure 1.8). See Nguyen (2005) for details about the preparation of physical separates from small chunks of meteorites.

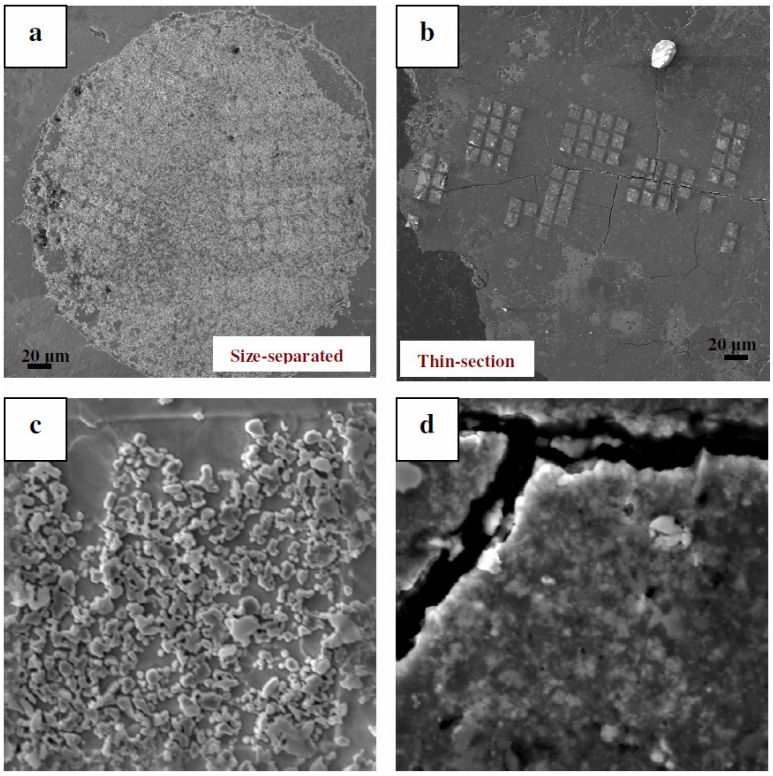

Figure 1.8: High-resolution secondary electron images acquired in the Auger Nanoprobe of some meteoritic samples used in this research. Figures a and b show size-separates of Acfer 094 matrix and matrix areas of the ALHA77307 thin-section, respectively. Figures c and d show a 10×10 μm^2 analyzed area on the grain size-separates of Acfer 094 and on the thin-section of ALHA77307, respectively.

There are benefits and limitations of both these samples with respect to laboratory analyses. A benefit for performing isotopic measurements on size-separated grains is that subsequent to the identification of presolar grains, location of the grain using image alignment programs is easier. Alignment of secondary electron images is difficult in the case of *in situ* analyses because the images from the NanoSIMS often look very different from the high-resolution images acquired in the Auger Nanoprobe. The primary disadvantage of identifying presolar grains in size-separates is that the petrographic context is lost. Auger Nanoprobe analyses of the grains on a Au mount (such as for size-separates) reveal that charging is reduced or completely eliminated. Thin-sections of

chondrites are typically C coated to avoid charging issues. The analyzed areas are separated by areas with C coating on them. Note that the carbonaceous chondrites don't charge in the areas devoid of the C coating because they contain carbonaceous material in their matrix.

1.5. Research Objectives

The primary research objective of this dissertation is the identification and characterization of presolar silicate grains in a number of primitive meteorites. It presents elemental compositions of numerous presolar silicate grains identified in physical size-separates and *in situ* in meteorite thin-sections. Subsequent to the initial characterization of large numbers of silicate grains, rare grains were chosen for further isotopic measurements of their major elements such as Si and Fe. For example, Fe was measured in some presolar grains (see chapter 3) because we found that numerous silicate grains are Fe-rich and Fe isotopic analyses can provide clues to the origin of the high Fe contents of these grains. Apart from presolar silicate grains, coordinated NanoSIMS and Auger Nanoprobe analyses allowed the identification of presolar oxide and SiC grains as well as interstellar or protosolar carbonaceous grains.

Overview of the subsequent chapters is as follows:

Chapter 2 presents the Auger Nanoprobe instrumentation, developmental work, and application of Auger spectroscopy to the study of sub-micrometer-sized phases. Prior to studying extraterrestrial materials, powdered terrestrial samples were analyzed as standards and to study the instrument's performance under different experimental conditions.

Chapter 3 titled "An Investigation into the origin of Fe-rich presolar silicates in Acfer 094" (2010) Bose M., Floss C., and Stadermann F. J. is published in The Astrophysical Journal (**714**, 1624-1636).

Chapter 4 titled "Stardust material in the paired enstatite meteorites: SAH 97096 and SAH 97159" (2010) Bose M., Zhao X., Floss C., Stadermann F. J., and Lin Y. is published in the Proceedings of Science for 11th Nuclei in the Cosmos held in Heidelberg (POS NIC XI 138).

Chapter 5 titled " Stellar and interstellar material in the CO3 chondrite ALHA77307: An isotopic and elemental investigation" is in preparation for submission to Geochimica et Cosmochimica Acta.

Chapter 6 offers potential future work.

References

Alexander C. M. O'D. (1993) Presolar SiC in chondrites: how variable and how many sources? *Geochimica et Cosmochimica Acta* **57**, 2869-2888.

Alexander C. M. O'D. and Nittler L. R. (1999) The galactic evolution of Si, Ti and O isotopic ratios. *The Astrophysical Journal* **519**, 222-235.

Amari S., Anders E., Virag A., and Zinner E. (1990) Interstellar graphite in meteorites. *Nature* **345**, 238-240.

Amari S., Hoppe P., Zinner E., and Lewis R. S. (1992) Interstellar SiC with unusual isotopic compositions: grains from a supernova? *The Astrophysical Journal* **394**, L43-L46.

Amari S., Lewis R. S., and Anders E. (1994) Interstellar grains in meteorites. I: Isolation

of SiC, graphite, and diamond; size distributions of SiC and graphite. *Geochimica et Cosmochimica Acta* **58**, 459-470.

Amari S., Hoppe P., Zinner E., and Lewis R. S. (1995a) Trace-element concentrations in single circumstellar silicon carbide grains from the Murchison meteorite. *Meteoritics* **30**, 679-693.

Amari S., Lewis R. S., and Anders E. (1995b) Interstellar grains in meteorites. III: Graphite and its noble gases. *Geochimica et Cosmochimica Acta* **59**, 1411-1426.

Amari S., Zinner E., and Lewis R. S. (1996) ^{41}Ca in presolar graphite of supernova origin. *The Astrophysical Journal* **470**, L101-L104.

Amari S., Nittler L. R., Zinner E., Gallino R., Lugaro M., and Lewis R. S. (2001a) Presolar SiC grains of type Y: origin from low-metallicity AGB stars. *The Astrophysical Journal* **546**, 248-266.

Amari S., Nittler L. R., Zinner E., Lodders K., and Lewis R. S. (2001b) Presolar SiC grains of type A and B: their isotopic compositions and stellar origins. *The Astrophysical Journal* **559**, 463-483.

Amari S., Gao X., Nittler L. R., Zinner E., Jose´ J., Hernanz M., and Lewis R. S. (2001c) Presolar grains from novae. *The Astrophysical Journal* **551**, 1065-1072.

Amari S., Zinner E., and Lewis R. S. (2004) Isotopic study of presolar graphite in the KFC1 separate from the Murchison meteorite. *Meteoritics and Planetary Science Supplement* 39, A13.

Amari S., Zinner E., and Lewis R. S. (2005) Isotopic analysis of presolar graphite from the KFB1 Murchison separate. *Meteoritics and Planetary Science Supplement* 40, A15.

Anders E. and Zinner E. (1993) Interstellar grains in primitive meteorites: diamond, silicon carbide, and graphite. *Meteoritics* **28**, 490-514.

Arnould M., Meynet G., and Paulus G. (1997) Wolf-Rayet stars and their nucleosynthetic signatures in meteorites. In: Astrophysical Implications of the Laboratory Study of Presolar Materials (eds. T. J. Bernatowicz and E. Zinner). AIP, New York, pp. 179-202.

Bernatowicz T., Fraundorf G., Tang M., Anders E., Wopenka B., Zinner E., and Fraundorf P. (1987) Evidence for interstellar SiC in the Murray carbonaceous meteorite. *Nature* **330**, 728-730.

Bernatowicz T. J., Gibbons P. C., and Lewis R. S. (1990) Electron energy loss spectrometry of interstellar diamonds. *The Astrophysical Journal* **358**, 246-255.

Bernatowicz T. J., Amari S., Zinner E. K., and Lewis R. S. (1991) Interstellar grains within interstellar grains. *The Astrophysical Journal* **373**, L73-L76.

Bernatowicz T. J., Cowsik R., Gibbons P. C., Lodders K., Fegley B., Jr., Amari S., and Lewis R. S. (1996) Constraints on stellar grain formation from presolar graphite in the Murchison meteorite. *The Astrophysical Journal* **472**, 760-782.

Bland P. A., Zolensky M. E., Benedix G. K., and Sephton M. A. (2006) Weathering of chondritic meteorites. In: Meteorites and the Early Solar System II (eds. D. S. Lauretta and H. Y. McSween Jr.), The University of Arizona Press, Tucson. pp. 853-868.

Black D. C. and Pepin R. O. (1969) Trapped neon in meteorites II. *Earth and Planetary Science Letters* **6**, 395-405.

Bonal L., Bourot-Denise M., Quirico E., Montagnac G., and Lewin E. (2006) Organic matter and metamorphic history of CO chondrites. *Geochimica et Cosmochimica Acta* **71**, 1605-1623.

Boothroyd A. I., Sackmann I.-J., and Wasserburg G. J. (1994) Predictions of oxygen isotope ratios in stars and of oxygen-rich interstellar grains in meteorites. *The Astrophysical Journal* **430**, L77-L80.

Boothroyd A. I. and Sackmann I.-J. (1999) The CNO isotopes: Deep circulation in red giants and first and second dredge-up. *The Astrophysical Journal* **510**, 232-250.

Brearley A. (1993) Matrix and fine-grained rims in the unequilibrated CO3 chondrite, ALHA77307: origins and evidence for diverse, primitive nebular dust components. *Geochimica et Cosmochimica Acta* **57**, 1521-1550.

Brearley A. (1999) Origin of graphitic carbon and pentlandite in the matrix olivines in the Allende meteorite. *Science* **285**, 1380-1382.

Brearley A. J. (2006) The action of water. In: Meteorites and the Early Solar System II (eds. D. S. Lauretta and H. Y. McSween Jr.), The University of Arizona Press, Tucson. pp. 587-624.

Busso M., Gallino R., and Wasserburg G. J. (1999) Nucleosynthesis in asymptotic giant branch stars: Relevance for galactic enrichment and solar system formation. *Annual Reviews of Astronomy and Astrophysics* **37**, 239-309.

Burbidge E. M., Burbidge G. R., Fowler W. A., and Hoyle F. (1957) Synthesis of the elements in stars. *Reviews of Modern Physics* **29**, 547-650.

Cameron A. G. W. (1957) Stellar evolution, nuclear astrophysics and nucleogenesis. *Publications of Astronomical Society Pacific* **69**, 201-222.

Cameron A. G. W. (1962) The formation of the sun and planets. *Icarus* **1**, 13-69.

Choi B.-G., Huss G. R., Wasserburg G. J., and Gallino R. (1998) Presolar corundum and spinel in ordinary chondrites: Origins from AGB stars and a supernova. *Science* **282**, 1284-1289.

Choi B.-G., Wasserburg G. J., and Huss G. R. (1999) Circumstellar hibonite and corundum and nucleosynthesis in asymptotic giant branch stars. *The Astrophysical Journal* **522**, L133-L136.

Clayton R. N., Grossman L., and Mayeda T. K. (1973) A component of primitive nuclear composition in carbonaceous meteorites. *Science* **182**, 485-488.

Clayton D. D. (1989) Origin of heavy xenon in meteoritic diamonds. *The Astrophysical Journal* **340**, 613-619.

Clayton D. D., Meyer B. S., Sanderson C. I., Russell S. S., and Pillinger C. T. (1995) Carbon and nitrogen isotopes in type II supernova diamonds. *The Astrophysical Journal* **447**, 894-905.

Clayton D. D. (2003) Presolar galactic merger spawned the SiC grain mainstream. *The Astrophysical Journal* **598**, 313-324.

Croat T. K., Bernatowicz T., Amari S., Messenger S., and Stadermann F. J. (2003) Structural, chemical, and isotopic microanalytical investigations of graphite from supernovae. *Geochimica et Cosmochimica Acta* **67**, 4705-4725.

Daulton T. L., Eisenhour D.D., Bernatowicz T. J., Lewis R. S., and Buseck P. R. (1996) Genesis of presolar diamonds: comparative high-resolution transmission electron microscopy study of meteoritic and terrestrial nanodiamonds. *Geochimica et Cosmochimica Acta* **60**, 4853-4872.

Daulton T. L., Bernatowicz T. J., Lewis R. S., Messenger S., Stadermann F. J., and Amari S. (2002) Polytype distribution in circumstellar silicon carbide. *Science* **296**, 1852-1855.

Dauphas N., Remusat L., Chen J. H., Roskosz M., Papanastassiou D. A., Stodolna J., Guan Y., Ma, C., and Eiler J. M. (2010) Neutron-rich chromium isotope anomalies in supernova nanoparticles. *The Astrophysical Journal* **720**, 1577-1591.

Floss C., Stadermann F. J., and Bose M. (2008) Circumstellar Fe oxide from the Acfer 094 carbonaceous chondrite. *The Astrophysical Journal* **672**, 1266-1271.

Gallino R., Raiteri C. M., Busso M., and Matteucci F. (1994) The puzzle of silicon, titanium and magnesium anomalies in meteoritic silicon carbide grains. *The Astrophysical Journal* **430**, 858-869.

Greshake A. (1997) The primitive matrix components of the unique carbonaceous chondrite Acfer 094: a TEM study. *Geochimica et Cosmochimica Acta* **61**, 437-452.

Gröner E. and Hoppe P. (2006) Automated ion imaging with the NanoSIMS ion microprobe. *Applied Surface Science* **252**, 7148-7151.

Grossman J. N. and Brearley A. (2005) The onset of metamorphism in ordinary and carbonaceous chondrites. *Meteoritics and Planetary Science* **40**, 87-122.

Gyngard F., Amari S., Zinner E., and Ott U. (2009) Interstellar exposure ages of large SiC grains from the Murchison meteorite. *The Astrophysical Journal* **694**, 359-366.

Gyngard F., Zinner E., Nittler L. R., Morgand A., Stadermann F. J., and Hynes K. M. (2010) Automated NanoSIMS measurements of spinel stardust from the Murray meteorite. *The Astrophysical Journal* **717**, 107-120.

Harris M. J. and Lambert D. L. (1984) Oxygen isotopic abundances in the atmospheres of

seven red giant stars. *The Astrophysical Journal* **285**, 674-682.

Harris M. J., Lambert D. L., Hinkle K. H., Gustafsson B., and Eriksson K. (1987) Oxygen isotopic abundances in evolved stars. III: 26 carbon stars. *The Astrophysical Journal* **316**, 294-304.

Heck P. R., Gyngard F., Meier M. M. M., Avila J. N., Amari S., Zinner E., Lewis R. S., Baur H., and Wieler R. (2008) *Lunar and Planetary Science* 39, Abstract #1239

Herwig F., Amari S., Lugaro M., and Zinner E. (2004) Could SiC A+B grains have originated in a post-AGB thermal pulse? In: Planetary Nebulae: Their Evolution and Role in the Universe (eds. S. Kwok, M. Dopita, and R. Sutherland). PASP Conf. Ser., IAU Symp, Canberra, Australia, vol. 209, pp. 311-312.

Hoppe P., Amari S., Zinner E., Ireland T., and Lewis R. S. (1994) Carbon, nitrogen, magnesium, silicon and titanium isotopic compositions of single interstellar silicon carbide grains from the Murchison carbonaceous chondrite. *The Astrophysical Journal* **430**, 870-890.

Hoppe P., Amari S., Zinner E., and Lewis R. S. (1995) Isotopic compositions of C, N, O, Mg, and Si, trace element abundances, and morphologies of single circumstellar graphite grains in four density fractions from the Murchison meteorite. *Geochimica et Cosmochimica Acta* **59**, 4029-4056.

Hoppe P., Strebel R., Eberhardt P., Amari S., and Lewis R. S. (1996) Type II supernova matter in a silicon carbide grain from the Murchison meteorite. *Science* **272**, 1314-1316.

Hoppe P. and Ott U. (1997a) Mainstream silicon carbide grains from meteorites. In: Astrophysical Implications of the Laboratory Study of Presolar Materials (eds. T. J.

Bernatowicz and E. Zinner). AIP, New York, pp. 27-58.

Hoppe P., Annen P., Strebel R., Eberhardt P., Gallino R., Lugaro M., Amari S., and Lewis R. S. (1997b) Meteoritic silicon carbide grains with unusual Si-isotopic compositions: Evidence for an origin in low-mass metallicity asymptotic giant branch stars. *The Astrophysical Journal* **487**, L101-L104.

Huss G. R., Fahey A. J., Gallino R., and Wasserburg G. J. (1994) Oxygen isotopes in circumstellar Al_2O_3 grains from meteorites and stellar nucleosynthesis. *The Astrophysical Journal* **430**, L81-L84.

Huss G. R. and Lewis R. S. (1995) Presolar diamond, SiC, and graphite in primitive chondrites: Abundances as a function of meteorite class and petrology type. *Geochimica et Cosmochimica Acta* **59**, 115-160.

Huss G. R., Hutcheon I. D., and Wasserburg G. J. (1997) Isotopic systematics of presolar silicon carbide from the Orgueil (CI) carbonaceous chondrite: implications for solar system formation and stellar nucleosynthesis. *Geochimica et Cosmochimica Acta* **61**, 5117-5148.

Huss G. R., Rubin A. E., and Grossman J. N. (2006) Thermal metamorphism in chondrites. In: Meteorites and the Early Solar System II (eds. D. S. Lauretta and H. Y. McSween Jr.), The University of Arizona Press, Tucson. pp. 567-586.

Hutcheon I. D., Huss G. R., Fahey A. J., and Wasserburg G. J. (1994) Extreme ^{26}Mg and ^{17}O enrichments in an Orgueil corundum: Identification of a presolar oxide grain. *The Astrophysical Journal* **425**, L97-L100.

Hynes K. M., Croat T. K., Amari S., Mertz A. F., and Bernatowicz T. J. (2010) Strustural and isotopic microanalysis of presolar SiC from supernovae. *Meteoritics and*

Planetary Science **45**, 596-614.

Jadhav M., Amari S., Zinner E., and Maruoka T. (2006) Isotopic analysis of presolar graphite grains from Orgueil. *New Astronomy Reviews* **50**, 591-595.

Jadhav M., Amari S., Marhas K. K., Zinner E., Maruoka T., and Gallino R. (2008) New stellar sources for high-density, presolar graphite grains. *The Astrophysical Journal* **682**, 1479-1485.

Jones C. L. and Brearley A. J. (2006) Experimental aqueous alteration of the Allende meteorite under oxidizing conditions: constraints on asteroidal alteration. *Geochimica et Cosmochimica Acta* **70**, 1040-1058.

Jørgensen U. G. (1988) Formation of Xe–HL-enriched diamond grains in stellar environments. *Nature* **332**, 702-705.

Lewis R. S., Srinivasan B., and Anders E. (1975) Host phase of a strange xenon component in Allende. *Science* **190**, 1251-1262.

Lewis R. S., Tang M., Wacker J. F., Anders E., and Steel E. (1987) Interstellar diamonds in meteorites. *Nature* **326**, 160-162.

Lewis R. S., Amari S., and Anders E. (1994) Interstellar grains in meteorites: II. SiC and its noble gases. *Geochimica et Cosmochimica Acta* **58**, 471-494.

Manuel O. K., Hennecke E. W., and Sabu D. D. (1972) Xenon in carbonaceous chondrites. *Nature* **240**, 99-101.

Messenger S., Keller L. P., Stadermann F. J., Walker R. M., and Zinner E. (2003) Samples of stars beyond the solar system: silicate grains in interplanetary dust. *Science* **300**, 105-108.

Mostefaoui S. and Hoppe P. (2004) Discovery of abundant in situ silicate and spinel

grains from red giant stars in a primitive meteorite. *The Astrophysical Journal* **613**, L149-L152.

McCulloch M. T. and Wasserburg G. J. (1978) Barium and neodymium isotopic anomalies in the Allende meteorite. *The Astrophysical Journal* **220**, L15-L19.

Nagashima K., Krot A. N., and Yurimoto H. (2004) Stardust silicates from primitive meteorites. *Nature* **428**, 921-924.

Nguyen A. N. and Zinner E. (2004) Discovery of ancient silicate stardust in a meteorite. *Science* **303**, 1496-1499.

Nguyen A. N. (2005) Characterization of presolar silicate grains in primitive meteorites by multi-detection raster ion imaging in the NanoSIMS. Ph.D. Thesis, pp. 194.

Nittler L. R., Alexander C. M. O'D., Gao X., Walker R. M., and Zinner E. K. (1994) Interstellar oxide grains from the Tieschitz ordinary chondrite. *Nature* **370**, 443-446.

Nittler L. R., Hoppe P., Alexander C. M. O'D., Amari S., Eberhardt P., Gao X., Lewis R., Strebel R., Walker R. M., and Zinner E. (1995) Silicon nitride from supernovae. *The Astrophysical Journal* **453**, L25-L28.

Nittler L. R., Amari S., Zinner E., Woosley S. E., and Lewis R. S. (1996) Extinct ^{44}Ti in presolar graphite and SiC: Proof of a supernova origin. *The Astrophysical Journal* **462**, L31-L34.

Nittler L. R., Alexander C. M. O'D., Gao X., Walker R. M., and Zinner E. (1997) Stellar sapphires: the properties and origins of presolar Al_2O_3 in meteorites. *The Astrophysical Journal* **483**, 475-495.

Nittler L. R. and Alexander C. M. O'D. (2003) Automated isotopic measurements of micron-sized dust: application to meteoritic presolar silicon carbide. *Geochimica*

et Cosmochimica Acta **67**, 4961-4980.

Nittler L. R., Alexander C. M. O'D., Stadermann F. J., and Zinner E. K. (2005) Presolar chromite in Orgueil. *Meteoritics and Planetary Science Supplement* 40, A114.

Nittler L. R., Alexander C. M. O'D., Gallino R., Hoppe P., Nguyen A. N., Stadermann F. J., and Zinner E. K. (2008) Aluminum-, calcium-, and titanium-rich oxide stardust in ordinary chondrite meteorites. *The Astrophysical Journal* **682**, 1450-1478.

Nollett K. M., Busso M., and Wasserburg G. J. (2003) Cool bottom processes on the thermally pulsing asymptotic giant branch and the isotopic composition of circumstellar dust grains. *The Astrophysical Journal* **582**, 1036-1058.

Nuth J. A. and Allen J. E. (1992) Supernovae as sources of interstellar diamonds. *Astrophysics and Space Science* **196**, 117-123.

Ott U. (1993) Interstellar grains in meteorites. *Nature* **364**, 25-33.

Ott U., Altmaier M., Herpers U., Kuhnhenn J., Merchel S., Michel R., and Mohapatra R. K. (2005) Spallation recoil II: Xenon evidence for young SiC grains. *Meteoritics and Planetary Science* **40**, 1635-1652.

Ozima M. and Mochizuki K. (1993) Origin of nanodiamonds in primitive chondrites: (1) Theory. *Meteoritics* **28**, 416-417.

Pellin M. J., Davis A. M., Calaway W. F., Lewis R. S., Clayton R. N., and Amari S. (2000) Zr and Mo isotopic constraints on the origin of unusual types of presolar SiC grains. *Lunar and Planetary Science Conference* 31, Abstract #1934.

Qin L., Nittler L. R., Alexander C. M. O'D., Wang J., Stadermann F. J., and Carlson R. W. (2011) Extreme Cr-rich nano-oxides in the CI chondrite Orgueil — Implications for a late supernova injection into the solar system. *Geochimica et Cosmochimica*

Acta **75**, 629-644.

Reynolds J. H. and Turner G. (1964) Rare gases in the chondrite Renazzo. *Journal of Geophysical Research* **69**, 3263-3281.

Russell S. S., Arden J. W., and Pillinger C. T. (1996) A carbon and nitrogen isotope study of diamond from primitive chondrites. *Meteoritics and Planetary Science* **31**, 343-355.

Sabu D. D. and Manuel O. K. (1976) Xenon record of the early solar system. *Nature* **262**, 28-32.

Scott E. R. D. and Krot A. N. (2005) Thermal processing of silicate dust in the solar nebula: clues from primitive chondrite matrices. *The Astrophysical Journal* **623**, 571-578.

Smith V. V. and Lambert D. L. (1990) The chemical composition of red giants. III. Further CNO isotopic and s-process abundances in thermally pulsing asymptotic giant branch stars. *The Astrophysical Journal Supplement* **72**, 387-416.

Srinivasan B.and Anders E. (1978) Noble gases in the Murchison meteorite: possible relics of s-process nucleosynthesis. *Science* **201**, 51-56.

Stadermann F. J., Croat T. K., Bernatowicz T. J., Amari S., Messenger S., Walker R. M., and Zinner E. (2005) Supernova graphite in the NanoSIMS: carbon, oxygen and titanium isotopic compositions of a spherule and its TiC sub-components. *Geochimica et Cosmochimica Acta* **69**, 177-188.

Stadermann F. J., Floss C., Bose M., and Lea A. S. (2009) The use of Auger spectroscopy for the in situ elemental characterization of sub-micrometer presolar grains. *Meteoritics and Planetary Science* **44**, 1033-1049.

Stadermann F. J., Isheim D., Zhao X., Daulton T. L., Floss C., Seidman D. N., Heck P. R., Pellin M. J., Savina M. R., Hillier J., Mane A., Elam J., Davis A. M., Stephan T., and Amari S. (2011) Atom-probe tomographic characterization of meteoritic nanodiamonds and presolar SiC. *Lunar and Planetary Science Conference* 42, Abstract #1595.

Stroud R. M., Nittler L. R., and Alexander C. M. O'D (2004) Polymorphism in presolar Al_2O_3 grains from asymptotic giant branch stars. *Science* **305**, 1455-1457.

Stroud R. M., Chisholm M. F., Heck P. R., and Alexander C. M. O'D. (2011) Discovery of glassy carbon in meteoritic nanodiamond residues: Implications for nanodiamond origins. *Lunar and Planetary Science Conference* 42, Abstract #1940.

Tang M. and Anders E. (1988) Isotopic anomalies of Ne, Xe, and C in meteorites. II: Interstellar diamond and SiC: carriers of exotic noble gases. *Geochimica et Cosmochimica Acta* **52**, 1235-1244.

Tielens A., Seab C., Hollenbach D., and McKee C. (1987) Shock processing of interstellar dust: Diamonds in the sky. *The Astrophysical Journal* **319**, LI09-L113.

Timmes F. X. and Clayton D. D. (1996a) Galactic evolution of silicon isotopes: application to presolar SiC grains from meteorites. *The Astrophysical Journal* **472**, 723-741.

Timmes F. X., Woosley S. E., Hartmann D. H., and Hoffman R. D. (1996b) The production of ^{44}Ti and ^{60}Co in supernovae. *The Astrophysical Journal* **464**, 332-341.

Travaglio C., Gallino R., Amari S., Zinner E., Woosley S., and Lewis R. S. (1999) Low-density graphite grains and mixing in type II supernovae. *The Astrophysical Journal* **510**, 325-354.

Virag A., Wopenka B., Amari S., Zinner E., Anders E., and Lewis R. S. (1992) Isotopic, optical, and trace element properties of large single SiC grains from the Murchison meteorite. *Geochimica et Cosmochimica Acta* **56**, 1715-1733.

Wasserburg G. J., Lee T., and Papanastassiou D. A. (1977) Correlated O And Mg isotopic anomalies in Allende Inclusions: II. Magnesium. *Geophysical Research letters* **4**, 299-302.

Wasserburg G. J., Boothroyd A. I., and Sackmann I.-J. (1995) Deep circulation in red giant stars: a solution to the carbon and oxygen isotope puzzles? *The Astrophysical Journal* **447**, L37-L40.

Weisberg M. K. and Prinz M. (1998) Sahara 97096: A highly primitive EH3 chondrite with layered sulfide metal-rich chondrules. *Lunar and Planetary Science Conference* 29, Abstract #1741.

Weisberg M. K., McCoy T. J., and Krot A. N. (2006) Systematics and evaluation of meteorite classification. In: Meteorites and the Early Solar System II (eds. D. S. Lauretta and H. Y. McSween Jr.), The University of Arizona Press, Tucson. pp. 19-52.

Zega T. J., Alexander C. M. O'D., Nittler L. R., and Stroud R. M. (2009) Transmission electron microscopy analysis of a presolar spinel grain. *Lunar and Planetary Science Conference* 40, Abstract #1342.

Zega T. J., Alexander C. M. O'D, Nittler L. R., and Stroud R. M. (2011) A transmission electron microscopy study of presolar hibonite. *The Astrophysical Journal*, in press.

Zinner E., Tang M., and Anders E. (1989) Interstellar SiC in the Murchison and Murray meteorites: Isotopic composition of Ne, Xe, Si, C, and N. *Geochimica et*

Cosmochimica Acta **53**, 3273-3290.

Zinner E., Amari S., Wopenka B., and Lewis R. S. (1995) Interstellar graphite in meteorites: isotopic compositions and structural properties of single graphite grains from Murchison. *Meteoritics* **30**, 209-226.

Zinner E., Amari S., Guinness R., Nguyen A., Stadermann F. J., Walker R. M., and. Lewis R. S (2003) Presolar spinel grains from the Murray and Murchison carbonaceous chondrites. *Geochimica et Cosmochimica Acta* **67**, 5083-5095.

Zinner E., Nittler L. R., Hoppe P., Gallino R., Straniero O., and Alexander C. M. O'D. (2005) Oxygen, magnesium and chromium isotopic ratios of presolar spinel grains. *Geochimica et Cosmochimica Acta* **69**, 4149-4165.

Zinner E., Nittler L. R., Alexander C. M. O'D., and Gallino R. (2006) The study of radioisotopes in presolar dust grains. *New Astronomy Reviews* **50**, 574-577.

Zinner E. (2007) Presolar Grains. In: Treatise on Geochemistry Update 1 (eds. H. D. Holland and K. K. Turekian; vol. ed. A. M. Davis), Elsevier Ltd., Oxford, Online update only. Vol. 1.02 pp. 1-33.

CHAPTER 2

AUGER NANOPROBE

Abstract

The underlying principles of Auger spectroscopy which form an integral part of the paper in *Meteoritics and Planetary Science* titled "The use of Auger spectroscopy for the *in situ* elemental characterization of sub-micrometer presolar grains" by Stadermann F. J., Floss C., Bose M., and Lea A. S. (2009) are briefly discussed in this chapter. The instrument parts associated with the PHI 700 Auger Nanoprobe at Washington University in St. Louis are elaborately discussed.

2.1. Introduction to Auger Spectroscopy

Auger spectroscopy is based on the Auger effect that was discovered by Lise Meitner and subsequently by Pierre Auger (e.g., Auger 1975). The basic principle for the production of Auger electrons is as follows: An electron beam hitting the sample knocks off an innermost electron of an atom (Figure 2.1). This is followed by a chain of events. An electron from the higher shell of the atom undergoes a transition to occupy this innermost energy state. The energy released in this process is normally released as an X-rays photon, which is measured in an energy dispersive X-ray spectrometer (EDXS) on a traditional scanning electron microscopy (SEM). Alternatively, an outer shell electron may be ejected in order to conserve energy; these electrons are called Auger electrons. Auger electrons with characteristics energies are measured in Auger spectroscopy.

If K is the innermost shell, L is the shell from which electrons make transitions to the K shell, and M is the shell from which Auger electrons are released (Figure 2.1), the characteristic energy with which the Auger electrons are released is

$$E = E_K - E_L - E_M$$

where energy E is associated with each shell. This transition is labeled KLM. Every element has unique energy levels; transitions of the type mentioned above allow the identification of Auger electrons that are characteristic of an element's energy levels and therefore, allows identification of the element. Transitions of the KLM type are not that common. The more common types of transitions include KLL, LMM, and MNN (Figure 2.2).

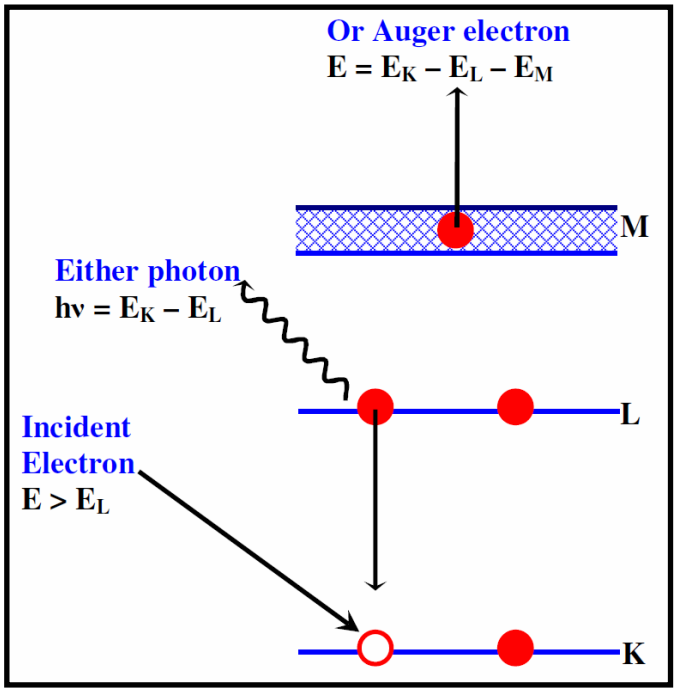

Figure 2.1: Schematic of the process involved in X-ray and characteristic Auger electron production.

A few elements do not produce characteristic Auger electrons. They include H and He because these elements do not have three electrons that can take part in the Auger process. Furthermore, Auger electrons cannot be generated from a single atom of Li because its outermost shell has only one electron (Bickel et al. 1969; Buchet et al. 1969). However, a group of Li atoms that share electrons in the valence shell can produce Auger electrons (Jackson et al. 1975).

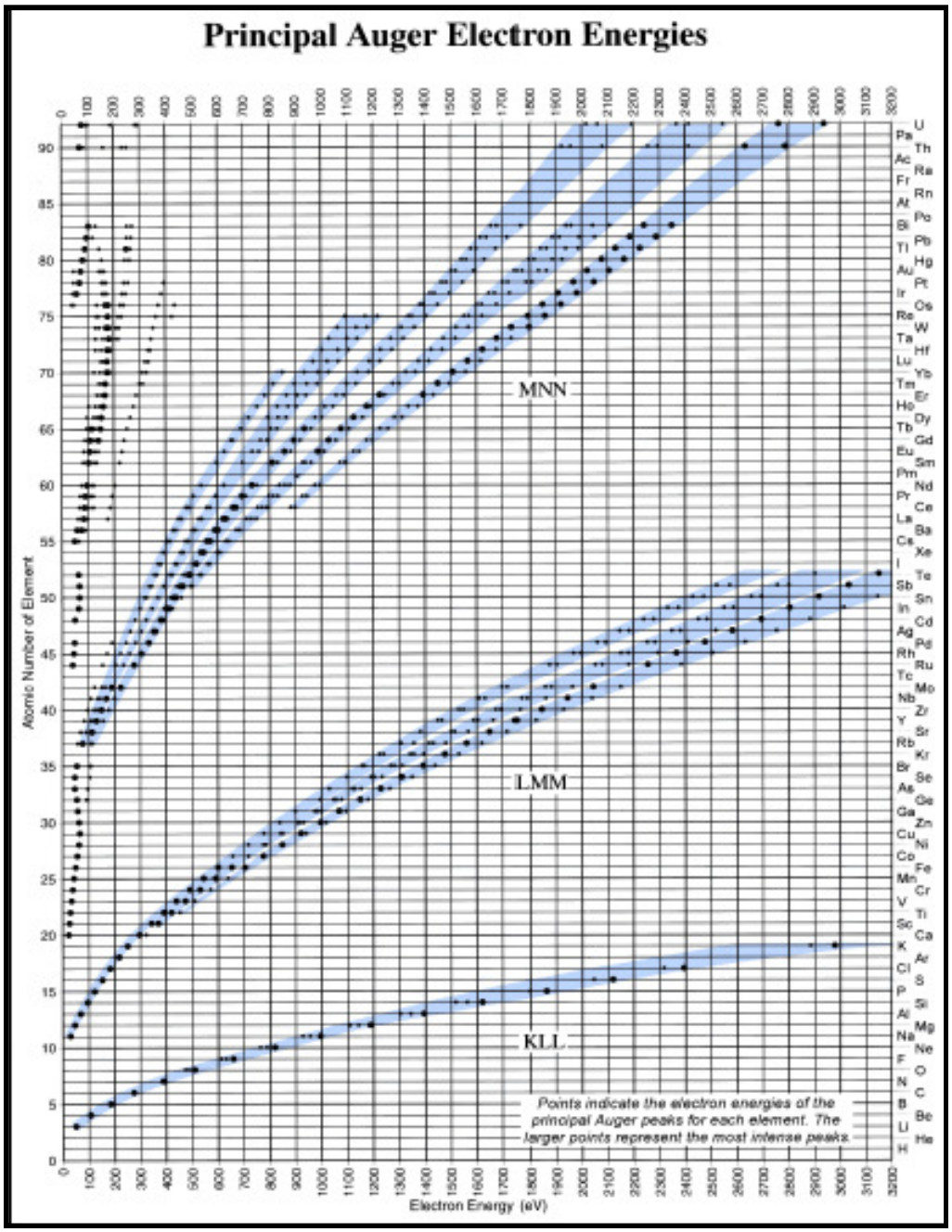

Figure 2.2: The Auger electron energy is plotted against atomic number. The Auger transitions for all elements from Li to U are indicated by dots. In many cases, multiple Auger peaks may appear. The sizes of the dots indicate the intensity of the Auger peaks. Figure from Childs et al. (1995).

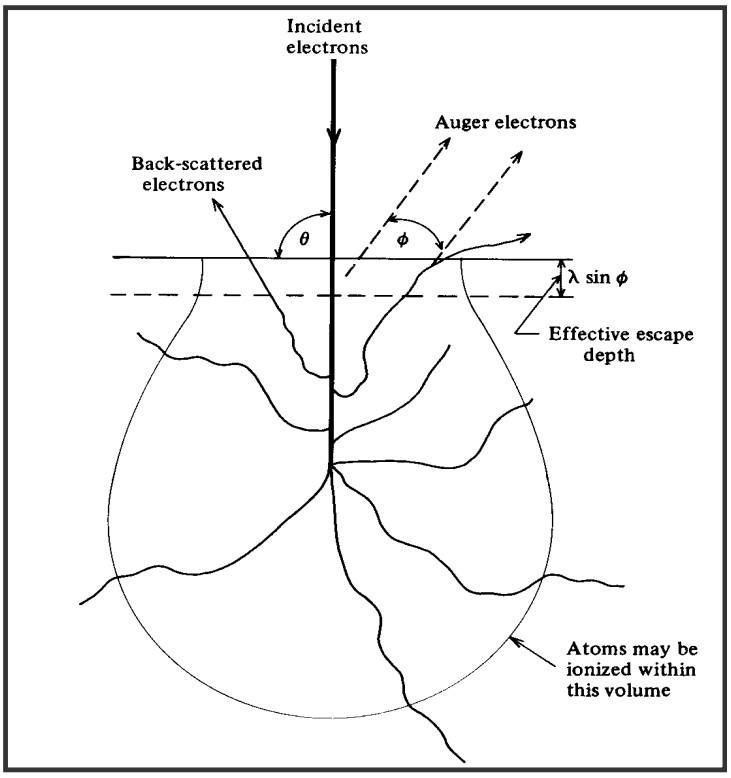

Figure 2.3: Schematic of the spatial distribution of Auger electron production and outcomes of electron-solid interaction. Picture from Bishop (1989).

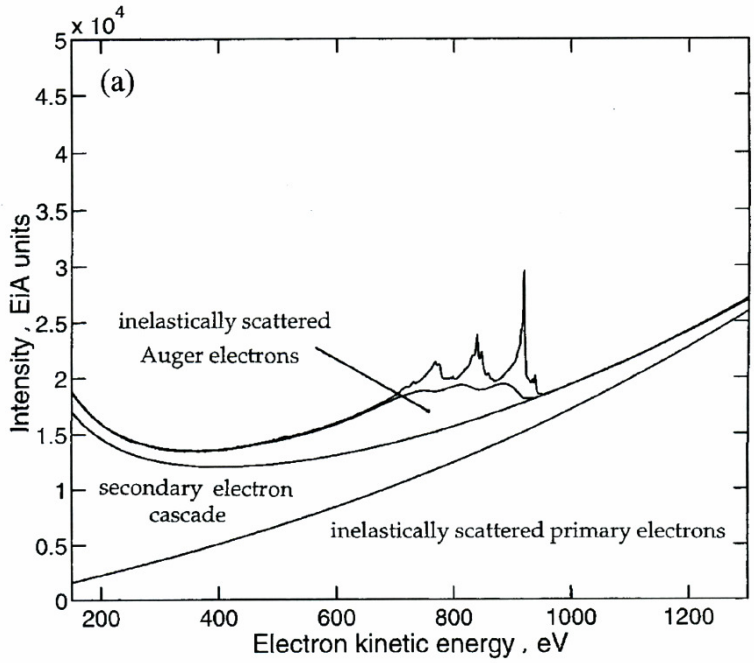

Figure 2.4: A typical Auger spectrum along with model fits of the various processes that contribute to the background. Picture from Seah (2003).

One of the most important attributes of Auger spectroscopy is its capability to image and characterize samples at high spatial resolution. The primary electron beam creates an 'onion-shaped' interaction volume, at the point of incidence, directly below the sample (Figure 2.3). Auger electrons are created within this volume but only those in the immediate vicinity of the sample surface are emitted with their *characteristic energies* and are subsequently detected in the Auger Nanoprobe. The finely focused electron beam used for analysis coupled with the fact that the characteristic Auger electrons are measured from the top 10–20 nm of the surface gives this technique a higher spatial resolution than SEM-EDXS.

An Auger spectrum is composed of the characteristic Auger peaks on a continuously increasing background of electrons (Figure 2.4). Electrons from deep within the "onion-shaped" region lose their energy, and contribute towards the background on which Auger peaks lie. The background of secondary electrons includes inelastically scattered primary electrons that form the dominant component and the secondary electron cascade. These background contributions increase with the electron energy. Apart from these, inelastically scattered Auger electrons are also part of the background. Auger peaks, themselves, have their own inelastic tails because some Auger electrons are excited slightly below the surface and have lost energy via collisions before escaping from the surface.

Prior to our work, Auger spectroscopy was used in the investigation of extraterrestrial materials such as lunar samples (Gold et al. 1974; Dikov et al. 1999), Fe-Ni meteorites (Marcus and Hackett 1974), and stratospheric dust particles (Mogk 1985). However, its widespread use as an analytical technique was largely stalled because sample charging

became an issue for insulating surfaces. Charging was not an issue in our studies because presolar grains are identified in physical size-separates that are dispensed onto gold foils on stainless steel mounts. The gold foil acts as a good conductor of any built-up electrical charge. Apart from size-separates, we identified presolar grains in a thin-section of a meteorite. Thin-sections are usually coated with C to provide a conductive surface. Prior to Auger Nanoprobe analysis, 12×12 μm^2 areas of the C coat is pre-sputtered in the NanoSIMS. The NanoSIMS analysis areas are separated by regions that are coated with C. As a result, the excess charge that can build-up will diminish quickly owing to the presence of the nearby conductive C coating. Other options that can be used to eliminate charging of samples include lowering the primary beam energy or introducing an Ar^+ ion beam to neutralize the charge, both of which were unnecessary for our measurements.

2.2. Instrumentation

A picture of the PHI 700 Auger Nanoprobe and its schematic shows the following main components (Figures 2.5 and 2.6):

2.2.1. Primary Electron Beam Optics

The primary beam optics consists of the electron source as well as electrostatic and magnetic lenses that are used to produce a fine electron beam. The electron source, also called the 'tip', is a single crystal of W that is coated with ZrO_2, which lowers the work function of the emitter surface and enhances electron production. The tip is slowly heated to 1800 K and subjected to an electrostatic field, which results in the emission of electrons. The emitting surface of the tungsten tip is about 20 nm and it produces an electron beam with a diameter of ~7 nm at 20 keV. One advantage of having a field

emission electron source is the production of a fine, coherent electron beam. Other advantages include long lifetimes and less stringent vacuum conditions (< 10^{-8} mbar). The chamber that contains the tip can be secluded from the rest of the instrument by an isolation valve.

The gun lens is the element that is closest to the tip's emitting surface (Figure 2.6). The emission of electrons of desired energy is dictated by the choice of the gun lens voltage. Subsequently, a combination of magnetic (e.g., objective lens close to the sample) and electrostatic (e.g., octupole and quadrupole) lenses is used to guide the electron beam through the center of the primary beam column. The gun steering and objective steering lenses also allow us direct the beam through the center of the primary column keeping the beam size to a minimum. In addition, the objective lens is used to focus the electron beam on the sample while the octupole lens corrects for astigmatism. The objective aperture has diameters of 0.004", 0.008", and 0.094" (bore hole). The smallest aperture is normally used in order to achieve the smallest beam size for a given primary beam current.

Predefined primary beam voltage and current settings are used for analyses. These settings are checked routinely and vary depending upon the tip's condition.

2.2.2. Electron energy analyzer-cylindrical mirror analyzer (CMA)

The Auger electrons emitted from the sample are analyzed using a CMA arrangement. The cylindrical mirror analyzer consists of inner and outer cylinders, both of which are kept at a fixed potential. The inner cylinder is grounded while the outer cylinder is held at a negative potential. The emitted Auger electrons pass through a mesh-

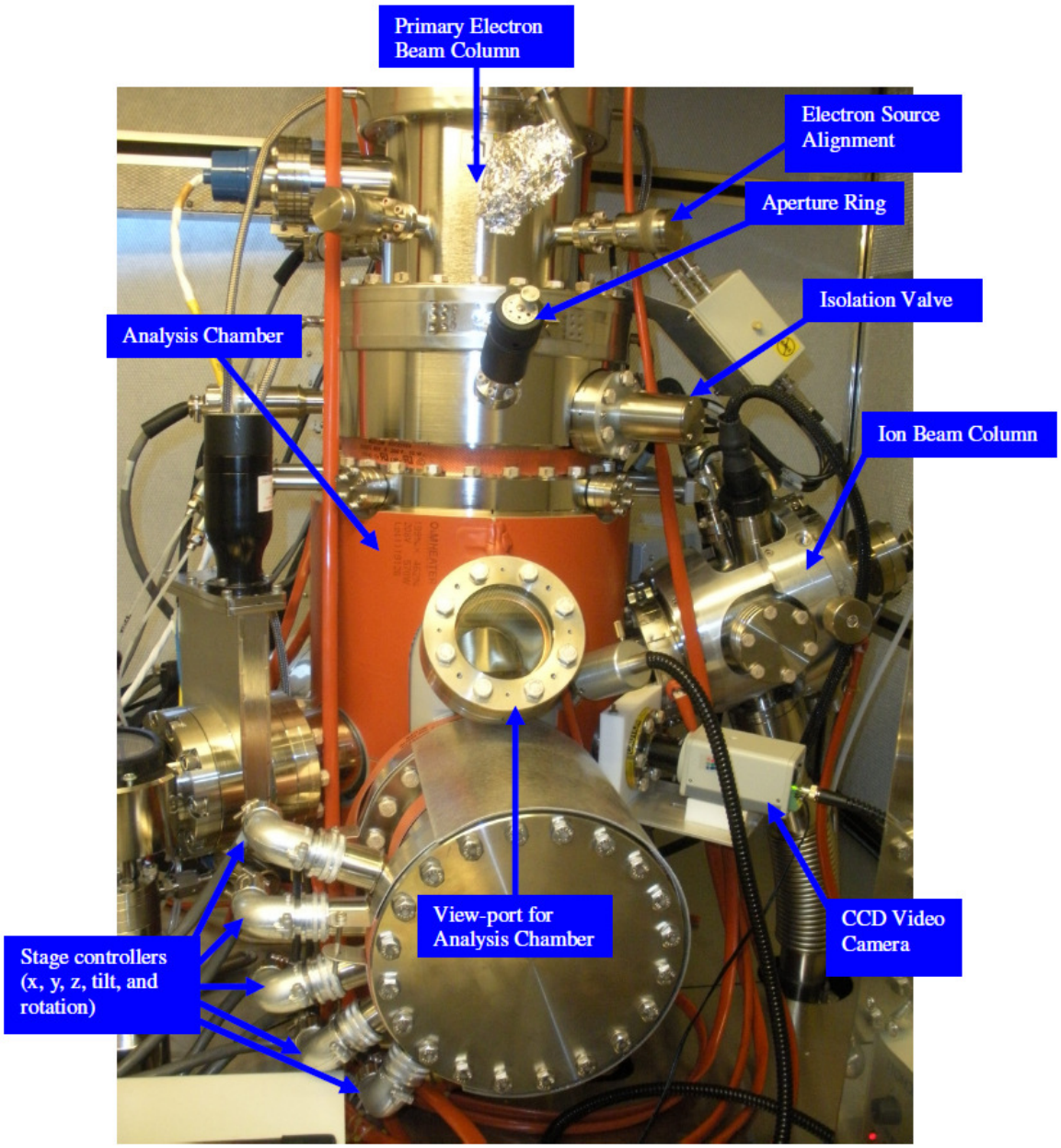

Figure 2.5: Labeled picture of the PHI 700 Auger Nanoprobe.

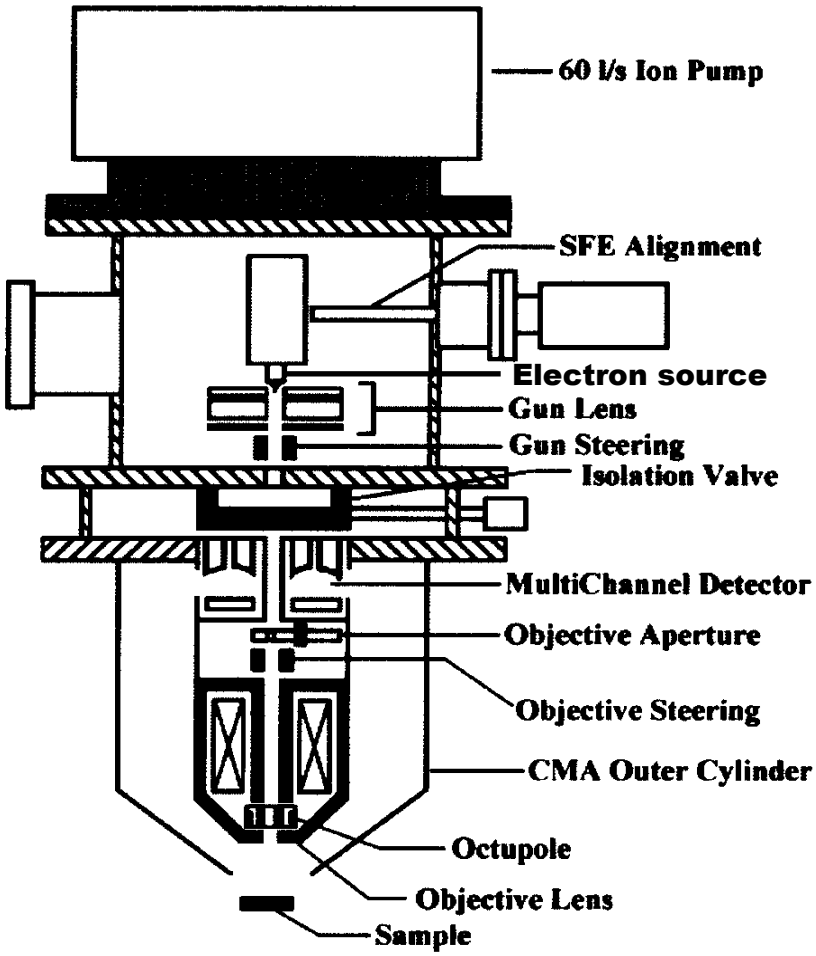

Figure 2.6: Cross-section of the PHI 700 Auger Nanoprobe from the instrument manual.

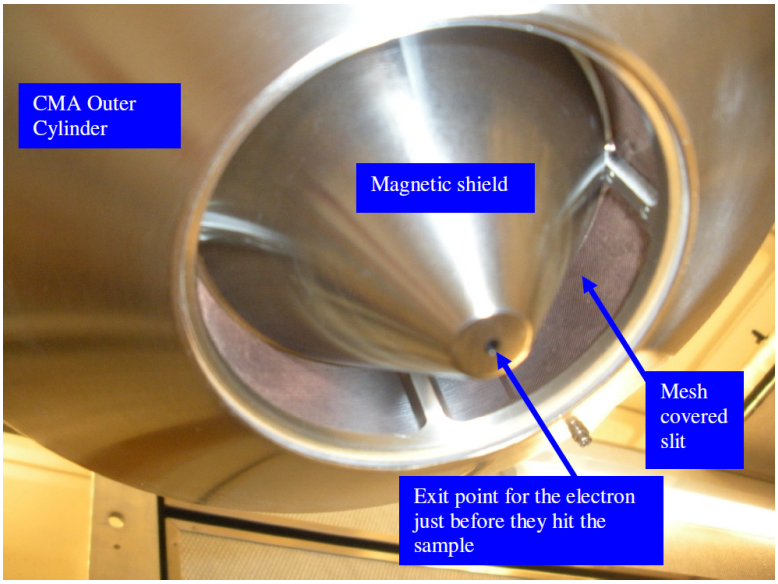

Figure 2.7: Close-up pictures of the primary electron optics.

covered slit (Figure 2.7) close to the sample, experience a repulsive field from the outer cylinder kept at a negative potential, and are deflected to pass through a second mesh slit close to the detectors, eventually coming to focus on the axis. If the emitted Auger electrons have high energy, they will hit the outer cylinder; electrons with low energy will be attracted to the inner cylinder. Therefore, Auger electrons within a very narrow energy range are allowed to reach the detector.

The primary advantage of the CMA arrangement is that the incoming electrons are perpendicular to the sample surface. This geometry is similar to the coaxial beam optics in the NanoSIMS 50. As a result no shadowing of the sample occurs in both cases during imaging. Furthermore, sample morphology and features *look* the same using the two instruments, which make it possible to precisely align both the secondary electron images. Precise alignment of the secondary electron images acquired by these complementary techniques is necessary to identify the isotopically anomalous grains.

Another advantage of the CMA design is that the electron gun is incorporated within the inner cylinder, which makes the instrument compact. However, it also makes tip replacement cumbersome. Additional disadvantages of the CMA design include a decrease in transmission and the appearance of aberrations because of the non-rigid meshes used at the slits in the inner cylinder.

2.2.3. Auger and Secondary Electron Detectors

Auger electron detectors for the PHI 700 Auger Nanoprobe are micro-channel plates, which are an array of miniature electron multipliers oriented parallel to each other. These micro-channel plates typically increase electron counts by factors of 10^6–10^7. The gain in electron counts in our instrument is further increased through the use of the micro-channel plates in a 'chevron' configuration. In this configuration, two micro-channel plates, separated by a small distance, are placed such that their axes are not parallel to each other but are biased at a small angle. As a result, an electron that may be produced at the output of the first plate is unable to travel to the second plate. Spurious signals occurring due to such electrons produced at the output of the first plate, thus, are eliminated. Concentric ring anodes are placed behind the micro-channel plates, which collect data from eight energy channels in parallel. The potential on the anode that is placed behind the micro-channel plates is varied from 30 to 2000 eV typically with a 0.5 or 1 eV per step resolution in energy. Auger electron counts are acquired at each voltage step as the anode voltage is increased. Typical dwell times for each voltage step used during measurements are 5 or 10 msec.

The primary beam hits the sample orthogonally producing Auger electrons and secondary electrons. The secondary electrons are detected by a secondary electron

detector consisting of a scintillator and photomultiplier. The secondary electrons are used to image the sample at high spatial resolution and help in sample navigation prior to analysis.

2.2.4. Ion Source

An Ar^+ ion source (Figure 2.5) is available in our instrument. It is used to sputter away the layer of contamination typically ~2×2 mm^2 area on the sample prior to analysis. The ion beam is at an angle of 30° to the axis of incoming electron beam. As a consequence, when a sample needs to be cleaned, the sample stage is tilted by an angle of 30°. In order to remove sample contamination *uniformly* over a given area, the stage is zalar rotated. Zalar rotation is the rotation of the sample stage with respect to a given point on the sample.

2.2.5. Other Relevant Details

The sample stage can be moved along the x, y, z directions and can be tilted (up to 30°) and rotated (Figures 2.5 and 2.8). The entire system is placed on a vibration table to minimize noise. Furthermore, a metal enclosure around the instrument maintains constant temperature and humidity.

Typical vacuums achieved in the source chamber and analysis chamber are better than ~1×10^{-10} and ~1×10^{-9} torr. Samples that outgas can be put in the introduction chamber and preheated in order to enhance the release of gases and subsequently put in the analysis chamber. Residual unwanted gases in the analysis chamber can be removed by Titanium Sublimation Pump (TSP) cycles, which can be preset to run overnight.

The SmartSoft (v4.1.1.27) software handles the day-to-day workings of the

instrument, while Multipak (v8.1B) software can be used for post-measurement data analysis. However, the multipak software was inept at doing certain things, e.g., alignment of the secondary electrons images acquired in the NanoSIMS and Auger Nanoprobe, and so numerous data analysis softwares were written by Dr. Frank J. Stadermann to address these issues. The software that aided in alignment is *Image Align.* Analysis of the elemental spectra and maps was done with *ReadSpectra* and *SEMphases*, respectively. Other data analysis softwares that are routinely used include those that check for shifts before and after measurements, and superimpose the 10×10 μm^2 NanoSIMS analysis areas on the secondary electron image of the thin-section.

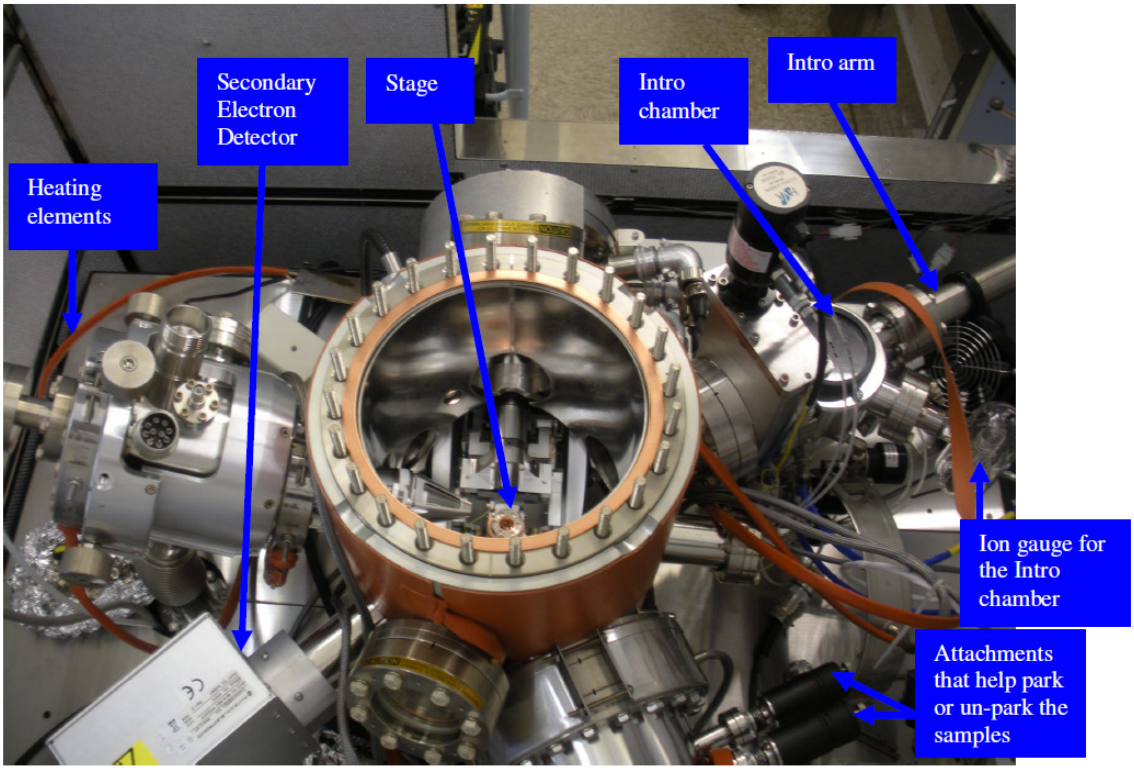

Figure 2.8: Top view of the sample chamber.

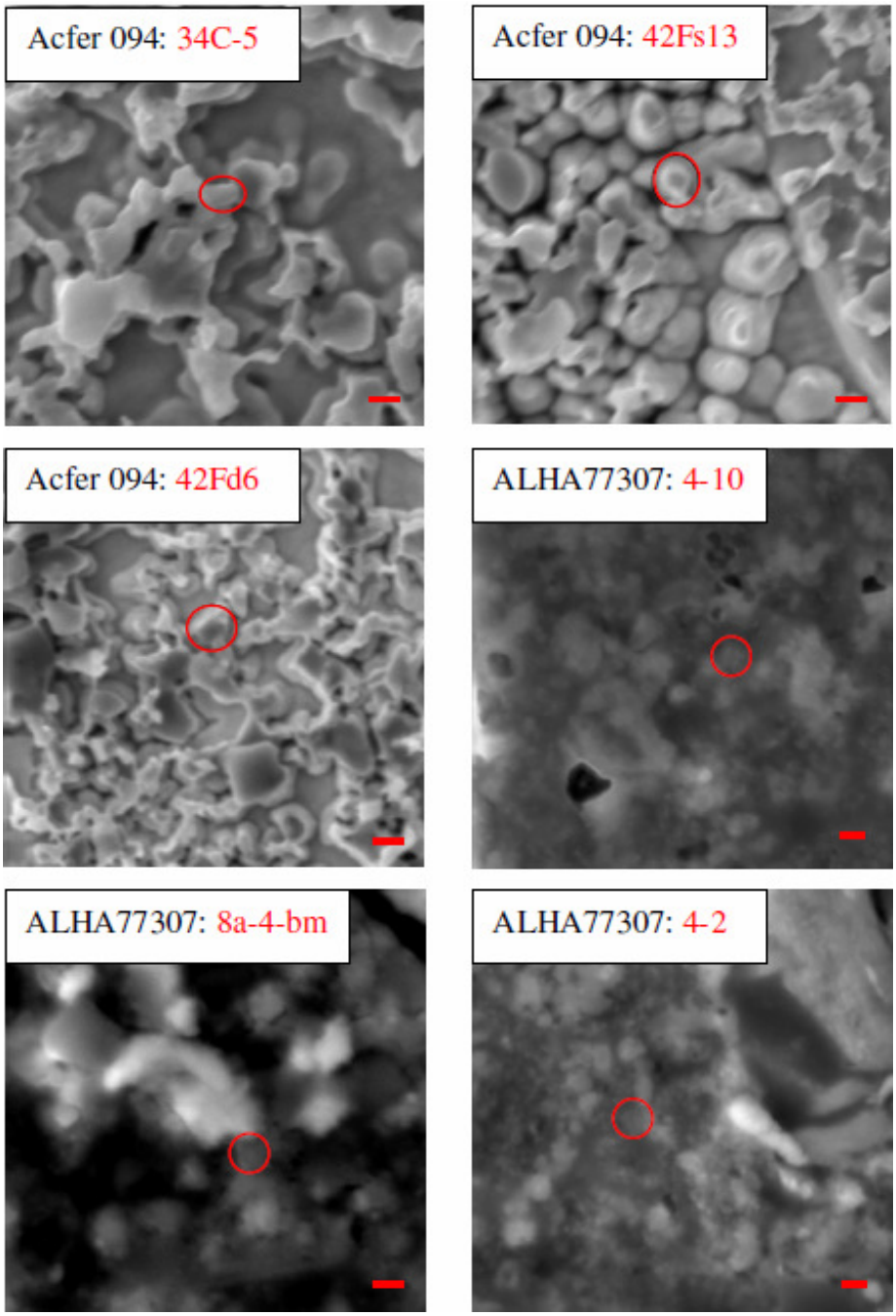

Figure 2.9: Presolar silicate grains in Type 3 carbonaceous chondrites, Acfer 094 and ALHA77307 (scale bars are 200 nm).

2.3. Initial Analyses

2.3.1. Samples for our Study

We are primarily interested in studying presolar silicate grains and interstellar or protosolar carbonaceous phases. These are small in size, especially the presolar silicate grains are predominantly smaller than 300 nm in diameter (Figure 2.9). The Auger Nanoprobe has the ability to take high-resolution pictures and obtain elemental compositions on a routine basis. Quantitative analysis can be rapidly (~20 min) carried out for the sub-micrometer grains.

Characterizing presolar phases in the Auger Nanoprobe is usually an intermediate step, after which some grains with unique isotopic and/or elemental signatures can be chosen for study using other analytical techniques.

2.3.2. Measurement Settings

We developed the methodology and analytical protocols for the acquisition of spectra and maps, specifically for presolar silicates. The best analytical parameters were obtained by repeated measurements on terrestrial standards. The detailed reasoning behind our choice of settings is laid out in Stadermann et al. (2009) and is briefly discussed here.

The optimal beam voltage setting is chosen based on a balance between achieving reasonably good spatial resolution and producing Auger electrons corresponding to the elements present in the samples. Images and maps at high spatial resolution can be achieved at either 20 keV or 10 keV voltage settings. Electrons at 10 keV will penetrate deeper into the particle and reduce edge effects that degrade spatial resolution (Ito et al. 1996). On the other hand, Auger peaks in the differentiated spectra exhibit a higher

intensity at 10 keV than at the 3 or 5 keV settings. An example of this can be seen in Figure 2.10, in which the O_{KLL} peak is most prominent at the highest beam voltage setting. Because we are interested in measuring Auger electrons up to 2 keV, using a lower energy beam will result in the loss of sensitivity at the higher end of the spectra. Therefore, on the basis of signal-to-noise and spatial resolution arguments, a good setting for the primary beam voltage is 10 keV.

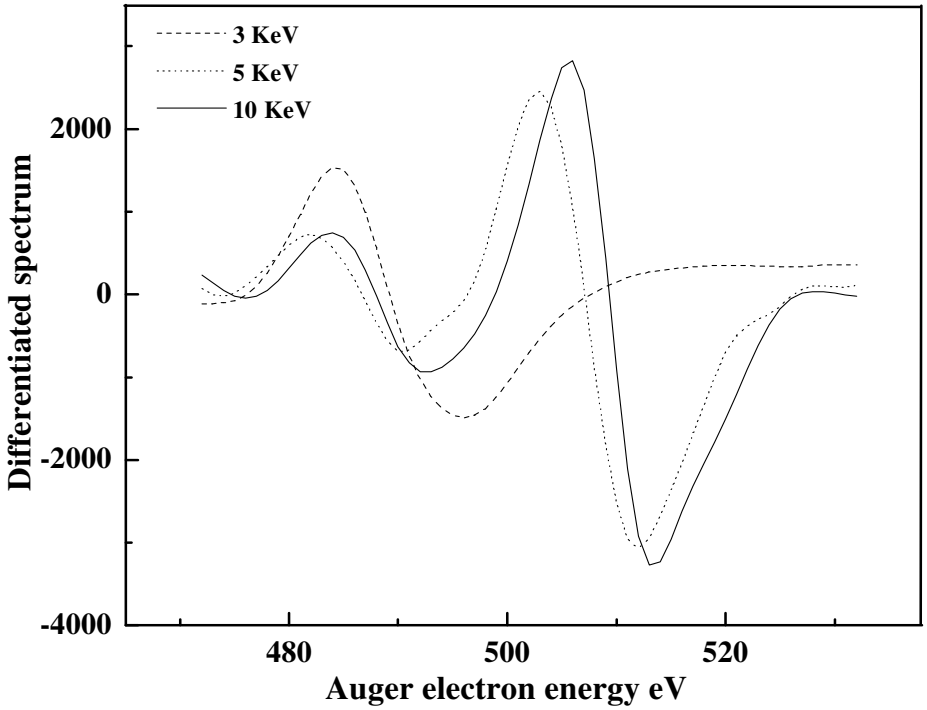

Figure 2.10: Variation of the O peak intensity with primary beam voltage.

The beam current is chosen to minimize damage to the samples. Baer et al. (2003) noted that the damage produced by the electron beam is positively correlated with the primary beam current. Electron beam damage is also material sensitive (Baer et al. 2003). The manner in which high electron beam current will affect the presolar grains was also

unknown. Based on the work with the standard grains, we observed changes in elemental composition during spectral acquisition. Therefore, we decided to use a low beam current of ~0.25 nA and obtain multiple spectra (10–20) on the grains, so that we could monitor the spectra for possible changes. A low beam current of ~0.25 nA is adequate for observing the prominent Auger peaks in the spectra during measurement and ensures that no changes in the intensity of Auger peaks occurred during data acquisition. In order to further limit the possibility of beam damage, the primary electron beam is rastered over a rectangular area on the grains. Subsequent to spectral analysis, elemental mapping at higher beam currents (5 or 10 nA) was done, which give us distribution of the elements of interest at high spatial resolution.

The aforementioned analytical parameters are kept constant for the samples of interest because they are the best settings for minimizing beam damage and eliminating any experimental biases.

2.3.3. Standards

Since the discovery of Auger electrons, they have been used to probe a variety of materials, especially in the semiconductor industry (Watts and Wolstenholme 2003). This application primarily studies materials composed of a single element, and therefore, necessitates the derivation of sensitivity factors for single elements (e.g., Childs et al. 1995). In order to use Auger spectroscopy for studying presolar silicate phases, we needed to acquire specific sensitivity factors from comparable materials e.g., silicate minerals because Auger sensitivity factors are matrix dependent (Seah 2003). For this purpose we chose terrestrial silicate minerals and one meteorite sample from Hofmeister and Pitman (2007). The silicate mineral standards have olivine and pyroxene

compositions because silicates with similar compositions are thought to condense in stars. The samples contain Fe, Mg, Si, and O with varying mg#s (mg# = Mg/(Fe+Mg)×100). A few samples contained small and varying concentrations of Ca and Al. Electron probe data from these standards are known and are listed in Table A2.1. The standards were prepared by mixing small quantities of the powders (in the size-range of ~500 nm) with a mixture of 25% methanol and 75% water, followed by ultrasonification for about an hour. Grains were dispensed onto high-purity gold foils that were pressed into stainless steel mounts.

2.3.4. Procedure for Measurements

The sample is introduced into the analysis chamber. Samples that outgas can be placed in the introduction chamber and heated until the pressure is lower than ~5×10^{-7} torr. In the analysis chamber, the first step is to move the sample stage to the focal plane of the objective lens. Subsequently, the grains of interest are located on the sample mount. The next step is to tilt the stage by 30° and setup for zalar rotation about an axis passing through the center of the grain. A 2 keV and 1 μm Ar^+ ion beam is rastered over the sample ~1–2 minutes to get rid of the surface contaminants. In order to check if the sample is free of C contaminants, spectra can be acquired on grains close to the presolar grains. After sample tilt is changed back to zero, one last step called image registration needs to be set up. This function in the software accounts for stage and beam shifts during the course of the measurements.

Spectra and elemental distribution maps are acquired, at the settings discussed above, using the AutoTool feature in the SmartSoft software. The AutoTool routine allows us to automate the software to perform a series of pre-defined operations, such as, acquisition

of a high-resolution image of a grain, followed by multiple spectral measurements over a ~100×100 nm^2 box on the grain. In order to minimize beam damage to the sample, at the end of the sequence of measurements, a different extractor steering setting or gun steering voltage (Figure 2.6) is used to deflect the beam away from the sample.

For acquisition of spectra, the energy range over which spectra are acquired and the number of cycles need to be defined. A number of parameters need to be checked while setting up for maps. For each element to be mapped, the energy range over which the Auger peak and the background are chosen. The background level after the Auger peak serves as the background in a two-point acquisition method, while background levels before and after the Auger peak form the background in a three-point acquisition method. In addition, the required spatial resolution also needs to be selected, which is between 32–512 pixels.

The voltage and current settings saved in the SmartSoft software are usually not checked every time prior to measurements. However, once in a while, these settings can be checked and the procedure to do so is described here.

- The largest aperture "bore" is chosen and the beam current is measured. For a 20 keV and 1 nA beam setting, the Keithley ammeter should read ~20 nA.
- The beam is centered by changing the extractor steering. Changing the extractor steering voltages will result in moving the beam in the X and Y plane. In each direction, the voltage is increased till maximum current is measured at the sample.
- A 0.004-inch aperture is then put in place and consequently the current drops. The extractor steering along both directions is again changed to center the beam.
- If the beam current is lower than 1 nA, the gun lens voltage is increased to achieve

the desired value of 1 nA, followed by beam centering.

- The new values are saved as a new setting.

2.3.5. Results–Standards

Spectra were acquired for the nine silicate standards using the analytical protocols and measurement settings described above. The initial step towards quantification is the deletion of spurious spectra and those that show shifts in the Auger peaks due to charging. Subsequently, multiple spectra for each of the standards are added to obtain an average spectrum. Prior to quantification, seven-point smoothening and differentiation of the average spectrum is done, which makes the peaks more prominent and allows identification of the Auger peaks with relative ease. Theoretically, after background subtraction, areas under the Auger peaks in the average spectrum can be determined, similar to that done for EDX spectrum. However, differentiation of the average spectrum allows us to discern the compositions of the grains, which have varying elemental concentrations and complex backgrounds. In the differentiated spectrum, the minimum is used to define the Auger transition. The peak to peak heights of the Auger peaks in differentiated spectra are a measure of the intensity of the elements in the analyzed sample.

The Auger peak intensities along with the elemental sensitivity factors allow us compute the elemental compositions of the grains. The atomic concentration C of the element "x" is defined as $C_x = (I_x/S_x)/ \sum(I_i/S_i)$, where I is the Auger intensity, and S is the sensitivity factor (Childs et al. 1995). We computed the sensitivity factors for Ca, O, Fe, Mg, Al, and Si, via repeated measurements on silicate standards (Table A2.2 from Stadermann et al. 2009). A comparison of the compositions of the standards derived from

Auger measurements to electron probe measurements was made, which show a good agreement between the two (Figure 2.11, from Stadermann et al. 2009). The spread in the compositions may be a result of sample contamination. We used primarily terrestrial standards that consist of grains of less than 0.5 μm size, which are prepared by grinding and crushing large grains. It is difficult to avoid contamination of the sub-micrometer-sized grains subsequent to grinding or crushing.

Auger Nanoprobe is capable of distinguishing silicates with different stoichiometries, which is extremely useful. The broad features in the astronomical spectra are well fitted by amorphous dust grains that predominantly have olivine compositions (Demyk et al. 2000), while the sharp crystalline spectral features can be explained by crystalline grains with enstatite compositions (Molster et al. 2002). Classifying the presolar silicate dust using Auger spectroscopy will enable us to distinguish grains with differing (Mg,Fe)/Si ratios and elucidate our understanding of their formation in evolved stars. Standard grains with olivine- and pyroxene-like stoichiometry are plotted in Figure 2.12 (Stadermann et al. 2009). The Fe+Mg(+Ca)/Si ratio is 1 for pyroxene-$(Fe,Mg)SiO_3$ and 2 for olivine-$(Fe,Mg)_2SiO_4$. The binomial distribution shows that olivine- and pyroxene-like grain populations are clearly distinguishable using the Auger Nanoprobe. The lack of a substantial overlap between the two Gaussian curves (Figure 2.12) indicates that statistically speaking a silicate inventory, which is predominately olivine-like can be differentiated from one which is dominated by pyroxene-like grains.

2.3.6. Applications–Extraterrestrial Material

Auger spectroscopy has been successfully applied to study presolar grains. It has led to the identification of new presolar grain types such as magnesiowüstite and SiO_2 grains

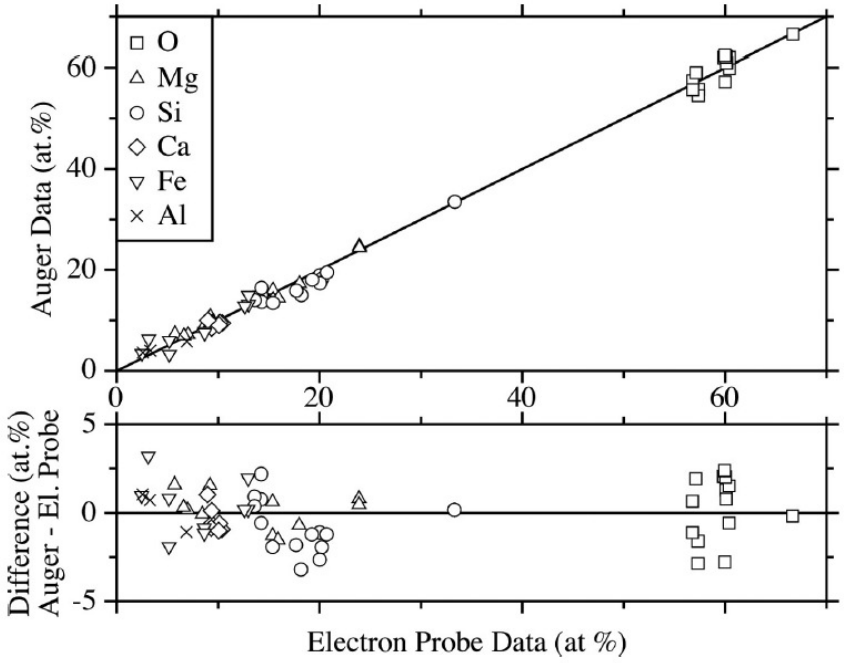

Figure 2.11: Comparison of the Auger and electron microprobe quantification data on silicate standards. Plot from Stadermann et al. (2009).

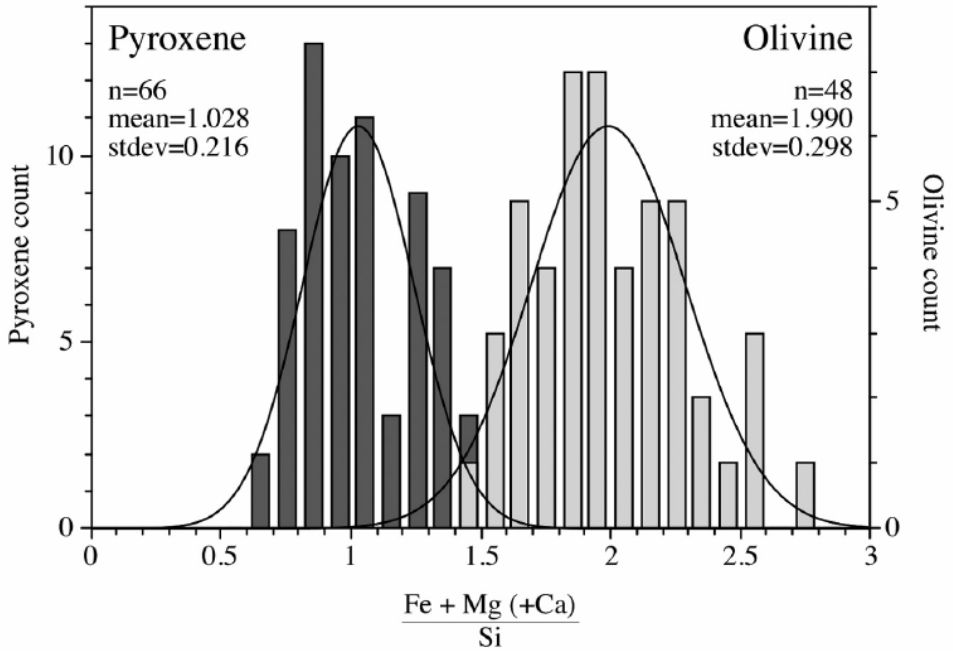

Figure 2.12: Histogram showing the Fe+Mg(+Ca)/Si ratios of olivine and pyroxene standards. Plot from Stadermann et al. (2009).

(Floss et al. 2008; Nguyen et al. 2010; Bose et al. 2010a). In addition, its high- resolution imaging capability has allowed the identification of grains composed of sub-grains (e.g., Vollmer et al. 2009; Floss and Stadermann 2010a; Chapter 5). Study of presolar silicates in meteorites belonging to different classes (Floss and Stadermann 2009a, 2010; Bose et al. 2010b, c; Zhao et al. 2010a, b) and a comparison of the silicate grain compositions in them has also helped us understand how secondary processes alter the meteorite matrices.

Apart from meteorites, the study of presolar silicates in comets has also enhanced our understanding of the preservation of presolar material in other objects in the solar system (Stadermann et al. 2007, 2008). Organic materials that form a vital component of meteorites and interplanetary dust particles have also been studied using Auger spectroscopy (Floss and Stadermann 2009b, 2011; Chapter 5). Recently, Croat et al. (2010) used Auger spectroscopy to study surface coatings over pristine presolar SiC grains.

To conclude, rapid, non-destructive, and quantitative measurements of sub-micrometer-sized material can be effectively done using Auger spectroscopy.

References

Auger P. 1975. The Auger effect. *Surface Science* **48**, 1-8.

Baer D. R., Gaspar D. J., Engelhard M. H., and Lea A. S. (2003) Beam effects during AES and XPS analysis, In: Surface Analysis by Auger and X-ray Photoelectron Spectroscopy (eds. D. Briggs and J. T. Grant). IM Publications, UK., pp. 211-233.

Bickel W. S., Bergström I., Buchta R., Lundin L., and Martinson I. (1969) Mean lives of

some doubly excited levels in lithium I. *Physical Review* **178**, 118-122.

Bishop H. E. (1989) Auger electron spectroscopy. In: methods of surface analysis (ed. J. M. Wells), Cambridge University Press, Great Britain, pp. 87-126.

Bose M., Floss C., Stadermann F. J.,. Stroud R. M, and Speck A. K. (2010a) The origin of presolar silica grains in AGB Stars. *Lunar and Planetary Science Conference* 41, Abstract #1812.

Bose M., Floss C., and Stadermann F. J. (2010b) An investigation into the origin of Fe-rich presolar silicates in Acfer 094. *The Astrophysical Journal* **714**, 1624-1636.

Bose M., Zhao X., Floss C., Stadermann F. J., Lin Y. (2010c) Stardust material in the paired enstatite meteorites: SAH 97096 and SAH 97159. *Proceedings of Nuclei in the Cosmos* XI, POS_NIC XI 138.

Buchet J. P., Denis A., Desesquelles J., and Dufay M. (1969) Doubly excited states of lithium. *Physical Letters* **28A**, 529-530.

Childs K. D., Carlson B. A., Vanier L. A., Moulder J. F., Paul D. F., Stickle W. F., and Watson D. G. (1995) Handbook of Auger electron spectroscopy. Physical Electronics.

Croat T. K., Lebsack E., and Bernatowicz T. J. (2010) Pristine SiC candidates: Spectral imaging and Auger analysis. *Lunar and Planetary Science Conference* 41, Abstract #1891.

Demyk K., Dartois E., Wiesemeyer H., Jones A. P. and d'Hendecourt L. (2000) Structure

and chemical composition of the silicate dust around OH/IR stars. *Astronomy and Astrophysics* **364**, 170-178.

Dikov Y. P., Wlotzka F., Ivanov A. V., Kantzel V. V., and Buleev M. I. (1999) Auger analysis of Apollo 17 orange soil sample 74220. *Lunar and Planetary Science Conference* 30, Abstract #1176.

Floss C., Stadermann F. J., and Bose M. (2008) Circumstellar Fe oxide from the Acfer 094 carbonaceous chondrite. *The Astrophysical Journal* **672**, 1266-1271.

Floss C. and Stadermann F. J. (2009a) Auger Nanoprobe analysis of presolar ferromagnesian silicate grains from primitive CR chondrites QUE 99177 and MET 00426. *Geochimica et Cosmochimica Acta* **73**, 2415-2440.

Floss C. and Stadermann F. J. (2009b) High abundances of circumstellar and interstellar C-anomalous phases in the primitive CR3 chondrites QUE 99177 and MET 00426. *The Astrophysical Journal* **697**, 1242-1255.

Floss C. and Stadermann F. J. (2010) Presolar silicate and oxide grains in the ungrouped carbonaceous chondrite Adelaide: effects of thermal annealing. *Lunar and Planetary Science Conference* 41, Abstract #1251.

Floss C., Stadermann F. J., Mertz A. F., and Bernatowicz T. J. (2011) A NanoSIMS and Auger Nanoprobe investigation of an isotopically primitive interplanetary dust particle from the 55P/Tempel-Tuttle targeted stratospheric dust collector. *Meteoritics and Planetary Science* **45**, 1889-1905.

Gold T., Bilson E., and Baron R. L. (1974) Observation of iron-rich coating on lunar grains and a relation to low albedo. *Lunar Science* 5, pp. 2413-2422.

Hofmeister A. M. and Pitman K. M. (2007) Evidence for kinks in structural and thermodynamic properties across the forsterite fayalite binary from thin-film IR absorption spectra. *Physics and Chemistry of Minerals* **34**, 319-333.

Ito H., Ito M., Magatani F., and Soeda F. (1996) Submicron particle analysis by the Auger microprobe (FE-SEM). *Applied Surface Science* **100**, 152-155.

Jackson A. J., tate C., Gallon T. E., Bassett P. J., and Mathew J. A. D. (1975) The KVV Auger spectrum of lithium metal. *Journal of Physics F: Metal Physics* **5**, 363-374.

Marcus H. L. and Hackett L. H. Jr. (1974) The low temperature fracture behavior of iron nickel meteorites. *Meteoritics* **9**, 371-376.

Mogk D. W. (1985) Auger spectroscopy of stratospheric particles: the influence of aerosols on interplanetary dust. *Lunar and Planetary Science Conference* 16, 569.

Molster F. J., Waters L. B. F. M., Tielens A. G. G. M., Koike C. and Chihara H. (2002) Crystalline silicate dust around evolved stars. III: A correlation study of crystalline silicate features. *Astronomy and Astrophysics* **382**, 241-255.

Nguyen A. N., Nittler L. R., Stadermann F. J., Stroud R. M., and Alexander C. M. O'D. (2010) Coordinated analyses of presolar grains in the Allan Hills 77307 and Queen Elizabeth Range 99177 meteorites. *The Astrophysical Journal* **719**, 166- 189.

Seah M. P. (2003) Quantification in AES and XPS. In: Surface Analysis by Auger and X-ray Photoelectron Spectroscopy (eds. D. Briggs and J. T. Grant). IM Publications, UK, pp. 345-375.

Stadermann F. J., Floss C., and Bose M. (2007) Correlated high spatial resolution elemental and isotopic characterization of Wild 2 cometary samples. *Lunar and Planetary Science Conference* 38, Abstract #1334.

Stadermann F. J. and Floss C. (2008) Abundance of presolar grains in comet Wild 2 and implications for transport and mixing in the solar nebula. *Lunar and Planetary Science Conference* 39, Abstract #1889.

Stadermann F. J., Floss C., Bose M., and Lea A. S. (2009) The use of Auger spectroscopy for the in situ elemental characterization of sub-micrometer presolar grains. *Meteoritics and Planetary Science* **44**, 1033-1049.

Vollmer C., Hoppe P., Stadermann F. J., Floss C., and Brenker F. E. (2009) NanoSIMS analysis and Auger electron spectroscopy of silicate and oxide stardust from the carbonaceous chondrite Acfer 094. *Geochimica et Cosmochimica Acta* **73**, 7127-7149.

Watts J. F. and Wolstenholme J. (2003) An Introduction to Surface Analysis by XPS and AES. Chichester: Wiley & Sons.

Zhao X., Stadermann F. J., Floss C., Bose M., and Lin Y. (2010a) Characterization of presolar grains from the carbonaceous chondrite Ningqiang. *Lunar and Planetary*

Science Conference 41, Abstract #1431.

Zhao X., Bose M., Floss C., Stadermann F. J., and Lin Y. (2010b) Investigation of presolar silicate grains from enstatite chondrites. *Meteoritics and Planetary Science Supplement* 45, A224.

CHAPTER 3

AN INVESTIGATION INTO THE ORIGIN OF FE-RICH PRESOLAR SILICATES IN ACFER 094

Abstract

Presolar silicate and oxide grains from primitive meteorites are recognized as "stardust" on the basis of their extremely anomalous O isotopic compositions. We report data on forty-eight O-anomalous grains that were identified in grain size-separates of the ungrouped carbonaceous chondrite Acfer 094. A majority of these grains exhibit high $^{17}O/^{16}O$ isotopic ratios along with solar to sub-solar $^{18}O/^{16}O$ ratios, and may have originated in low-mass stars with close-to-solar metallicity. Four silicate grains that contain ^{18}O enrichments were also measured for their Si isotopes. A comparison of their O and Si isotopic compositions with model predictions indicate that these ^{18}O-rich grains may have formed in supernova ejecta.

Four of the O-anomalous grains are oxides while the remaining forty-four are silicates, based on elemental compositions determined by Auger spectroscopy. The presolar oxides include a TiO_2 grain and a grain with spinel stoichiometry. The silicate grains largely exhibit ferromagnesian compositions, although a few grains also contain small amounts of Ca and/or Al. Stoichiometric silicates were further classified as either olivine-like or pyroxene-like, and in this study pyroxene-like grains are more abundant than olivine-like ones.

The majority of silicates contain more Fe than Mg, including a few grains with Fe-rich end-member compositions. Spectroscopic observations indicate the presence of Mg-rich silicates in the atmospheres of stars and the interstellar medium. Mg-rich minerals such as forsterite and enstatite form by equilibrium condensation in stellar environments. However, non-equilibrium condensation can result in higher Fe contents and the occurrence of such processes in the outflows of stars may account for the Fe-rich grains. Alternatively, secondary processes may play a role in producing the Fe enrichments observed in the presolar silicate grains identified in the matrix of Acfer 094.

3.1. Introduction

Small dust grains condense in the expanding atmospheres of red giant (RG) and asymptotic giant branch (AGB) stars as well as in the ejecta of supernovae (SNe). Some of them survived travel in the interstellar medium (ISM) and were included in the molecular cloud from which our solar system formed. The refractory dust grains that

escaped homogenization in the solar nebula can be extracted from extraterrestrial samples, such as meteorites, by acid dissolution. The enormous variations in isotopic ratios of these grains compared to solar system materials indicate their stellar origins. The first presolar grains that were discovered in the laboratory were carbonaceous phases, including SiC (Bernatowicz et al. 1987) and graphite (Amari et al. 1990). In addition to C-rich dust, oxides, such as corundum and spinel have been identified (Huss et al. 1994; Hutcheon et al. 1994; Nittler et al. 1994, 1997). Comparison of the isotopic data for presolar oxide grains from meteorites with stellar observations and models of dust producing stars indicates that most of these grains formed in low-mass RG or AGB stars, with a small fraction having formed in supernova (SN) ejecta (Choi et al. 1998; Nittler et al. 1997, 1998).

Spectroscopic observations of envelopes surrounding evolved stars (Waters et al. 1996; Demyk et al. 2000) and circumstellar disks around young stellar objects (Waelkens et al. 1996) indicate the presence of silicate minerals. In particular, the 9.7 and 18 μm emission features observed in O-rich stars have been attributed to amorphous silicates (e.g., Waters et al. 1996). However, amorphous silicates cannot fully account for the infrared emission from these stars; an additional crystalline component is required (e.g., Waelkens et al. 1996). Circumstellar silicate grains were first discovered in interplanetary dust particles (Messenger et al. 2003), followed by their identification in the primitive meteorites Acfer 094 and NWA 530 (Nguyen and Zinner 2004; Nagashima et al. 2004). Acfer 094 is classified as an ungrouped carbonaceous chondrite (Newton et al., 1995). The matrix of this meteorite is composed of fine-grained olivines, pyroxenes, Fe-Ni sulfides, and amorphous material (Greshake 1997), as well as abundant presolar SiC and

nanodiamonds (Newton et al. 1995; Gao et al. 1996). Numerous studies have been carried out to search for presolar silicates in Acfer 094 (Nguyen and Zinner 2004; Mostefaoui and Hoppe 2004; Nagashima et al. 2004; Nguyen et al. 2007; Vollmer et al. 2009a) and estimates of the matrix-normalized abundance of such grains range from about 90 to 160 ppm (Nguyen et al. 2007; Vollmer et al. 2009a).

Recent studies demonstrate that coordinated isotopic and elemental analyses of presolar silicates in the laboratory can provide valuable insight into their formation in stellar environments (Floss et al. 2008; Floss and Stadermann 2009; Vollmer et al. 2009a). Here we report on the O isotopic and elemental compositions of presolar silicates and oxides identified from grain size-separates of Acfer 094. Preliminary results were reported in Bose et al. (2007, 2008a, b).

3.2. Methods

3.2.1. Sample Preparation

Grain size-separates (0.1–0.5 μm and 0.5–1.0 μm) originally prepared by A. N. Nguyen were used for the measurements in this study. The procedure is discussed in detail in Nguyen (2005) and is briefly outlined here. A small fragment of Acfer 094 was placed in distilled water and disaggregated by a rapid "freeze-thaw" process, followed by ultrasonification. The sample was then repeatedly washed in distilled water and soluble organic compounds, such as toluene, to remove precipitates that might have formed during the disaggregation process and to achieve optimal dispersion of the grains. Size-separates of the grains were produced by repeated centrifugation, and the grains were then dispensed onto gold foils pressed into stainless steel stubs. Areas on the gold foils

that were densely covered with grains were chosen for measurements in the NanoSIMS.

3.2.2. NanoSIMS Measurements

Oxygen isotopic measurements were done with a Cs^+ primary beam of a few pA in the Washington University NanoSIMS 50. The beam was rastered over 10×10 μm^2 or, in some cases, 20×20 μm^2 areas in imaging mode (256^2 or 512^2 pixels). Secondary ions of $^{12}C^-$, $^{13}C^-$, $^{16}O^-$, $^{17}O^-$, and $^{18}O^-$ or $^{16}O^-$, $^{17}O^-$, $^{18}O^-$, $^{28}Si^-$, and $^{24}Mg^{16}O^-$ were measured in multi-collection mode together with secondary electrons. The analyses consisted of multiple (5 to 25) scans, with analysis times of up to 20 minutes for each scan. The individual layers were added together to make a single image for each analyzed species. Isotopic compositions of the presolar grains were determined following the data reduction procedures discussed in Stadermann et al. (2005), assuming normal (solar) compositions for the bulk of the matrix grains analyzed ($^{17}O/^{16}O = 3.8\times10^{-4}$ and $^{18}O/^{16}O = 2.0\times10^{-3}$). A grain was considered presolar if at least one of its O isotopic ratios differed by more than 5σ from those of the normal grains and the anomaly was present in at least three consecutive layers.

Following the O isotopic analyses, four ^{18}O-enriched presolar grains were also measured for Si isotopes. For these measurements the Cs^+ beam was rastered over a 3×3 μm^2 area (256^2 pixels) centered on the grain, while detecting $^{16}O^-$, $^{18}O^-$, $^{28}Si^-$, $^{29}Si^-$, and $^{30}Si^-$ secondary ions for 10 imaging scans. The Si isotopic ratios of the presolar grains were normalized by assuming that the surrounding material has solar ratios of $^{29}Si/^{28}Si$ (5.08×10^{-2}) and $^{30}Si/^{28}Si$ (3.36×10^{-2}). The normalized Si isotopic ratios were then computed as delta values, indicating deviations from solar ratios in parts per thousand.

Iron isotopic measurements were performed for two relatively large (~300×200 nm^2) grains using an O^- primary ion beam and combined analysis mode, in which multi-collection is combined with magnetic peak jumping; the details of the measurement procedure are described by Floss et al. (2008). A correction was made for the contribution of $^{54}Cr^+$ on $^{54}Fe^+$ and the Fe isotopic ratios were normalized to the average $^{54}Fe/^{56}Fe$ and $^{57}Fe/^{56}Fe$ ratios of surrounding isotopically normal silicate grains present on the grain mounts.

3.2.3. Auger Nanoprobe Measurements

The PHI 700 Auger Nanoprobe, which was recently installed at Washington University, was used to obtain the elemental compositions of the O-anomalous grains. Prior to acquiring spectra or elemental maps, controlled sputter cleaning with a diffuse 2 keV, 1 μA Ar^+ ion beam was done in order to remove surface contaminants. Iterative Auger electron energy spectra of the presolar grains were obtained at a primary beam accelerating voltage of 10 keV and a current of 0.25 nA in the energy range 30–1730 eV. The low current used during the measurements, combined with rastering the electron beam over the area of the grain, reduces the potential for beam damage to the grains (Stadermann et al. 2009). Multiple iterations of the spectra of a given grain were added together to obtain a single spectrum. The average spectrum was differentiated, using a 7-point Savitsky-Golay smoothing and differentiation routine, followed by identification of the elements on the basis of their characteristic peaks (Childs et al. 1995). Compositions of the grains are calculated from peak to peak heights in the differentiated spectra and are then corrected for elemental sensitivities. The sensitivity factors computed from repeated Auger measurements on powdered olivine and pyroxene standards, under the same

analytical conditions as used in this study, are as follows: Ca: 0.626; O: 0.194; Fe: 0.150; Mg: 0.234; Al: 0.160; Si: 0.121 (Stadermann et al. 2009). The Auger peaks used for quantification are the same as those specified in Stadermann et al. (2009) e.g., KLL transition peak of O and LMM peak of Fe. The sensitivity factors have the following 1σ uncertainties: Ca: 10.8%; O: 3.6%; Fe: 11.2%; Mg: 9.4%; Al: 24.9%; Si: 11.0% (Stadermann et al. 2009). The high uncertainty for Al reflects the fact that the standards measured to date contain relatively low concentrations of this element. Oxide grain compositions may have greater uncertainties associated with them because the sensitivity factors listed above were computed from measuring silicate mineral standards. Additional errors, such as those associated with the presence of surface contaminants, sample charging and background noise, are not included in the reported errors, which should therefore be considered lower limits.

Information from the spectra was supplemented with Auger elemental distribution maps of the presolar grains and surrounding areas. Maps were acquired by rastering the areas of interest (3×3 μm^2 or 5×5 μm^2) at 10 keV and 10 nA for 5–30 scans. The elemental maps provide detailed qualitative information about the elements present in the grains, their spatial distribution, and possible contributions to the Auger spectra from surrounding grains.

3.3. Results

Forty-eight O-anomalous presolar grains were identified in a total analyzed area of 42,000 μm^2 on the grain mounts. Grains were located in two size-separates of Acfer 094: grains in the size range 0.1–0.5 μm have names that start with ‘42’ and those in the size

range 0.5–1.0 μm have names that start with '34', followed by the specific area on the mount (e.g., 'F') and finally by grain names (e.g., 's8', '7', 'e8O17').

3.3.1. Isotopic Compositions

Forty O-anomalous grains (i.e., 83%) exhibit ^{17}O enrichments of up to ~7 times solar, with sub-solar to solar $^{18}O/^{16}O$ ratios (Table A3.1). These ^{17}O-rich grains (Figure 3.1) are classified as group 1 grains (Nittler et al. 1997). While there are no group 2 grains in our presolar grain inventory, which would have greater ^{18}O depletions than group 1 grains, there is a possibility that a few grains currently identified as group 1 actually belong to

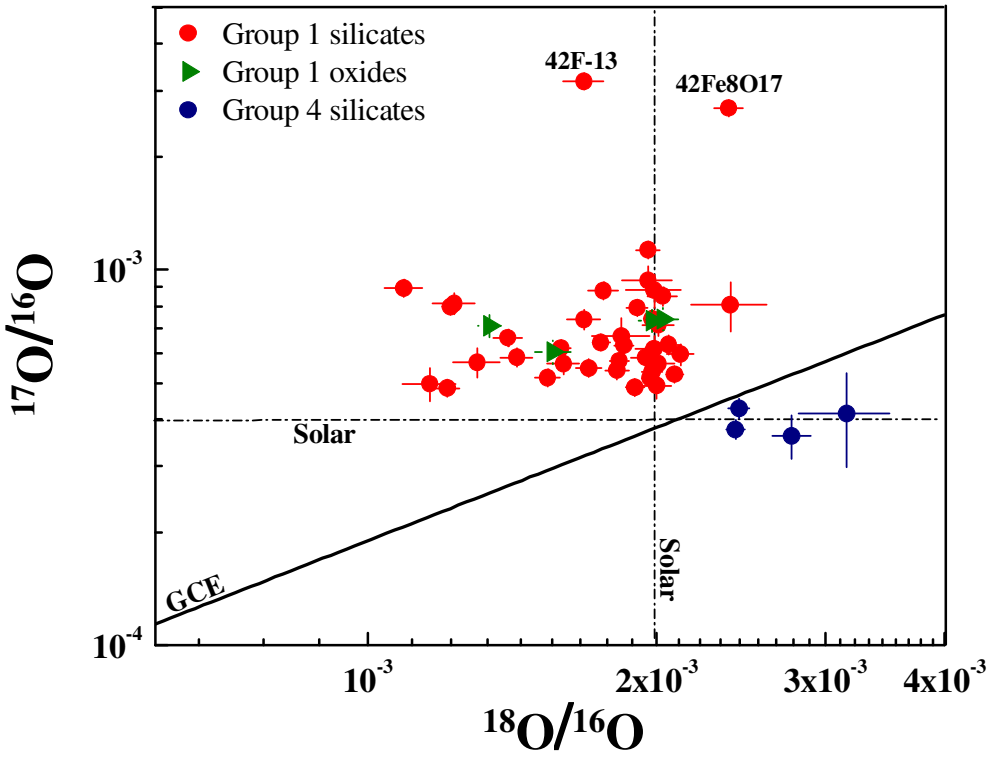

Figure 3.1: Oxygen three-isotope plot of presolar silicates (circles) and oxides (triangles) identified in Acfer 094. Silicate grains are classified into group 1 (red symbols) and group 4 (blue symbols) based on their O isotopic groups defined by Nittler et al. (1997). The dashed lines represent solar values. The solid line labeled 'GCE' indicates the expected evolution of O isotopic ratios with increasing metallicity (Timmes et al. 1995). Errors are 1σ.

the group 2 category (discussed later in section 3.4.1.). Grains with ^{16}O-rich compositions do not exist in our inventory.

Four grains with ^{18}O excesses, classified as group 4 (Figure 3.1), were identified. The Si isotopic ratios of these grains are plotted in Figure 3.2. The grains have normal Si isotopic compositions within 1σ errors, except for grain 34A-4, which has a slight enrichment (64±26‰) in ^{30}Si (Table A3.1).

Two group 1 grains that were measured for Fe isotopes have normal ^{54}Fe/^{56}Fe and ^{57}Fe/^{56}Fe isotopic ratios. Grain 42Fe14 has δ^{54}Fe/^{56}Fe = -107±53‰ and δ^{57}Fe/^{56}Fe = -192±87‰, and grain 42Ff11 has δ^{54}Fe/^{56}Fe= -113±46‰ and δ^{57}Fe/^{56}Fe= -75±87‰. Nickel isotopic ratios could not be calculated because count rates were too low.

3.3.2. Elemental Compositions

All 48 presolar grains were characterized in the Auger Nanoprobe via elemental spectra and high-resolution maps. Figure 3.3 shows an example of an undifferentiated and differentiated Auger spectrum of the presolar ferromagnesian silicate grain 42Fb2 (size ~160×120 nm^2). Cesium was implanted in the sample during NanoSIMS measurements and appears as a complex peak, at around 572 eV in the spectrum. The elemental compositions of the forty four silicate and four oxide grains are listed in Table A3.2, along with the Mg+Fe(+Ca)/Si and (Mg/Mg+Fe)×100 (mg#) ratios. Grains containing O, Fe and Mg (with or without Al, Ca, and Si) with mg#s less than 45 are considered Fe-rich and those with mg#s greater than 55 are considered Mg-rich. Grains are classified as either olivine-like or pyroxene-like if their Mg+Fe(+Ca)/Si ratios fall within 1σ of the theoretical ratios of 2 for olivine $(Mg,Fe)_2SiO_4$ and 1 for pyroxene $(Mg,Fe)SiO_3$.

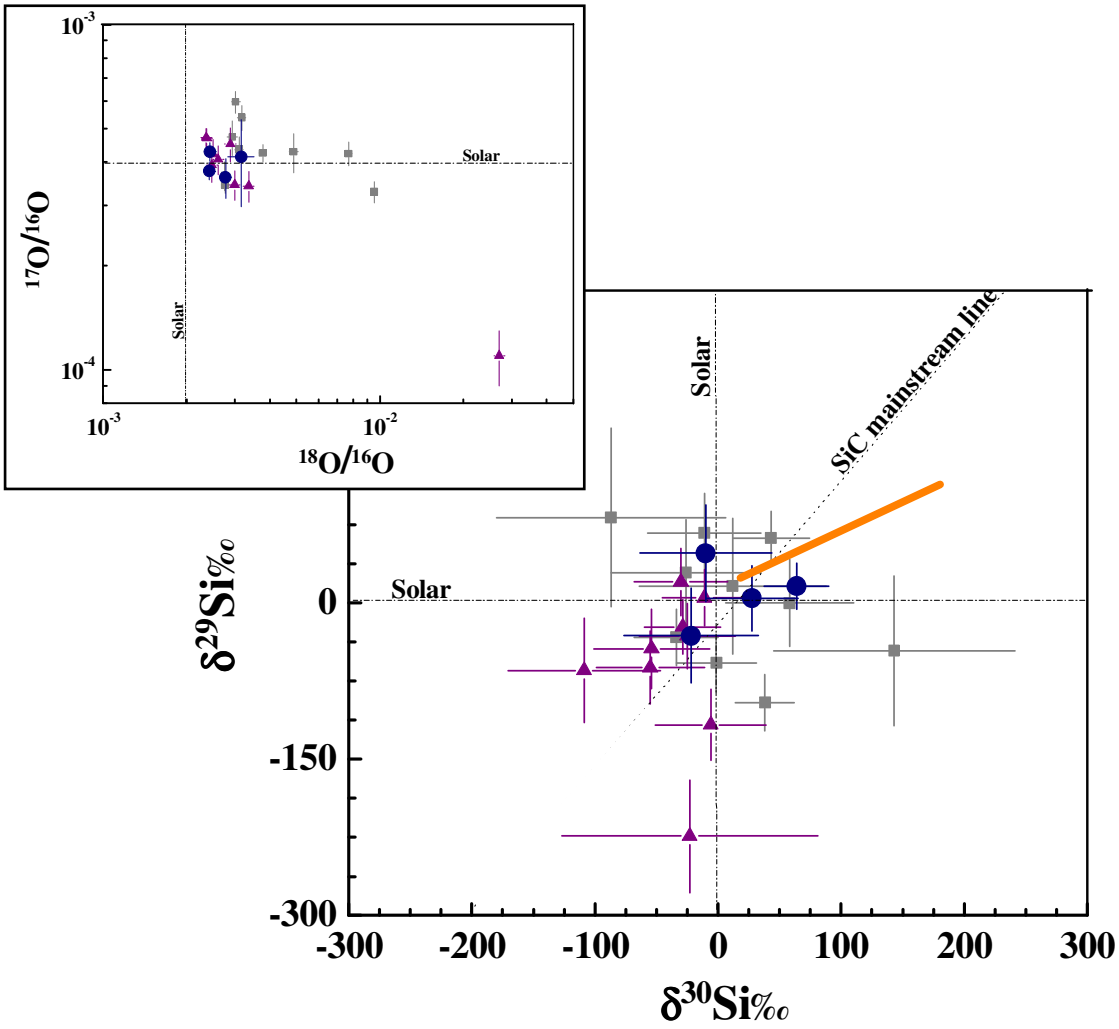

Figure 3.2: Silicon three-isotope plot in delta notation shows the compositions of group 4 presolar grains identified in this study (blue symbols). Mixing calculations were also performed for ten grains (gray symbols) from the literature (Mostefaoui and Hoppe 2004; Bland et al. 2007; Yada et al. 2008; Floss and Stadermann 2009). Additional group 4 grains from Vollmer et al. (2008) and Messenger et al. (2005) are plotted in purple. Calculated Si isotopic ratios based on mixing of material from the H envelope to the He/C and O/C zones are represented by the thick orange line. Also shown for reference is the SiC mainstream line (slope = 1.37). The inset shows the O isotopic compositions of these grains using identical symbols. Error bars are 1σ.

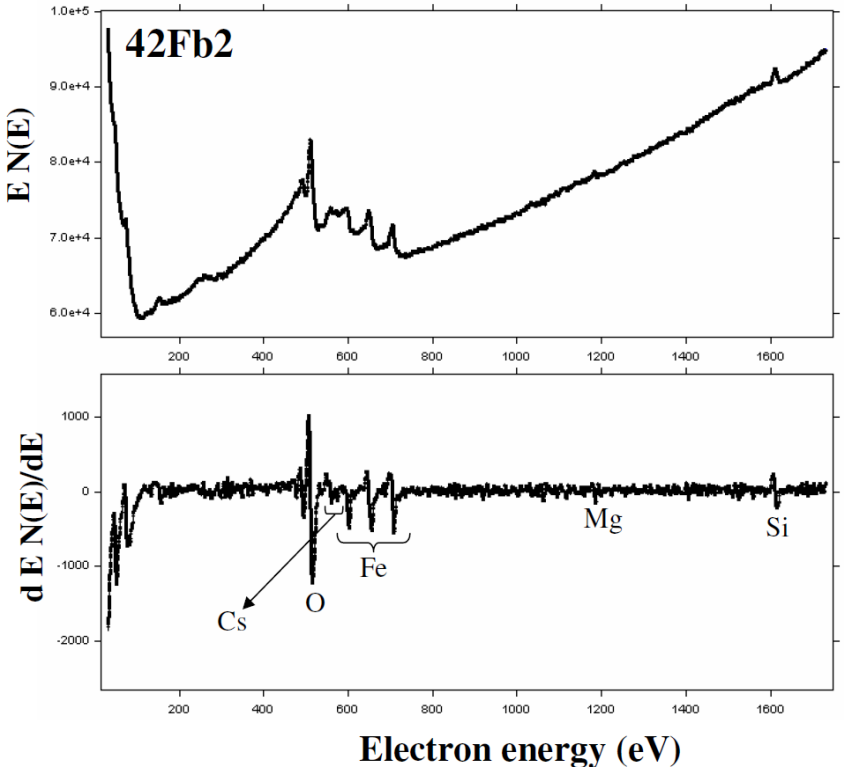

Figure 3.3: Auger elemental spectrum of presolar ferromagnesian silicate grain 42Fb2 with intermediate composition (1 < Mg+Fe(+Ca)/Si < 2). The undifferentiated spectrum is shown in the top panel and the same spectrum after smoothing and performing a 7-point Savitsky-Golay differentiation is shown in the bottom panel. The elements present in the grain are also indicated.

Twelve grains have Mg+Fe(+Ca)/Si ratios with pyroxene-like compositions and six grains have olivine-like compositions (Figure 3.4). Since O is not included in the Mg+Fe(+Ca)/Si ratio, but must also be present in stoichiometric proportions, two additional ratios, namely cation/O and O/Si, were evaluated. These ratios can provide additional verification of whether the classification of a silicate grain is consistent with olivine or pyroxene and can identify grains that do not contain O in stoichiometric proportions. The classification of three olivine-like and six pyroxene-like silicate grains is less certain based on these criteria; these grains are marked with asterisks in Table A3.2 and Figure 3.4. A large number of grains (16 out of 40) have Mg+Fe(+Ca)/Si ratios intermediate between 1 and 2 (1.3–1.7; Figure 3.4). Finally, ten grains have Mg+Fe(+Ca)/Si ratios that are either significantly lower than 1 or higher than 2; these are listed under the category of 'Other Silicates' in Table A3.2.

Silicate grains that are olivine-like include one grain, 42Fw3, with a forsterite (i.e., Mg-rich end-member) composition (Figure 3.5). The other olivine-like grains have elevated Fe concentrations (mg#s ranging from 17 to 31). Among the pyroxene-like silicates, one grain, 42Fs13, has an enstatite-like composition. However, the majority of pyroxene-like grains are Fe-rich with mg#s from 27 to 40, including two grains that have compositions that are consistent with Fe-rich end-member pyroxene and fall in the "forbidden zone" of the pyroxene quadrilateral (Deer et al. 1992). None of the pyroxene-like grains contain Al and only one grain contains Ca.

The majority of the silicate grains that have intermediate Mg+Fe(+Ca)/Si ratios are also Fe-rich. Two of these intermediate silicates have non-stoichiometric Fe-rich end-member compositions. A few grains in this category contain small detectable amounts of

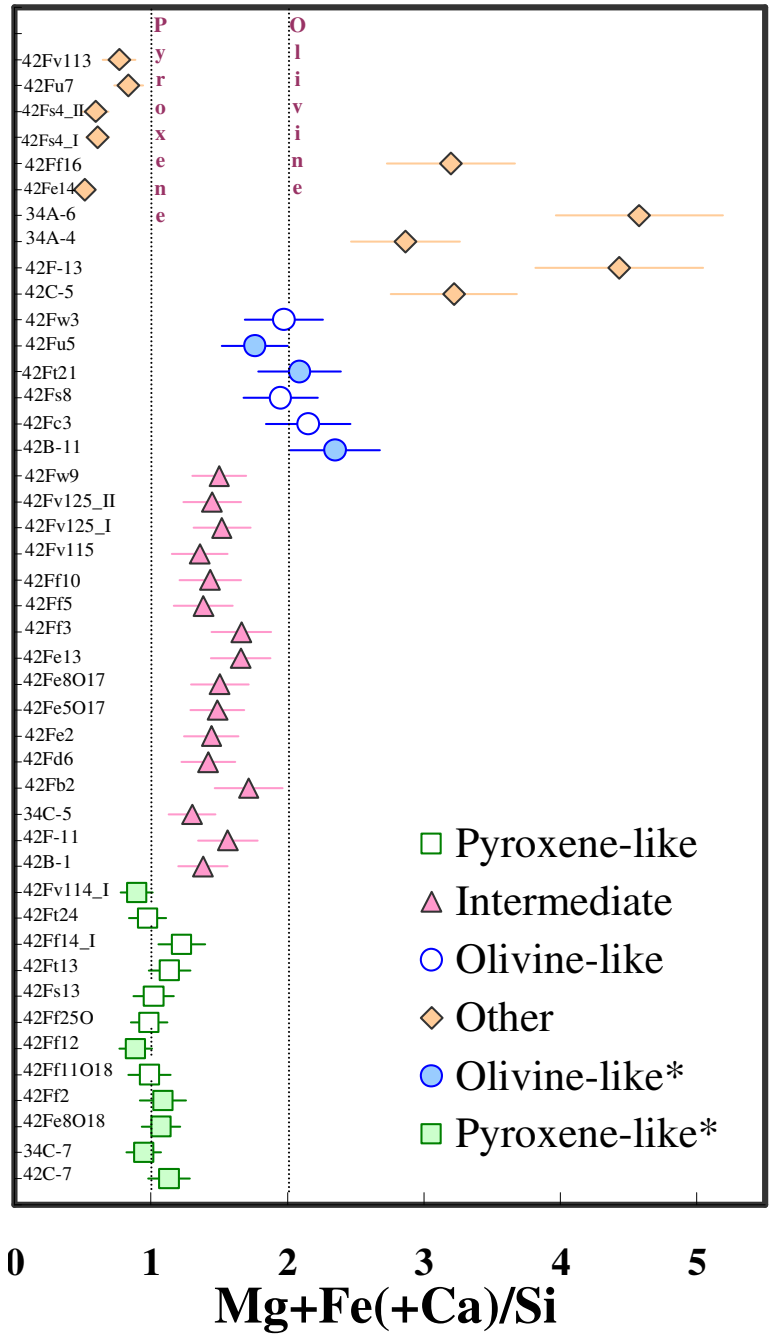

Figure 3.4: Plot of Mg+Fe(+Ca)/Si ratios in presolar ferromagnesian silicates. The dashed lines indicate theoretical ratios for olivine and pyroxene. Olivine like- and pyroxene like-grains whose cation/O and O/Si ratios are non-stoichiometric are indicated by 'closed symbols'and are marked with an asterisk (*) in Tables A3.1 and A3.2.

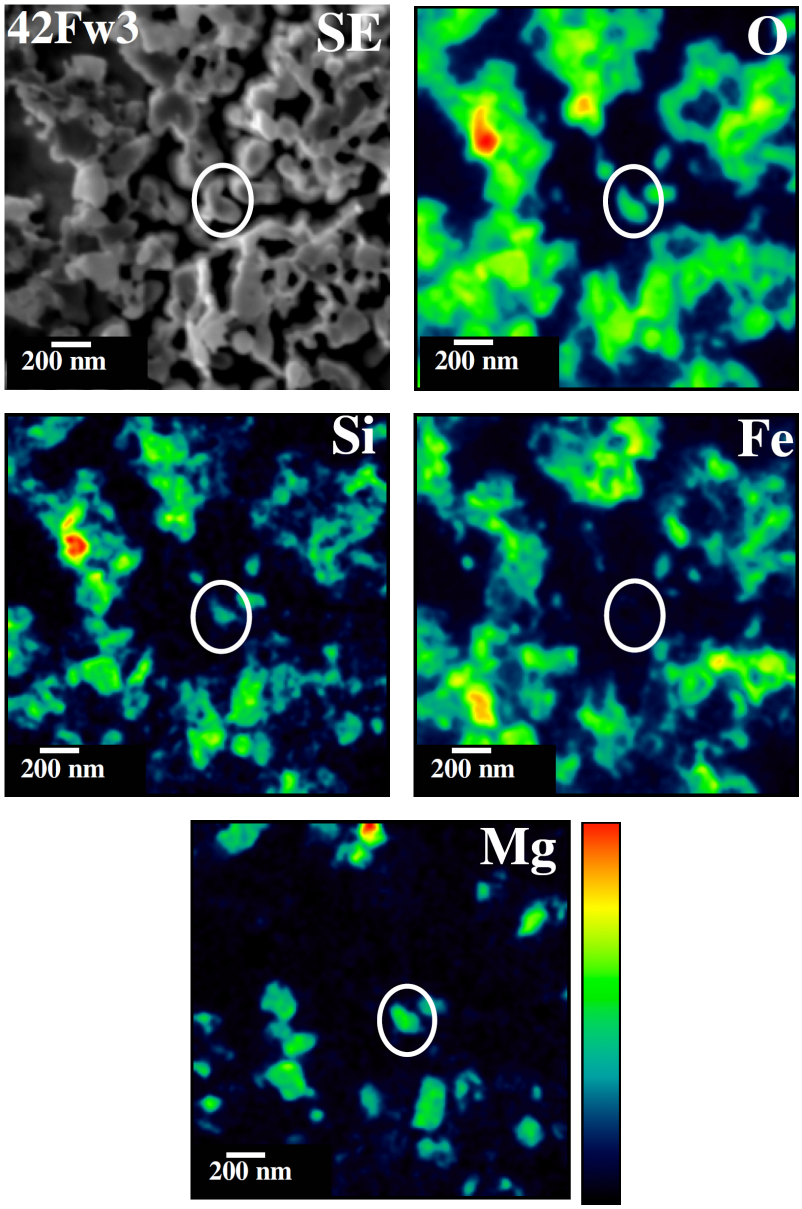

Figure 3.5: False color Auger elemental maps and secondary electron (SE) image of presolar silicate 42Fw3, which has a forsterite-like composition.

Ca (1.8 to 5.7 at.%) in addition to O, Fe, Mg, and Si. The exact classification of individual grains as olivine- or pyroxene-like on the basis of elemental ratios is accompanied by significant uncertainties, but the study of the statistical distributions of various grain types is much more robust. Olivine and pyroxene grain standards cluster around their expected Mg+Fe(+Ca)/Si ratios of 2 and 1, respectively (Stadermann et al. 2009), yet a number of standard grains have Mg+Fe(+Ca)/Si ratios between 1 and 2. Thus, it is possible that some of the silicate grains with intermediate compositions belong to either the olivine- or pyroxene-like categories. However, the number of such grains in our study is significantly larger than what is expected statistically if the inventory was only comprised of olivine and pyroxene grains, indicating that most of the intermediate grains represent a distinct group.

Six of the 10 presolar grains labeled 'Other Silicates' in Tables A3.1 and A3.2 contain Ca and/or Al along with Fe and Mg. Three of these grains, 34A-6, 42F-13 and 42Fv113, are Al-rich with only the first two exhibiting very high Mg+Fe(+Ca)/Si ratios. One grain, 42Fe14, is rich in Si with an O/Si ratio of 1.8±0.2 and contains only minor amounts of Fe and Mg. Two other grains (42Fs4_I and 42Fs4_II) also have Si-rich compositions with O/Si ratios of ~2. Eight grains classified as 'Other Silicates' contain more Fe than Mg (mg# $\leq$ 40) and two grains show no detectable Mg at all. Grain 42C-5 has the highest Fe content (47.1±5.3 at.%) among all the presolar silicate grains characterized in this work. Finally, grain 42Fu7 has Mg+Fe(+Ca)/Si, cation/O, and O/Si ratios that are only slightly outside the 1σ range for pyroxene.

Among the four oxides, two grains, 34C-6 and 42Fs6, contain Al, Fe, and Mg, one grain, 42Fb3, is spinel-like and the final grain, 42Ff26, is probably a TiO_2 grain (O/Ti =

1.9; Figure 3.6). Quantification of the Ti-oxide spectrum was done using a sensitivity factor for Ti determined from a TiO standard, which suggests a Ti concentration of 34 at.% in the grain. The Ti error was calculated by assuming a relative uncertainty of 10% (Table A3.2).

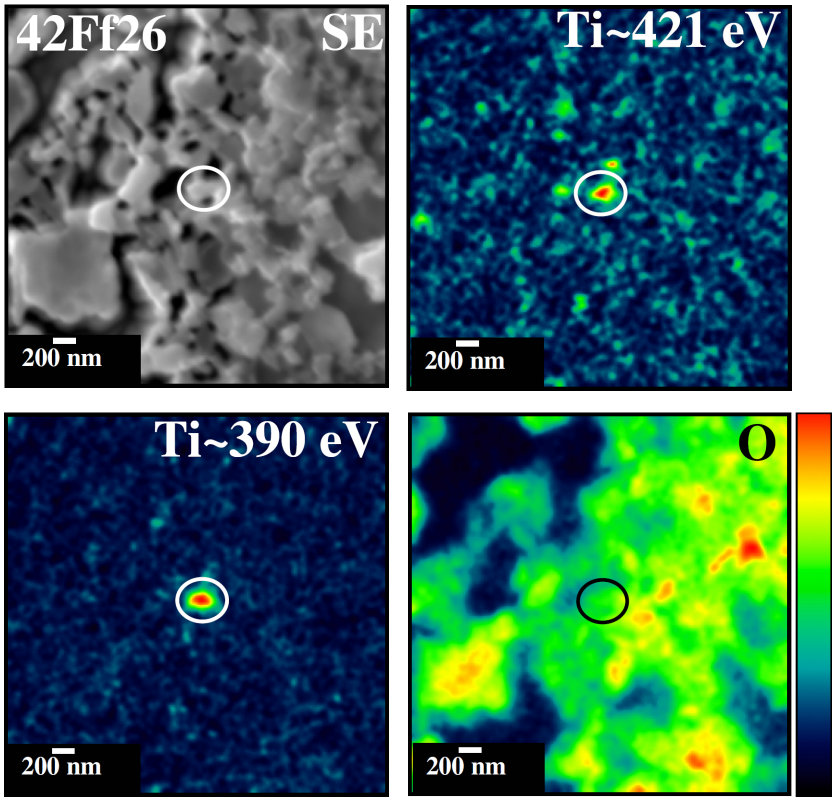

Figure 3.6: False color Auger elemental maps and secondary electron (SE) image of TiO_2 grain. Titanium has two Auger peaks at about 390 and 421 eV; hotspots appear at both the energies in the false colored map.

3.4. Discussion

3.4.1. Group 1 Grains

A majority of the silicate and oxide grains (44 out of 48) identified in the grain size-separates of Acfer 094 are group 1 grains, rich in ^{17}O and with close-to-solar or sub-solar $^{18}O/^{16}O$ ratios (e.g., Nittler et al. 1997). When a star runs out of H fuel in its core, it

expands, cools and undergoes an episode of deep convection called the first dredge-up, which mixes material from the deep layers of the star into the envelope, thus changing its composition (Boothroyd and Sackmann 1999). This mixing brings CNO products of partial H-burning to the surface. The CNO cycle produces ^{17}O but destroys ^{18}O, and as a result, in the first dredge-up the $^{17}O/^{16}O$ ratio of the surface increases drastically and the $^{18}O/^{16}O$ ratio decreases slightly, relative to the initial composition of the star. For stars with masses between 1–2.5$M_\odot$, the $^{17}O/^{16}O$ ratio increases with increasing mass but it decreases in stars that are more massive (Boothroyd et al. 1994; Boothroyd and Sackmann 1999). The $^{18}O/^{16}O$ ratio, however, is not a function of mass but depends primarily on the initial metallicity of the parent star. These predictions are in reasonable agreement with O isotopic ratios that have been measured spectroscopically in evolved stars (e.g., Harris et al. 1988). All the group 1 silicate grains found in this study have compositions consistent with an origin in low-mass RG and AGB stars with near solar metallicities. Copious amounts of silicate dust can form in stars with initial masses > 4$M_\odot$ that undergo third dredge-up (Gail et al. 2009). However the O-isotopic composition of silicate grains from such stars should exhibit $^{17}O/^{16}O > 0.002–0.004$ (Nittler 2009), which is rarely observed for silicate grains, including ones identified in this study. Two ferromagnesian silicate grains, 42F-13 and 42Fe8O17, are characterized by higher $^{17}O/^{16}O$ isotopic ratios than the other group 1 grains (Figure 3.1) but are still well below the maximum $^{17}O/^{16}O$ ratios predicted for first dredge-up in stars of near solar metallicity (Nittler et al. 2008).

Modeling by Nguyen et al. (2007) has shown that ion imaging measurements of tightly-packed grains in the NanoSIMS are diluted by the surrounding isotopically

normal silicates, resulting in measured isotopic compositions that are closer to solar values than the intrinsic compositions of the grains. While this dilution affects all measured compositions, the effect is most pronounced for grains with compositions that are depleted in the low-abundance isotopes relative to solar, such as the ^{18}O-depleted group 2 grains (Nittler et al. 1997). Because of this dilution effect, some of our Group 1 grains with $^{18}O/^{16}O$ ratios close to 10^{-3} (e.g., 42B-1) may actually belong to group 2. Large ^{18}O depletions in group 2 grains indicate that they probably formed in low-mass AGB stars (1.2–1.8$M_{\odot}$) undergoing cool bottom processing (Wasserburg et al. 1995; Nollett et al. 2003). Cool bottom processing, also referred to as 'deep mixing', occurs when material from the envelope circulates down into the radiative zone above the H shell, and rapidly brings up nuclear processed material. The processed material is devoid of ^{18}O that has been rapidly destroyed, via the reaction ^{18}O (p, α) ^{15}N.

Our oxide grain population contains a presolar TiO_2 grain (42Ff26) with a solar $^{18}O/^{16}O$ ratio and a $^{17}O/^{16}O$ ratio that is 1.9 times the solar value. Individual presolar Ti oxide grains have previously been identified in residues of several meteorites (Nittler et al. 2008). Three group 1 Ti oxide grains found by Nittler et al. (2008) have close-to-solar Ti isotopic ratios. Titanium isotopes are affected by neutron capture reactions and small shifts in the Ti abundances are predicted to occur after third dredge-up in low-mass AGB stars (Zinner et al. 2007). However, we are not able to acquire Ti isotopic data for the TiO_2 grain found in this study due to the small size (270×120 nm^2) of this grain (Figure 3.6) and the fact that Ti isotopic measurements in the NanoSIMS need to be made with an O^- primary beam, which has a spatial resolution of no better than 300 nm.

Another group 1 oxide grain 42Fb3 has a spinel-like ($MgAl_2O_4$) composition with an

Al/Mg ratio of 1.6±0.4. Abundant presolar spinel grains have been identified in acid residues from meteorites including Tieschitz, Bishunpur, and Semarkona (Nittler et al. 1994, 1997, 2008; Choi et al. 1998). Most of these spinels have O isotopic compositions that are consistent with theoretical values obtained from models of O-rich RG or AGB stars (e.g., Lugaro et al. 2007). Several authors (e.g., Choi et al. 1998; Zinner et al. 2005) have reported variable Al/Mg ratios of presolar spinel grains determined from NanoSIMS isotopic measurements, suggesting that these grains may be non-stoichiometric. However, the Auger measurement of grain 42Fb3 shows that it is, within errors, consistent with stoichiometric spinel. TEM analysis of another presolar spinel, UOC-S2, also indicates a stoichiometric composition (Zega et al. 2009). It remains unclear whether most presolar spinels tend to be non-stoichiometric or whether the variable ratios are due to SIMS matrix effects. Spinel grains form in the envelopes of AGB and RG stars as a result of a solid-gas interaction of Al_2O_3 with gaseous Mg (Lodders and Fegley 1999) and condensation of our spinel grain may have occurred via such a process. Finally, the O isotopic compositions of the remaining two oxide grains, 34C-6 and 42Fs6 are also compatible with an AGB source.

3.4.2. Group 4 Grains

In the present study, four silicate grains (Table A3.1) show ^{18}O enrichments and normal Si isotopic compositions (within 2σ; Figure 3.2). Elemental analyses of the four grains indicate that two have Fe-rich end-member compositions, including one with a pyroxene-like stoichiometry. The remaining grains have Fe-rich ferromagnesian compositions, one with an olivine-like stoichiometry, while the other is non-stoichiometric and contains Al and Ca.

Several possible stellar sources have been suggested for group 4 grains: early dredge-up events in evolved stars (Nittler et al. 1997), high-metallicity stars (Nittler et al. 1997), and SN explosions (e.g., Choi et al. 1998; Nittler et al. 2008). In the first scenario, the production of ^{18}O occurs via the $^{14}N + \alpha$ reaction during He-burning and the ^{18}O-rich material is brought up to the stellar surface during third dredge-up events, which occurs before ^{18}O is destroyed in later pulses. However, AGB models do not predict the occurrence of third dredge-up during the earliest thermal pulses, as is required to produce large surface enhancements in ^{18}O (Nittler et al. 2008) and, therefore, our group 4 grains probably did not form by this process. The high $^{18}O/^{16}O$ ratios of our group 4 grains could also reflect the initial ratios of high metallicity parent stars. Galactic Chemical Evolution (GCE; Fig. 1) predicts that the abundances of the heavier isotopes (e.g., $^{17, 18}O$ relative to ^{16}O) increase over time and, therefore, lead to higher metallicities (Timmes et al. 1995). Similarly, Si isotopes of grains that condense in higher metallicity stars should exhibit $^{29, 30}Si$ enrichments relative to ^{28}Si and evolve along the SiC mainstream line (Figure 3.2). Therefore, grains condensing in high-metallicity stars should exhibit high $^{17, 18}O/^{16}O$ and $^{29, 30}Si/^{28}Si$ isotopic ratios. If the very high $^{18}O/^{16}O$ ratios of our grains are due to GCE, this would imply a parent star with metallicity several times higher than solar. Aside from the fact that such stars are exceedingly rare and probably were even more so at the time of solar system formation, such stars are also expected to have high $^{17}O/^{16}O$ ratios, both because of GCE and the first dredge-up. Moreover, an enrichment in $^{29,30}Si$ would also be expected. However, none of the ^{18}O-rich group 4 grains identified in this work show correlated excesses in ^{17}O. In addition, all the grains exhibit normal Si isotopic ratios (within 2σ). Thus, the group 4 grains from this study probably did not

originate in high-metallicity stars.

Finally, an origin in a SN environment has been used to explain the compositions of several group 4 grains (e.g., Choi et al. 1998; Messenger et al. 2005). Grains that condense from the debris of a core-collapse SN may contain material from different zones of a pre-SN star. Recently, Nittler (2007) showed that it was possible to reproduce the compositions of some group 4 grains by mixing material from the H-envelope with contributions from the He/C zone, which is ^{18}O-rich, and the inner O-rich zones (O/Si, O/Ne, and O/C). We attempted to reproduce the O isotopic compositions of the group 4 grains found in this study by using this mixing model to see how this would affect the Si isotopes of the same grains. A comparison with the observed compositions could provide additional constraints about these grains' provenance. The O and Si isotopic abundances in the zones of a $15M_{\odot}$ pre-SN star (Rauscher et al. 2002), specifically model s15a28c, were used to model the compositions of the four group 4 grains identified in this work (Table A3.3). The O and Si isotopic abundances of the different zones are shown in Figure 3.7. These mixing calculations were also carried out for ten group 4 grains from Mostefaoui and Hoppe (2004), Bland et al. (2007), Yada et al. (2008), and Floss and Stadermann (2009). The average O isotopic ratios from each of the five zones (H-envelope, He/C, O/Si, O/Ne, and O/C) were mixed in different proportions to achieve the measured O isotopic compositions of the grains. An additional constraint for the condensation of O-rich dust grains, that the carbon content in the gas should be less than the oxygen content, i.e. C/O < 1, was also satisfied. All O isotopic compositions could be reproduced by mixing 92–99% material from the H envelope and considerably less material from the O-rich zones and the He/C zone (Table A3.3). A small amount (1–

1.9%) of material from the ^{18}O enriched He/C zone is sufficient to account for the observed ^{18}O anomalies.

We then assumed that the Si isotopic ratios were mixed in the same proportions as the O isotopes and calculated the predicted Si compositions of the grains. However, using the same mixing ratios results in predicted $\delta^{29}Si$ and $\delta^{30}Si$ values that range from +87‰ to +207‰ and +425‰ to +1035‰, respectively, significantly higher than those measured in the grains. This is a reflection of the fact that the O-rich zones are also Si-rich and are enriched in the heavy isotopes of Si (Figure 3.7). Thus, including even small amounts of material from the O-rich zones alters the $^{29}Si/^{28}Si$ and $^{30}Si/^{28}Si$ ratios of the resulting mixture dramatically. Clearly, this mixing model is unable to simultaneously produce the ^{18}O enrichments and the solar Si isotopic ratios of the analyzed grains. Next we tested if mixing of material from the H envelope, the He/C zone and only the O/C zone (which has the lowest Si abundance of the three O-rich zones) could explain the O and Si isotopic compositions of the fourteen group 4 grains. In this case, the predicted Si isotopic ratios fall on the broad orange line in Figure 3.2, in qualitative agreement with almost all of the grain data, indicating that it may indeed be possible to obtain close-to-normal Si isotopic ratios with this SN mixing model.

Several group 4 silicate grains studied elsewhere (Messenger et al. 2005; Bland et al. 2007; Vollmer et al. 2008) were found to be ^{29}Si-depleted (Figure 3.2) and their compositions cannot be explained by either of the mixing models discussed here. One of these group 4 silicates shows an extreme ^{18}O isotopic enrichment, accompanied by a large ^{17}O depletion. Its formation was suggested to have occurred as a result of the mixing of O-rich material from the He/C and O/C zones with the Si-rich material

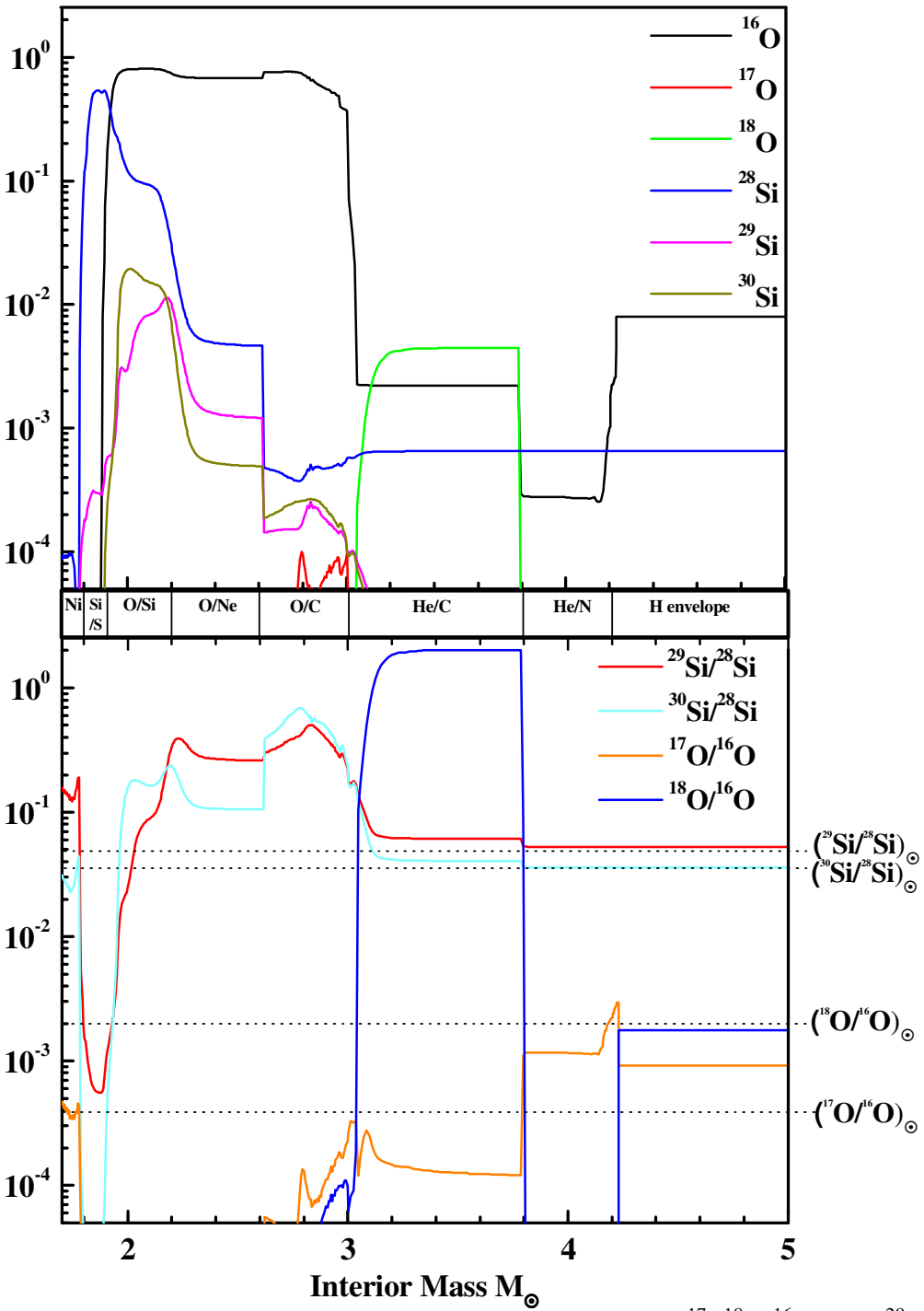

Figure 3.7: Oxygen and Si isotopic abundances (top) as well as $^{17,\ 18}O/^{16}O$ and $^{29,\ 30}Si/^{28}Si$ isotopic ratios (bottom) as a function of stellar mass in a $15M_{\odot}$ pre-SN star (Rauscher et al. 2002). The different zones in the star are labeled in the middle panel. Solar O and Si isotopic ratios are shown as dotted lines.

from the Si/S and Ni zones (Messenger et al. 2005). Vollmer et al. (2008) also identified a few group 4 grains that are ^{29}Si-depleted. These authors argued for a SN origin for these grains by performing SN mixing calculations that required mixing material from six zones, including the He/N and inner ^{28}Si-rich, Si/S zones. While contributions from the inner ^{28}Si-rich Si/S zone are required to explain the Si isotopic compositions of the ^{29}Si-depleted group 4 grains, the compositions of the four grains from our study can be reproduced with contributions from only the several SN zones described above.

3.4.3. Silicon-Rich, Silicon-Poor, and Aluminum-Rich Grains

Three group 1 grains (42Fe14, 42Fs4_I and 42Fs4_II) have Si-rich compositions. Two grains are ferromagnesian silicates while one grain contains no Mg at all (Table A3.2). The formation of Si-rich phases is possible under non-equilibrium conditions in low-metallicity stars with low Mg/Si ratios (Ferrarotti and Gail 2001). However, stars with low metallicities exhibit low ^{18}O/^{16}O ratios. The ^{18}O/^{16}O ratios of our grains are too high i.e., greater than $(1.75\pm0.03)\times10^{-3}$ to have originated in low-metallicity stars, even if we consider substantial dilution of the isotopic ratios (e.g., Nguyen et al. 2007). Moreover, it is questionable whether dust grains can form under such low metallicity conditions at all (Gail et al. 2009). Nagahara and Ozawa (2009) concluded that Si-rich phases may condense in kinetically fractionating systems where the condensation of Fe metal onto forsterite prevents the equilibration of Si-rich gas with the forsterite to produce enstatite, thereby allowing the formation of Si-rich grains.

Four ferromagnesian grains (34A-4, 34A-6, 42F-13, and 42Ff16) that exhibit Al and Ca Auger peaks in their spectra have Si-poor compositions given by Mg+Fe(+Ca)/Si ratios of ~2.9–4.6. None of these grains resemble any stoichiometric Al- and/or Ca-

bearing mineral phases. All the grains exhibit Fe-rich compositions with mg#s from ~10–35. Another grain (42Fv113) is similar with respect to the high Al contents (~23 at.%), but has a lower Mg+Fe(+Ca)/Si ratio. Abundant presolar Al_2O_3 grains have been identified in acid-residues of meteorites (e.g., Nittler et al. 1994, 1997). Aluminum oxide is predicted to be the first condensate to form in an O-rich circumstellar environment (Lodders and Fegley 1999). As temperatures decrease, Al_2O_3 can act as a nucleation site for the subsequent condensation of ferromagnesian silicates (Gail and Sedlmayr 1999) or can react with the gas to form Al-bearing silicates. The 'complex' silicate grains containing Al-rich subgrains (> 200 nm) identified by Vollmer et al. (2009a) provide evidence for the former process. The Al-bearing silicate grains from our study may be products of the latter scenario, in which the influence of kinetics is significant, resulting in non-stoichiometric compositions. Grain 34A-4 is a group 4 grain and may have condensed under non-equilibrium conditions in SN ejecta, where a sharp drop in temperature resulting in the incorporation of Fe into the condensing grains may result in the formation of ferromagnesian silicate minerals (Gail and Sedlmayr 1999; Ferrarotti and Gail 2001; Gail 2003).

3.4.4. Olivine- and Pyroxene-like Grains

Both amorphous and crystalline silicates have been discovered around young main sequence stars (Waelkens et al. 1996; Malfait et al. 1998) as well as O-rich AGB stars (Waters et al. 1996; Demyk et al. 2000). Demyk et al. (2000) suggest that the broad stellar spectral features of amorphous silicates primarily indicate olivine-like compositions, with pyroxene-like compositions being relatively rare (< 10%). On the other hand, enstatite appears to be much more abundant than forsterite among crystalline

silicates (Molster et al. 2002). Grains with pyroxene-like compositions are twice as abundant as olivine-like grains in our inventory. The (Mg+Fe)/Si ratios of the majority of silicate grains identified by Vollmer et al. (2009a) in Acfer 094 scatter around a value of 1, which also indicates an over-abundance of pyroxene-like grains compared to olivine-like compositions. Although Auger spectroscopy does not provide structural information about the phases and, therefore, we do not know whether the grains are crystalline or amorphous, the higher proportion of pyroxene-like grains may suggest that some grains are crystalline (e.g., Molster et al. 2002). However, stoichiometric presolar silicates in the CR3 chondrites QUE 99177 and MET 00426 consist of approximately equal numbers of olivine-like and pyroxene-like grains (Floss and Stadermann 2009), which suggests that the apparent over-abundance of pyroxene-like grains in Acfer 094 may be simply a statistical effect. To date, only a small fraction of presolar silicates have been analyzed using transmission electron microscopy (TEM). A few of these silicate grains are crystalline circumstellar grains with olivine compositions (Messenger et al. 2003, 2005); Vollmer et al. (2007) also found an unusual presolar silicate in Acfer 094 with a perovskite structure. However, the majority of presolar silicate grains studied in the TEM are heterogeneous on the scale of ~20–50 nm, have overall non-stoichiometric compositions, and amorphous structures (Nguyen et al. 2007; Vollmer et al. 2009b; Stroud et al. 2008, 2009). Therefore, it is possible that most of the silicate grains are indeed amorphous.

Shocks, irradiation, and sputtering processes in the ISM may alter the structure and composition of crystalline dust grains (e.g., Lodders and Amari 2005). For example, Demyk et al. (2001) showed that crystalline olivine can transform into amorphous

pyroxene when irradiated by low-energy He^+ ions. Such an irradiation process is probably responsible for the low abundance of crystalline silicates in the ISM and the transition from olivine grains around evolved stars to pyroxene grains around protostars (Demyk et al. 2001). The large number of grains with pyroxene-like compositions in our study may have resulted from such a process in the ISM. Amorphous silicate grains with stoichiometries in-between olivine and pyroxene may also be the result of irradiation and sputtering events (Jones 2000; Min et al. 2007). A large fraction of the silicates found in this study have elemental compositions intermediate between olivine and pyroxene (Figure 3.4). However, Min et al. (2007) predict the existence of Mg-rich grains (mg#s > 90) with stoichiometry between olivine and pyroxene in the ISM, which is in sharp contrast to the Fe-rich compositions of the grains in our inventory.

3.4.5. Iron-Rich Silicate Grains

Figure 3.8 shows the distribution of mg#s for olivine- and pyroxene-like silicates, as well as for grains with compositions intermediate between these two stoichiometries. Silicates with high Fe/Mg ratios dominate our presolar grain inventory. The addition of the oxide grains or the 'other' silicate grains does not change the distribution substantially. Relatively Fe-rich presolar silicate grains have been previously reported in Acfer 094 (Nguyen and Zinner 2004; Nguyen et al. 2007; Vollmer et al. 2009a), as well as in the CR3 chondrites, QUE 99177 and MET 00426 (Floss and Stadermann 2009) and the CO3 chondrite, ALHA77307 (Nguyen et al. 2008; Bose et al. 2009). The possible origin of these Fe-rich silicates is discussed in the following sections.

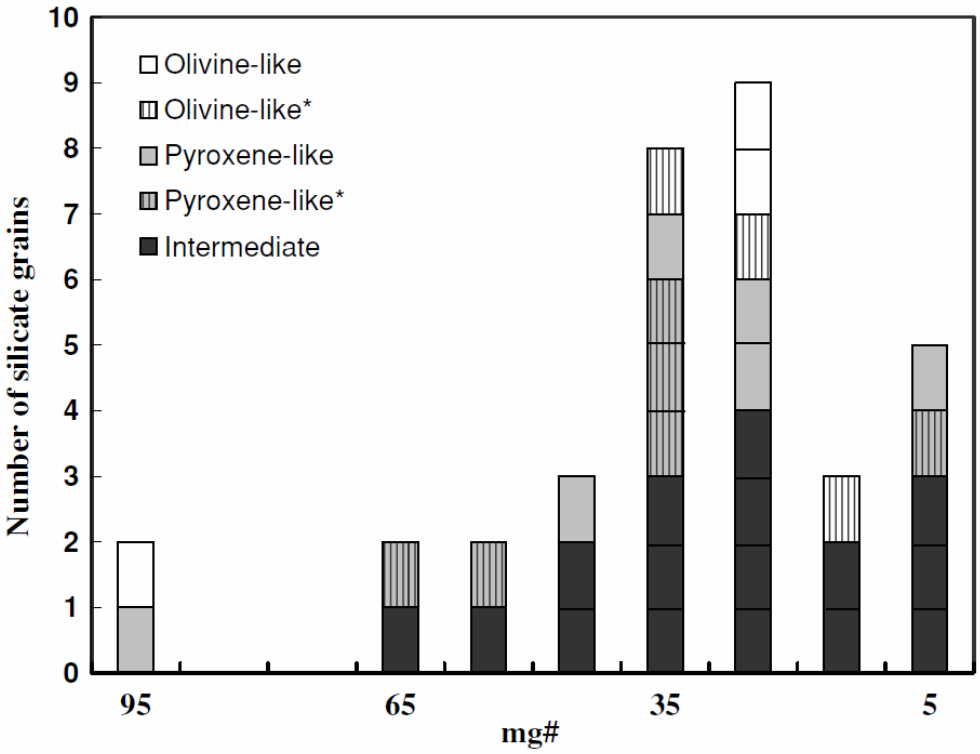

Figure 3.8: Histogram displaying the Fe-Mg distributions in presolar olivine-like, pyroxene-like and intermediate silicates. Categories correspond to those shown in Figure 3.4.

3.4.5.1. Primary Processes: Condensation in Stars

Equilibrium condensation models predict that silicates with Mg-rich end-member compositions, such as forsterite and enstatite, are the first silicate minerals to condense at high (~1000 K) temperatures in stellar envelopes (Lodders and Fegley 1999; Ferrarotti and Gail 2001; Gail 2003). Although earlier studies had suggested higher Fe contents in amorphous silicates (e.g., Molster et al. 2002; Demyk et al. 2000), recent models using realistic particle shapes suggest that amorphous silicate grains are more Mg-rich (mg# > 90) than previously assumed (Min et al. 2007). In addition, the best fit to the scattered emission spectra from interstellar dust requires a Mg:Fe abundance of ~2–3.6 (Costantini

et al. 2005). A viable primary mechanism that may produce Fe-rich silicates is non-equilibrium condensation of grains occurring in the outflows of stars. The dusty gas in stars is lost rapidly by radiation pressure, resulting in a sharp drop in temperature in which equilibrium may not be maintained, allowing a considerable fraction of Fe to be incorporated into condensing silicate grains (Gail and Sedlmayr 1999; Ferrarotti and Gail 2001; Gail 2003). In such a non-equilibrium environment, a large fraction of Mg may condense into other solid phases (e.g., Ferrarotti and Gail 2001). Evidence for the incorporation of Fe into silicates in circumstellar environments has also been obtained from laboratory experiments carried out to understand non-equilibrium condensation of silicates (e.g., Rietmeijer et al. 1999; Nuth et al. 2000). These laboratory experiments show that condensates with ferrosilica and magnesiosilica compositions form directly from the vapor, but that grains with FeMgSiO compositions are not among the primary condensates (Rietmeijer et al. 1999). Thus, silicates with Fe-rich end-member compositions, such as those found in this study, may have formed under similar circumstances. Rietmeijer et al. (1999) suggest further that dust aggregates form by accretion of simple end-member silicates, which then undergo energetic reactions and result in the formation of grains with ferromagnesian silicate compositions. High-resolution secondary electron images of the silicate grains from our study (Figure 3.9) show a predominance of silicate grains with single complete grain boundaries with uniform O isotopic and elemental compositions, unlike the aggregates expected from such a process. However, the physical separation procedure carried out to produce the grain size-separates could have resulted in the preferential survival of larger and more compact grains. Aggregates such as those postulated by Rietmeijer et al. (1999) have

been observed in TEM studies, which show that many presolar silicates exhibit composite structures with heterogeneous elemental distributions (e.g., Stroud et al. 2009; Vollmer et al. 2009b).

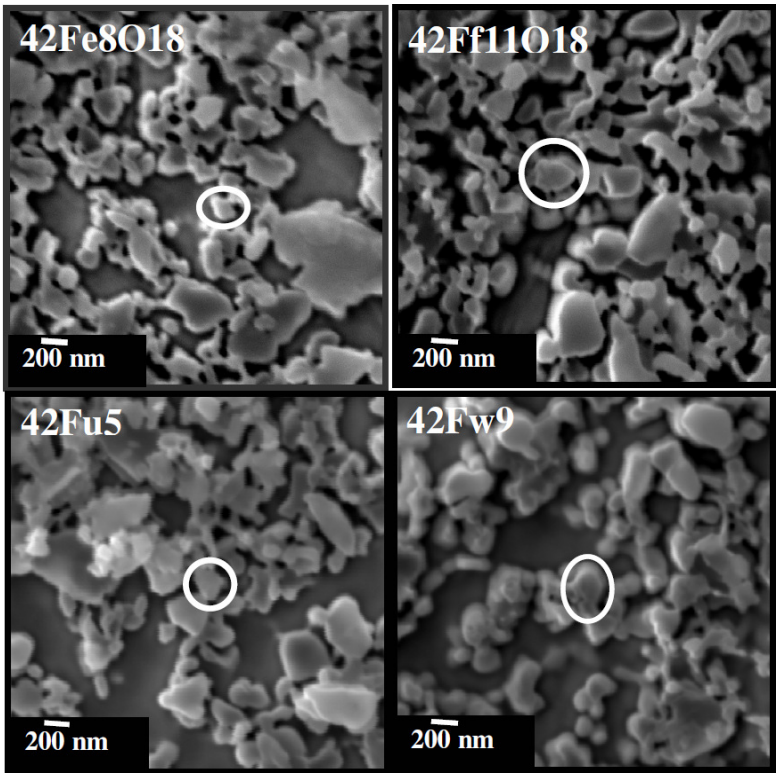

Figure 3.9: Field emission secondary electron Auger images of presolar ferromagnesian silicates with compact grain morphologies.

One consequence of non-equilibrium condensation is the formation of olivine as the dominant mineral species rather than pyroxene (Ferrarotti and Gail 2001). The apparent conflict with the observation of more pyroxene-like compositions among our grains may be due to possible transformation in the ISM, as discussed above.

3.4.5.2. Secondary Processes

Secondary processes such as aqueous alteration or thermal metamorphism could also be responsible for the relatively high Fe contents in the circumstellar silicates from this

study. The changes that occur at various stages of aqueous alteration include hydration of matrix material, oxidation of Fe-Ni metal, and formation of carbonates (Brearley 2006). Recently Vollmer et al. (2009a) reported cracks and fissures in several presolar silicate grains in Acfer 094, which they attributed to aqueous alteration. However, apart from small amounts of phyllosilicate minerals, such as serpentine and chlorite, found in the matrix of Acfer 094, secondary phases, such as carbonates, are scarce in this meteorite which, in general, exhibits little evidence of aqueous alteration (Greshake 1997).

Thermal metamorphism, leading to the introduction of Fe via diffusion (e.g., Jones and Rubie 1991) could also account for the high Fe contents observed in our presolar silicate grains. Carbon-rich grains (~100 nm in size) located within the fine-grained matrix of Acfer 094 have probably undergone limited graphitization by mild heating in the solar nebula (Brearley 2008). However, Raman measurements on insoluble organic matter (IOM) show that the Acfer 094 parent body did not experience significant thermal metamorphism (Busemann et al. 2007). In addition, Kimura et al. (2006) argued that the Fe-Ni metal in Acfer 094 shows very little plessitic intergrowth, another indicator for a low degree of metamorphism experienced by the parent body.

Changes in elemental compositions can occur in the grains during erosional processes in the ISM, which preferentially remove Si compared to Mg, and both Mg and Si compared to Fe (Jones 2000), resulting in Fe-rich grain compositions. In this case, the timescales for which the circumstellar grains remain in the ISM is crucial e.g., cosmic ray exposure ages of large presolar SiC grains vary from ~10 Myr to ~1 Gyr (e.g., Ott and Begemann 2000; Gyngard et al. 2009). Most of these refractory SiC grains show no signs of processing in the ISM such as sputtering or cratering, despite their long lifetimes.

Silicate grains on the other hand, are not as refractory as SiC grains, and because both SiC and silicate grains have similar long residence lifetimes in the ISM (Jones et al. 1994), preferential erosion may contribute to the high Fe contents observed in many of our silicate grains. However preferential erosion certainly requires that the presolar grains already contain some Fe of primary origin.

Acfer 094 was found in the Algerian Sahara and is classified as W2: moderately weathered (Bischoff and Geiger 1995). The presence of ferrihydrite (~2 mol.%) in the matrix of Acfer 094 has been attributed to alteration in the Sahara (Greshake 1997). Additional evidence for terrestrial weathering is found in the low C abundance of IOM in Acfer 094, suggesting that it was partially destroyed (Alexander et al. 2007) and in the presence of Fe^{3+}-bearing phyllosilicates (Bland et al. 2008). The degree of weathering that a hot desert meteorite experiences on the surface of the Earth has been positively correlated with its terrestrial age (Bland et al. 1996, 1998a). The terrestrial age of Acfer 094 as determined by ^{36}Cl dating is 160±60 kyr (K. Nishiizumi, pers. comm.), which is longer than the residence times of many other chondritic falls (Bland et al. 1998a). Although weathering can be extremely variable in hot desert environments depending on the climatic conditions and meteorite class, most weathering occurs rapidly, probably in the first hundred years after the fall (Bland et al. 1998b), suggesting that Acfer 094 may have experienced at least some terrestrial alteration. Laboratory experiments, such as stepped combustion of chondrites (Ash and Pillinger 1995), performed to understand the weathering effects in Saharan meteorites, indicate H, C, and N elemental depletions due to the removal of organic C. The effects of weathering may also include losses of significant Na, Mg, Si, and S from the bulk meteorite (Dreibus et al. 1993). Fayalitic

olivines have greater dissolution rates than fosteritic olivines, which would suggest that the Fe-rich ferromagnesian silicate grains found in our inventory would be quickly destroyed (Wogelius and Walther 1992). On the other hand, Bland et al. (1998a) observed a decrease in Si and Mg (and minor decreases in Na and Ca) in the bulk ordinary chondritic compositions while no significant changes were observed in the Fe elemental concentrations. These authors argue that the dissolution products of ferromagnesian silicates are flushed out as weathering proceeds, except for Fe, which remains bound in hydrated Fe oxides. Assuming that carbonaceous chondrites are affected by alteration processes in a similar manner, progressive removal of certain elements, such as Mg, could contribute to the relatively high observed Fe contents in the silicate grains. The fact that such alteration does not appear to have affected other components of the bulk meteorite such as the Fe-Ni and troilite (Bland et al. 2008) may imply the involvement of only small amounts of fluid reacting preferentially with the fine-grained matrix materials.

3.4.5.3. Sources of Fe Enrichments

In summary, it appears that the Fe-rich presolar silicate grains from Acfer 094 probably condensed in stellar outflows under non-equilibrium conditions, followed by minimal processing in the ISM and the solar nebula, as well as some degree of terrestrial alteration. The relative contribution to the presolar grain compositions from any of these processes remains an open question. In order to constrain the primary vs. secondary nature of the Fe-enrichments in presolar silicates, we have measured Fe isotopes in two grains. The Fe isotopic ratios of these grains, 42Fe14 and 42Ff11O18, did not yield any significant anomalies within 2σ errors. However, these results may have been affected by

the relatively large beam size of the O^- primary beam compared to the sizes of the grains (which necessarily results in the inclusion of some surrounding matter in the analysis) and low secondary ion signals. Iron isotopic ratios have been measured in two other O-anomalous grains, to date, and both exhibit anomalous Fe isotopic compositions (Mostefaoui and Hoppe 2004; Floss et al. 2008), indicating that these grains may have acquired their isotopic compositions by primary processes occurring in stellar environments.

3.4.6. Silicate/Oxide Ratios

This study identified forty-four presolar silicates and four presolar oxides (silicate/oxide ratio ~11^{+11}_{-5} with 1σ errors; Gehrels 1986) in Acfer 094. The silicate/oxide ratios for the O-anomalous grains identified in other studies of the same meteorite range from 1^{+1}_{-5} to 7^{+2}_{-1} (Nguyen et al. 2007; Vollmer et al. 2009a); the latter ratio is within 1σ of the silicate/oxide ratio obtained in our work. The rather low silicate/oxide ratio obtained by Nguyen et al. (2007) may be attributed to using the NanoSIMS to ascertain whether an O-anomalous grain is a silicate or an oxide grain. Phase identification on the basis of NanoSIMS secondary ion yields alone may lead to misidentifications and subsequent errors in the silicate/oxide ratios. In contrast to the low silicate/oxide ratios in Acfer 094, a total of 53 silicates and only one oxide grain were identified in the matrices of two CR chondrites: QUE 99177 and MET 00426 (Floss and Stadermann 2009). In addition, recent Auger measurements of O-anomalous grains in the CO3 chondrite ALHA77307 show high silicate/oxide ratios from 31^{+58}_{-25} (prelim. data from our lab.) to 35^{+67}_{-29} (A. N. Nguyen, pers. comm.). Such comparisons of the presolar silicate/oxide ratios in various

meteorite classes can provide a gauge for the effects of secondary processing on presolar grain survival.

The variable silicate/oxide ratios observed in the primitive meteorites studied to date can be the result of a variety of factors including local heterogeneity in the ISM, secondary alteration processes or insufficient statistics. However, it is generally thought that silicate grains are more susceptible to destruction or alteration than oxide grains (e.g., Nguyen et al. 2007; Floss and Stadermann 2009). If this is the case, and if the high ratios observed in ALHA77307 and the CR chondrites MET 00426 and QUE 99177 are indeed representative of these meteorites, then these ratios may represent the initial proportion of presolar silicate and oxide grains in the protosolar molecular cloud from which the solar system evolved. This would further imply that the lower silicate/oxide ratios of Acfer 094 are the result of secondary processing and that this meteorite is, therefore, not as primitive as previously thought. This argument is supported by the low silicate/oxide ratio (3^{+2}_{-3}) that was found from measurements of the CR chondrite NWA 530 (Leitner et al. 2009). These authors suggested that the parent body alteration experienced by NWA 530 may have destroyed a significant fraction of the silicate grains. Similarly, the low abundance of presolar silicates in the CM2 chondrite, Murchison, is probably due to aqueous alteration experienced by this meteorite (Nagashima et al. 2005). As noted above, however, the Acfer 094 matrix is almost devoid of secondary phases that form as a result of aqueous alteration (e.g., Greshake 1997). Aqueous alteration may, therefore not have played a significant role in destroying silicates in this meteorite. Similarly, the low degree of heating experienced by Acfer 094 suggests that thermal metamorphism probably did not significantly affect the silicate/oxide ratios either. On the other hand,

Acfer 094 does seem to have experienced some weathering on Earth leading to the presence of abundant ferric Fe in the matrix (Bland et al. 2008) and the alteration of the IOM in Acfer 094 (Alexander et al. 2007). Thus, terrestrial weathering, resulting in the destruction of silicates, could account for the low silicate/oxide ratios in this meteorite. This suggests that the silicate grain abundance calculated for Acfer 094 may be a lower limit.

3.5. Conclusions

The O-isotopic signatures of the forty-four group 1 presolar grains found in this study reflect first and second dredge-up episodes in low-mass RG and AGB stars. Four grains with ^{18}O enrichments and normal Si isotopic ratios could have condensed in core-collapse Type II SNe. Elemental compositions acquired in the Auger Nanoprobe enabled the classification of the grains into oxides and silicates. Our presolar grain inventory contains mainly ferromagnesian silicates, some of which can be classified as olivine-like or pyroxene-like; the pyroxene-like grains are statistically more abundant. The majority of silicates are essentially Ca- and/or Al-free.

Most of the presolar silicates in this study are Fe-rich. These grains most likely originated in stellar environments controlled by non-equilibrium dust forming processes. However, the Fe enrichments observed in the grains may not solely be a primary effect. Although it is difficult to deconvolve the specific effects of terrestrial alteration and possible pre-terrestrial alteration, secondary processing may also have affected the silicate grain compositions. Additional studies of the presolar silicate populations in other meteorites may help shed more light on this question, as stellar or ISM processes would affect all grains, while parent-body and terrestrial alterations may vary by meteorite.

Finally, the large number of non-stoichiometric silicates and the predominance of pyroxene-like over olivine-like silicates in Acfer 094 may be a result of sputtering and irradiation in shock fronts in the ISM. Indeed, collisional erosion, radiation damage and sputtering are all expected to affect grains in the ISM on relatively short timescales.

Acknowledgements. We thank A. N. Nguyen for preparing the grain-size separates that were used in this study and Tim Smolar for maintenance of the NanoSIMS and Auger Nanoprobe. This work was supported by NASA grants NNX07AU8OH, NNX08AI13G and NNXO7AI82G.

REFERENCES

Alexander C. M. O'D., Fogel M., Yabuta H., and Cody G. D. (2007) The origin and evolution of chondrites recorded in the elemental and isotopic compositions of their organic matter. *Geochimica et Cosmochimica Acta* **71**, 4380-4403.

Amari S., Anders A., Virag A., and Zinner E. (1990) Interstellar graphite in meteorites. *Nature* **345**, 238-240.

Ash R. D. and Pillinger C. T. (1995) Carbon, nitrogen and hydrogen in Saharan chondrites: The importance of weathering. *Meteoritics* **30**, 85-92.

Bernatowicz T., Fraundorf G., Ming T., Anders E., Wopenka B., Zinner E., and Fraundorf P. (1987) Evidence for interstellar SiC in the Murray carbonaceous chondrite. *Nature* **330**, 728-730.

Bischoff A. and Geiger T. (1995) Meteorites from the Sahara: Find locations, shock classification, degree of weathering and pairing. *Meteoritics* **30**, 113-122.

Bland P. A., Berry F. J., Smith T. B., Skinner S. J., and Pillinger C. T. (1996) The flux of meteorites to the Earth and weathering in hot desert ordinary chondrite falls. *Geochimica et Cosmochimica Acta* **60**, 2053-2059.

Bland P. A., et al. (1998a) Climate and rock weathering: A study of terrestrial age dated ordinary chondritic meteorites from hot desert regions. *Geochimica et Cosmochimica Acta* **62**, 3169-3184.

Bland P. A., Sexton A. S., Franchi I. A., Berry F. J., and Pillinger C. T. (1998b) rapid weathering in Holbrook: An iron-57 Mössbauer spectroscopy study. *Meteoritics and Planetary Science* **33**, 127-129.

Bland P. A., Stadermann F. J., Floss C., Rost D., Vicenzi E., Kearsley A. T., and Benedix G. (2007) A cornucopia of presolar and early solar system materials at the micrometer size range in primitive chondrite matrix. *Meteoritics and Planetary Science* **42**, 1417-1427.

Bland P. A., Howard K. T., Cressey G., and Benedix G. K. (2008) The terrestrial component of primitive chondrite alteration. *Meteoritics and Planetary Science Supplement* 43, A26.

Boothroyd A. I., Sackmann I. J., and Wasserburg G. J. (1994) Predictions of oxygen isotopic ratios in stars and of oxygen-rich interstellar grains in meteorites. *The Astrophysical Journal* **430**, L77-L80.

Boothroyd A. I. and Sackmann I. J. (1999) The CNO isotopes: Deep circulation in red giants and first and second dredge-up. *The Astrophysical Journal* **510**, 232-250.

Bose M., Floss C., and Stadermann F. J. (2007) Acfer 094 presolar silicates characterized using NanoSIMS and Auger Nanoprobe. *Meteoritics and Planetary Science*

Supplement 42, A23.

Bose M., Floss C., and Stadermann F. J. (2008a) An investigation into the origin of group 4 stardust grains. *Lunar and Planetary Science Conference* 39, Abstract #1099.

Bose M., Floss C., and Stadermann F. J. (2008b) Iron-enriched stardust grains in the meteorites Acfer 094, QUE 99177, and MET 00426. *Meteoritics and Planetary Science Supplement* 43, A27.

Bose M., Floss C., and Stadermann F. J. (2009) Presolar silicate and oxide dust in ALHA77307. *Meteoritics and Planetary Science Supplement* 44, A36.

Brearley A. J. (2006) The action of water. In: Meteorites and the Early Solar System II (eds. D. S. Lauretta and H. Y. McSween Jr.), The University of Arizona Press, Tucson. pp. 587-624.

Brearley A. J. (2008) Amorphous carbon-rich grains in the matrices of the primitive carbonaceous chondrites, ALH77307 and Acfer 094. *Lunar and Planetary Science Conference* 39, Abstract #1494.

Busemann H., Alexander C. M. O'D., and Nittler L. R. (2007) Characterization of insoluble organic matter in primitive meteorites by microRaman spectroscopy. *Meteoritics and Planetary Science* **42**, 1387-1416.

Childs K. D., Carlson B. A., LaVanier L. A., Moulder J. F., Paul D. F., Stickle W. F., and Watson D. G. (1995) Handbook of Auger Electron Spectroscopy (3rd ed.: Eden prairie: Physical Electronics)

Choi B. -G., Huss G., Wasserburg G., and Gallino R. (1998) Presolar corundum and spinel in ordinary chondrites: Origins from AGB stars and a supernova. *Science* **282**, 1284-1289.

Costantini E., Freyberg M. J., and Predehl P. (2005) Absorption and scattering by interstellar dust: an XMM-Newton observation of Cyg X-2. *Astronomy and Astrophysics* **444**, 187-200.

Deer W. A., Howie R. A., and Zussman J. (1992) An Introduction to the Rock-Forming Minerals (2nd ed.: New York: John Wiley & Sons).

Demyk K., Dartois E., Wiesemeyer H., Jones A. P., and d'Hendecourt L. (2000) Structure and chemical composition of the silicate dust around OH/IR stars. *Astronomy and Astrophysics* **364**, 170-178.

Demyk K., Carrez Ph., Leroux H., Cordier P., Jones A. P., Borg J., Quirico E., Raynal P. I., and d'Hendecourt L. (2001) Structural and chemical alteration of crystalline olivine under low energy He+ irradiation. *Astronomy and Astrophysics* **368**, L38-L41.

Dreibus G., Palme H., Spettel B., and Wänke H. (1993) Sulfur and selenium in chondritic meteorites. *Meteoritics* **28**, 343.

Ferrarotti A. S. and Gail H.-P. (2001) Mineral formation in stellar winds II. Effects of Mg/Si abundance variations on dust composition in AGB stars. *Astronomy and Astrophysics* **371**, 133-151.

Floss C., Stadermann F. J., and Bose M. (2008) Circumstellar Fe oxide from the Acfer 094 carbonaceous chondrite. *The Astrophysical Journal* **672**, 1266-1271.

Floss C., and Stadermann F. (2009) Auger Nanoprobe analysis of presolar ferromagnesian silicate grains from primitive CR chondrites QUE 99177 and MET 00426. *Geochimica et Cosmochimica Acta* **73**, 2415-2440.

Gail H.-P. and Sedlmayr E. (1999) Mineral formation in stellarwinds. I: Condensation sequence of silicate and iron grains in stationary oxygen rich outflows. *Astronomy*

and Astrophysics **347**, 594-616.

Gail H.-P. (2003) Formation and evolution of minerals. In Astromineralogy (ed. T. Henning). Springer-Verlag, Berlin, pp. 55-120.

Gail H. P., Zhukovska S. V., Hoppe P., and Trieloff M. (2009) Stardust from asymptotic giant branch stars. *The Astrophysical Journal* **698**, 1136-1154.

Gao X., Amari S., Messenger S., Nittler L. R., Swan P. D., and Walker R. M. (1996) Survey of circumstellar grains in the unique carbonaceous chondrite Acfer 094. *Meteoritics and Planetary Science Supplement* 31, A48.

Gehrels N. (1986) Confidence limits for small numbers of events in astrophysical data. *The Astrophysical Journal* **303**, 336-346.

Greshake A. (1997) The primitive matrix components of the unique carbonaceous chondrite Acfer 094: a TEM study. *Geochimica et Cosmochimica Acta* **61**, 437-452.

Gyngard F., Amari S., Zinner E., and Ott U. (2009) Interstellar exposure ages of large presolar SiC grains from the Murchison meteorite. *The Astrophysical Journal* **694**, 359-366.

Harris M. J., Lambert D. L., and Smith V. V. (1988) Oxygen isotopic abundances in evolved stars. IV - Five K giants. *The Astrophysical Journal* **325**, 768-775.

Huss G. R., Fahey A. J., Gallino R., and Wasserburg G. J. (1994) Oxygen isotopes in circumstellar Al2O3 grains from meteorites and stellar nucleosynthesis. *The Astrophysical Journal* **430**, L81-L84.

Hutcheon I. D., Huss G. R., Fahey A. J., and Wasserburg G. J. (1994) Extreme Mg-26 and O-17 enrichments in an Orgueil corundum: Identification of a presolar oxide grain. *The Astrophysical Journal* **425**, L97-L100.

Jones A. P., Tielens A. G. G. M., Hollenbach D. J., and McKee C. F. (1994) Grain destruction in shocks in the interstellar medium. *The Astrophysical Journal* **433**, 797-810.

Jones A. P. (2000) Depletion patterns and dust evolution in the interstellar medium. *Journal of Geophysical Research* **105**, 10257-10268.

Jones R. H. and Rubie D. C. (1991) Thermal histories of CO3 chondrites: application of olivine diffusion modelling to parent body metamorphism. *Earth and Planetary Science Letters* **106**, 73-86.

Kimura M., Weisberg M. K., and Grossman J. N. (2006) Fe-Ni Metal and Sulfides in Acfer 094: Thermal History of the Most Primitive Chondrite. *Meteoritics and Planetary Science Supplement* 41, A96.

Leitner J., Hoppe P., and Zipfel J. (2009) NanoSIMS investigation of presolar silicates and oxides in primitive solar system materials. *Lunar and Planetary Science Conference* 40, Abstract #1512.

Lodders K. and Amari S. (2005) Presolar grains from meteorites: Remnants from the early times of the solar system. *Chemie der Erde* **65**, 93-166.

Lodders K. and Fegley B. (1999) Condensation chemistry of circumstellar grains. In: Asymptotic Giant Branch Stars (eds. T. Le Bertre, A. Lebre and C. Waelkens), IAU Symposium No. 191. Astronomical Society of the Pacific, San Francisco, CA, pp. 279-289.

Lugaro M., Karakas A. I., Nittler L. R., Alexander C. M. O'D., Hoppe P., Iliadis C., and Lattanzio J. C. (2007) On the asymptotic giant branch star origin of peculiar spinel grain OC2. *Astronomy and Astrophysics* **461**, 657-664.

Malfait K., Waelkens C., Waters L. B. F. M., Vandenbussche B., Huygen E., and de Graauw M. S. (1998) The spectrum of the young star HD 100546 observed with the Infrared Space Observatory. *Astronomy and Astrophysics* **332**, L25-L28.

Messenger S., Keller L. P., Stadermann F. J., Walker R. M., and Zinner E. (2003) Samples of stars beyond the solar system: silicate grains in interplanetary dust. *Science* **300**, 105-108.

Messenger S., Keller L. P. and Lauretta D. S. (2005) Supernova olivine from cometary dust. *Science* **309**, 737-741.

Min M., Waters L. B. F. M., de Koter A., Hovenier J. W., Keller L. P., and Markwick-Kemper F. (2007) The shape and composition of interstellar silicate grains. *Astronomy and Astrophysics* **462**, 667-676.

Molster F. J., Waters L. B. F. M., Tielens A. G. G. M., Koike C., and Chihara H. (2002) Crystalline silicate dust around evolved stars. III. A correlations study of crystalline silicate features. *Astronomy and Astrophysics* **382**, 241-255.

Mostefaoui S. and Hoppe P. (2004) Discovery of abundant in situ silicate and spinel grains from Red giant stars in a primitive meteorite. *The Astrophysical Journal* **613**, L149-L152.

Nagashima K., Krot A. N., and Yurimoto H. (2004) Stardust silicates from primitive meteorites. *Nature* **428**, 921-924.

Nagahara H. and Ozawa K. (2009) Condensation kinetics of forsterite and metal and chemical fractionation in the proto solar nebula. *Lunar and Planetary Science Conference* 40, Abstract #2158.

Nagashima K., Sakamoto N., and Yurimoto H. (2005) Destruction of presolar silicates by

aqueous alteration observed in Murchison CM2 chondrite. *Lunar and Planetary Science Conference* 36, Abstract #1671.

Newton J., Bischoff A., Arden J. W., Franchi I. A., Geiger T., Greshake A., and Pillinger C. T. (1995) Acfer 094, a uniquely primitive carbonaceous chondrite from the Sahara. *Meteoritics* **30**, 47-56.

Nguyen A. N. and Zinner E. (2004) Discovery of ancient silicate stardust in a meteorite. *Science* **303**, 1496-1499.

Nguyen A. N. (2005) Characterization of presolar silicate grains in primitive meteorites by multi-detection raster ion imaging in the NanoSIMS. Ph. D. Thesis, pp. 202.

Nguyen A. N., Stadermann F. J., Zinner E., Stroud R. M., Alexander C. M. O'D., and Nittler L. R. (2007) Characterization of presolar silicate and oxide grains in primitive carbonaceous Chondrites. *The Astrophysical Journal* **656**, 1223-1240.

Nguyen A. N., Stadermann F. J., Nittler L. R. and Alexander C. M. O'D. (2008) Characterization of presolar silicate and oxide grains using NanoSIMS and Auger spectroscopy. *Lunar and Planetary Science Conference* 39, Abstract #2142.

Nittler L. R., Alexander C. M. O'D., Gao X., Walker R. M., and Zinner E. (1994) Interstellar oxide grains from the Tieschitz ordinary chondrite. *Nature* **370**, 443-446.

Nittler L. R., Alexander C. M. O'D., Gao X., Walker R. M., and Zinner E. (1997) Stellar sapphires: the properties and origins of presolar Al2O3 in Meteorites. *The Astrophysical Journal* **483**, 475-495.

Nittler L. R., Alexander C. M. O'D., Wang J., and Gao X. (1998) Meteoritic oxide grain from supernova found. *Nature* **393**, 222-223.

Nittler L. R. (2007) Presolar grain evidence for low-mass supernova injection into the

solar nebula. In: Workshop on the Chronology of Meteorites and the Early Solar System, pp. 125-126.

Nittler L. R., Alexander C. M. O'D., Gallino R., Hoppe P., Nguyen A. N., F. J. Stadermann, and E. K. Zinner (2008) Aluminum-, Calcium- and Titanium-rich oxide stardust in ordinary chondrite meteorites. *The Astrophysical Journal* **682**, 1450-1478.

Nittler L. R. (2009) On the mass and metallicity distributions of the parent AGB stars of O-rich presolar stardust grains. *Publications of the Astronomical Society of Australia* **26**, 271-277.

Nollett K. M., Busso M., and Wasserburg G. J. (2003) Cool bottom processes on the thermally pulsing asymptotic giant branch and the isotopic composition of circumstellar dust grains. *The Astrophysical Journal* **582**, 1036-1058.

Nuth J. A., Hallenbeck S. L., and Rietmeijer F. J. M. (2000) Laboratory studies of silicate smokes: Analog studies of circumstellar materials. *Journal of Geophysical Research* **105**, 10387-10396.

Ott U. and Begemann F. (2000) Spallation recoil and age of presolar grains in meteorites. *Meteoritics and Planetary Science* **35**, 53-63.

Rauscher T., Heger A, Hoffman R. D., and Woosley S. E. (2002) Nucleosynthesis in massive stars with improved nuclear and stellar physics. *The Astrophysical Journal* **576**, 323-348.

Rietmeijer F. J. M., Nuth J. A., and Karner J. M. (1999) Metastable Eutectic Condensation in a Mg-Fe-SiO-H_2-O_2 Vapor: Analogs to Circumstellar Dust. *The Astrophysical Journal* **527**, 395-404.

Stadermann F. J., Croat T. K., Bernatowicz T. J., Amari S., Messenger S., Walker R. M.,

and Zinner E. (2005) Supernova graphite in the NanoSIMS: Carbon, oxygen and titanium isotopic compositions of a spherule and its TiC sub-components. *Geochimica et Cosmochimica Acta* **69**, 177-188.

Stadermann F. J., Floss C., Bose M., and Lea A. S. (2009) The use of Auger spectroscopy for the in situ elemental characterization of sub-micrometer presolar grains. *Meteoritics and Planetary Science* **44**, 1033-1049.

Stroud R. M., Nguyen A. N., Alexander C. M. O'D., Nittler L. R., and Stadermann F. J. (2008) Transmission electron microscopy of in situ presolar silicates in Alan Hills 77307. *Meteoritics and Planetary Science Supplement* 43, A148.

Stroud R. M., Floss C. and Stadermann F. J. (2009) Structure, elemental composition and isotopic composition of presolar silicates in MET 00426. *Lunar and Planetary Science Conference* 40, #1063.

Timmes F. X., Woosley S. E. and Weaver T. A. (1995) Galactic chemical evolution: hydrogen through zinc. *The Astrophysical Journal Supplement* **98**, 617-658.

Vollmer C., Hoppe P., Brenker F. E., and Holzapfel C. (2007) Stellar MgSiO3 perovskite: A shock-transformed stardust silicate found in a meteorite. *The Astrophysical Journal* **666**, L49-L52.

Vollmer C., Hoppe P., and Brenker F. E. (2008) Si isotopic compositions of presolar silicate grains from Red Giant stars and Supernovae. *The Astrophysical Journal* **684**, 611-617.

Vollmer C., Hoppe P., Stadermann F. J., Floss C., and Brenker F. E. (2009a) NanoSIMS analysis and Auger electron spectroscopy of silicate and oxide stardust from the carbonaceous chondrite Acfer 094. *Geochimica et Cosmochimica Acta* **73**, 7127-

7149.

Vollmer C., Brenker F. E., Hoppe P., and Stroud R. M. (2009b) Direct laboratory analysis of silicate stardust from Red Giant stars. *The Astrophysical Journal* **700**, 774-782.

Waelkens C., Waters L. B. F. M., de Graauw M. S., Huygen E., Malfait K., Plets H., Vandenbussche B., Beintema D. A., Boxhoorn D. R., Habing H. J., Heras A. M., Kester D. J. M., Lahuis F., Morris P. W., Roelfsema P. R., Salama A., Siebenmorgen R., Trams N. R., van der Bliek N. R., Valentijn E. A. and Wesselius P. R. (1996) SWS observations of young main-sequence stars with dusty circumstellar disks. *Astronomy and Astrophysics* **315**, L245-L248.

Wasserburg G. J., Boothroyd A. I., and Sackmann I. J. (1995) Deep circulation in red giant stars: a solution to the carbon and oxygen isotope puzzles? *The Astrophysical Journal* **447**, L37-L40.

Waters L. B. F. M., Molster F. J., de Jong T., Beintema D. A., Waelkens C., A. C. A. Boogert, Boxhoorn D. R. et al. (1996) Mineralogy of oxygen-rich dust shells. *Astronomy and Astrophysics* **315**, L361-L364.

Wogelius R. A. and Walther J. V. (1992) Olivine dissolution kinetics at near surface conditions. *Chemical Geology* **97**, 101-112.

Yada T., Floss C., Stadermann F. J., Zinner E., Nakamura T., Noguchi T., and Lea A. S. (2008) *Meteoritics and Planetary Science* **43**, 1287-1298.

Zega T. J., Alexander C. M. O'D., Nittler L. R., and Stroud R. M. (2009) Transmission electron microscopy analysis of a presolar spinel grain. *Lunar and Planetary Science Conference* 40, Abstract #1342.

Zinner E., Nittler L. R., Hoppe P., Gallino R., Straniero O., and Alexander C. M. O'D. (2005) Oxygen, magnesium and chromium isotopic ratios of presolar spinel grains. *Geochimica et Cosmochimica Acta* **69**, 4149-4165.

Zinner E., Amari S., Guinness R., Jennings C., Mertz A. F., Nguyen A. N., Gallino R., Hoppe P., Lugaro M., Nittler L. R., and Lewis R. S. (2007) NanoSIMS isotopic analysis of small presolar grains: Search for Si_3N_4 grains from AGB stars, and Al and Ti isotopic compositions of rare presolar SiC grains. *Geochimica et Cosmochimica Acta* **71**, 4786-4813.

CHAPTER 4

STARDUST MATERIAL IN THE PAIRED ENSTATITE CHONDRITES: SAH 97096 AND SAH 97159

Abstract

Stardust grains, more commonly referred to as *presolar grains*, are solid condensates of stars that are studied in terrestrial laboratories with a variety of analytical techniques. Here we report on sub-micrometer silicate, oxide and carbonaceous stardust grains identified in the paired enstatite chondrites SAH 97096 and SAH 97159. A majority of the grains with O isotopic anomalies exhibit ^{17}O excesses and probably originated in the dusty envelopes of low-mass AGB or RG stars. One grain is highly ^{17}O-rich and has a normal Si isotopic composition; based on its O and Si isotopic composition, an origin in a nova is most likely. However, another scenario that may explain this grain's O isotopic composition is a binary star system consisting of an evolved or mainstream star accreting material from its nova companion. Elemental characterization of the O-anomalous grains shows the presence of eleven magnesian silicate grains with or without Fe and three Fe-oxide grains; none of the grains contain Ca or Al. Carbon-anomalous grains have $^{12}C/^{13}C$ ratios from 19–78; most are probably SiC. The abundances of the O- and C-anomalous grains are 98±34 and 51±13 ppm, respectively, which is much higher than previously observed in other enstatite chondrites, and close to that of some carbonaceous chondrites.

4.1. Introduction

Silicate stardust exhibits large O isotopic anomalies and can be found in the form of sub-micrometer sized grains in primitive extraterrestrial materials. These grains survived interstellar processing, heating in the early solar nebula and accretion into parent bodies, as well as possible aqueous alteration, impacts, and thermal metamorphism on those parent bodies. Most searches for silicate stardust grains have been carried out in carbonaceous chondrites (e.g., Floss and Stadermann 2009; Bose et al. 2010), and much less information is available about silicate stardust in enstatite chondrites. However, these chondrites are of interest because they formed under highly reducing conditions, which

may allow the preferential survival of certain types of grains. In addition, comparison of stardust grain abundances in enstatite versus carbonaceous and ordinary chondrites can provide information about conditions in the early solar nebula.

Here we report on the search for stardust grains in the enstatite chondrites, SAH 97096 (100–500 nm grain size-separates) and SAH 97159 (polished thin-section) using the Washington University NanoSIMS 50 (secondary ion mass spectrometry) and PHI 700 Auger Nanoprobe. These two meteorites are paired and are among the most primitive EH3 chondrites (Weisberg and Prinz 1998). A discussion of the analytical techniques used can be found in Stadermann et al. (2005) and Stadermann et al. (2009).

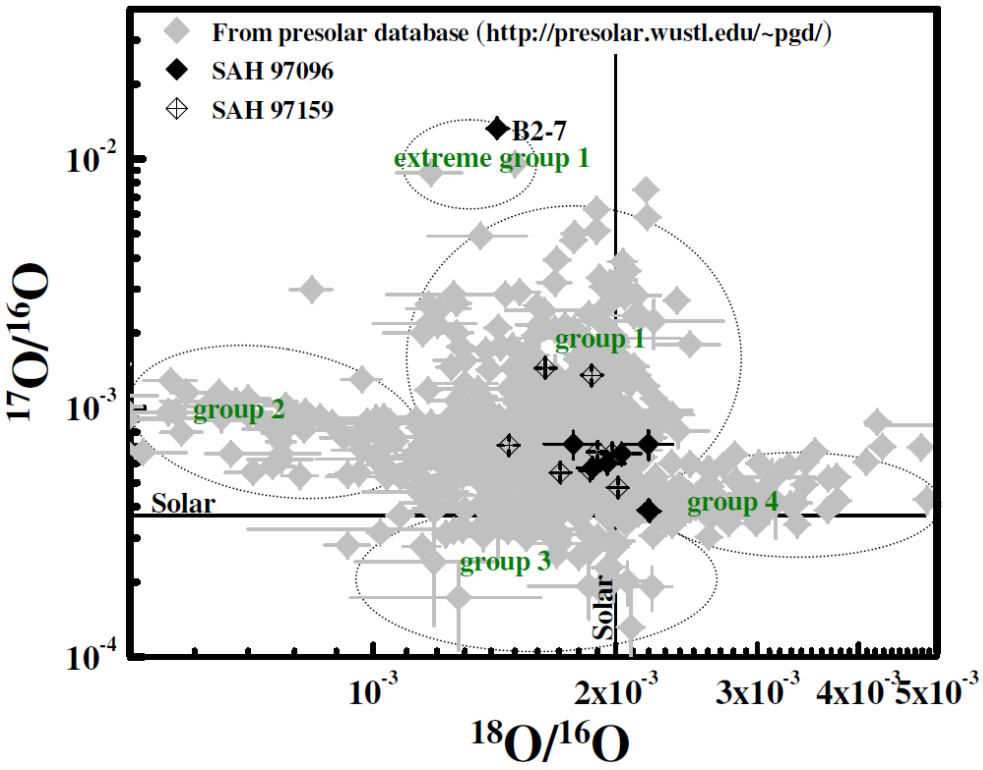

Figure 4.1: Oxygen isotopic ratios of presolar oxide and silicate grains from this study (black symbols) and grains from the presolar grain database (gray symbols). Ellipses indicate the O-isotopic groups defined by [5, 7]. Errors are 1σ.

4.2. Results

We identified eight O-anomalous and four C-anomalous grains by ion isotope searches on 14,400 μm^2 of dispersed grains from SAH 97096. In SAH 97159, where we measured a total matrix area of 10,800 μm^2, we found eight O-anomalous grains and fifteen C-anomalous grains. Of the sixteen O-anomalous grains (Table A4.1), thirteen grains have enrichments in ^{17}O and are largely normal in their $^{18}O/^{16}O$ ratios while two grains show enrichments in ^{18}O (Figure 4.1). One grain, B2-7, exhibits a large enrichment in ^{17}O with a $^{17}O/^{16}O$ ratio of $(1.33\pm0.01) \times 10^{-2}$, and an $^{18}O/^{16}O$ ratio of $(1.43\pm0.04) \times 10^{-3}$. The Si isotopic composition of B2-7 is $\delta^{29}Si = 21\pm56$ ‰ and $\delta^{30}Si = 57\pm69$ ‰, i.e., normal within 1σ. The eighteen C-anomalous grains have $^{12}C/^{13}C$ ratios that range from 19 to 78. Auger Nanoprobe analyses of SAH 97159 were complicated by extensive sample charging issues and the Auger spectra will only be discussed qualitatively. However, because the grain size-separates from SAH 97096 were deposited on Au foil, we did not have similar charging issues with these grains. All the O-anomalous grains in SAH 97159 are ferromagnesian silicate grains; two grains are Fe-rich. Three of the O-anomalous grains from SAH 97096 are silicate grains and three are Fe-oxides. Grain E20-33 has an (Fe+Mg)/Si ratio of 1.2±0.2 suggesting that it has a pyroxene-like stoichiometry. Grains D-1 and 3-7 from SAH 97159 are Si-rich, as is grain E5-112 from SAH 97096; this grain contains no Mg and has 21±2 at.% Fe. Grain B2-7 is 460×400 nm^2 in size and contains more Mg than forsterite. Calcium and Al are below detection in all grains (~3 at.%).

Among the C-anomalous grains, six grains were characterized as SiC based on the presence of C and Si peaks in their Auger spectra. The remaining C-anomalous grains

were either sputtered away at the end of the NanoSIMS measurements or could no longer be located.

4.3. Discussion

4.3.1. Isotopic Compositions

The O isotopic compositions of the presolar oxide and silicate grains found in SAH 97096 and 97159 fall within the range of presolar oxide groups (Nittler et al. 2008). Thirteen grains have ^{17}O-rich compositions consistent with a group 1 classification and are likely to have originated in low-mass RG or AGB stars (~1.1–2.5$M_{\odot}$) with close-to-solar or slightly lower-than-solar metallicity (Nittler et al. 2008). Two grains are ^{18}O-rich and belong to group 4; these grains may have Type II supernova origins, as suggested by Nittler et al. (2008). Grain B2-7 has O and Si isotopic compositions similar to other "extreme group 1" grains that have been identified in Acfer 094 (Vollmer et al. 2008; Nguyen et al. 2010), and that may be nova condensates. For example, the ^{17}O-rich composition and normal Si isotopic ratios of an extreme group 1 silicate from Acfer 094 can be explained by nucleosynthetic models of a 0.8$M_{\odot}$ CO nova (Nguyen et al. 2010). However, much larger ^{25}Mg isotopic anomalies are predicted by this CO nova model, than are seen in this grain. Furthermore, ONe nova models can *qualitatively* account for the observed O and Si isotopic signatures of three additional extreme group 1 silicates but a quantitative comparison reveals large discrepancies (Vollmer et al. 2008). In these cases, grain formation in binary star systems, where material is transferred from a nova explosion to a main sequence star or an evolved star, has been suggested (Nittler et al. 2008; Gyngard et al. 2010). A similar formation scenario for grain B2-7 is likely.

The $^{12}C/^{13}C$ isotopic ratios of the C-anomalous grains reflect compositions similar to mainstream SiC grains, which make up 93% of the SiC grain population (Zinner 2007). These mainstream SiC grains probably originate in C-rich AGB stars (Zinner 2007).

4.3.2. Fe-rich Elemental Compositions

Three silicate grains in our inventory have Fe-rich compositions, like presolar silicates identified in some carbonaceous chondrites (e.g., Floss and Stadermann 2009; Bose et al. 2010). Based on equilibrium condensation calculations, Mg-rich phases are suggested to form at high-temperatures while the formation of Fe-containing phases is inhibited (Lodders and Fegley 1999). Iron-rich grains can condense either at low temperatures (~700K) or under non-equilibrium conditions (Ferrarotti and Gail 2001), wherein a rapid fall in temperature allows the incorporation of Fe in the silicate grains. Iron can also be introduced by secondary processes in the parent body or on Earth. For example, thermal metamorphism in the meteorite parent bodies can lead to the introduction of Fe, via diffusion, into grains with low Fe contents (Jones and Rubie 1991). Incorporation of Fe into silicate grains may also occur in the nebular environment during gas-grain interactions. Mineral composition studies of SAH 97096 and its pairs show that these EH3 chondrites have experienced little parent body metamorphic heating (e.g., Patzer and Schultz 2001). Although little is known about the temperatures experienced by these meteorites prior to accretion, diffusion is slow during gas-grain interactions at low temperatures in a solar composition gas (Palme and Fegley 1990), which may largely prevent the diffusion of Fe into silicate grains. Furthermore, alteration during the meteorite's residence time on Earth may lead to the loss of Mg and/or Si, and result in Fe-rich silicate grains (e.g., Bland et al. 1998). However, Patzer and Schultz

(2001) argues for little terrestrial alteration of the SAH chondrites studied here based on Ar and Ne cosmic ray exposure ages. The high Fe contents observed in the silicate stardust grains therefore may primarily arise due to formation under non-equilibrium conditions in the outflows of young and evolved stars; secondary processing has probably contributed only to a small extent.

4.3.3. Comparison between Chondrite Classes: Abundance Estimates and Elemental Compositions

Abundance calculations on grain size-separates (i.e., SAH 97096) are difficult to carry out because of the large errors involved in determining the mass fraction of the separates. However, the abundances of presolar silicate and carbonaceous grains determined in the thin-section of SAH 97159 are 98±34 and 51±13 ppm, respectively. The abundance of O-anomalous grains from this work is higher than that found in other enstatite (e.g., Ebata et al. 2006) and ordinary chondrites, and is close to that of some carbonaceous chondrites (Figure 4.2). The lack of presolar silicates in SAH 97072, which is paired with SAH 97159/97096, may be due to analytical differences (Ebata et al. 2006). The abundance of O-anomalous grains in the paired SAH chondrites studied here is somewhat lower than in the most primitive carbonaceous chondrites. Other enstatite chondrites (Figure 4.2) also exhibit low abundances of O-anomalous grains. It has been argued that the material that accreted to form the enstatite chondrites has experienced nebular thermal processing (e.g., Huss and Lewis 1995). Calcium-aluminum-rich inclusions in SAH 97159 are highly altered (Lin et al. 2003) and exotic FeO-rich silicates show evidence for reduction (Kimura et al. 2003). These effects, as well as the low presolar silicate abundances, may be a result of such nebular processing.

Our abundance estimate for C-anomalous grains is similar to presolar SiC abundances in the CR chondrites (~65 ppm; Floss and Stadermann 2009) indicating that the pre-accretionary thermal processing experienced by the SAH chondrites has not destroyed these more refractory carbonaceous stardust grains.

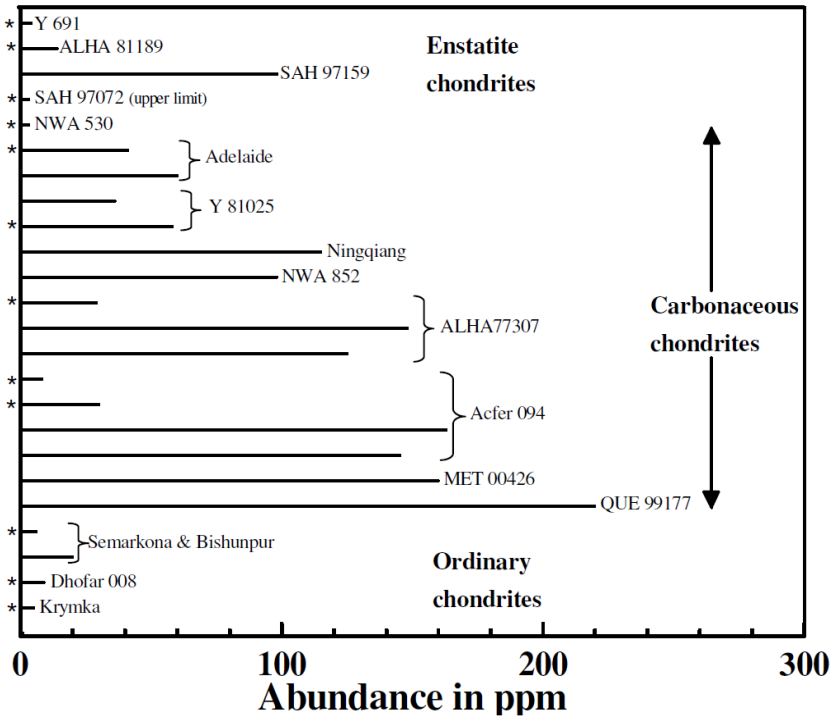

Figure 4.2: Bar graph showing the matrix-normalized abundances (ppm) of presolar silicate grains in various chondrites. Those marked with an asterisk are samples measured using the IMS 1270 with a SCAPS detector.

The presolar silicate grains identified in the enstatite chondrites have similar elemental compositions as those observed in other carbonaceous chondrites (Floss and Stadermann 2009; Bose et al. 2010). However, the silicate/oxide grain ratio of ~4 in the SAH chondrites is lower than that observed in a few carbonaceous chondrites (e.g., ~11 in Acfer 094 (Bose et al. 2010) and 53 in QUE 99177 and MET 00426, combined (Floss and Stadermann 2009)). Silicate grains may have been destroyed as a consequence of

thermal processing (Huss and Lewis 1995).

4.4. Conclusions

Our data show that a significant fraction of stardust grains have survived the thermal episode(s) in the nebular environment experienced by and recorded in the material that accreted to form the enstatite chondrites. Abundances of stardust phases in the enstatite chondrites studied here are higher than previously reported and are close to what has been observed for some carbonaceous and ordinary chondrites. Observations of high Fe contents in the silicate grains suggest that kinetics play a key role in the condensation of dust grains in stellar outflows, as discussed by Bose et al. (2010).

Acknowledgement. We would like to thank Dr. Larry R. Nittler for his comments that helped improve the paper.

References

Bland P. A., Sexton A. S., Jull A. J. T., Bevan A. W. R., Berry F. J., Thornley D. M., Astin T. R., Britt D. T., and Pillinger C. T. (1998) Climate and rock weathering: a study of terrestrial age dated ordinary chondritic meteorites from hot desert regions. *Geochimica et Cosmochimica Acta* **62**, 3169-3184.

Bose M., Floss C., and Stadermann F. J. (2010) An investigation into the origin of Fe-rich presolar silicates in Acfer 094. *The Astrophysical Journal* **714**, 1624-1636.

Ebata S., Nagashima K., Itoh S., Kobayashi S., Sakamoto N., Fagan T. J., and Yurimoto H. (2006) Presolar silicate grains in enstatite chondrites. *Lunar and Planetary Science*

Conference 37, Abstract #1619.

Ferrarotti A. S. and Gail H.-P. (2001) Mineral formation in stellar winds II: Effects of Mg/Si abundance variations on dust composition in AGB stars. *Astronomy and Astrophysics* **371**, 133-151.

Floss C. and Stadermann F. J. (2009) Auger Nanoprobe analysis of presolar ferromagnesian silicate grains from primitive CR chondrites QUE 99177 and MET 00426. *Geochimica et Cosmochimica Acta* **73**, 2415-2440.

Gyngard F., Zinner E., Nittler L. R., Morgand A., Stadermann F. J., and Hynes K. M. (2010) Automated Nanosims measurements of spinel stardust from the Murray meteorite. *The Astrophysical Journal* **717**, 107-120.

Huss G. R. and Lewis R. S. (1995) Presolar diamond, SiC, and graphite in primitive chondrites: abundances as a function of meteorite class and petrologic type. *Geochimica et Cosmochimica Acta* **59**, 115-160.

Jones R. H. and Rubie D. C. (1991) Thermal histories of CO3 chondrites: application of olivine diffusion modeling to parent body metamorphism. *Earth and Planetary Science Letters* **106**, 73-86.

Kimura M., Hiyagon H., Lin Y., and Weisberg M. K. (2003) FeO-rich silicates in the Sahara 97159 (EH3) enstatite chondrite: Mineralogy, oxygen isotopic compositions, and origin*, Meteoritics and Planetary Science* **38,** 389-398.

Lin Y., Kimura M., Hiyagon H.**,** and Monoi A. (2003) Unusually abundant refractory inclusions from Sahara 97159 (EH3): a comparative study with other groups of chondrites. *Geochimica et Cosmochimica Acta* **67**, 4935-4948.

Lodders K. and Fegley B. (1999) Condensation chemistry of circumstellar grains. In:

Asymptotic Giant Branch Stars, IAU Symposium No. 191 (eds. T. Le Bertre, A. Lebre and C. Waelkens). Astronomical Society of the Pacific, pp. 279-289.

Nguyen A. N., Messenger S., Ito M., and Rahman Z. (2010) Mg isotopic measurement of FIB-isolated presolar silicate grains. *Lunar and Planetary Science Conference* 41, #2413.

Nittler L. R., Alexander C. M. O'D., Gallino R., Hoppe P., Nguyen A. N., Stadermann F. J., and Zinner E. K. (2008) Aluminum-, calcium- and titanium-rich oxide stardust in ordinary chondrite meteorites. *The Astrophysical Journal* **682**, 1450-1478.

Palme H. and Fegley B. (1990) High-temperature condensation of iron-rich olivine in the solar nebula. *Earth and Planetary Science Letters* **101**, 180-195.

Patzer A. and Schultz L. (2001) Noble gases in enstatite chondrites I: exposure ages, pairing, and weathering effects. *Meteoritics and Planetary Science* **36**, 947-961.

Stadermann F. J., Croat T. K., Bernatowicz T., Amari S., Messenger S., Walker R. M., and Zinner E. (2005) Supernova graphite in the NanoSIMS: carbon, oxygen and titanium isotopic compositions of a spherule and its TiC sub-components. *Geochimica et Cosmochimica Acta* **69**, 177-188.

Stadermann F. J., Floss C., Bose M., and Lea A. S. (2009) The use of Auger spectroscopy for the in situ elemental characterization of sub-micrometer presolar grains. *Meteoritics and Planetary Science* **44**, 1033-1049.

Vollmer C., Hoppe P., and Brenker F. E. (2008) Si isotopic compositions of presolar silicate grains from red giant stars and supernovae. *The Astrophysical Journal* **684**, 611-617.

Weisberg M. K. and Prinz M. (1998) Sahara 97096: A highly primitive EH3 chondrite

with layered sulfide-metal-rich chondrules. *Lunar and Planetary Science Conference* 24, Abstract #1741.

Zinner E. (2007) Presolar Grains. In: Treatise on Geochemistry Update 1 (eds. H. D. Holland and K. K. Turekian; vol. ed. A. M. Davis), Elsevier Ltd., Oxford, Online update only. Vol. 1.02 pp. 1-33.

CHAPTER 5

STELLAR AND INTERSTELLAR MATERIAL IN THE CO3 CHONDRITE ALHA77307: AN ISOTOPIC AND ELEMENTAL INVESTIGATION

Abstract

Presolar grains can provide unique information on the composition of dust that existed in the solar neighborhood before the formation of the solar system and the types of stellar sources from which this dust originated. Here we report the isotopic and elemental compositions of presolar silicate, oxide, and SiC grains that are identified in the matrix of ALHA77307. Most of the grains with O isotopic anomalies (84%) are ^{17}O-enriched and come from 1.1–2.5$M_{\odot}$ asymptotic giant branch (AGB) stars of close-to-solar or lower-than-solar metallicity. One grain with an extremely large ^{17}O enrichment ($^{17}O/^{16}O \sim 89.3\times10^{-4}$) may have formed in a binary star system with some (~5%) contribution from a nova. About 8% of the O-anomalous grains in this study show ^{18}O excesses; these grains appear to have condensed either in Type II supernova (SN) ejecta or in higher than solar metallicity AGB stars. Out of the remaining grains, 6% exhibit ^{17}O excesses with $^{18}O/^{16}O$ ratios that are as low as $\sim6\times10^{-4}$. Their compositions may be explained by cool bottom processing in low-mass stars during the AGB phase. One grain (~1%) has a ^{16}O-rich composition consistent with formation in a star with lower-than-solar metallicity.

Elemental characterization of the O-anomalous grains led to their classification into 67 silicate grains, three Al-oxide grains, two Fe-oxide grains, three SiO_2 grains, and two 'composite' grains (i.e., composed of multiple subgrains exhibiting different elemental compositions). One grain contains only Mg and O, and has a stoichiometry consistent with MgO; this is the first observation of this presolar grain type. The Fe contents in the silicate grains are as high as 26 at.%, and are most likely due to formation of the grains under non-equilibrium conditions. The Mg+Fe(+Ca)/Si ratios of the majority of the silicate grains fall between 1 (pyroxene) and 2 (olivine), and there is a predominance of olivine-like rather than pyroxene-like silicate grain compositions, consistent with astrophysical predictions. Supernovae appear to produce more olivine- than pyroxene-like grains in their ejecta.

Among the twenty-five SiC grains identified in ALHA77307, twenty-three have $^{12}C/^{13}C$ ratios between 11 and 75, and can be identified as mainstream SiC grains that may have formed in 1–3$M_{\odot}$ AGB stars. One SiC A+B grains may have formed in J-type or born again AGB stars, while one SiC Y grain in our presolar SiC inventory has a likely origin in a lower-than-solar metallicity AGB star. All the SiC grains are less than 300 nm in size, except four grains, which are larger in size with a diameter of ~400 nm.

The matrix-normalized abundances of silicate and SiC grains in ALHA77307 are 119±14 ppm and 109±22 ppm, respectively. The high O-anomalous grain abundance is consistent with the lack of substantial processing experienced by this meteorite. The sub-micrometer-sized SiC abundance in this meteorite is an order of magnitude greater than bulk abundances from noble gas measurements and from SiC grains identified by ion imaging of insoluble organic matter. The SiC abundance in ALHA77307 is high and can be either attributed to heterogeneity within the meteorite or heterogeneous distribution of presolar material in the parent molecular cloud.

Apart from the presolar phases, particularly notable is the high abundance (160±30 ppm) of material with excesses in ^{15}N (409–1266‰) relative to the terrestrial $^{15}N/^{14}N$ ratio. These phases with N isotopic anomalies probably formed in cold molecular clouds via ion-molecule reactions. Except in three cases in which the material exhibits ^{13}C excesses (45±10‰, 70±10‰, and 90±15‰), the material has normal C isotopic compositions. Although, we can't completely rule out presolar graphite as the carrier phase of some ^{15}N-rich hotspots, the hotspots are more likely carbonaceous material that occasionally contains Si, Fe, and Mg. Out of all the N-anomalous grains, three nanoglobules have been observed. Two of these exhibit C anomalies similar to that observed in the nanoglobule identified in the CR3 chondrite MET 00426.

5.1. Introduction

Presolar material that can today be found in a variety of primitive extraterrestrial materials includes grains that formed around evolved stars. Presolar material also include organic matter that formed in cold molecular clouds and may coat stellar dust grains. All these materials survived the collapse of the molecular cloud from which our solar system originated and are available for investigation in primitive meteorites, comets, interplanetary dust particles (IDPs), and Antarctic micrometeorites. Coordinated analyses using various analytical techniques can provide information about the stellar sources of the grains and allow the testing of grain condensation models. Laboratory studies of this material that survived the conditions and processes in the early solar system can also give us insight into processing in the early solar nebula, in the interstellar medium as well as in the parent body.

It is now well established that presolar silicates are the most abundant presolar grain

type besides nanodiamonds. Abundances of ~375 ppm in primitive IDPs (Floss et al. 2006) and up to ~200 ppm in primitive chondrites (Nguyen et al. 2007; Floss and Stadermann 2009a; Vollmer et al. 2009a; Nguyen et al. 2010a) have been reported to date. However, the presolar silicate abundances differ widely among meteorites belonging to different classes. Presently it is unclear whether these differences are due to different degrees of aqueous or thermal processing, or heterogeneity of the silicate dust acquired from the numerous stellar sources. Most presolar silicate grains formed either in the outflows of low-mass red giant (RG) and asymptotic giant branch (AGB) stars or in the ejecta of Type II supernovae (SNe). Presolar silicates that have been identified and characterized to date include amorphous and crystalline phases (Nguyen et al. 2007; Stroud et al. 2008; Vollmer et al. 2009b), crystalline olivine (Messenger et al. 2003, 2005), and silicate grain with perovskite structure (Vollmer et al. 2007). In addition to the silicate grains, abundant presolar SiC has been found *in situ* of meteorites (e.g., Floss and Stadermann 2009a). Distinct from this collection, various phases with N isotopic anomalies have been identified in insoluble organic matter (IOM) isolated from meteorites (e.g., Busemann et al. 2006). Such material is generally thought to have formed in interstellar molecular clouds (IMCs) or in the solar protoplanetary disk, via ion-molecule reactions (Aléon 2010), and in some cases also contains C anomalies, as is observed in IDPs and the CR3 chondrites (Floss et al. 2004, 2006; Floss and Stadermann, 2009b).

The Antarctic find ALHA77307 (Allan Hills, Antarctica) is a CO3.0 chondrite (Brearley 1993). Its fine-grained matrix consists of abundant amorphous dust and other components (size range 0.05–1.00 μm) consisting of unequilibrated assemblages of Fe-

and Si-rich material (Scott and Jones 1990). Although in general ALHA77307 has experienced minimal thermal metamorphism and aqueous alteration (e.g., Scott and Jones 1990; Brearley 1993; Grossman and Brearley 2005; Bonal et al. 2007), based on recent Raman analyses of IOM from ALHA77307, Busemann et al. (2007) concluded that ALHA77307 has experienced thermal metamorphism to some extent. Presolar silicate grains are more susceptible to alteration mechanisms than refractory SiC grains. One of the topics we investigate here is whether such secondary alteration has modified the elemental compositions of silicate grains and destroyed organic material of protosolar origin. Furthermore, study of this meteorite could lead to the identification of *new* presolar grain phases and additional silicates. Presolar grains with SiO_2 composition were discovered in this meteorite (e.g., Nguyen et al. 2010a; Bose et al. 2010a). In addition, correlated isotopic and elemental characterization of numerous presolar silicates may allow us to conclude if any correlations exist between the isotopic compositions of the silicate grains that indicate the stellar sources, and their elemental compositions.

Here we report the compositions and abundances of presolar material in ALHA77307. Preliminary data were reported by Bose et al. (2009; 2010a, b; 2011).

5.2. Samples and Experimental

5.2.1. Documentation

A polished thin-section of ALHA77307 was obtained from the curatorial facility at the Johnson Space Center, Houston. Prior to analyzing the thin-section in the NanoSIMS, transmitted and reflected light images were obtained using an Olympus BH-2 optical microscope. The transmitted light images enabled the identification of the dark fine-

grained matrix areas, where presolar grains are sited, while the reflected light images aid in sample navigation through comparison to optical images in the NanoSIMS. High-resolution microscope pictures were taken in an array and the pictures were stitched together with image processing software.

5.2.2. NanoSIMS 50 Measurements

Oxygen-anomalous grain searches were done in the NanoSIMS by rastering a primary Cs^+ beam (~100 nm) of about 1 pA and collecting $^{12,13}C^-$ and $^{16,17,18}O^-$ secondary ions (set 1) and secondary electrons (SEs) in multi-collection mode. Nitrogen-anomalous grain searches were also done in the matrix of ALHA77307 by automated mapping of $^{12,13}C^-$, $^{12}C^{14}N^-$, $^{12}C^{15}N^-$, $^{28}Si^-$ ions and SEs (set 2). Prior to acquiring isotopic data for 10×10 μm^2 areas (256^2 pixels), 12×12 μm^2 areas in the matrix were sputtered at a higher beam current (~25 pA), in order to locally remove the carbon coating on the thin-section. Measurements were carried out by automatic stage movements following a predefined grid pattern and each measurement was made as a series of 5–10 layers. During data processing, possible image-shifts during measurements were corrected for, followed by addition of consecutive layers to constitute a single image measurement. A second round of O isotopic measurements was performed for the FIB section containing the grain 21420 (see below).

The O- and N-anomalous grains can be identified from the $^{17}O/^{16}O$, $^{18}O/^{16}O$, and $^{12}C^{14}N^-/^{12}C^{15}N^-$ ratio images, respectively. Presolar grain searches, using sets 1 and 2 mentioned above, also resulted in the identification of grains with C anomalies on the basis of $^{12}C/^{13}C$ ratio images. A grain is considered presolar if any of its O, N, or C isotopic ratios are different from normal ratios by 5σ and the isotopic 'hotspots' can be

traced through the images for at least three consecutive layers. Isotopic ratios in all cases were internally normalized, which assumes that the compositions of the bulk matrix are normal. The O- and C-anomalous grain compositions are normalized relative to the solar isotopic ratios ($^{16}O/^{17}O = 2625$; $^{16}O/^{18}O = 499$; $^{12}C/^{13}C = 89$; Anders and Grevesse 1989), whereas the N-anomalous areas are normalized relative to the terrestrial N isotopic ratio ($^{14}N/^{15}N = 272$). We were able to use this procedure for calculating the isotopic ratios because the anomalous hotspots are spatially localized in the matrix. Some chondrites exhibit an anomalous bulk IOM (Alexander et al. 2007), but that is not the case with ALHA77307 and, therefore, internal normalization could be used for N isotopes. Additional details about isotope imaging measurements in the NanoSIMS and subsequent image processing can be found in Stadermann et al. (2005).

5.2.3. PHI 700 Auger Nanoprobe Measurements

Subsequent to the identification of isotopically anomalous phases, high-resolution SE images of the grains were acquired in the Auger Nanoprobe. Image alignment of the SE images acquired in the NanoSIMS and Auger Nanoprobe was done to locate the anomalous grains. Elemental compositions of the anomalous grains were acquired at electron beam settings of 10 keV and 0.25 nA. We use a standard operating procedure for such analysis, which is described in Bose et al. (2010c). Multiple Auger spectra were acquired over the grain of interest numerous times (~20) and were then added together. Elemental compositions of the O-anomalous grains were calculated using sensitivity factors for O, Si, Fe, Mg, Ca, and Al obtained from olivine and pyroxene standards of various compositions (Stadermann et al. 2009), and their corresponding errors were calculated by using the estimated 1σ uncertainties based on these standards. The

experimentally derived sensitivity factors and the relative uncertainties (in square brackets) are O: 0.194 [3.6%], Si: 0.121 [11.0%], Mg: 0.234 [9.4%], Fe: 0.150 [11.2%], Ca: 0.626 [10.8%], and Al: 0.160 [24.9%] (Stadermann et al. 2009). The errors associated with the measurements may also be affected by the presence of contaminants and low signal to noise ratios, and are, therefore, assumed to be lower limits. In the case of the C- and N-anomalous grains, we used the Auger spectra and maps to differentiate between SiC and other carbonaceous phases. For some grains (see section 5.3.2) the classification required other considerations like C and N isotopic compositions, and elemental ratios from the NanoSIMS measurements. Quantitative Auger Nanoprobe data are not reported for the SiC and carbonaceous grains. Standards with hematite (Fe_2O_3) and MgO compositions were measured in the Auger Nanoprobe in order to obtain elemental compositions for a few grains.

Elemental spectra were often complemented by maps of specific elements (e.g., Ca, O, Fe, Mg, Al, Si) at electron beam settings of 10 keV and 5 nA. Elemental mapping consisted of 3–40 scans over 2×2 μm^2 or 4×4 μm^2 areas that contained the grain of interest.

5.2.4. Transmission Electron Microscopy (TEM) Measurement

One presolar grain, 21420, was chosen for chemical and structural investigations using the 200 kV JEOL 2200FS TEM at the Naval Research Laboratory. Prior to characterization in the TEM, the sample was extracted by focused ion beam (FIB) lift-out using the Nova NanoLab 600. Although a brief description of the technique used in creating and extracting *in situ* sections is given here, see Zega et al. (2007) for a detailed discussion. Once the grain of interest is located, a circular Pt 'cap' of ~20 nm thickness is

deposited above the grain to ensure that the grain surface is protected. Subsequently, Pt is again deposited using a low current ion beam along a line, referred to as a 'strap', through the center of the Pt cap in order to identify the orientation of the grain with greater accuracy. A C layer is then deposited over the Pt strap to minimize sample-charging effects. The section is created by milling away material surrounding this C layer, lifted out of the mount using a micromanipulator tip, and welded to a Cu-grid holder with Pt deposition. Final thinning of the section is performed using low ion beam currents in multiple steps. Because only the front sample surface is seen in the SEM, the sample is rotated after each step in order to control and monitor the thinning process. Subsequent to thinning of the section to less than 100 nm, the section is investigated in the TEM. Energy dispersive X-ray (EDX) analysis was performed on the grain to determine its chemistry. For EDX analysis, the probe was focused onto the grain of interest and spectra were acquired with an EDX spectrometer. We also mapped the distribution of selected elements (Al, Ca, Fe, Mg, O, and Si) on a 0.7×0.7 μm^2 area on the section with a total acquisition time of a few hours. Bright and dark field imaging and selected area electron diffraction were acquired, where possible, to identify the crystal structure of grains in the section.

5.3. Results

5.3.1. Isotopic and Elemental Compositions of O-anomalous Grains

Eighty-eight O-anomalous grains were identified from the measurement of 17,100 μm^2 area on the matrix (Figure 5.1; Table A5.1). The size estimates in Table A5.1 have been determined from the secondary electron images acquired in the Auger Nanoprobe;

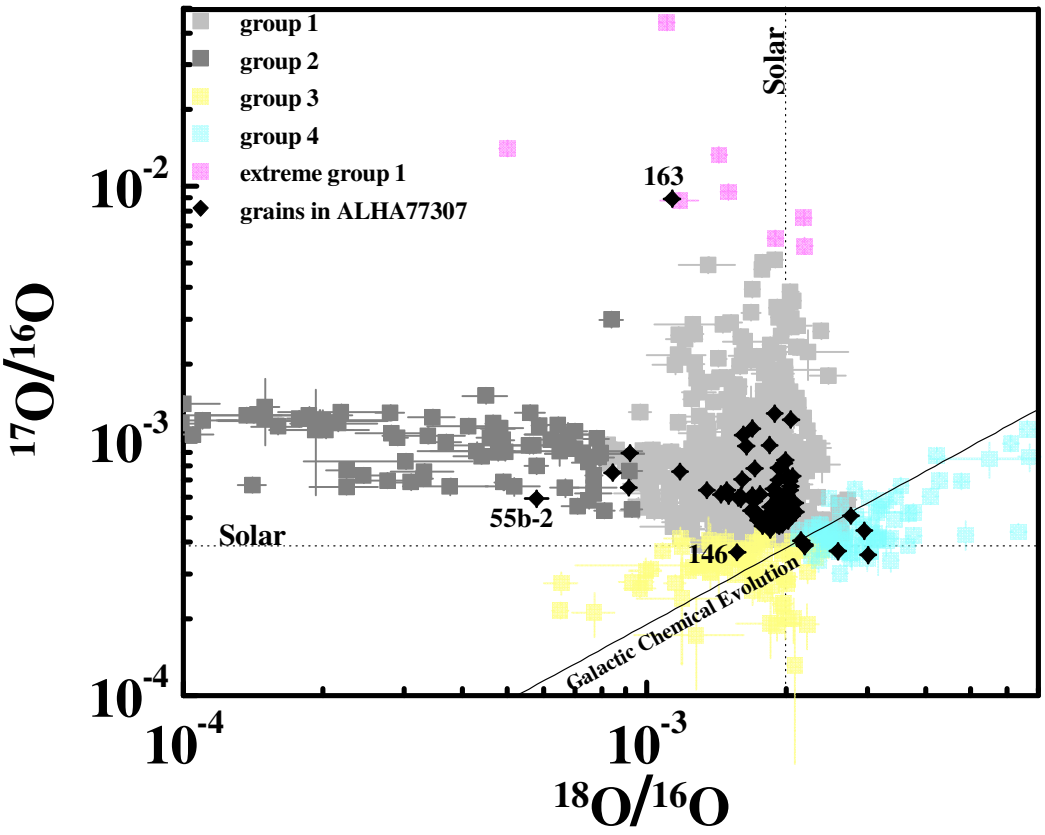

Figure 5.1: Oxygen three-isotope plot showing the O-anomalous grains from ALHA77307. Other data (gray squares) are from the presolar grain database (http://presolar.wustl.edu/~pgd/). See text for the definition of the Galactic Chemical Evolution line. Error bars are 1σ.

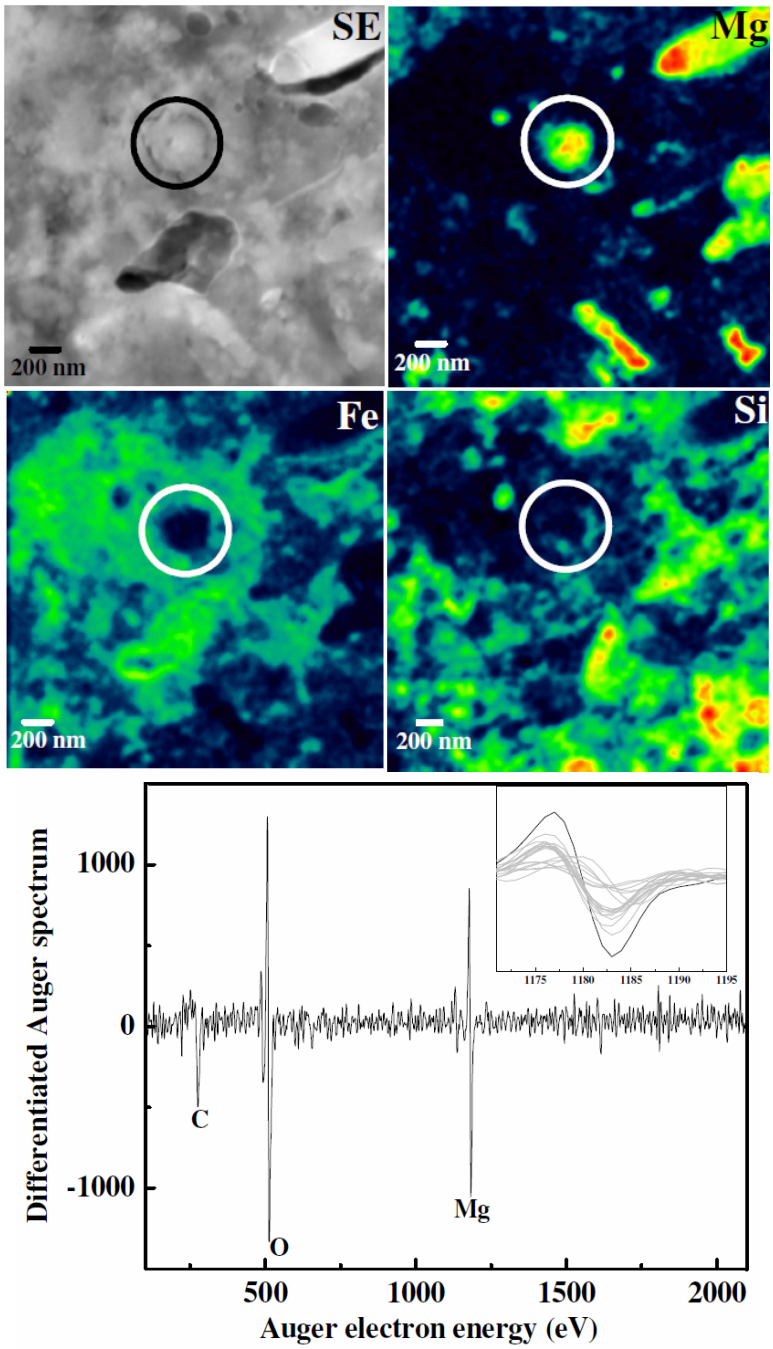

Figure 5.2: Secondary electron image of the Mg-oxide grain 55b-4 with Mg, Fe, and Si elemental maps, and Auger spectrum of the Mg oxide grain showing O and Mg peaks. The inset shows the Mg Auger peak of the grain (black) compared to the Mg peak in ferromagnesian silicate grains (gray) identified in ALHA77307. Here the O Auger peaks of the latter grains have been scaled to match the peak-to-peak height of grain 55b-4 and so the Y-axis has arbitrary units.

the sizes for the grains that could not be characterized in the Auger Nanoprobe (see below) were calculated from NanoSIMS ion images. Seventy-four grains (~84%) exhibit ^{17}O-rich compositions with close-to-solar $^{18}O/^{16}O$ ratios. One grain (163) shows an unusually high ^{17}O enrichment with a $^{17}O/^{16}O$ ratio of $(89.3\pm0.6)\times10^{-4}$ (Figure 5.1). Five grains (~6%) show ^{17}O enrichments and larger depletions in $^{18}O/^{16}O$ ratios than the group 1 grains (Figure 5.1). Oxygen-16-rich grains are rare in our study (~1%) and only one such grain (146) has been identified (Figure 5.1). Seven grains (~8%) are ^{18}O-rich and most of these grains exhibit close-to-solar $^{17}O/^{16}O$ ratios. Of these seven grains, two grains (45 and 10-4-O18) exhibit small ^{17}O excesses while one grain (54-5) shows a slight ^{17}O depletion.

Characterization of 78 O-anomalous grains in the Auger Nanoprobe allowed their classification into 67 silicate, six oxide, three SiO_2, and two complex grains (Tables A5.2a and A5.2b). We were unable to characterize ten grains in the Auger Nanoprobe (marked with ¶ in Table A5.1) because they were sputtered away during the NanoSIMS measurements. Of the oxide grains, one is a Mg-oxide, three are Al-oxide, and two are Fe-oxide (Table A5.2b). Detailed descriptions of the silicate and oxide grains are as follows:

MgO Grain: The grain 55b-4 is ^{17}O-rich and ^{18}O-poor (group 2). The SE image of this grain shows a near-spherical grain, which is about 420 nm in diameter. The Auger spectrum of the Mg-oxide grain shows the presence of Mg and O peaks, and the absence of all other elements (Figure 5.2). The C Auger peak in the spectrum of this grain is most likely due to surface contamination. Comparison of the grain composition to an MgO standard indicates a Mg/O ratio of 1.0±0.1. The height of the Mg Auger peak observed

for 55b-4 is larger than those of ferromagnesian silicate grains (see inset in Figure 5.2). This is the first time that a presolar grain with MgO composition has been observed.

SiO_2 Grains: Three group 1 grains (21420, 2132, and 10-4-bm) exhibit O/Si ratios of 2.2±0.3, 2.2±0.3, and 1.9±0.2, respectively and match SiO_2 composition. These grains have no detectable Mg or Fe in their spectra (Figure 5.3). The very small Fe peak that is seen in the Auger spectrum of 10-4-bm can be attributed to backscattered Auger electrons from an adjacent grain containing Fe. Silica grain 2132 has a diameter of about 220 nm with an unclear grain boundary while grain 10-4-bm is the largest of the three with a diameter of 320 nm. Grain 21420 has a complete grain boundary and is about 300 nm in diameter.

In order to determine the crystallinity of the SiO_2-like grain 21420 we produced an electron transparent section including the grain of interest. Although the structural form of the SiO_2 grain could not be ascertained from TEM analysis, spectra and high-resolution EDX maps confirmed the presence of a 140×50 nm^2 Si-rich area in the FIB section (Figure 5.4). Only a thin slice of the SiO_2 grain remained after NanoSIMS analysis, which may be the reason that a diffraction pattern could not be acquired. Therefore, the size of the Si-rich region was too small to acquire definitive structural information or observe an O anomaly in the post-nanoSIMS measurement of the section.

Al-oxide Grains: Grains 31 and 52-4-O are ^{17}O-rich while the grain 45 is ^{18}O-rich. Elemental spectra of the grains are dominated by large O and Al peaks; minor elemental peaks of Mg, Fe, and Si are observed in the case of grain 45. These Auger peaks for grain 45 can be attributed to either an overlap of the analysis box onto surrounding material or shifting of the analysis box during the measurement. Therefore, because Mg, Fe, and Si

are not intrinsic to the grain 45, the elemental compositions are re-normalized to exclude these peaks in Table A5.2b. The Al/O ratios of the grains 31, 45, and 52-4-O are 0.4, 0.4, and 0.5, respectively. These grains appear more O-rich than an Al_2O_3 composition, which suggests that the silicate sensitivity factors used for quantification of Al-oxide spectra may not be completely appropriate for these grains. Auger elemental maps clearly exhibit the absence of Mg in the grains of interest (Figure 5.5).

Fe-oxide Grains: Grain 21412 is a group 4 grain while grain 54-7 is a group 1 grain. These two grains are about 165 nm in diameter and show only Fe and O Auger peaks in their spectra. The former grain has Fe/O = 0.8±0.1, while the latter grain has a ratio of 0.5±0.1, using the sensitivity factors derived from a hematite standard (Fe_2O_3). Thus comparison of the grain spectra with those of a hematite standard (Fe_2O_3) shows that grain 21412 has a higher proportion of Fe to O than hematite and the grain 54-7 has a ratio lower than hematite.

Silicate Grains: Some grains with silicate compositions were classified as stoichiometric olivine- and pyroxene-like, based primarily on their Mg+Fe(+Ca)/Si ratios (Figure 5.6; Table A5.2a). This ratio is 2 for olivine-$(Mg,Fe)_2SiO_4$, and 1 for pyroxene-$(Mg,Fe)SiO_3$. Fifteen grains have olivine-like compositions while ten grains have pyroxene-like compositions. Cation/O and O/Si ratios were calculated to further constrain the stoichiometry of the grains (Table A5.2a). Only two and eight grains that are classified as pyroxene-like and olivine-like, respectively, contain O in stoichiometric proportions (see Table A5.2a for the cation/O and O/Si ratios for olivine and pyroxene grains).

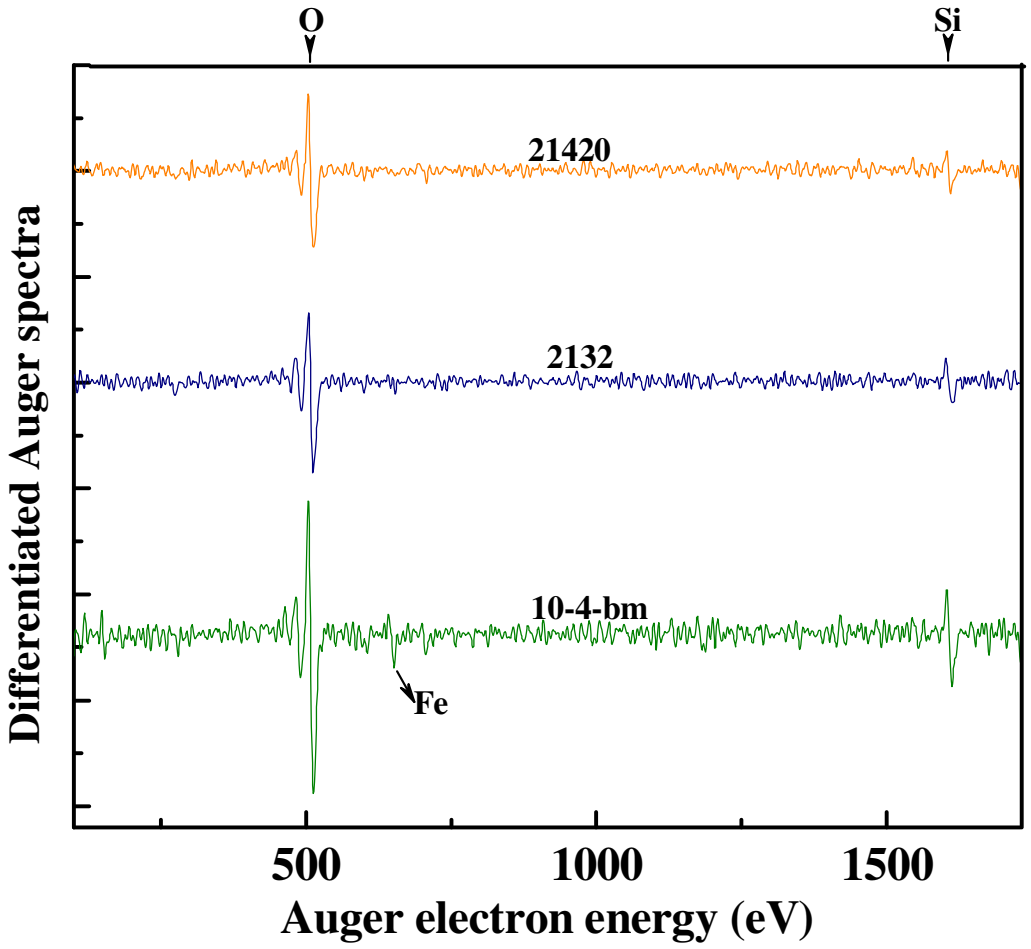

Figure 5.3: Auger spectra of the silica grains, 21420, 2132, and 10-4-bm. The small Fe peak in grain 10-4-bm is attributed to the backscattered Auger electrons from a Fe-rich region adjacent to the grain.

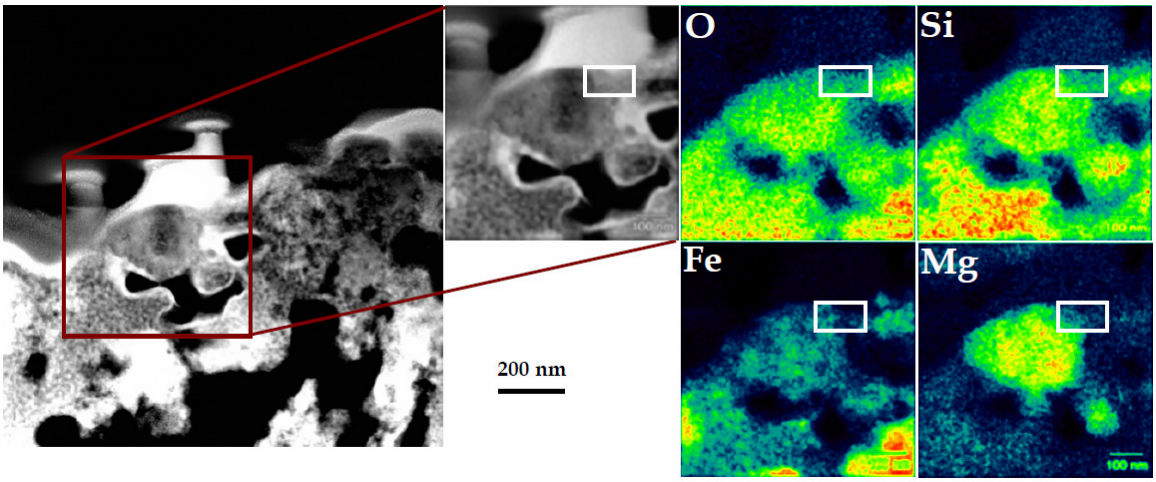

Figure 5.4: Z-contrast image (left-most) of the FIB section with the region of interest within the red square. The position of the silica grain 21420 is indicated by the white box below the white Pt cap. High-resolution elemental maps of the area containing the SiO_2 grain show a Si-rich area.

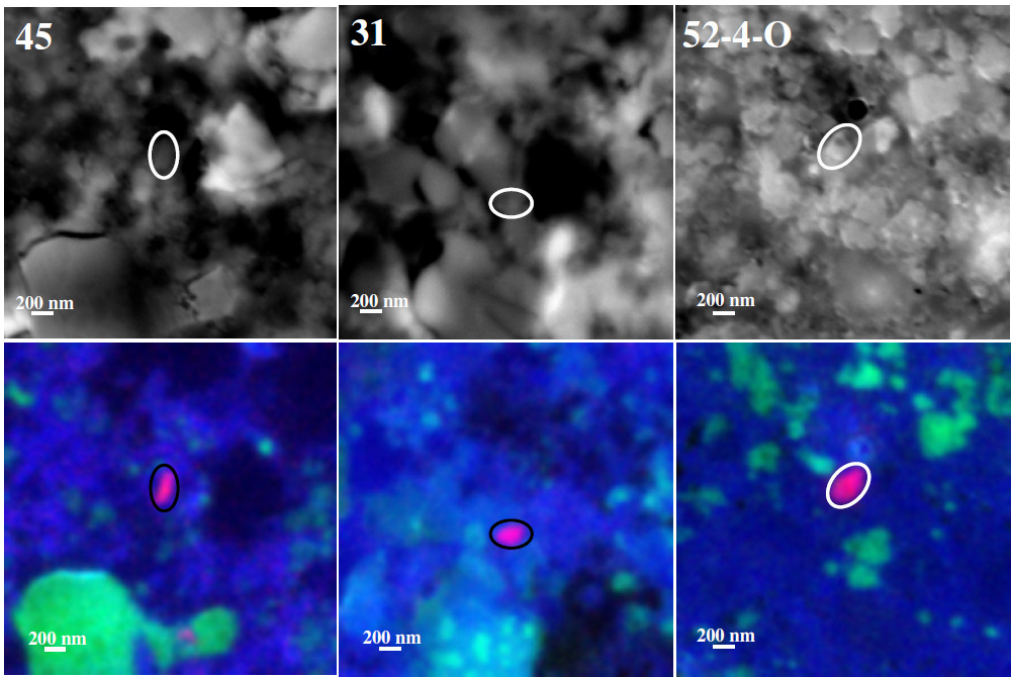

Figure 5.5: Secondary electron and RGB (Red=Al; Green=Mg; Blue=O) images of the Al-oxide grains, 45, 31, and 52-4-O.

Of the olivine-like grains, two grains have forsterite-like compositions. Of the pyroxene-like grains, 11-1-lt, 15-5-bm, and 48-bm, contain Al (5.8–7.3 at.%) while one, 54-1, contains Ca (4.9±0.5 at.%; Table A5.2a). One grain with a pyroxene-like composition, 5b-7, contains both Al (5.8±1.4 at.%) and Ca (1.9±0.2 at.%). Five olivine-like grains and four pyroxene-like grains have Fe-rich compositions with mg#s < 40 (Table A5.2a). Of the remaining (16) stoichiometric grains, only five grains have mg#s > 60 (i.e., Mg-rich). Olivine-like grains are more abundant than pyroxene-like grains in our inventory (Figure 5.6).

Twenty-three silicate grains have Mg+Fe(+Ca)/Si ratios between 1 and 2 and, thus, have compositions intermediate between olivine and pyroxene (Table A5.2a). Among these grains, 51-9 has a magnesian composition while grain 2-14-25-O2 contains Fe, Si, and O. Eleven intermediate grains have Mg contents comparable to Fe contents (40 < mg#s < 60), while only four are Mg-rich. Numerous intermediate silicate grains contain Ca and/or Al. One ferromagnesian grain, 15-5-tp, contain an Al content of about 9 at.%. Stadermann et al. (2009) observed variations in the Fe+Mg(+Ca)/Si ratios for olivine and pyroxene standards. They noted that despite the large spread in Fe+Mg(+Ca)/Si ratios for the standard grains, grain populations with olivine compositions can be clearly distinguished from those with pyroxene compositions. Furthermore, we see a much larger population of presolar grains with intermediate compositions than what is expected from the distribution of olivine and pyroxene grains in standard samples discussed in Stadermann et al. (2009). This indicates that grains with intermediate compositions are a real presolar grain population and not an artifact of the measurement technique.

Non-stoichiometric grains includes nine ferromagnesian silicate grains that have

Mg+Fe(+Ca)/Si ratios between 2.2–3.3 and eight that show Mg+Fe(+Ca)/Si ratios between 0.5–0.7 (under "other" in Table A5.2a). Among the grains under "other" (Table A5.2a) a few grains contain Ca and/or Al. Two grains (52-4-O17 and 54-5) with a Mg+Fe(+Ca)/Si ratios of 2 within 1σ errors (i.e., olivine-like) are also placed in this category because the grains contain Al or Ca, which is not present in olivine. Three silicate grains in this category, 131, 13-5 and 1710, have no Fe while one grain, 105, has no Mg; the remaining grains have ferromagnesian silicate compositions. In addition, some grains under "other", e.g., 16a-3 and 19-1, are slightly Si-rich (~25 at.%) compared to the stoichiometric silicate grains. The former ferromagnesian grain contains Al (6.4±1.6 at.%) and the latter magnesian grain contains Ca (3.4±0.4 at.%). Finally grain 33 is Si-poor with a high Mg+Fe/Si ratio (~8; Table A5.2a; not plotted in Figure 5.6). This grain has the highest content of Al (9.3±2.3 at.%) of all the silicate grains identified in this inventory.

About 4–8 at.% S is present in the spectra of some silicate grains. We do not have a sensitivity factor for S and so the S concentration is based on Childs et al. (1995). However, investigation of the S distribution in the region of interest for a few cases showed that S was not present at the location of the O anomaly but was close to the grain of interest. The observed S Auger peaks can be attributed to either an overlap of the analysis box onto surrounding material or shifting of the analysis box during the spectra acquisition. Therefore, S has not been included in the quantification of the silicate grain compositions.

Composite Grains: In addition to this large collection of silicates with mostly non-stoichiometric elemental compositions, two relatively large ~400×400 μm^2 composite

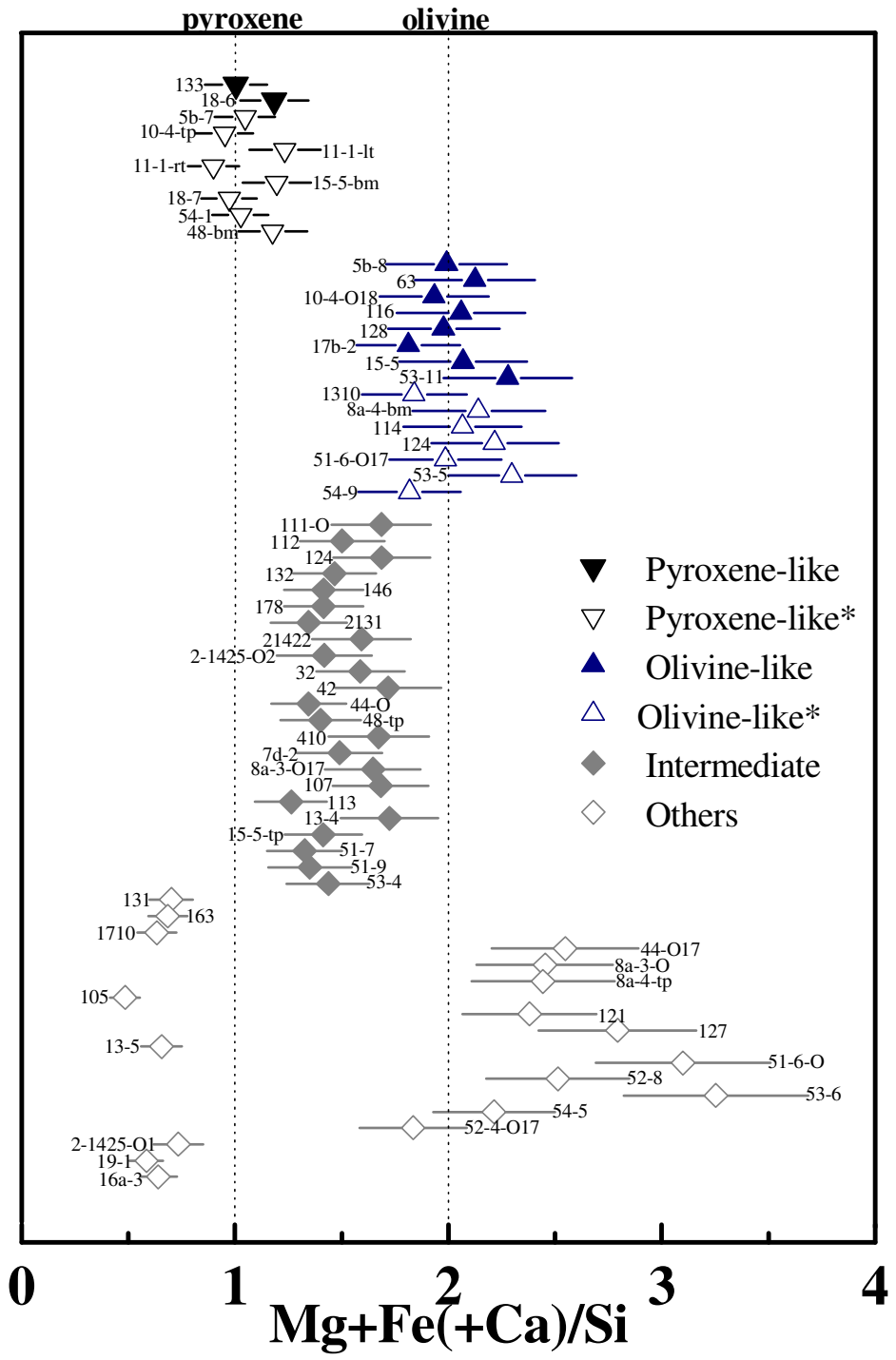

Figure 5.6: The Fe+Mg(+Ca)/Si ratios of pyroxene-like, olivine-like, and non-stoichiometric grains have been plotted with grain names. Pyroxene-like and olivine-like grains that have other ratios (see text) > 1σ away from the theoretical values are shown with an * in the legend.

grains (51-1 and 51-8) exist in our silicate grain inventory. The extents of the O-anomalies in the O ion images clearly encompass areas with multiple entities and so Auger spectra were acquired for the sub-grains to check if their compositions were similar to each other.

Grain 51-8 shows a ^{17}O excess and ^{18}O depletion (Figure 5.7a); the extent of the O-anomalies observed in the ion images encompasses an area that has multiple subgrains (Figure 5.7a). Although the $\delta^{17}O$ image shows the same distribution throughout, a variation appears in the $\delta^{18}O$ image. The grain shows slightly larger ^{18}O depletion towards the left part of the outlined grain, although it is not statistically significant (within 2σ; Figure 5.7a). The secondary electron image of this grain shows that the subgrains are predominantly oval or irregularly shaped. Each subgrain is ~50–70 nm in diameter and has a near-circular shape. Elemental spectra were acquired for each of the two subgrains because the composition of the subgrains in the two halves of the composite grain 51-8 is the same within 1σ errors. Table A5.2b shows the average composition over the left (lt) and right (rt) portions of the grain 51-8. The left part of grain 51-8 (Figure 5.7b) also shows 3.9±0.4 at.% Ca (Table A5.2b). However, no Ca is present in the right subgrains of 51-8 within detection limits, which primarily shows a pyroxene-like composition.

The second composite grain 51-1 contains two subgrains, both of which show the same ^{17}O excesses (Figure 5.8a). The subgrain 51-1-tp (top) is about 200 nm in diameter while the subgrain 51-1-bm (bottom) is 160×140 nm^2 in size. Spectra show that both subgrains are composed predominantly of Fe, Mg, Si, and O. The bottom subgrain exhibits an olivine-like composition while the top one has a non-stoichiometric elemental

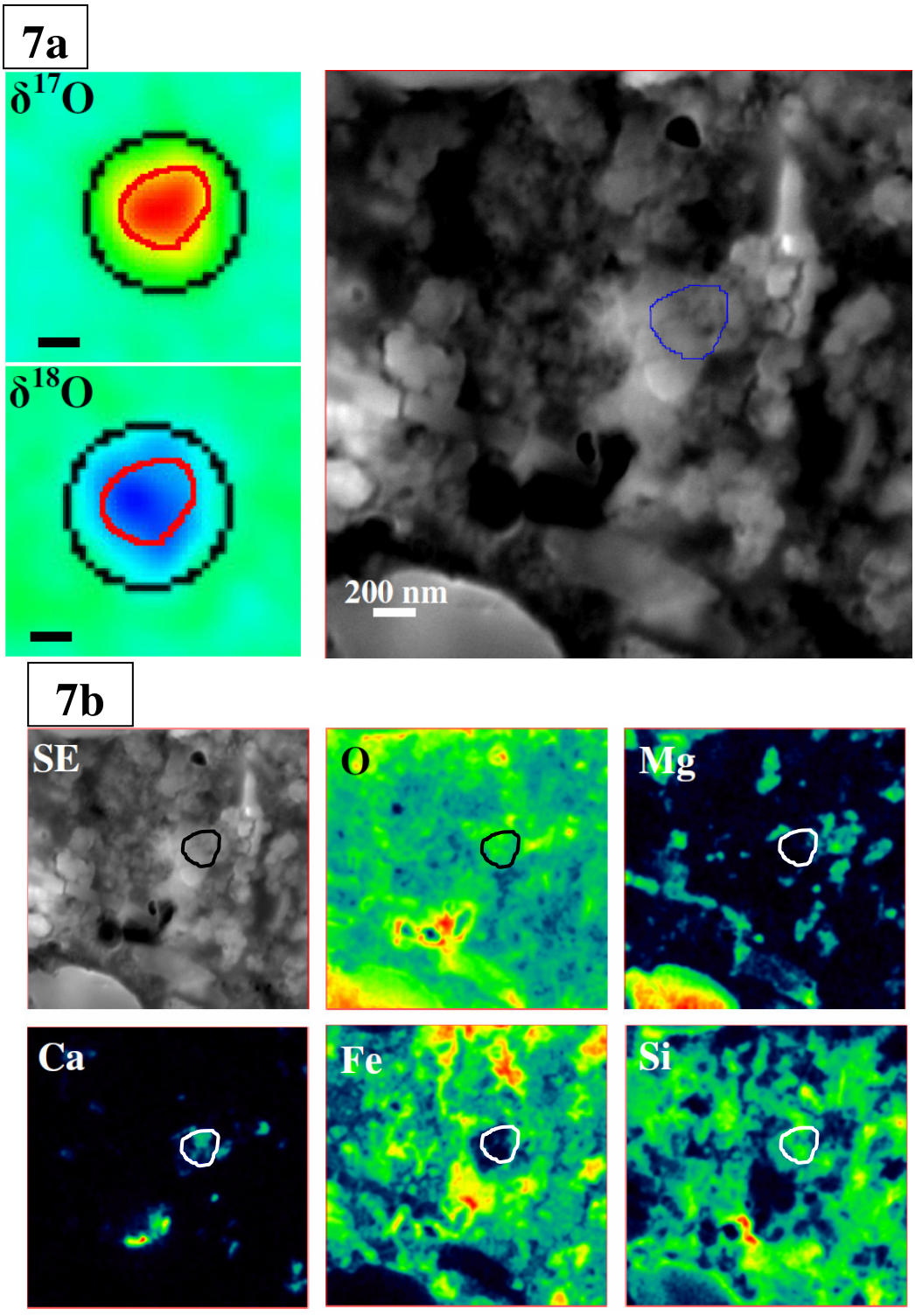

Figure 5.7a: Oxygen delta images of the composite grain 51-8. The secondary electron image of the area containing the composite grain with the O-anomaly outlined in blue. **Figure 5.7b:** Elemental maps of grain 51-8, which clearly shows the Ca-containing sub-grain on the left. Iron is predominantly present in the sub-grains on the right. The scale bars for the elemental maps are the same as the SE image.

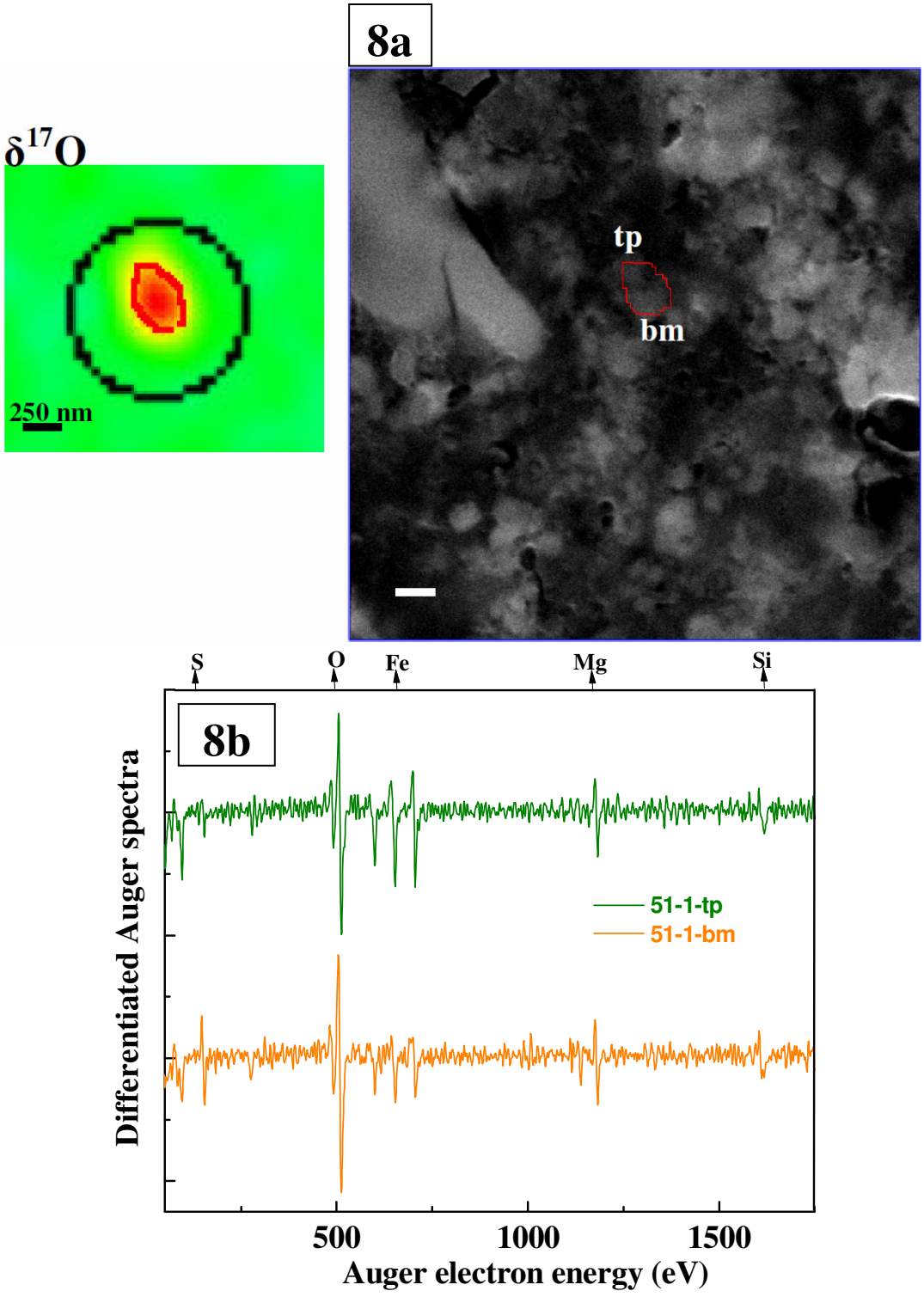

Figure 5.8a: Oxygen isotope image of the composite grain 51-1. The secondary electron image of the area containing the grain with the O-anomaly outlined in red. The sub-grains with the gap in-between are labeled. **Figure 5.8b:** Spectra of the subgrains 51-5-tp and 51-1-bm showing that both sub-grains have ferromagnesian silicate compositions.

composition.

5.3.2. Isotopic and Elemental Compositions of C- and N-anomalous Grains

In addition to the O-anomalous grains that were identified during C- and O-isotopic imaging over a 17,100 μm^2 area on the matrix, we identified twenty-two C-anomalous grains (Table A5.3). Forty-seven C- and/or N-anomalous grains were also identified over a 6,700 μm^2 area, via C- and N-imaging (Table A5.3). The grains identified using the former imaging conditions lack N isotopic data and so these grains have arbitrarily been plotted on the line representing the terrestrial isotopic ratio ($^{14}N/^{15}N = 272$) in Figure 5.9. Based on the Auger Nanoprobe measurements, the majority of the grains were classified into presolar SiC and carbonaceous phases; classification for some grains (see below) was solely based on the isotopic and elemental ratios (e.g., $^{12}C^-/^{28}Si^-$) derived from the NanoSIMS ion images. Eleven grains could not be located in the thin-section because of movement/shifting of the matrix, due to formation of cracks, which made spatial alignment of the NanoSIMS and Auger Nanoprobe images difficult. Furthermore, a few grains were difficult to identify due to their small sizes or because they were almost completely sputtered away by the NanoSIMS measurements (marked with * in Table A5.3). The sizes of the grains that got sputtered away in the NanoSIMS have been calculated from delta images. Four grains (light grey circles in Figure 5.9), 146, 21414, 21419, and 51 were not classified and are discussed in section 5.3.2.2. Carbonaceous phases are irregularly shaped C-containing areas in the matrix and appear to be dark/gray in the SE images acquired in the Auger Nanoprobe. These areas also tend to be larger (> 350 nm) than the SiC grains found in ALHA77307.

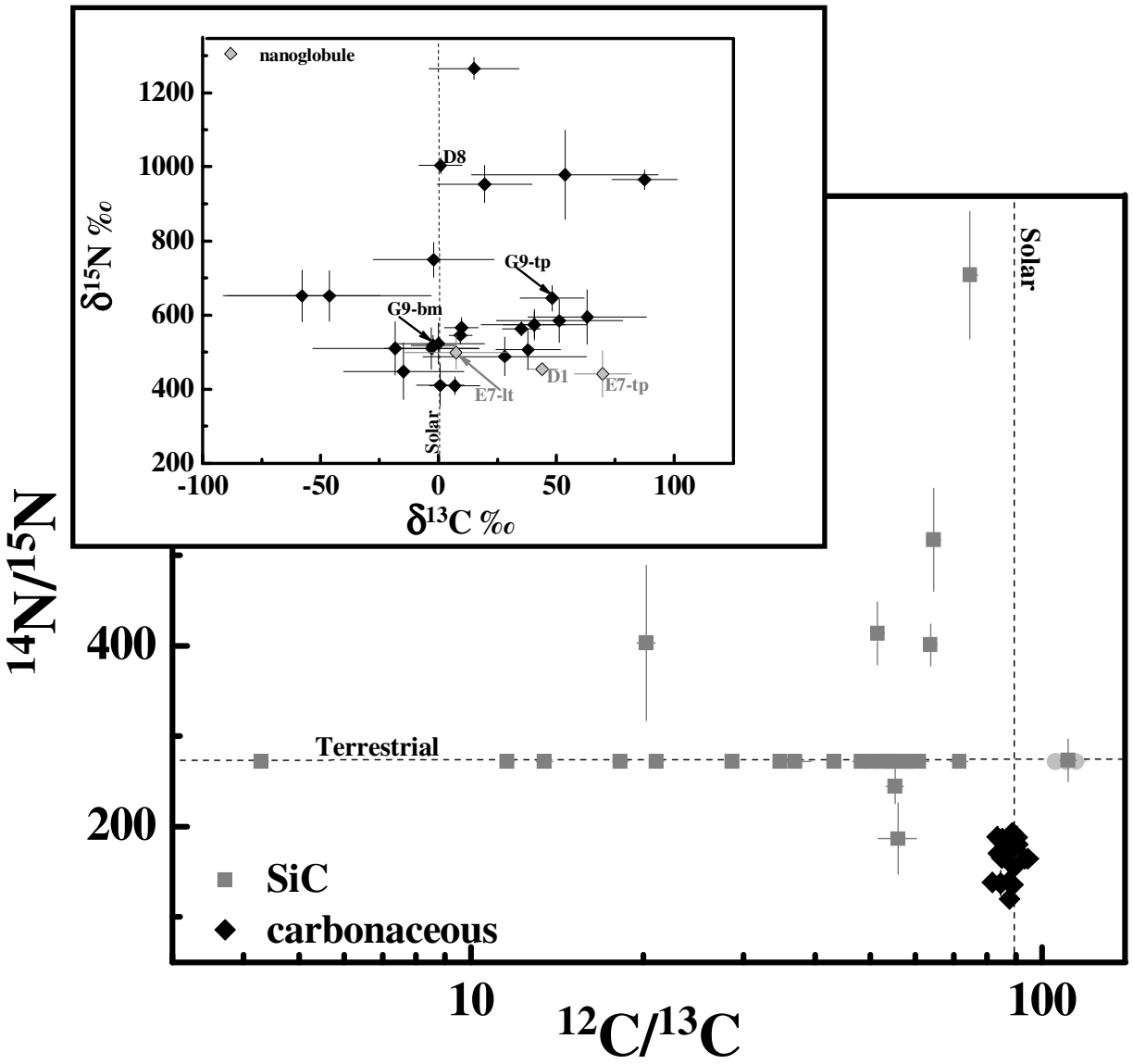

Figure 5.9: Isotopic compositions of SiC and carbonaceous phases in ALHA77307. The inset is an enlarged plot of the carbonaceous grains (black) in delta-notation [$\delta^{15}N = ((^{15}N/^{14}N)_{sample}/(^{15}N/^{14}N)_{standard}-1)\times1000$]. Carbonaceous grains discussed in the text are labeled (see inset). Grains with $^{12}C/^{13}C$ ratios > 89 that have not been classified are in gray circles. Errors are 1σ.

Only one grain, G3-tp, exhibited a N Auger peak in its spectrum; N is absent (less than 3 at.%) in all other N-anomalous grains. As a result, we were unable to determine the relationship between the ^{15}N enrichments and N contents observed in the grains from Auger Nanoprobe measurements. Less than 10 at.% S is present in some N-anomalous hotspots (Table A5.3).

5.3.2.1 SiC Grains

The $^{12}C/^{13}C$ ratios of the SiC grains vary from ~4 to 111 with a majority of the grains on the ^{13}C-rich side of the normal value ($^{12}C/^{13}C$ = 89) (Figure 5.9; Table A5.3). One grain, B2, exhibits a 200±35‰ excess in ^{12}C. The spread in the $^{14}N/^{15}N$ isotopic ratios of the SiC grains is ~245–811 ($^{14}N/^{15}N_{terrestrial}$ = 272). The $^{12}C^-/^{28}Si^-$ ratios for the SiC grains identified in the C and N imaging range from 0.5 to 1.7 (Table A5.3). However, high uncertainties in such ratios derived from ion images have been observed earlier (e.g., Floss and Stadermann 2009b). The sizes of SiC grains (Table A5.3) are only about 2–4times larger than the diameter (~100 nm) of the primary Cs^+ beam used in the NanoSIMS. As a result, there can be a significant contribution to the measured ratios from surrounding grains. In addition, the NanoSIMS detection efficiencies vary among different sets of measurements and as a consequence give a wider range of values for the nominal ratio of 1 for SiC grains, and therefore phase designations that are only based only on NanoSIMS elemental ratios should be considered preliminary. Auger spectra are more suitable for determining the composition of sub-micrometer-sized grains (Stadermann et al. 2009). Typical Auger spectra of two SiC grains are shown in Figure 5.10. The sizes of the grains range from ~100 to 500 nm along the longer axis (Table A5.3). A majority of the SiC grains are less than 300 nm in size and are roughly

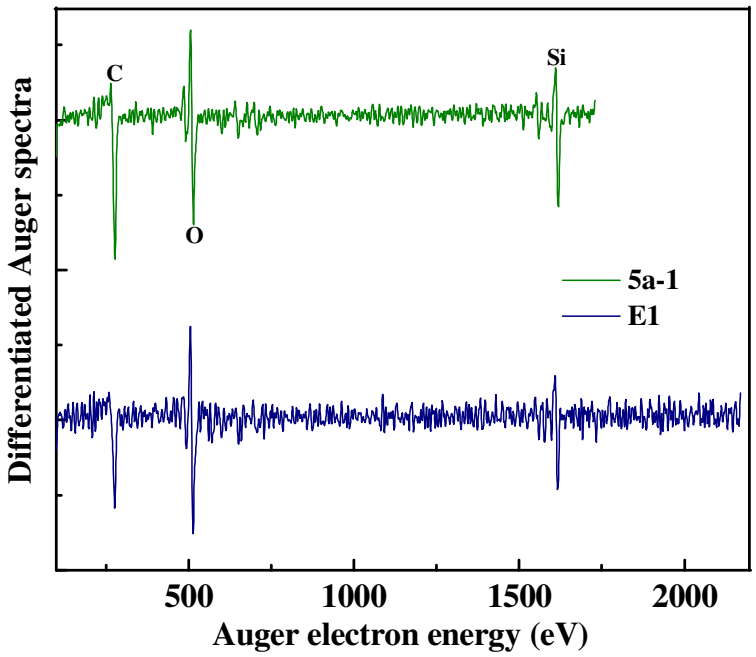

Figure 5.10: Auger spectra of SiC grains 5a-1 and E1.

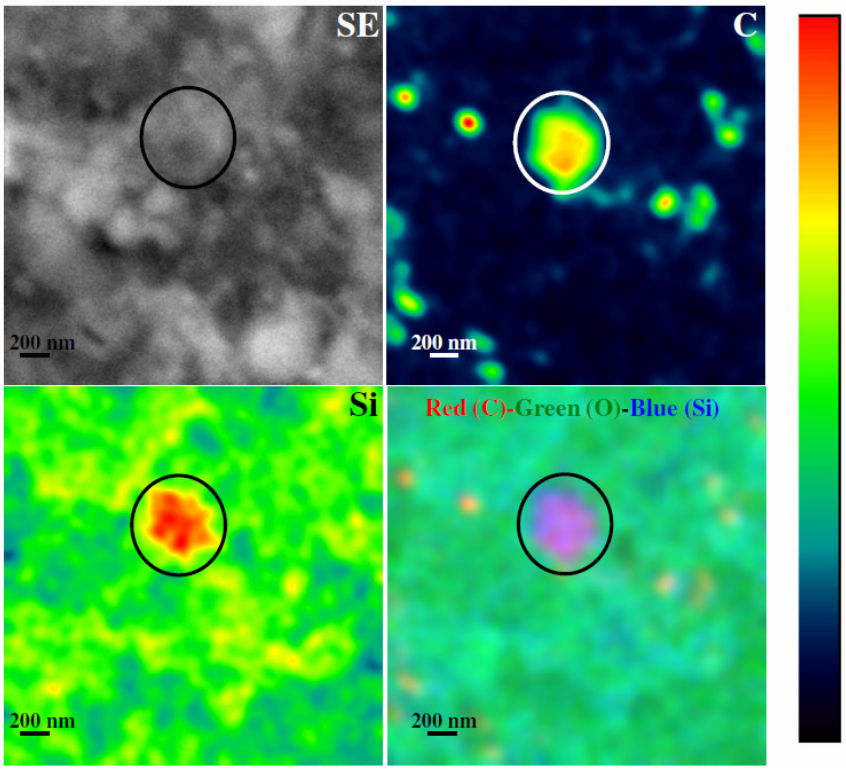

Figure 5.11: Carbon and Si elemental maps and RGB (Red=C; Green=O; Blue=Si) image along with SE image of the SiC grain 5a-1.

circular in shape. Four grains are larger, ~460×340 nm^2, with two exhibiting a triangular morphology. Elemental maps of the SiC grain 5a-1 clearly show a C- and Si-rich area that has less O (Figure 5.11).

Oxygen is often present in the Auger spectra of the SiC and carbonaceous grains. Therefore, we made an attempt to calculate the O contents associated with the SiC grains using the silicate sensitivity factors (Stadermann et al. 2009); these turned out to be ~10 at.% for the larger SiC grains. Oxygen tends to form a thin layer over the grain within a few minutes of the samples' exposure to air. A combination of other factors such as the backscatter effect, image shifts during spectra acquisition, and surface contamination also contribute to the O Auger peak observed in SiC grains. However, the amount of O that can be attributed to each of these factors is rather uncertain.

5.3.2.2 Carbonaceous Grains

Twenty-eight areas exhibit close-to-solar $^{12}C/^{13}C$ ratios and $\delta^{15}N$ values from 409 to 1266‰ (Figure 5.9; Table A5.3). Among them, three localized hotspots, D1 (Figure 5.12a), E7-tp, and F1-17 show ^{15}N and ^{13}C excesses ($\delta^{13}C$ = 44±10‰, 70±10‰, and 90±15‰). The $^{12}C^-/^{28}Si^-$ elemental ratios of the N-anomalous areas exhibit a large variation (Table A5.3); however, the predominantly high $^{12}C^-/^{28}Si^-$ ratios suggest their carbonaceous nature. As discussed before, grain classification was not done for four grains (146, 21414, 21419, 51) that showed $^{12}C/^{13}C$ ratios > 89 (gray circles in Figure 5.9; Table A5.3). However, based on the fact that most carbonaceous grains are ^{12}C-rich (Floss and Stadermann 2009b), these grains are likely carbonaceous in nature.

The high-resolution images acquired in the Auger Nanoprobe indicate that some of

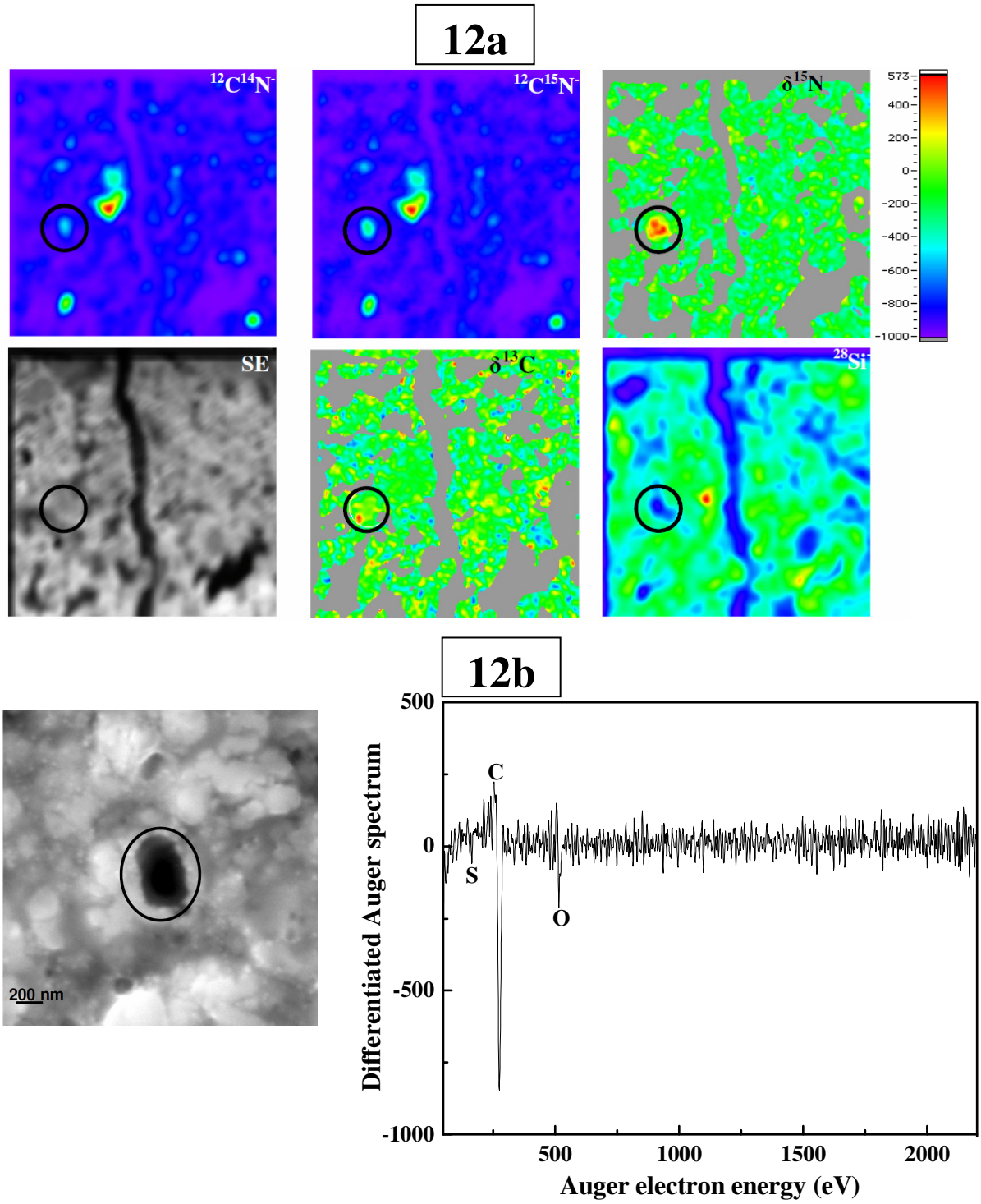

Figure 5.12 (a): Nitrogen- and C anomalous hotspot D1 is encircled. Here the field of view is 10 µm. **Figure 5.12 (b):** Secondary electron image shows a nanoglobule, which exhibits a large C and small O peak.

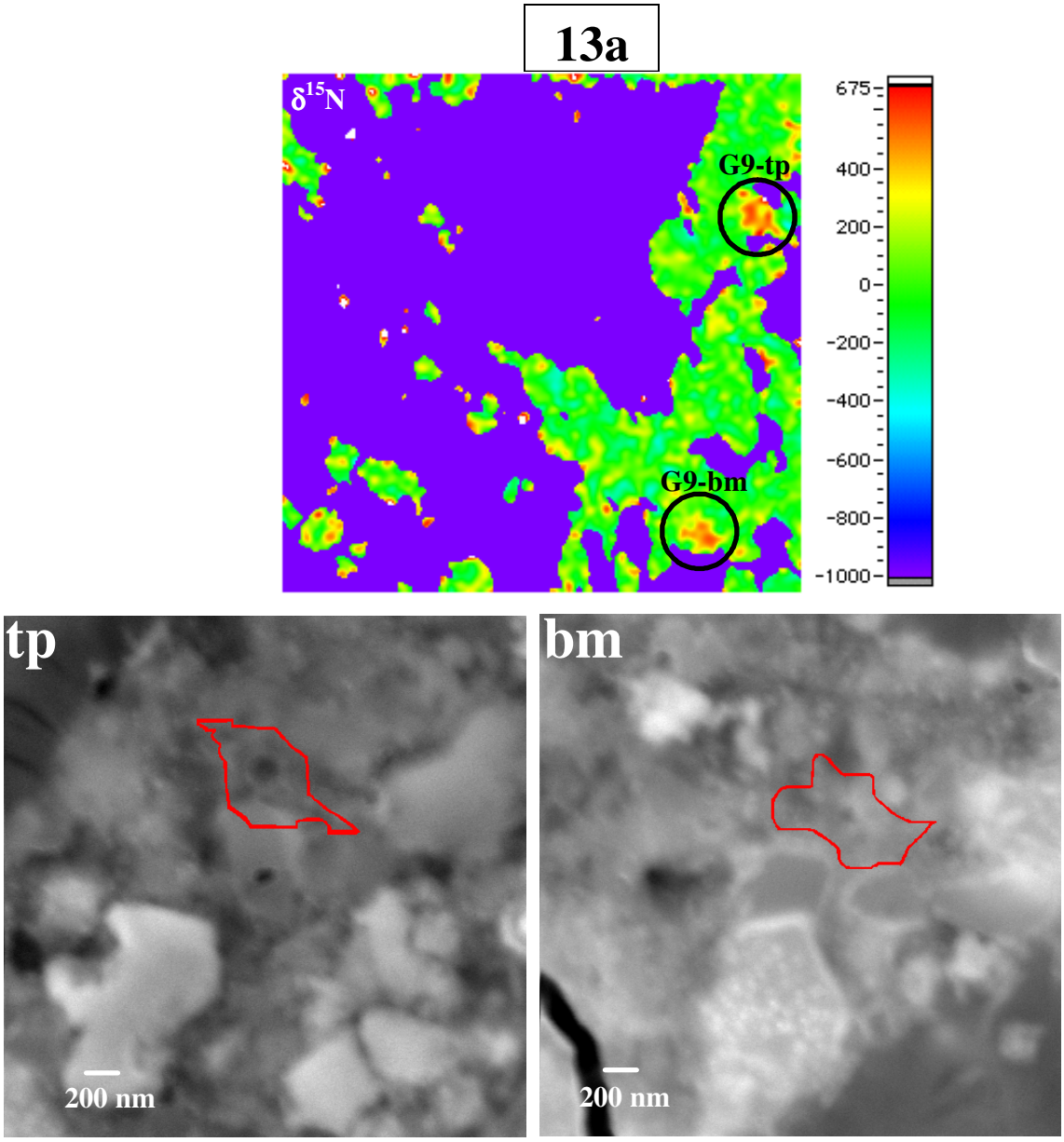

Figure 5.13 (a): Nitrogen delta image of area G9 containing two hotspots. Here the field of view is 10 µm. Secondary electron images of the hotspots G9-tp and G9-bm with the ^{15}N-rich area outlined in red are shown.

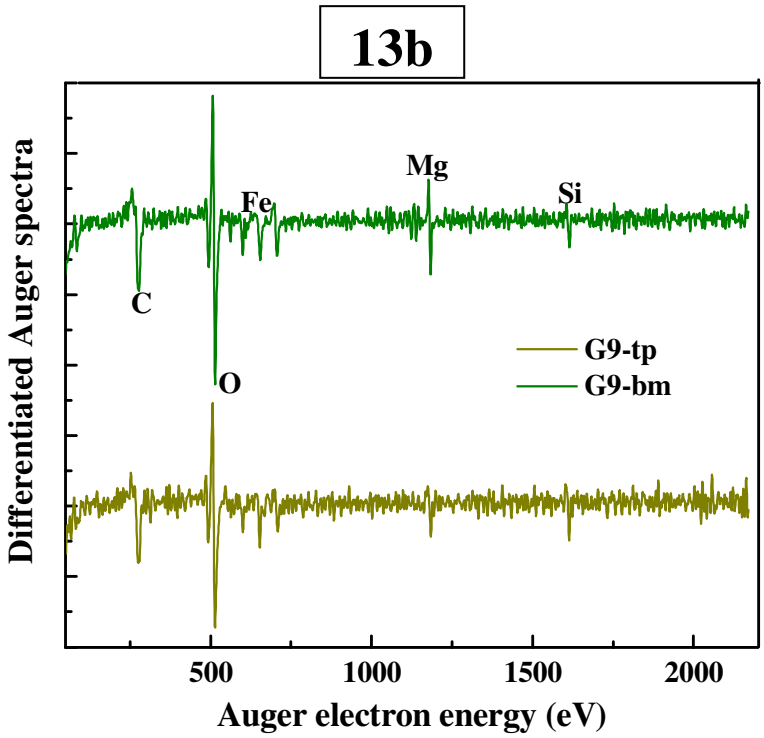

Figure 5.13 (b) The hotspots exhibit C, O, Mg, Si, and Fe Auger peaks.

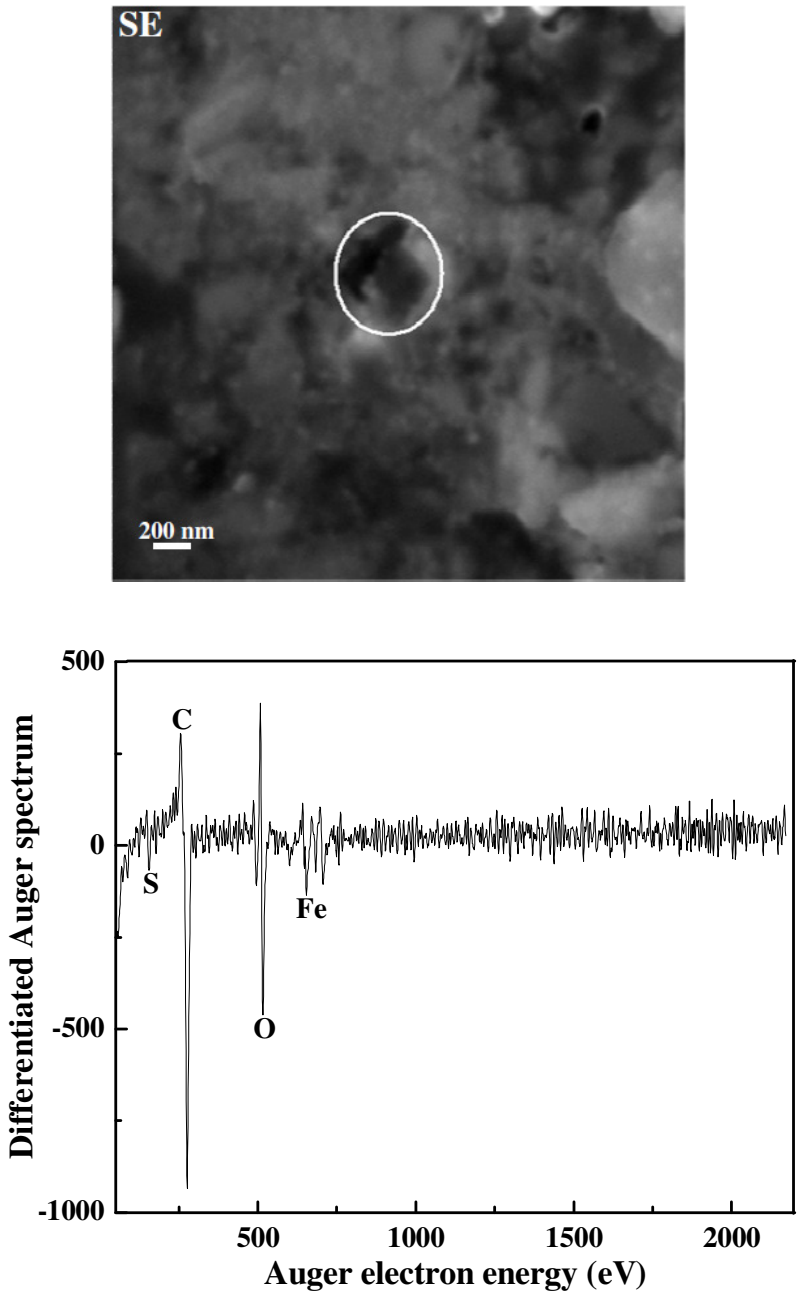

Figure 5.14: Secondary electron image and spectrum showing C, O, and Fe Auger peaks of the hotspot D8.

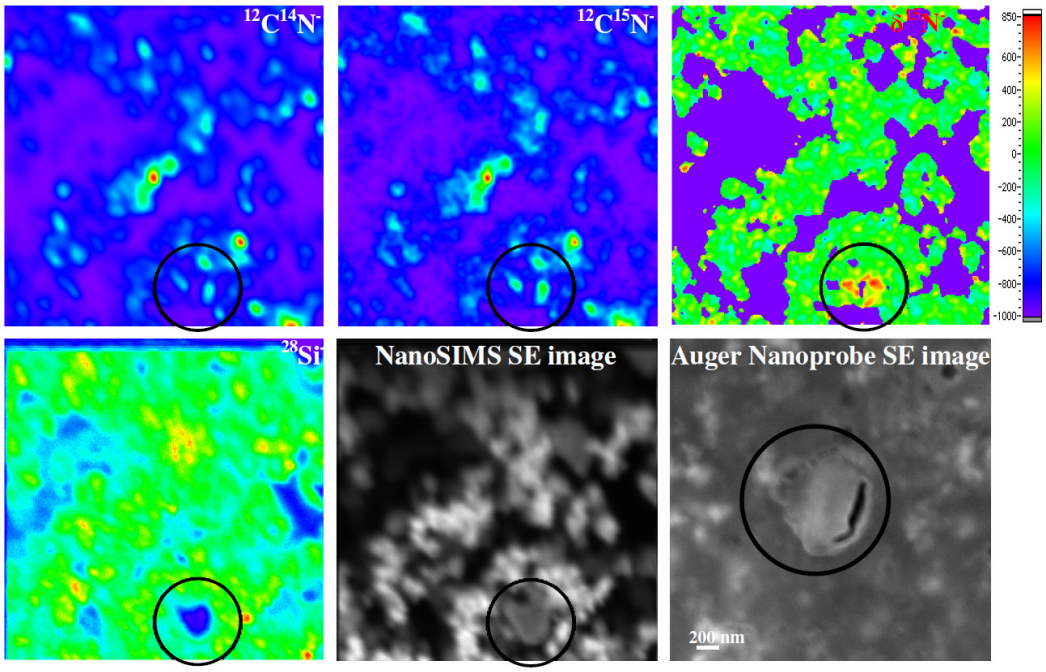

Figure 5.15: Nitrogen-anomalous hotspot G4 is encircled. Note the spatial distribution of the ^{15}N excess and the absence of Si. The color scale for the NanoSIMS image is from red (high) to blue (low); here the field of view is 10 μm. The SE image at higher magnification shows that the grain has a platy surface.

the N hotspots appear to be nanoglobules (e.g., D1; Figure 5.12b) while others are highly irregular in shape (Figure 5.13a). Hotspots were classified to be nanoglobules based on their almost circular dark appearances and probable hollow structures in the Auger SE images (Figure 5.12b). Some carbonaceous grains appear platy and single-grain. Most of the carbonaceous grains are greater than 500×500 nm^2 in size (Table A5.3). Auger spectra of the carbonaceous grains show large C peaks, and no Si (e.g., Figure 5.12b) or only a relatively small Si peak (e.g., Figure 5.13b). Some hotspots also show the presence of Mg and Fe (e.g., Figures 5.13b and 5.14). The Fe, Mg, Si, and O Auger peaks observed in the Auger spectra of hotspots are probably associated with silicates embedded in or intermixed with the N-anomalous material. Sulfur is also present in some N-anomalous hotspots (Table A5.3) but its concentration is low. The N- anomalous grain

abundance in ALHA77307 using the NanoSIMS ion images is 160±30 ppm; we were able to calculate the abundance because this meteorite has a normal bulk N isotopic composition, which is not the case in other primitive meteorites such as the CR chondrites.

In our inventory we have also found ^{15}N-rich (750‰) carbonaceous material G4, which shows normal C isotopic composition. It is present at the periphery of a large (~1 μm in diameter) grain with a platy, flat appearance (Figure 5.15). Based on the distribution of the N-anomalous hotspots mainly along the grain boundary (Figure 5.15), we suspect that the carbonaceous carrier of the anomaly may have formed a pristine surface over the other grain. The large host grain that has solar C isotopic composition with 1σ errors exhibits Fe and C Auger peaks in its spectum.

5.4. Discussion

5.4.1. Oxygen Isotopic Compositions and Stellar Sources of Silicates and Oxides

Four populations of presolar silicates and oxides can be discerned on the basis of their O isotopic compositions (Nittler et al. 1997a, 2008; see Figure 5.1). Grains with ^{17}O excesses and solar to sub-solar ^{18}O/^{16}O ratios that constitute group 1 make up the majority of the O-anomalous grain inventory. Low-mass stars (1.1–2.2$M_{\odot}$) with solar to sub-solar metallicity in thermally pulsing AGB or Red Giant Branch (RGB) phases of evolution are likely sources of these grains (e.g., Nittler et al. 1997a). The compositions of group 1 grains show imprints of first and/or second dredge-up episodes that bring ^{17}O-rich material formed during the H-burning phase, via the CNO cycle, into the stellar envelope (Nittler et al. 2008). A positive correlation exists between the ^{17}O/^{16}O ratios of

group 1 grains and the masses of the progenitor stars (Nittler et al. 2008).

Models of low-mass stars undergoing dredge-up episodes cannot explain the O isotopic compositions of group 2 grains that show large ^{18}O depletions ($^{18}O/^{16}O < 10^{-3}$; Nittler et al. 1997a). Their compositions can be understood by assuming an additional process called Cool Bottom Processing (CBP; Wasserburg et al. 1995). During CBP, deep circulation currents transport material from the envelope through hot H-burning regions to partially process the material, destroying ^{18}O in the process (Nollett et al. 2003). In fact, Nittler et al. (2008) suggested that some of the spread in the $^{18}O/^{16}O$ ratios in group 1 grains can also reflect the effects of CBP. Among eight optically-visible, moderately-evolved MS and S stars, Harris et al. (1985) observed that four have $^{18}O/^{16}O$ ratios below 5×10^{-4}. The percentage of group 2 grains (~6%) in the presolar grain population does not compare very well to stellar observations (~50%; Harris et al. 1985) possibly because of low statistics of such observations. Another reason for this discrepancy may be associated with the raster imaging analysis of samples. Individual sub-micrometer-sized presolar grains are surrounded by grains of comparable size but with normal isotopic compositions in the matrices of meteorites. Ion imaging measurements in such circumstances will result in isotopic dilution and as a result ^{18}O-depleted grains will appear to be normal or less ^{18}O-depleted. Therefore, the number of group 2 grains in our inventory is a lower limit.

The ^{16}O-rich grains fall in group 3 while the ^{18}O-rich grains belong to group 4. Type II SNe have been proposed to be likely sources of a fraction of grains with ^{18}O and ^{16}O excesses. Another fraction of group 3 and group 4 grains may originate in low-mass stars with lower-than- and higher-than-solar metallicity, respectively. The ratio of the

secondary isotopes of O i.e., $^{17}O/^{18}O$, is constant and is equal to 0.19 (labeled as Galactic Chemical Evolution (GCE) line in Figure 5.1). The lone group 3 grain in our inventory falls above this GCE line and most likely formed in a low-mass star with lower-than-solar metallicity, accompanied with some dredge-up leading to an increase in its $^{17}O/^{16}O$ isotopic ratio. A SN is a less likely stellar source for this grain because most of the O ejected by SN grains is ^{16}O synthesized in the inner zones, and one might expect a priori that a SN grain should be highly ^{16}O-rich, and should thus have a $^{17}O/^{18}O$ ratio below the GCE (Nittler et al. 2008). Three (out of seven) of the group 4 grains plot on the galactic evolution line i.e., they show ^{17}O and ^{18}O excesses, and may therefore have condensed in high metallicity stars. Of course, assigning this stellar source to these three group 4 grains is difficult because high metallicity stars i.e., young stars, should have been rare in the solar neighborhood around 4.6 billion years ago. The remaining four group 4 grains with ^{18}O excesses but close-to-solar $^{17}O/^{16}O$ ratios most likely formed in the SN ejecta.

Nucleosynthesis in AGB stars of masses up to ~2.2$M_\odot$ results in an upper limit for $^{17}O/^{16}O$ isotopic ratios of ~4×10^{-3} (Nittler et al. 2008; Gyngard et al. 2010). One grain in our inventory (163; Table A5.1) has a $^{17}O/^{16}O$ ratio higher than this value and may have formed in nova ejecta (Nittler et al. 2008; Gyngard et al. 2010). The $^{17}O/^{16}O$ ratio of the grain is a lower limit because of the ubiquitous problem of isotopic dilution, which decreases the $^{17}O/^{16}O$ ratios and increases the $^{18}O/^{16}O$ ratios. Nuclear burning of white dwarf during a nova outburst causes fast CNO processing that can produce large ^{17}O excesses (José et al. 2004). Quantitatively, the CO nova models are more adept at explaining the O isotopic composition of grain 163 than the ONe models (José et al. 2004). José et al. (2004) mixed different proportions of solar composition material to the

nova ejecta. Model CO4 from José et al. (2004), which corresponds to a mix of 50% material from the core of a $0.8M_{\odot}$ CO nova and 50% material of solar composition fits the grain data the best. Therefore the cosmic setting where such a mixing can take place is a binary star system composed of the evolved star that goes nova and its solar composition companion star. Very few O-anomalous grains with large ^{17}O excesses have been identified and even fewer grains (i.e., Gyngard et al. 2010; Bose et al. 2010d) have been measured for another isotopic system. Note that Vollmer et al. (2008) classified some grains with $^{17}O/^{16}O$ ratio below 5×10^{-3} into this nova category; these grains are not considered for the remaining discussion. We measured Si isotopic ratios in the lone extreme group 1 silicate grain B2-7 identified in SAH 97096 (Bose et al. 2010d). Although the error bars on the Si isotopic ratios of this grain are so large that they hinder an accurate assessment, the Si isotopic composition of extreme group 1 silicate grain B2-7 is solar within 1σ (e.g., Bose et al. 2010d). Large Si isotopic anomalies are expected from nova models, e.g., predicted $\delta^{30}Si$ values range from -1000 to 47000 (José et al. 2004), but are not observed in grain B2-7. Oxide grain C4-8 identified by Gyngard et al. (2010) is enriched in both $\delta^{25}Mg$ and $\delta^{26}Mg$ by ~1000‰. These observed excesses can be qualitatively explained by $0.6M_{\odot}$ CO nova model; however, the model produces larger enrichments in both the isotopes of Mg by at least an order of magnitude (Gyngard et al. 2010). New calculations for the CO and ONe nova model with updated reaction rates (Gyngard et al. 2011) are also in complete disagreement with the grain data. Discrepancy between the grain data and the models may be due to issues with the models, which is also the case for SiC nova grains. Presolar SiC grains with high $^{13}C/^{12}C$, $^{15}N/^{14}N$, and $^{30}Si/^{28}Si$ ratios have been argued to condense in nova ejecta mixed with 90% solar

composition material (e.g., Amari et al. 2001a). Amari et al. (2001a) pointed out that the predicted isotopic compositions vary widely, depending on parameters of the models including stellar mass, peak temperature, and mass transfer rate (Kovetz and Prialnik 1997; Starrfield et al. 1997; José and Hernanz 1998). Additional work is needed to search for ^{17}O-rich grains and to perform multi-element isotopic analysis on them in order to further constrain their stellar sources.

5.4.2. Olivine and Pyroxene Grains

Circumstellar environments of evolved stars contain both amorphous and crystalline forms of silicate grains (e.g., Waters et al. 1996). A typical abundance of crystalline silicates in the winds of low-mass, post-main-sequence stars is on the order of 10% or less of the total silicate mass (Kemper et al. 2001), although rare stars with up to 75% crystalline silicates have been observed (Molster et al. 2001a). Fits of laboratory mineral spectra to stellar spectra reveal that olivine compositions are dominant among amorphous silicate grains (Demyk et al. 2000). We identified fifteen olivine-like grains compared to ten pyroxene-like grains in ALHA77307. Although we do not have structural information for the grains in this study, it is likely that most are amorphous because dust around stars is dominated by amorphous silicates (Molster et al. 2001b; Molster and Waters 2003). In spite of low statistics, our observation of the predominance of presumably amorphous olivine-like grains is consistent with stellar observations.

Sub-millimeter continuum observations suggest that 60–75% of the O-rich dust injected into the ISM is produced by Type II SNe (Dunne et al. 2003). Whether this dust is predominantly olivine or pyroxene is still unknown. However, in our inventory, four

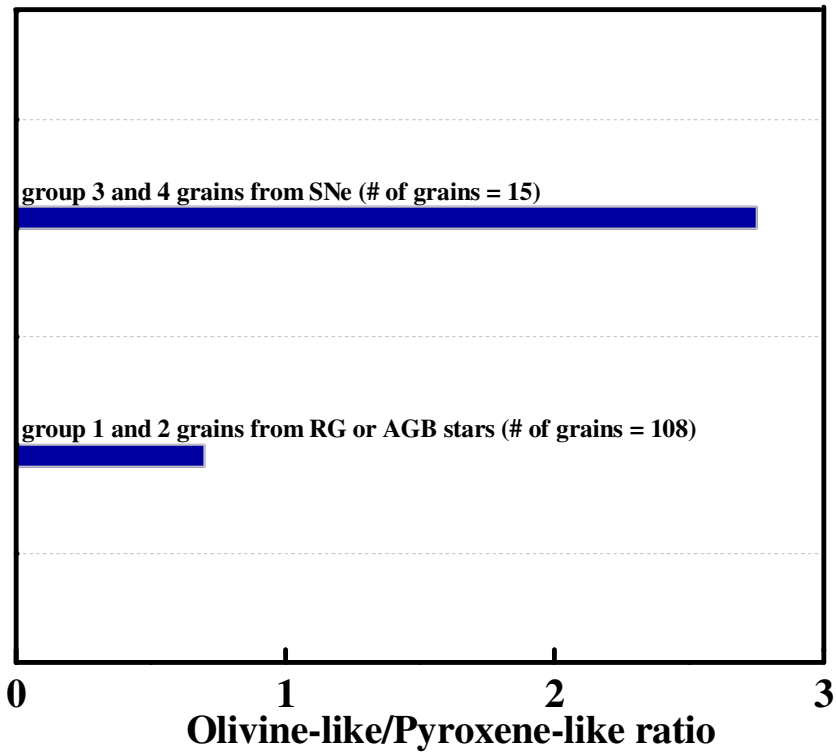

Figure 5.16: Comparison of the number of olivine-like to pyroxene-like grains in the carbonaceous chondrites ALHA77307 (This work; Nguyen et al. 2010a), Acfer 094 (Bose et al. 2010c; Vollmer et al. 2009a, b), QUE 99177 and MET 00426 (Floss and Stadermann 2009a). Olivine and pyroxene grains identifications made using the TEM (Messenger et al. 2005; Floss et al. 2006; Busemann et al. 2009; Nguyen et al. 2010b) are also included in the plot.

out of seven group 4 silicate grains exhibit olivine-like compositions. Furthermore, a large fraction of the group 3 and 4 grains of a SN origin have olivine compositions (Messenger et al. 2005; Floss and Stadermann 2009a; Vollmer et al. 2009a, b; Bose et al. 2010c; Nguyen et al. 2010b), while the group 1 and 2 grains that condense in AGB or RG stars contain approximately equal number of olivine- and pyroxene-like grains (Figure 5.16). This suggests that Type II SNe could be a significant source of olivine grains. Our observation is in qualitative agreement with the study of Todini and Ferrara (2008), which discussed the initial dust mass composition and fraction of the dust components in stars that explode as core-collapse SNe. Although the low-mass stars produce almost

equal dust masses of forsterite and enstatite grains, stars with larger masses, i.e., > $25M_{\odot}$ and a high kinetic energy of explosion produce more forsterite. One limitation of this model (Todini and Ferrara 2008), however is that forsterite grains form only in greater than $25M_{\odot}$ stellar models.

5.4.3. Non-stoichiometric Elemental Compositions

Out of 193 silicate grains characterized to date in ALHA77307 (This work; Nguyen et al. 2010a), and in other carbonaceous chondrites (Floss and Stadermann 2009a; Vollmer et al. 2009a; Bose et al. 2010c; Nguyen et al. 2010b), 104 grains are non-stoichiometric. Changes in the grain structure, chemical composition, and porosity are induced by irradiation of grains in SNe shock waves (e.g., Demyk et al. 2001). This process may selectively eliminate some elements, e.g., a decrease in O/Si and Mg/Si ratios in olivine grains was observed as a result of low-energy ion irradiation (Carrez et al. 2002). Amorphization and loss of compactness in the grains may also occur due to ion irradiation (Carrez et al. 2002). It may play a role in transforming stoichiometric grains into grains with compositions different from olivine or pyroxene type, as seen in this study. In fact, the stoichiometry of irregularly shaped particles modeled by Min et al. (2007) lies between pyroxene and olivine type silicates (O/Si ≈ 3.5).

Due to the high abundance of non-stoichiometric grains in the presolar silicate inventory, spectra from structurally and chemically modified silicate grains should be used to fit astronomical data. At present, only silicate grains containing Mg and Fe with varying Mg/Fe ratios are synthesized in the laboratory (Jäger et al. 1998; Dorschner et al. 1995); a comparison of their laboratory spectra to astronomical spectra suggests that forsterite and enstatite could account for the peaks in the astronomical spectra. This does

not imply that these stoichiometric phases are the only silicate dust grains to condense in the circumstellar environments. Therefore, experiments with dust analogoues exhibiting heterogeneous aggregates or non-stoichiometric elemental compositions are needed to check whether laboratory spectra from these phases will fit the astronomical spectra better than forsterite and enstatite, which is generally assumed to be the representative of grain compositions.

5.4.4. Elemental Compositions of Silicates and Oxides, and Possible Formation Scenarios

Theoretical studies of grain formation are often based on the assumption of thermodynamic equilibrium and consider only the formation of stoichiometric silicate minerals as part of a fractional condensation sequence (Grossman and Larimer 1974; Lattimer and Grossman 1978; Lodders and Fegley 1999; Ferrarotti and Gail 2001; Gail 2003). In complete chemical equilibrium, different minerals composed of the same chemical elements compete and the most stable condensates deplete all available atoms from the gas phase (e.g., Grossman and Larimer 1974). However, the process of condensation of dust grains in stellar winds can take place far from chemical equilibrium (e.g., Ferrarotti and Gail 2001). In the following sections (5.4.3.1.–5.4.3.5.), we consider the possible effects of non-equilibirum processes on the formation of composite grains, the formation of pure metal oxides such as SiO_2 grains, and the high Fe contents in silicate grains.

5.4.4.1. Composite Grains: 51-1 and 51-8

The group 1 grain, 51-1, is an aggregate of two ferromagnesian subgrains. It does not exhibit a variation in its O isotopic composition, but shows different Fe+Mg/Si ratios. Condensation of Mg-containing silicate phases, such as the subgrains in 51-1, can occur in a solar composition O-rich gas when the gas cools from ~1500 K in thermodynamic equilibrium (Lodders and Fegley 1999). Iron gets incorporated into the grains at a much lower temperature in the stellar outflows; see section 5.4.4.5., which discusses the mechanism of Fe inclusion in silicate grains. The variation observed in the subgrain elemental compositions is most likely attributable to differences in temperature and pressure conditions in the RG or AGB star envelope, which determines the concentration of elements condensing into grains.

The other composite group 1 grain, 51-8, contains a number of subgrains that vary in shape and size. The composite grain exhibits a spatial variation in Ca content that correlates with the ^{18}O anomaly (Figures 5.7a and 5.7b). The variation in ^{18}O compositions may be an artifact because observing O isotopic anomalies at a scale of less than 100 nm, comparable to the size of the subgrains, is difficult with the NanoSIMS. However, if it is real, our observation indicates either an O isotopic heterogeneity in the stellar gas or partial equilibration in the grain. In addition, the grain 51-8-lt has a pyroxene-like composition while 51-8-rt is non-stoichiometric, which suggests that subsequent to their formation under differing conditions, the subgrains in 51-8 aggregated together. In the condensation sequence described by Lodders and Fegley (1999), Ca-containing phases form subsequent to Al_2O_3, and prior to Mg-rich phases and this may be the mechanisms by which one of the subgrain, 51-8-lt, in the composite grain formed. The possibility that 51-8 was a single large grain that got broken up is small because in

that case, we would expect to see a homogeneous elemental composition throughout the grain.

5.4.4.2. SiO_2 Grains: 21420, 2132, and 10-4-bm

In this study, we have identified three group 1 SiO_2 grains. Prior to this work, two presolar SiO_2 grains, all belonging to the group 1, have been identified in meteorites, including MET 00426 and ALHA77307 (Floss and Stadermann 2009a; Nguyen et al. 2010a). Thermodynamic calculations show that silica is not formed from a mixture of standard elemental abundances under chemical equilibrium because formation of Mg- or Fe-containing silicates is thermodynamically more favorable (e.g. Gail and Sedlmayr 1999). It nevertheless may condense in stellar winds under non-equilibrium conditions when only part of the gas-phase SiO is consumed by formation of the Mg-Fe-silicates, which can occur in stars with low Mg/Si ratios and low mass-loss rates (Gail and Sedlmayr 1999; Ferrarotti and Gail 2001). In addition, Nagahara and Ozawa (2009) carried out experiments of kinetically condensing systems that consist of numerous elements including Mg, Si, and Fe, assuming solar abundance ratios. During slow cooling, forsterite nucleates homogeneously, making the residual gas Mg-poor. As the temperature drops further, the forsterite grains get coated with Fe that condenses heterogeneously onto the forsterite grains. Consequently, enstatite grain formation is inhibited and the probability of crystalline SiO_2 grain condensation is enhanced. Furthermore, Rietmeijer et al. (2009) have shown that non-equilibrium condensation experiments do produce silica aggregates, specifically the silica phase-tridymite.

Astronomical observations show the presence of the 13 μm feature in about half of all AGB stars, where it is predominantly associated with semi-regular (SR) variable stars

and, to a lesser extent, is found in Mira variable stars (e.g., Sloan et al. 1996). Various attempts have been made to constrain the phase responsible for the 13 μm feature by comparing stellar spectra to those acquired from mineral phases in the laboratory (Glaccum 1995; Kozasa and Sogawa 1997; Posch et al. 1999, 2003; Fabian et al. 2001). Although the carrier of the 13 μm spectral feature remains speculative, presolar silica grains like those reported here, could be one plausible contributor (Speck et al. 2000) along with from Al_2O_3 (Sloan et al. 2003). However, arguments that have been raised against SiO_2 as the carrier of the 13 μm feature include opacity issues leading to reduced emission at the IR wavelengths and the absence of a correlation between the 13 and ~10 μm silicate features in all stellar spectra (e.g., Fabian et al. 2001). If silica is indeed a product of non-equilibrium condensation, as proposed earlier, it may be a carrier in SR variable stars. These stars have lower mass-loss rates than Mira variable stars, leading to a lower gas density at the dust-forming radius (Ivezic and Knapp 1999). At these lower densities, Si is less likely to react with other circumstellar species (e.g., MgO) to form magnesian silicates and, thus, may survive as SiO_2. In order to get an unambiguous correlation between the 13 μm spectral feature and its associated mineralogy, optical constants from all possible polytypes of SiO_2 are required, e.g., optical constants for cristobalite and tridymite, which are the crystalline forms of SiO_2 are missing (Depew 2000). Recently, spectra of BP Piscium, a first ascent giant star, were modeled by material that includes crystalline sub-micrometer-sized cristobalite (Melis et al. 2010), another polymorph of silica. Additional FIB-TEM characterizations of other SiO_2 grains are required.

5.4.4.3. Si-poor Grain: 33

The lone Si-poor grain, 33, has a relatively low mg# (14) and 9±2 at.% Al (Table A4.2a). At equilibrium the mineralogy of the first condensates predicted from a gas with solar elemental ratios is corundum, which occurs at high temperature in the outflows of evolved stars (Lodders and Fegeley 1999). Following the formation of the Al-containing grain, Fe can be introduced in the grain as the gas cools down. However, the diffusion rates for the incorporation of Fe are small. Therefore, a more likely scenario for the formation of grain 33 is its condensation under non-equilibrium conditions in a stellar environment (Gail and Sedlmayr 1999; Ferrarotti and Gail 2001). See section 5.4.4.5. for the discussion of mechanisms that form Fe-rich grains.

5.4.4.4. Mg- and Fe-oxide Grains: 55b-4, 21412 and 54-7

Grain 55b-4 has a periclase-like composition (Figure 5.2; Table A5.2b) and the isotopic signature of this grain suggests formation in a low-mass star that has undergone CBP. In a circumstellar environment, MgO grains may form soon after the onset of silicate condensation at a temperature only slightly below the stability limits of silicates under equilibrium conditions (Ferrarotti and Gail 2003). Subsequent seclusion of this phase will result in its preservation. Non-negligible amounts of periclase grains may form in Mg-rich AGB stars ($1 < Mg/Si < 2$) at low mass-loss rates (dM/dt per year = 5×10^{-6}; Ferrarotti and Gail 2001). These authors also suggested that if more Mg is present in the gaseous mixture than can be bound in forsterite, the excess Mg forms MgO. However, the abundance of periclase decreases as mass-loss rates increase (Ferrarotti and Gail 2001). In addition, models involving thermodynamic non-equilibrium suggest that periclase is one of the allowed condensates that can form when ion exchange efficiency (the model parameter that defines the exchange process of Fe^{2+} and Mg^{2+} ions at grain

surfaces) is low (Gail and Sedlmayr 1999). Stars on the AGB that have low mass-loss rates are predominantly SR variables, which is the most likely stellar source of the MgO grain. In spite of theoretical studies predicting the condensation of MgO, these grains may not always survive in the stars because the fraction of presolar grains with periclase composition is small. Prior to our observation of the presolar MgO grain, grains with such composition had not been observed.

Two Fe-oxide grains, 21412 and 54-7, exist in our presolar inventory. A previous study by Floss et al. (2008) discovered a magnesiowüstite grain with ~2 at.% Mg, which has a composition similar to grain 21412 in our inventory. As stated above, MgO condensation becomes possible soon after the onset of silicate condensation and prior to the formation of solid Fe (Ferrarotti and Gail 2003). These authors argued that MgO starts incorporating considerable amounts of Fe if the temperature drops below the ~850K, with the solid solution containing up to ~40% FeO. Iron-oxide grains, 21412 and 54-7, contain much more Fe than such estimates. However, the amount of Fe that can be incorporated into grains strongly depends not only on the temperature but also on the evaporation coefficients for MgO and FeO, which are not well known (Floss and Stadermann 2009a). Furthermore, amorphous grains are suggested to be more Fe-rich (Molster et al. 2002), and it is possible that the Fe oxide grains in our collection are largely amorphous. However, Min et al. (2007) used realistic grain shapes to model interstellar grains and concluded that amorphous grains are Mg-rich. Therefore, TEM studies of Fe-oxide grains are required to solve the puzzle.

5.4.4.5. Iron Contents in Silicate Grains

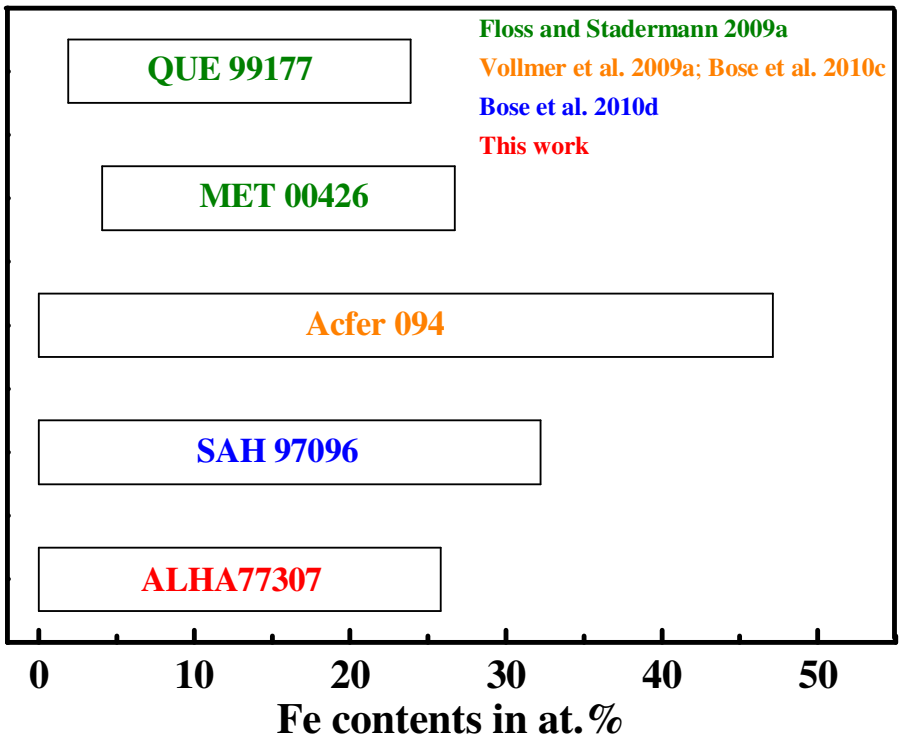

Figure 5.17: Range of Fe contents in presolar silicate grains from ALHA77307 and other chondrites measured by Auger Nanoprobe.

Iron-bearing silicate grains have been identified in the matrices of a number of chondrites (Nguyen and Zinner 2004; Floss et al. 2006; Nguyen et al. 2007; Floss and Stadermann 2009a; Vollmer et al. 2009a; Bose et al. 2010c, 2010d). The Fe contents of the presolar silicate grains found in ALHA77307 span a small range similar to that of the silicates from pristine CR chondrites MET 00426 and QUE 99177, and the enstatite chondrite SAH 97096 (Figure 5.17). SAH 97096 is a type 3 enstatite chondrite and is considered pristine (e.g., Weisberg and Prinz 1998), although enstatite chondrites are known to have experienced thermal alteration in the nebular protoplanetary phase of solar system evolution. The range of Fe contents observed in silicate grains identified in Acfer 094 is the largest (Bose et al. 2010c). The authors discussed in length the various mechanisms especially the role of terrestrial alteration, which may have modified the

elemental compositions of silicate grains in Acfer 094. A more likely explanation for Fe-rich silicate grains is their formation under non-equilibrium conditions, where Fe-rich silicate grains can become stable condensates along with Mg-rich grains (Gail and Sedlmayr 1999; Ferrarotti and Gail 2001). These authors suggested that dust in stellar outflows more closely resembles a rapidly cooling environment, which can enable a larger concentration of Fe to be incorporated in the grains than is allowed under chemical equilibrium. Furthermore, infrared spectra of AGB stars are commonly fitted with laboratory spectra of olivines and pyroxenes with high Mg/Fe ratios (e.g., Dorschner et al. 1995; Fabian et al. 2000), and these models suggest the predominant formation of Mg-rich silicate grains in stars. However, a recent study successfully matched far-infrared spectral dust features of the star T Cep with silicates with high Fe contents (Niyogi and Speck 2010), which indicates that modeling using Fe-rich silicate dust analogues are required to better constrain the chemical compositions of the circumstellar dust grains.

Recent studies discussed elaborately the effects of secondary processes on the Fe contents of silicate grains in QUE 99177, MET 00426, and Acfer 094 (Floss and Stadermann 2009a; Bose et al. 2010c). ALHA77307 is a pristine, highly unequilibrated CO chondrite, in which the matrix components are well preserved (Scott and Krot 2005). These authors suggested that this meteorite contains phyllosilicates and anhydrite that were probably produced in the parent body, although Brearley (1993) proposed that they might be weathering products from Antarctica. Presolar grains are likely to be destroyed during aqueous alteration (e.g., Nagashima et al. 2005); however, Fe contents will not be enhanced during this process. Iron contents can be increased via diffusion at temperatures above 500°C during thermal metamorphism in the meteorite parent body (e.g., Jones and

Rubie 1991). However, the low content of Cr_2O_3 in Fe-rich olivine in chondrules from ALHA77307 indicates that this meteorite has escaped significant effects of thermal metamorphism (Abreu and Brearley 2010). Although this chondrite was first classified as a petrology type 3.0 (Scott and Jones 1990) based on silicate compositions and the mineralogical similarities of ordinary and CO chondrites, it was reclassified as 3.1 based on thermoluminescence technique (Sears et al. 1991). In the year 2007 its classification was refined as 3.03 (Bonal et al. 2007) using the maturity of the organic matter as the scale, indicating the limited extent of thermal metamorphism. The second order C peak in the ALHA77307 Raman spectra lacks structure, which indicates its least mature organic matter (Bonal et al. 2007). Apparently thermal metamorphism at the low temperatures (~200°C) experienced by the ALHA77307 parent body is probably not sufficient to destroy silicate grains because high abundances of presolar silicates have been identified in its matrix (Nguyen et al. 2010a; this work).

Although the elemental distribution of Fe does provide some clues (such as when seen in rims around grains or in cracks within them), Fe isotopic measurements would be helpful to clarify the origin of the high Fe content. Iron isotopic measurements of two group 4 (Mostefaoui and Hoppe 2004; Floss et al. 2008) Fe-containing presolar grains show anomalies in ^{54}Fe, in contrast to thirteen group 1 grains that exhibit solar Fe isotopic compositions (Vollmer et al. 2010; Bose et al. 2010c). Note that the small sizes of the silicate grains give rise to large uncertainties in the Fe isotopic ratios. Furthermore, the absence of Fe isotopic anomalies in the group 1 grains of AGB origin may be due to isotopic dilution by material from surrounding solar system silicates, which is unavoidable when a ~200 nm O^- beam is used to obtain Fe isotopic ratios from less than

300 nm presolar grains. In contrast to Fe isotopic compositions in silicate grains, a large majority of mainstream SiC grains from solar-metallicity AGB stars exhibit -300 to +200‰ anomalies in ^{57}Fe and have solar ^{54}Fe/^{56}Fe isotopic ratios (Marhas et al. 2008). However, the conditions (e.g., C/O ratio) under which SiC and silicate grains form are drastically different. SiC grains form when the dredge-up of ^{12}C-rich material results in C~O in the stellar envelope, while the silicate grains form when the star is O-rich and the third-dredge-up episodes may not have occurred. As a result, the heavy isotopes of Fe from the He intershell may not have been dredged up to the star's envelope. Therefore, in order to pursue the question about the primary or secondary origin of the Fe contents in silicate grains, Fe isotopic measurements on numerous Fe-rich silicate and oxide grains are required.

5.4.5. Al-oxide Grains

In our inventory, two grains have Al-oxide compositions. One grain (31) shows a ^{17}O excess with a sub-solar ^{18}O/^{16}O ratio while the other grain (45) is ^{18}O-rich (^{18}O/^{16}O = (2.76±0.03)×10^{-3}; Table A5.1; Figure 5.1). A few sub-micrometer Al-oxide grains have been identified *in situ* in other meteorites (e.g., Floss and Stadermann 2009a), and abundant Al-oxide grains have been identified in residues (Nittler et al. 1997a; Zinner et al. 2003). Grain 45 belongs to group 4 and may have condensed in SN ejecta. During a SN explosion, materials from zones of different isotopic compositions are mixed explosively (Woosley and Weaver 1995). The O isotopic signature of grain 45 indicates that this grain formed primarily from a mixture of materials from the He/C zone (enriched in ^{18}O) and the H envelope.

The other Al-oxide grain (31) belongs to group 1 and formed in an AGB star of < $2.2M_{\odot}$. Nearly all S type AGB stars show broad emission features consistent with alumina dust (e.g., Sloan and Price 1998). Under thermodynamic equilibrium, alumina is expected to condense at ~1500 K, well above the stability limit for silicates (Tielens et al. 1998). In cases where the gas density has become too low for significant dust growth, a "freeze-out" of the dust condensation sequence occurs, and alumina remains the dominant dust component. In fact, AGB stars with low mass-loss rates (10^{-9}–$10^{-7}M_{\odot}$ per year) have been found to contain significant fractions of alumina (Blommaert et al. 2006; Heras and Hony 2005), and this fraction decreases with increasing mass-loss rate, as observed in AGB stars in the Large Magellan Cloud (Dijkstra et al. 2005).

5.4.6. SiC Grains

A total of twenty-five SiC grains were located in the matrix of ALHA77307 on the basis of C isotopic anomalies, $^{12}C^{-}/^{28}Si^{-}$ ratios, and elemental compositions. The O isotopic data at the locations of the SiC grains did not show any anomalies, as expected because SiC grains contain only trace amounts of O. The morphologies of a few SiC grains found *in situ* in ALHA77307 are triangular or hexagonal (e.g., Figure 5.11), and are similar to presolar SiC grains obtained from acid residues (Amari et al. 1994). Some grains are also circular in shape.

Twenty-three grains with $^{12}C/^{13}C$ ratios between ~21 and 75 (Table A5.3) can be classified as mainstream SiC grains (Hoppe et al. 1994; Hoppe and Ott 1997). This includes twelve grains for which we don't have Auger data. Note that these twenty-three grains can also either be SiC X or SiC Z grains, but we classified them as SiC mainstream grains because mainstream grains are the most abundant fraction (~93%) in the SiC

population (Zinner 2007b). Mainstream SiC grains show an imprint of the CNO cycle, i.e., ^{13}C and ^{14}N excesses, and third dredge-up in $1-3M_{\odot}$ AGB stars (Hoppe et al. 1994).

Grain 106 shows a $^{12}C/^{13}C$ ratio of 4.28±0.04 and therefore is most likely a SiC A+B grain (Table A5.3). J-type C stars and born-again AGB stars have been suggested as the stellar sources of A+B grains (Amari et al. 2001b).

One of the SiC grain (B2) from this study is a probable Y grain (Amari et al. 2001c). These grains make up less than 1% of the SiC population and are characterized by $^{12}C/^{13}C$ ratios of > 100 and Si isotopic compositions that fall to the right of the mainstream SiC correlation line in a Si three-isotope plot. These grains have an origin in AGB stars with metallicities that are lower than solar. However, the N isotopic composition of this grain ($\delta^{15}N$ = -5±93‰) does not fit well with Y grains, and given the lack of Si isotopic data for this grain, its classification as a Y-grain is tentative.

5.4.7. Carbonaceous Grains: Protosolar Remnants

5.4.7.1. Isotopic and Elemental Compositions

Abundant N anomalies are present in ALHA77307 as discrete hotspots with large ^{15}N enrichments ($\delta^{15}N$ up to about 1266‰) that are heterogeneously distributed in the matrix (Figure 5.9; Table A5.3). Note that the $\delta^{15}N$ values calculated for the hotspots in ALHA77307 have been calculated relative to terrestrial atmospheric N but the Sun has isotopically lighter N (e.g., $\delta^{15}N$ = -390±180‰; Marty 2010). Carbonaceous grains, D1 and E7-tp show ^{13}C excesses and exhibit circular nanoglobule-like morphologies. Except for these two nanoglobules and grain F1-17 the remaining ^{15}N-rich hotspots are not accompanied by C anomalies.

The carriers of the N anomalies are often large (Table A5.3) and irregularly shaped. Elemental characterization of the N-anomalous hotspots shows that the Auger spectra contain large C peaks and occasionally contain O, Fe, Mg, Si, and S. The N-anomalous grains exhibit high $^{12}C^{-}/^{28}Si^{-}$ ratios as well as large C and small Si Auger peaks; therefore presolar SiC can be ruled out as the carriers of the N anomalies. The possibility that some of the grains could be presolar graphite cannot be ruled out. Although rare, low-density graphite grains with solar C isotopic compositions and ^{15}N-rich compositions have been identified in Orgueil (Jadhav et al. 2006). Furthermore, circumstellar graphite grains are generally spherules (Jadhav 2009) and grain D1 (e.g., Figure 5.12b), for example, has a morphology that is consistent with graphite. However, additional structural data from the carbonaceous grains are required to explore this possibility. Alternatively, the presence of C, O, Fe, Mg, and Si in the Auger spectra of some grains suggests that the bearers of the N-anomalies are more likely to be organic material, which is often found mixed with silicates and metal. The carbonaceous grains identified here resemble those in other carbonaceous chondrites (Floss and Stadermann 2009b; Zega et al. 2010). The carrier of the ^{15}N-rich component in ALHA77307 is probably the same IOM component that has been extracted from meteorites in residue form (Busemannn et al. 2006; Alexander et al. 2007).

Carbonaceous material G4 exhibits an N anomaly (Figure 5.15) and coats a possible Fe- and C-containing solar system grain. Croat et al. (2009) analyzed a few pristine presolar SiC grain surfaces and found evidence for a ^{15}N-rich surface coating on a SiC with a bulk ^{14}N excess. Such ^{15}N-rich coatings may have a protosolar or interstellar origin. The carbonaceous coating G4 over a solar composition grain may be an

affirmation of the scenario where grains get coated with N-anomalous early solar system material, via grain chemistry.

5.4.7.2. Sources of Isotopic Anomalies

Nitrogen anomalies in the form of ^{15}N excesses - independent of those seen in SiC grains - were first reported in IDPs by Stadermann et al. (1989) followed by observations in numerous primitive meteorites (e.g., Messenger 2000; Alexander et al. 1998; Busemann et al. 2006). Chemical fractionation in IMCs or in the protosolar nebula is a likely source of N isotopic anomalies in primitive extraterrestrial materials (Terzieva and Herbst 2000; Charnley and Rodgers 2002; Clayton 2002; Aléon and Robert 2004; Rodgers and Charnley 2008). The nucleosynthetic processes that are capable of producing up to 1000‰ enrichments in ^{15}N will also result in large isotopic anomalies in C and O in presolar components (Aléon et al. 2003). Such processes include explosive H-burning nucleosynthesis in novae (José and Hernanz 2007), and explosive neutrino induced nucleosynthesis in Type II SNe (Rauscher et al. 2002). However, stellar nucleosynthesis would also produce large C isotopic anomalies, which are not observed. Thus ion-molecule reactions at low temperatures in N-containing IMCs are a more likely cause of the ^{15}N enrichments (e.g., Rodgers and Charnley 2008). In dense IMCs, ion-molecule exchange reactions produce enhancements in the $^{15}N/^{14}N$ ratios on the order of ~2–7 (Rodgers and Charnley 2008), which is sufficient to account for the hotspots with ^{15}N excesses observed in ALHA77307, and in the IOM of several meteorites (Busemann et al. 2006). Nitrogen-15 anomalies can also be produced in the outer regions of the solar nebula via molecular depletion from the gas phase onto surfaces of dust grains at 10 K (Aléon and Robert 2004). Grain surface mediated reactions that occur at low

temperatures involve adsorption of atoms or molecules (predominantly C, O and N-containing) from the gas, followed by surface diffusion, and reaction with other species (Terzieva and Herbst 2000).

Carbon and N anomalies are observed in three carbonaceous grains in this study. In general these cases are rare (e.g., Floss et al. 2004, 2006, 2011; Floss and Stadermann, 2009b; Busemann et al. 2006). Floss et al. (2004) reported a grain in the IDP Benavente that shows ^{15}N excess associated with ^{13}C depletion, while Floss et al. (2006) found a grain with ^{13}C- and ^{15}N-rich composition in IDP Hess. Recently, numerous grains with C isotopic anomalies were identified in two CR3 chondrites (Floss and Stadermann 2009b); N isotopic data are not available for many of these grains. Similar to N, chemical fractionation of C isotopes can occur in dense IMCs by multiple gas phase reactions (e.g., Langer et al. 1984). Carbon isotopic anomalies are absent in most extraterrestrial materials and so it was suggested that fractionation effects in opposite directions balance each other and do not produce C anomalies (Sandford et al. 2001). Floss et al. (2009b) suggested that the presence of associated C and N isotopic anomalies in the carbonaceous materials might not require the same reaction pathways. Different reaction pathways depending on the composition of the ices will result in grains of different isotopic compositions. In ALHA77307, the presence of abundant N-anomalous grains with no C anomalies implies that the dominant reaction pathways do not fractionate C isotopes. Although ALHA77307 has experienced minimal processing (Busemann et al. 2007), it is possible that the anomalous C signatures have been erased by secondary processing in the parent body or in the protosolar stage of evolution. In general, carbonaceous grains with low $^{12}C/^{13}C$ ratios are rarer than those with high $^{12}C/^{13}C$ ratios (e.g., Floss and

Stadermann 2009b; this work). It is possible that the gas phase molecular species associated with the reaction channels that produces ^{12}C enrichments (e.g., C_2H_2 and CH_4) are more dominant than those that produce ^{13}C enrichments (e.g., CO molecule; Cronin et al. 1993). However, some carbonaceous grains that exhibit ^{13}C excesses have also been identified in IDPs (e.g., Floss et al. 2006, 2011), and owing to the limited statistics, conclusions about the dominant reaction channels cannot be made at present.

The magnitude of the N anomalies observed in ALHA77307 is similar to that in primitive IDPs (Floss et al. 2004, 2006; Keller et al. 2004). These observations support the view that ALHA77307 has preserved primitive organic matter. Meteoritic IOM often exhibits bulk N-anomalous compositions with ^{15}N-rich hotspots (Busemann et al. 2006; Alexander et al. 2007); e.g., the CR3 chondrites QUE 99177 and MET 00426 contain macromolecular organic matter with bulk $\delta^{15}N$ on the order of 175–190‰ (Alexander et al. 2007) and also contain localized hotspots with $\delta^{15}N$ values up to ~2500‰ (Floss and Stadermann 2009b). In contrast, N-anomalous hotspots in ALHA77307 are only localized. Whether the N isotopic anomalies preserved in ALHA77307 indicate that the carbonaceous material has been resistant to isotopic equilibration or is the residue of *more* anomalous material needs further clarification. Busemann et al. (2007) showed that peak metamorphic temperatures are the lowest (~200°C) for the CR chondrites and ALHA77307. Metamorphism of the IOM will result in low elemental ratios (e.g., H/C and N/C) and high $^{14}N/^{15}N$ ratios, as the more labile material is removed (Busemann et al. 2007). Low N/C and especially low H/C for ALHA77307 compared to the CRs reflect incomplete transition of the ALHA77307 IOM from disordered amorphous C to nanocrystalline graphite due to thermal alteration, which implies that ALHA77307 is

more processed than the CRs (Busemann et al. 2007). However, the high D band widths observed in the Raman spectra of ALHA77307 IOM indicate low degrees of metamorphism experienced by this meteorite (Busemann et al. 2007; Bonal et al. 2007). The fragile carrier of the bulk $\delta^{15}N$ enrichments may have been destroyed, even with such a low degree of parent body processing. The localized ^{15}N excesses in the matrix of this meteorite (this work), which are present with an abundance of 160±30 ppm support the view that processing has not been pervasive as to lead to the complete destruction of N anomalies in the bulk matrix.

5.4.7.3. Nanoglobules

An interesting subpopulation of organic grains is nanoglobules. High-resolution images in the Auger Nanoprobe indicate that three of our ^{15}N-rich hotspots are circular in shape, may be hollow (e.g., D1 in Figure 5.12b), and are therefore similar to the nanoglobules seen in Tagish Lake and Bells (Nakamura-Messenger et al. 2006; Messenger et al. 2008). The carbonaceous grains observed in ALHA77307 that are nanoglobule candidates are sub-micrometer in size (Table A5.3). The nanoglobules seen in other meteorites (i.e., Nakamura-Messenger et al. 2006; Messenger et al. 2008) vary vastly in size, ranging from ~50 nm to 2 μm. Two of the nanoglobules in ALHA77307 exhibit ^{13}C (40 and 70‰) and ^{15}N (453 and 442‰) excesses (Table A5.3). The first nanoglobule that exhibited C (140±15‰) and N (630±75‰) isotopic anomalies was found in the matrix of MET 00426 (Floss and Stadermann 2009b). The lower C isotopic anomalies of organic nanoglobules in ALHA77307 compared to those in CR3 chondrites may indicate alteration histories of the meteorite parent bodies; ALHA77307 is more processed than MET 00426.

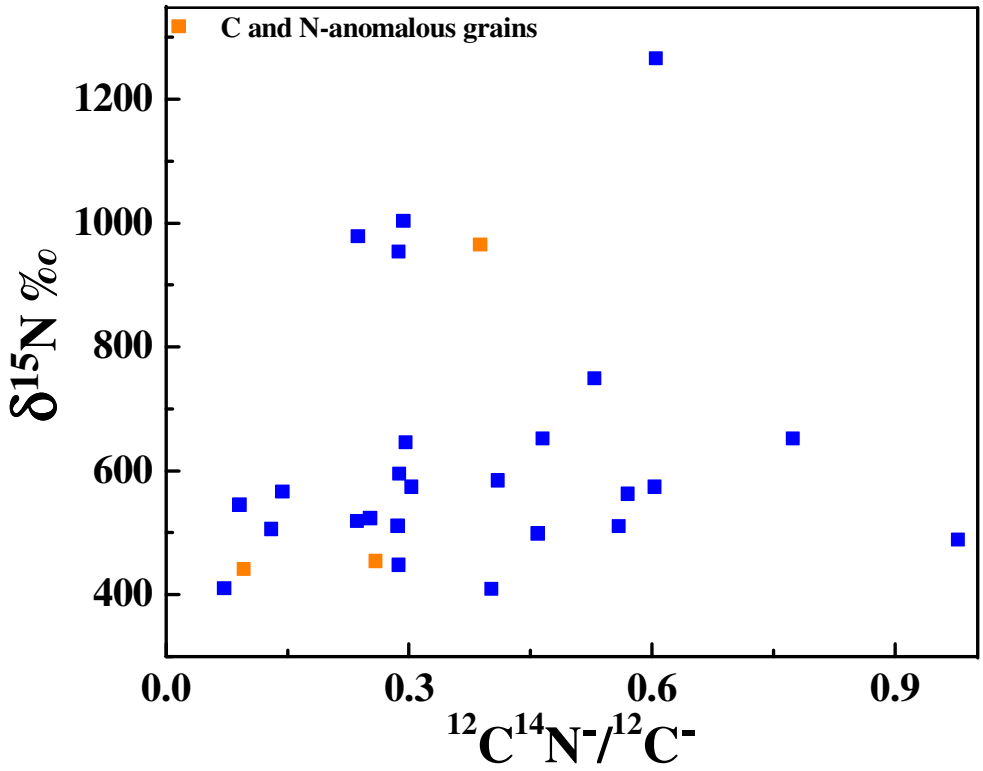

Figure 5.18: The CN^-/C^- ratios plotted against the N isotopic compositions in the hotspots from ALHA77307.

Several mechanisms have been proposed to explain the formation of the N-anomalous nanoglobules. Organic nanoglobules may form via UV irradiation of organic-rich interstellar ice grains, followed by sublimation of the interior ice (Nakamura-Messenger et al. 2006). Alternatively, spherical globules may be created during aqueous alteration on meteorite parent bodies (Cody et al., 2005). However, formation of globules may require significant exposure to water, which is contrary to the conditions experienced by the ALHA77307 parent body (Brearley 1993).

5.4.7.4. CN^-/C^- ratios versus the N isotopic compositions

Figure 5.18 plots $\delta^{15}N$ values against the CN^-/C^- ratios of the N-anomalous hotspots in ALHA77307. The hotspots with anomalous N isotopic compositions have a range of

CN^-/C^- ratios from 0.1 to 1.0. Note that N contents from Auger measurements could not be used because N was below the detection limits in the Auger measurements. Although, a large degree of scatter is seen in the $\delta^{15}N$ and CN^-/C^- ratios of the carbonaceous grains, there is a weak positive correlation (Figure 5.18). Five hotspots (D6, D8, F1-17, G2-me, and G3-rt) do not exhibit this weak positive trend; four hotspots cluster together with high ^{15}N excesses and low CN^-/C^- (~0.3) ratios. None of the points that fall off the weak positive trend have different $^{12}C/^{28}Si^-$ elemental ratios or exhibit obvious compositional differences from the other hotspots. Based on a calibration of CN^-/C^- ratios in organic material with variable N contents, Aléon et al. (2003) showed that the excesses in ^{15}N were positively correlated with high N concentration (greater than 10 wt.%). Floss et al. (2006) studied a suite of IDPs using the NanoSIMS, and concluded that the most anomalous IDPs have the lowest CN^-/C^- ratios. Furthermore, these authors observed that the IDPs with normal bulk N isotopic have also been observed in IDPs from 55P/Tempel Tuttle (Floss et al. 2011). In contrast to all these observations, Busemann et al. (2009) noted no obvious correlation between these parameters for IDPs from NASA's dedicated "Grigg-Skjellerup collection". Although it is unclear whether calibration curves from measurements made under different experimental conditions can be used to estimate N concentrations, such estimates may provide clues to the kind of material carrying these anomalies. Using the calibration scale of Aléon et al. (2003), the hotspots in ALHA77307 have CN^-/C^- ratios corresponding to N concentrations of less than 5 wt.%, which is in fair agreement with estimates from Floss et al. (2006). The inferred N contents in the carbonaceous material in ALHA77307 are also in agreement with the Auger data, which show no detectable N (< 3 at.%) in the spectra. The variation in the ^{15}N values can be

caused by different degrees of fractionation in different N-containing molecules during the protostellar periods. Nitrogen-bearing molecules such as NH_3 or HCN may produce different degrees of N enrichments compared to N_2 (e.g., Sandford et al. 2001). In that case, the variations in the N isotopic ratios in the carbonaceous materials identified in meteorites reflect the predominant molecular species and the evolutionary timescales in the early solar system nebula.

5.4.8. Abundance Estimates

5.4.8.1. Silicate and Oxide Grains

Abundance calculations for the silicate and oxide grains were done on the basis of grain sizes measured in the Auger Nanoprobe. For the grains that were sputtered away in the NanoSIMS, the ion images were used to calculate the grain sizes. The silicate grain abundance in ALHA77307 is 119±14 ppm (not corrected for detection efficiencies), which is different (within 1σ) from that calculated for presolar silicates in the same chondrite (177±17 ppm) by Nguyen et al. (2010a). The difference in the abundances may be attributed to heterogeneity in the two samples. Floss and Stadermann (2009a) and others have found that certain regions of the matrix are more abundant in presolar phases than others. The silicate grain abundance in ALHA77307 lies within the range of abundances observed in most primitive carbonaceous chondrites (Figure 5.19). Note that the O-anomalous grain abundance for MET 00426 is plotted in Figure 5.19 (Floss and Stadermann 2009a), in which only one oxide grain was found.

The observed differences in the average abundance numbers (given in brackets in Figure 5.19) among the most unequilibrated carbonaceous chondrites are either due to

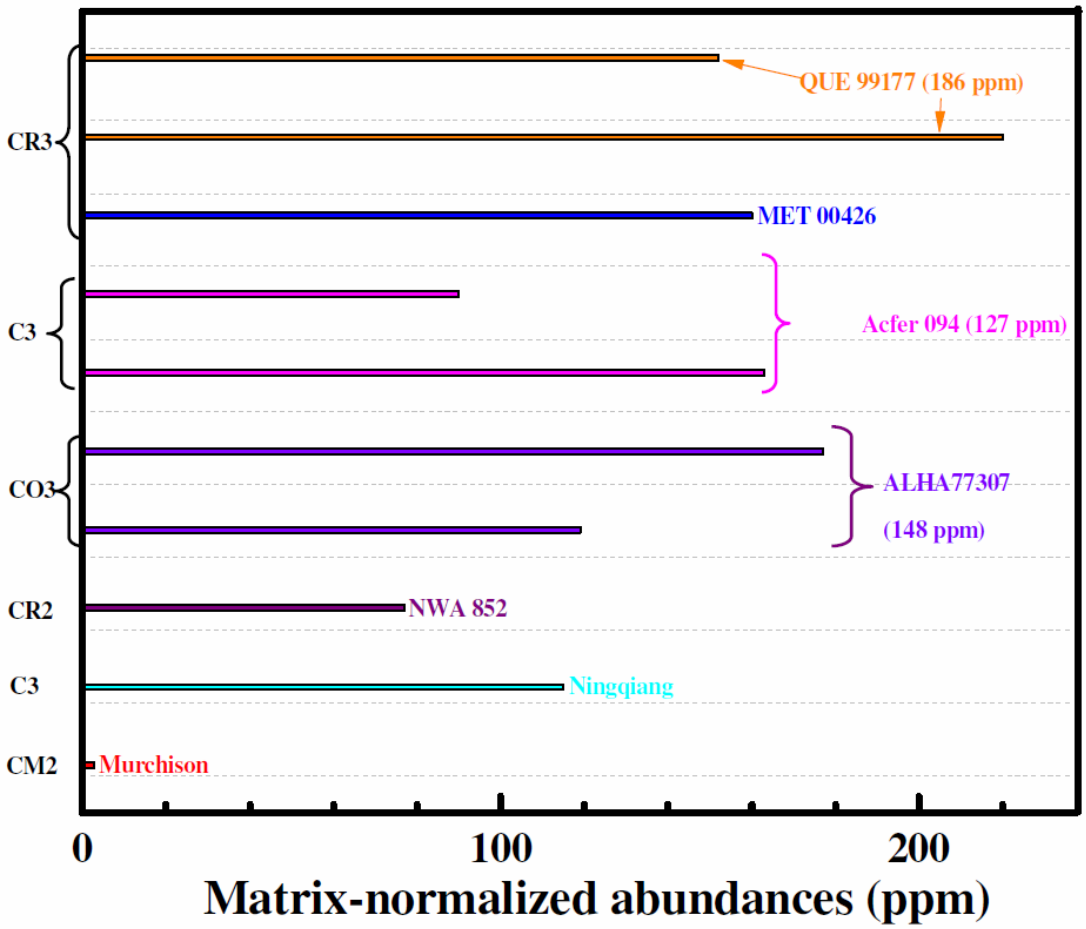

Figure 5.19: The abundance of silicate grains in ALHA77307 and in other carbonaceous chondrites (Nagashima et al. 2005; Nguyen et al. 2007, 2010a; Floss and Stadermann 2009a; Vollmer et al. 2009a; Nguyen et al. 2010; Leitner et al. 2010; Zhao et al. 2010; this work). The average abundances for QUE 99177, Acfer 094, and ALHA77307 are indicated in brackets.

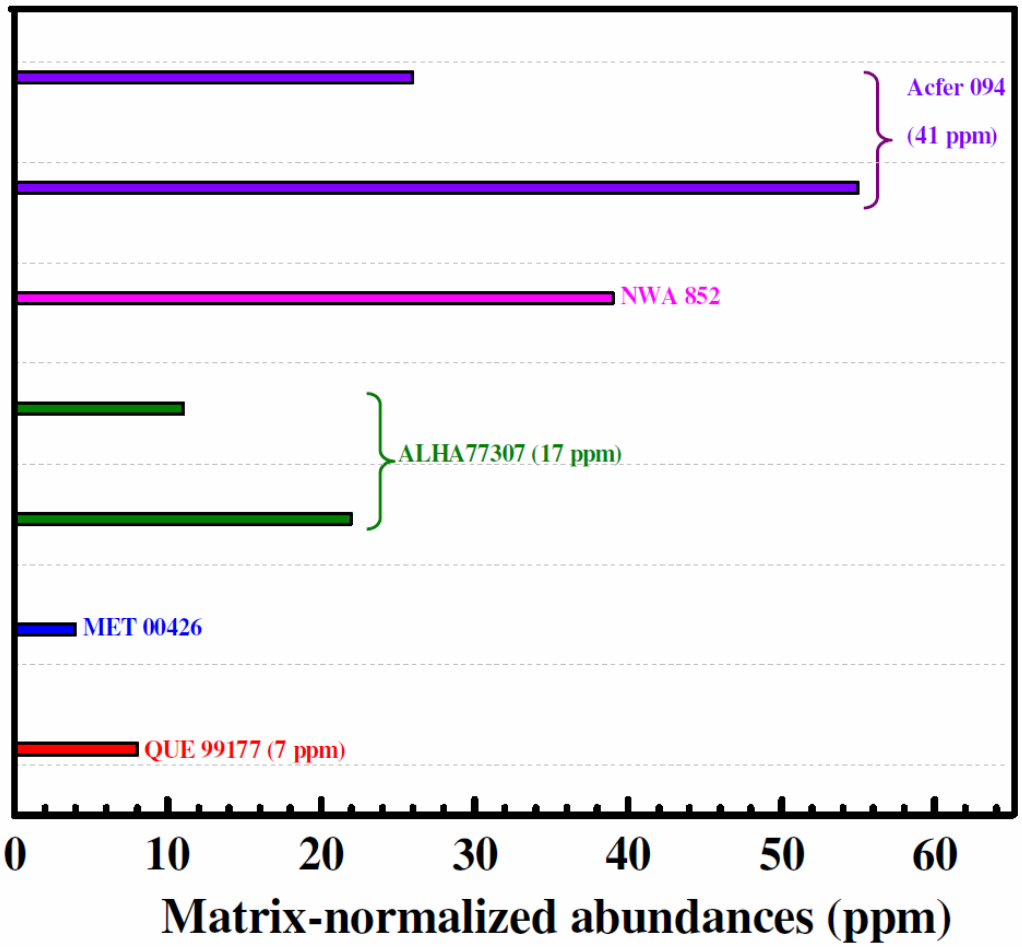

Figure 5.20: The abundance of oxide grains in ALHA77307 and in other carbonaceous chondrites (Nguyen et al. 2007; Floss and Stadermann 2009a; Vollmer et al. 2009a; Nguyen et al. 2010a; Leitner et al. 2010; this work).

secondary alteration in the protosolar nebula or in the parent body. For example, the CR3 chondrite QUE 99177 (186 ppm) has the highest silicate abundance, and was argued to be the most pristine carbonaceous chondrite studied to date (Floss and Stadermann 2009a). Similarly, the high abundance of presolar silicates in ALHA77307 indicates the pristine nature of this meteorite. A comparison of the presolar silicate abundances in a number of meteorites supports the fact that chondrites accreted similar fractions of presolar silicate grains. As discussed earlier, ALHA77307 has experienced very mild thermal alteration (Busemann et al. 2007). Whether this is enough to destroy presolar silicate grains needs more investigation. The abundance of presolar silicates in Murchison is significantly lower because this CM chondrite has experienced aqueous alteration that led to the destruction of silicate grains (Figure 5.19; Nagashima et al. 2005). The CR2 chondrite NWA 852 also shows a lower abundance of presolar silicates than its more primitive CR3 chondrites, QUE99177 and MET 00426 because of secondary alteration (Leitner et al. 2010). Furthermore, both the ungrouped carbonaceous chondrites, Ningqiang and Acfer 094 have similar abundances of presolar silicate grains, which are lower than the abundance in QUE 99177 within 1σ errors. Ningqiang shows secondary alteration signatures (Zhao et al. 2010), e.g., this meteorite appears to have undergone Fe-alkali-halogen metasomatism (Krot et al. 1995), while Acfer 094 has suffered some degree of terrestrial alteration (Bose et al. 2010c).

The presolar silicate abundance is ~10 times greater than the presolar oxide grain abundance in ALHA77307 (this work; Nguyen et al. 2010a), consistent with that seen in Acfer 094 (~6; Vollmer et al. 2009a). The silicate to oxide grain abundance ratio is much higher (> 20) in the CR3 chondrites (Floss and Stadermann 2009a; Figure 5.20).

However, low silicate grain abundances have been observed in meteorites that have experienced more extensive processing. For example, many oxide grains have been found in Murchison (Nittler et al. 1997b), which is aqueously altered but this CM chondrite does not contain a high abundance (~3 ppm) of presolar silicates (Nagashima et al. 2005). Oxide grains have been studied in meteorites e.g., OC Tieschitz (Nittler et al. 1994) and EH Indarch (Zinner et al. 2007b), but presolar silicate grain searches have not been performed. The lack of studies on oxide and silicate grains in the same meteorites makes comparison difficult and better statistics for oxide grain abundances are required to observe the correlation between the petrographic type and the ratio of silicate to oxide grains.

5.4.8.2. SiC Grains

The abundance of SiC grains were calculated on the basis of the NanoSIMS ion images. The abundance of SiC grains determined *in situ* in ALHA77307 (this study) is 109±22 ppm, which is ~10 times higher than that observed by ion imaging of IOM residues in the same meteorite (Davidson et al. 2009; Figure 5.21). This difference could be due to the destruction of SiC grains present in the IOM during sample preparation, and/or analytical differences. However, this seems unlikely because for MET 00426 the abundance of SiC *in situ* (Floss and Stadermann 2009b) is only twice that calculated from acid residues (Davidson et al. 2009), and for Renazzo, the SiC estimates are comparable (Figure 5.21). Furthermore, other carbonaceous chondrites that show abundant sub-micrometer-sized SiC grains in their matrices include QUE 99177 (45 ppm), MET 00426 (90 ppm), and Renazzo (50 ppm; Floss and Stadermann 2009b). Leitner et al. (2010) reported ~160 ppm abundance of SiC grains in NWA 852. The abundance of SiC grains

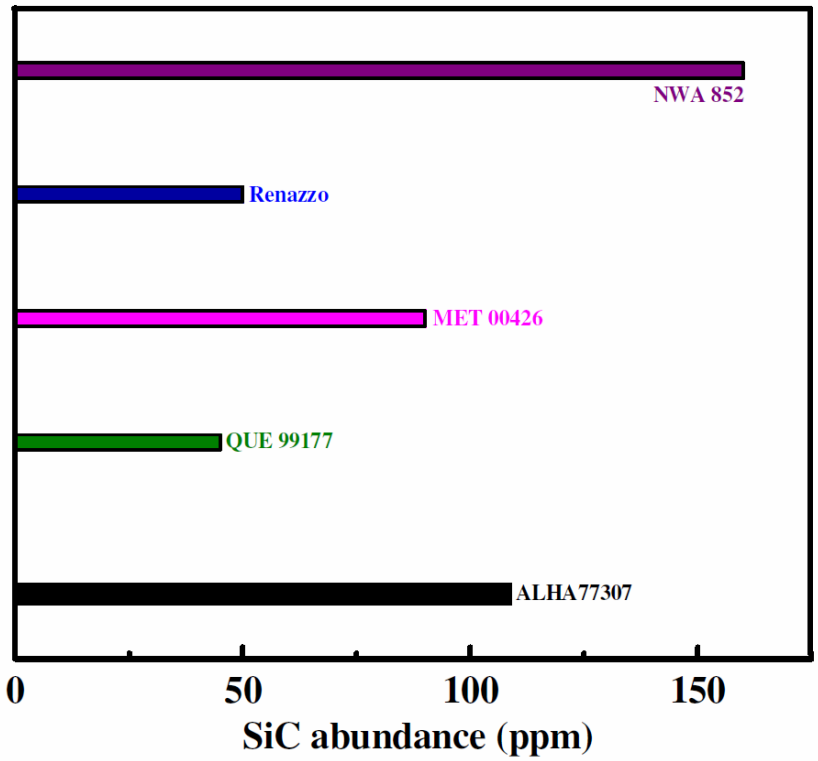

Meteorite	SiC Abundance in ppm		
	In situ	Acid residues	Noble gas
MET 00426	90	44	Nk
Renazzo	50	36	~2
ALHA77307	109	10	9

Figure 5.21: The abundance of SiC grains in ALHA77307 and in other carbonaceous chondrites (Floss and Stadermann 2009a; Leitner et al. 2010; this work). The SiC abundances in ALHA77307 calculated from noble gas measurements (Huss et al. 2003) and NanoSIMS ion imaging of IOM (Davidson et al. 2009) are also compared. Similar measurements for meteorites MET 00426 and Renazzo from Floss and Stadermann (2009b) are also listed in the table. "Nk" stands for Not known.

in ALHA77307 agrees well with those of other primitive meteorites. Some of these primitive meteorites do not show large discrepancies in SiC abundances between *in situ* and IOM studies. The disagreement between the SiC abundance calculated here and in Davidson et al. (2009) may be associated with sample differences. As discussed earlier, recent studies have observed that certain matrix areas in meteorites (e.g., Acfer 094, QUE99177, and MET 00426) are packed with presolar grains while others have almost none (Vollmer et al. 2009a; Floss and Stadermann 2009a). This is the most likely cause of the observed abundance differences in ALHA77307.

The SiC abundances in ALHA77307 and Renazzo from noble gas measurements, however, are drastically different from *in situ* imaging of the matrices (Huss et al. 2003; Figure 5.21). Observations from Renazzo indicate that the SiC grains in these two meteorites were degassed during their residence in the parent body. As discussed in section 4.7.2., ALHA77307 was mildly heated in the parent body, which is likely to have resulted in the release of noble gases.

5.5. Conclusions

The presolar grain population in ALHA77307 is dominated by materials formed in C- and O-rich outflows from AGB or RG stars, with moderate contributions from SNe. One extremely ^{17}O-rich grain in our inventory may have its origin in a binary star system with contributions from nova ejecta. A majority of the presolar silicate grains in ALHA77307 exhibit non-stoichiometric ferromagnesian elemental compositions. Some presolar silicate grains with olivine- and pyroxene-like compositions also exist in this inventory. Olivine-like grains are more abundant than pyroxene-like grains, which is in agreement

with stellar observations, and in contrast to that seen in Acfer 094, QUE 99177, and MET 00426.

We found a correlation between the isotopic and elemental compositions of silicate grains. Core collapse SNe produce about three times more olivine-like grains than pyroxene-like grains. Furthermore, chemical non-equilibrium in the circumstellar shells surrounding SR variable stars that are characterized by low mass-loss rates may play a significant role in the condensation of MgO and SiO_2 grains. In addition, the high Fe contents in the silicate grains most likely originated in the stellar environment by non-equilibrium dust-forming processes. Finally, the presence of a composite grain with subgrains exhibiting variable elemental compositions indicates the dynamic conditions that exist in the stellar environment. All of the aforementioned cases indicate that the fundamental assumption of equilibrium may not be always appropriate for a realistic description of circumstellar environments. Despite the arguments about condensation under non-equilibrium, it should be noted that we also observe presolar SiC grains in ALHA77307, whose formation can be explained by equilibrium condensation (Lodders and Fegley 1999). Silicate grains are the most common grain type found in ALHA77307.

The carbonaceous grains are characterized by high $^{12}C^-/^{28}Si^-$ elemental ratios and large C Auger peaks in their spectra. Two nanoglobules with ^{13}C and ^{15}N excesses exist in this inventory. Abundant carbonaceous matter that is N-anomalous is produced in ion-molecule reactions, which suggests that similar material with modest C anomalies also has a non-stellar origin. The absence of ^{13}C-depleted grains in ALHA77307 suggests that the reactions on grain surfaces involving CO may be dominant. The small extent of thermal metamorphism experienced by the meteorite destroyed some of the labile

carbonaceous material. However, the high abundances of O- and C-anomalous grains indicate that ALHA77307 is as primitive as QUE 99177 and MET 00426, and that it escaped substantial processing.

Acknowledgements. We thank Tim Smolar and Eric Inazaki for maintenance of the NanoSIMS 50 and PHI 700 Auger Nanoprobe. This work was supported by NASA grants, NNX08AI13G (PI: Dr. Frank J. Stadermann) and NNXO7AI82G (PI: Dr. Christine Floss). I would like to thank the NASA Earth and Space Science Fellowship program (NNX07AU8OH) for the three-year fellowship.

REFERENCES

Abreu N. M. and Brearley A. J. (2010) Early solar system processes recorded in the matrices of two highly pristine CR3 carbonaceous chondrites, MET 00426 and QUE 99177. *Geochimica et Cosmochimica Acta* **74**, 1146-1171.

Aléon J., Robert F., Chaussidon M., and Marty B. (2003) Nitrogen isotopic composition of macromolecular organic matter in interplanetary dust particles. *Geochimica et Cosmochimica Acta* **67**, 3773-3783.

Aléon J. and Robert F. (2004) Interstellar chemistry recorded by nitrogen isotopes in solar system organic matter. *Icarus* **167**, 424-430.

Aléon J. (2010) Multiple origins of nitrogen isotopic anomalies in meteorites and comets. *The Astrophysical Journal* **722**, 1342-1351.

Alexander C. M. O'D., Russell S. S., Arden J. W., Ash R. D., Grady M. M., and Pillinger C. T. (1998) The origin of chondritic macromolecular organic matter: a carbon and nitrogen isotope study. *Meteoritics and Planetary Science* **33**, 603-622.

Alexander C. M. O'D., Fogel M., Yabuta H., and Cody G. D. (2007) The origin and evolution of chondrites recorded in the elemental and isotopic compositions of their organic matter. *Geochimica et Cosmochimica Acta* **71**, 4380-4403.

Amari S., Lewis R. S., and Anders E. (1994) Interstellar grains in meteorites. I - Isolation of SiC, graphite, and diamond; size distributions of SiC and graphite. II - SiC and its noble gases. *Geochimica et Cosmochimica Acta* **58**, 459-470.

Amari S., Gao X., Nittler L. R., and Zinner E. (2001a) Presolar grains from novae. *The Astrophysical Journal* **551**, 1065-1072.

Amari S., Nittler L. R., Zinner E., Lodders K., and Lewis R. S. (2001b) Presolar SiC grains of Type A and B: Their isotopic compositions and stellar origins. *The Astrophysical Journal* **559**, 463-483.

Amari S., Nittler L. R., Zinner E., Gallino R., Lugaro M., and Lewis R. S. (2001c) Presolar SIC Grains of type Y: Origin from low-metallicity asymptotic giant branch stars. *The Astrophysical Journal* **546**, 248-266.

Anders E. and Grevesse N. (1989) Abundances of the elements: Meteoritic and solar. *Geochimica et Cosmochimica Acta* **53**, 197-214.

Arnett W. D. and Truran J. W. (1969) Carbon-burning nucleosynthesis at constant

temperature. *The Astrophysical Journal* **157**, 339-365.

Blommaert J. A. D. L., Groenewegen M. A.T., Okumura K., Ganesh S., Omont A., Cami J., Glass I. S., Habing H. J., Schultheis M., Simon G., and van Loon J. Th. (2006) ISO mid-infrared spectroscopy of galactic bulge AGB stars. *Astronomy and Astrophysics* **460**, 555-563.

Bonal L., Bourot-Denise M., Quirico E., Montagnac G., and Lewin E. (2007) Organic matter and metamorphic history of CO chondrites. *Geochimica et Cosmochimica Acta* **71**, 1605-1623.

Bose M., Floss C., and Stadermann F. J. (2009) Presolar silicate and oxide dust in ALHA77307. *Meteoritics and Planetary Science Supplement* 44, A36.

Bose M., Floss C., Stadermann F. J., Stroud R. M., and Speck A. K. (2010a) The origin of presolar silica grains in AGB Stars. *Lunar and Planetary Science Conference* 41, Abstract #1812.

Bose M., Floss C., and Stadermann F. J. (2010b) Nitrogen isotopic anomalies in ALHA77307. *Meteoritics and Planetary Science Supplement* 45, A19.

Bose M., Floss C., and Stadermann F. J. (2010c) An investigation into the origin of Fe-rich presolar silicates in Acfer 094. *The Astrophysical Journal* **714**, 1624-1636.

Bose M., Zhao X., Floss C., Stadermann F. J., and Lin Y. (2010d) Stardust material in the paired enstatite meteorites: SAH 97096 and SAH 97159. *Proceedings of Nuclei in the Cosmos* XI, POS_NIC XI 138.

Bose M., Floss C., and Stadermann F. J. (2011) Carbonaceous N-anomalous grains in the CO3.0 meteorite ALHA77307. *Lunar and Planetary Science Conference* 42, Abstract #1444.

Brearley A. J. (1993) Matrix and fine-grained rims in the unequilibrated CO3 chondrite, ALHA77307 - Origins and evidence for diverse, primitive nebular dust components. *Geochimica et Cosmochimica Acta* **57**, 1521-1550.

Busemann H., Young A. F., Alexander C. M. O'D., Hoppe P., Mukhopadhyay S., and Nittler L. R. (2006) Interstellar chemistry recorded in organic matter from primitive meteorites. *Science* **312**, 727-730.

Busemann H., Alexander C. M. O'D., and Nittler L. R. (2007) Characterization of insoluble organic matter in primitive meteorites by microRaman spectroscopy. *Meteoritics and Planetary Science* **42**, 1387-1416.

Busemann H., Nguyen A. N., Cody G. D., Hoppe P., Kilcoyne A. L. D., Stroud R. M., Zega T. J., and Nittler L. R. (2009) Ultra-primitive interplanetary dust particles from the comet 26P/Grigg-Skjellerup dust stream collection. *Earth and Planetary Science Letters* **288**, 44-57.

Busso M., Gallino R., and Wasserburg G. J. (2003) Short-lived nuclei in the early solar system: A low mass stellar source? *Publications of the Astronomical Society of Australia* **20**, 356-370.

Carrez P., Demyk K., Cordier P., Gengembre L., Grimblot J., D'Hendecourt L., Jones A.

P., and Leroux H. (2002) Low-energy helium ion irradiation-induced amorphization and chemical changes in olivine: Insights for silicate dust evolution in the interstellar medium. *Meteoritics and Planetary Science* **37**, 1599-1614.

Charnley S. B. and Rodgers S. D. (2002) The end of interstellar chemistry as the origin of nitrogen in comets and meteorites. *The Astrophysical Journal* **569**, L133-L137.

Childs K. D., Carlson B. A., Vanier L. A., Moulder J. F., Paul D. F., Stickle W. F., and Watson D. G. (1995) Handbook of Auger Electron Spectroscopy. Physical Electronics.

Clayton R. N. (2002) Solar System: Self-shielding in the solar nebula. *Nature* **415**, 860-861.

Cody G. and Alexander C. M. O'D. (2005) NMR studies of chemical structural variation of insoluble organic matter from different carbonaceous chondrite groups. *Geochimica et Cosmochimica Acta* **69**, 1085-1097.

Croat T. K., Bernatowicz T. J., and Stadermann F. J. (2009) Auger and NanoSIMS investigations of pristine presolar SiC surfaces. *Lunar and Planetary Science Conference* 40, Abstract #1887.

Cronin J. R., Pizzarello S., Epstein S., and Krishnamurthy R. V. (1993) Molecular and isotopic analyses of the hydroxy acids, dicarboxylic acids, and hydroxydicarboxylic acids of the Murchison meteorite. *Geochimica et Cosmochimica Acta* **57**, 4745-4752.

Davidson J., Busemann H., Alexander C. M. O'D., Nittler L. R., Schrader D. L., Orthous-

Daunay F. R., Quirico E., Franchi I. A., and Grady M. M. (2009) Presolar SiC abundances in primitive meteorites by NanoSIMS raster ion imaging of insoluble organic matter. *Lunar and Planetary Science Conference* 40, Abstract #1853.

Demyk K., Dartois E., Wiesemeyer H., Jones A., D'Hendecourt L., Jourdain de Muizon M., and Heras A. M. (2000) Composition of the silicates around evolved stars and protostars. In: ISO beyond the peaks: The 2nd ISO Workshop on Analytical Spectroscopy 456, p. 183.

Demyk K., Carrez Ph., Leroux H., Cordier P., Jones A. P., Borg J., Quirico E., Raynal P. I., and d'Hendecourt L. (2001) Structural and chemical alteration of crystalline olivine under low energy He+ irradiation. *Astronomy and Astrophysics* **368**, L38-L41.

DePew K. (2000) Astromineralogy of the 13 micron feature in oxygen-rich asymptotic giant branch stars. M.S. Thesis, pp. 79.

Dijkstra C., Speck A. K., Reid R. B., and Abraham P. (2005) The 10 μm feature of M-Type stars in the Large Magellanic Cloud and the dust condensation sequence. *The Astrophysical Journal* **633**, L133-L136.

Dorschner J., Begemann B., Henning Th., Jäger C., and Mutschke H. (1995) Steps toward interstellar silicate mineralogy II. Study of Mg-Fe-silicate glasses of variable composition. *Astronomy and Astrophysics* **300**, 503-520.

Dunne L., Eales S., Ivison R., Morgan H., and Edmunds M. (2003) Type II supernovae as a significant source of interstellar dust. *Nature* **424**, 285-287.

Fabian D., Jäger C., Henning Th., Dorschner J., and Mutschke H. (2000) Steps toward interstellar silicate mineralogy V. Thermal evolution of amorphous magnesium silicates and silica. *Astronomy and Astrophysics* **364**, 282-292.

Fabian D., Posch Th., Mutschke H., Kerschbaum F., and Dorschner J. (2001) Infrared optical properties of spinels. A study of the carrier of the 13, 17 and 32 μm emission features observed in ISO-SWS spectra of oxygen-rich AGB stars. *Astronomy and Astrophysics* **373**, 1125-1138.

Ferrarotti A. S. and Gail H.-P. (2001) Mineral formation in stellar winds. II. Effects of Mg/Si abundance variations on dust composition in AGB stars. *Astronomy and Astrophysics* **371**, 133-151.

——— (2003) Mineral formation in stellar winds. IV. Formation of magnesiowüstite. *Astronomy and Astrophysics* **398**, 1029-1039.

Floss C., Stadermann F. J., Bradley J., Dai Z. R., Bajt S., and Graham G. (2004) Carbon and Nitrogen isotopic anomalies in an anhydrous interplanetary dust particle. *Science* **303**, 1355-1358.

Floss C., Stadermann F. J., Bradley J. P., Dai Z. R., Bajt S., Graham G., and Lea A. S. (2006) Identification of isotopically primitive interplanetary dust particles: A NanoSIMS isotopic imaging study. *Geochimica et Cosmochimica Acta* **70**, 2371-2399.

Floss C., Stadermann F. J., and Bose M. (2008) Circumstellar Fe oxide from the Acfer

094 carbonaceous chondrite. *The Astrophysical Journal* **672**, 1266-1271.

Floss C. and Stadermann F. J. (2009a) Auger Nanoprobe analysis of presolar ferromagnesian silicate grains from primitive CR chondrites QUE 99177 and MET 00426. *Geochimica et Cosmochimica Acta* **73**, 2415-2440.

Floss C. and Stadermann F. J. (2009b) High abundances of circumstellar and interstellar C-anomalous phases in the primitive CR3 chondrites QUE 99177 and MET 00426. *The Astrophysical Journal* **697**, 1242-1255.

Floss C., Stadermann F. J., Mertz A. F., and Bernatowicz T. J. (2011) A NanoSIMS and Auger Nanoprobe investigation of an isotopically primitive interplanetary dust particle from the 55P/Tempel-Tuttle targeted stratospheric dust collector. *Meteoritics and Planetary Science* **45**, 1889-1905.

Gail H.-P. and Sedlmayr E. (1999) Mineral formation in stellar winds. I. Condensation sequence of silicate and iron grains in stationary oxygen rich outflows. *Astronomy and Astrophysics* **347**, 594-616.

Gail H.-P. (2003) Formation and evolution of minerals. In: Astromineralogy (ed. T. Henning) Springer-Verlag, Berlin, pp. 55-120.

Glaccum W. (1995) Infrared dust features of late-type stars and planetary nebulae. *Airborne Astronomy Symposium on the Galactic Ecosystem* **73**, 395-396.

Grossman J. N. and Brearley A. J. (2005) The onset of metamorphism in ordinary and carbonaceous chondrites. *Meteoritics and Planetary Science* **40**, 87-122.

Grossman L. and Larimer J. W. (1974) Early chemical history of the solar system. *Reviews of Geophysics* **12**, 71-101.

Gyngard F., Zinner E., Nittler L. R., Morgand A., Stadermann F. J., and Hynes K. M. (2010) Automated NanoSIMS measurements of spinel stardust from the Murray meteorite. *The Astrophysical Journal* **717**, 107-120.

Gyngard F., Nittler L. R., Zinner E., and Jose´ J. (2011) Oxygen-rich stardust grains from novae. *Proceedings of Nuclei in the Cosmos* XI, POS_NIC XI 141.

Harris M. J., David L., and Smith V. V. (1985) Oxygen isotopic abundances in evolved stars. II. Eight MS and S stars. *The Astrophysical Journal* **299**, 375-385.

Heras A. M. and Hony S. (2005) Oxygen-rich AGB stars with optically thin dust envelopes. *Astronomy and Astrophysics* **439**, 171-182.

Huss G. R., Meshik A. P., Smith J. B., and Hohenberg C. M. (2003) Presolar diamond, silicon carbide, and graphite in the carbonaceous chondrites: Implications for thermal processing in the solar nebula. *Geochimica et Cosmochimica Acta* **67**, 4823-4848.

Hoppe P., Amari S., Zinner E., Ireland T., and Lewis R. S. (1994) Carbon, nitrogen, magnesium, silicon and titanium isotopic compositions of single interstellar silicon carbide grains from the Murchison carbonaceous chondrite. *The Astrophysical Journal* **430**, 870-890.

Hoppe P. and Ott U. (1997) Mainstream silicon carbide grains from meteorites. In:

Astrophysical Implications of the Laboratory Study of Presolar Materials (eds. T. J. Bernatowicz and E. Zinner). AIP, New York, pp. 27-58.

Ivezic Z. and Knapp G. R. (1999) Link between mass-loss and variability Type for AGB stars? *Proceedings of IAU Symposium* 191, 395-400.

Jadhav M., Amari S., Zinner E., and Maruoka T. (2006) Isotopic analysis of presolar graphite grains from Orgueil. *New Astronomy Review* **50**, 591-595.

Jadhav M. (2009) Multi-element isotopic analyses of presolar graphite grains from Orgueil. Ph.D. Thesis, pp. 164.

Jäger C., Molster F. J., Dorschner J., Henning Th., Mutschke H., and Waters L. B. F. M. (1998) Steps toward interstellar silicate mineralogy. IV. The crystalline revolution. *Astronomy and Astrophysics* **339**, 904-916.

Jones R. H. and Rubie D. C. (1991) Thermal histories of CO3 chondrites - Application of olivine diffusion modeling to parent body metamorphism. *Earth and Planetary Science Letters* **106**, 73-86.

José J. and Hernanz M. (1998) Nucleosynthesis in Classical Novae: CO versus ONe White Dwarfs. *The Astrophysical Journal* **494**, 680-690.

José J., Hernanz M., Amari S., Lodders K., and Zinner E. (2004) The imprint of nova nucleosynthesis in presolar grains. *The Astrophysical Journal* **612**, 414-428.

José J. and Hernanz M. (2007) The origin of presolar nova grains. *Meteoritics and*

Planetary Science **42**, 1135-1143.

Keller L. P., Messenger S., Flynn G. J., Clemett S., Wirick S., and Jacobsen C. (2004) The nature of molecular cloud material in interplanetary dust. *Geochimica et Cosmochimica Acta* **68**, 2577-2589.

Kemper F., Waters L. B. F. M., Koter A. de, and Tielens A. G. G. M. (2001) Crystallinity versus mass-loss rate in asymptotic giant branch stars. *Astronomy and Astrophysics* **369**, 132-141.

Kovetz A. and Prialnik D. (1997) The composition of nova ejecta from multicycle evolution models. *The Astrophysical Journal* **477**, 356-367.

Kozasa T. and Sogawa H. (1997) Formation of Al_2O_3 grains and the 13 μm feature in circumstellar envelopes of oxygen-rich AGB stars. *Astrophysics and Space Science* **255**, 437-443.

Krot A. N., Scott E. R. D., and Zolensky M. E. (1995) Mineralogical and chemical modification of components in CV3 chondrites: Nebular or asteroidal processing? *Meteoritics* **30**, 748-775.

Langer W. D., Graedel T. E., Frerking M. A., and Armentrout P. B. (1984) Carbon and oxygen isotope fractionation in dense interstellar clouds. *The Astrophysical Journal* **277**, 581-590.

Lattimer J. M. and Grossman L. (1978) Chemical condensation sequences in supernova ejecta. *Moon and Planets* **19**, 169-184.

Leitner J., Hoppe P., Vollmer C., and Zipfel J. (2010) The inventory of presolar grains in primitive meteorites: A NanoSIMS study of C-, N-, and O-isotopes in NWA 852. Nuclei in the Cosmos Symposium XI, POS_NIC XI 144.

Lodders K. and Fegley B. (1999) Condensation chemistry of circumstellar grains. In: Asymptotic Giant Branch Stars (eds. T. Le Bertre, A. Lebre and C. Waelkens), IAU Symposium No. 191. Astronomical Society of the Pacific, San Francisco, CA, pp. 279-289.

Marhas K. K., Amari S., Gyngard F., Zinner E., and Gallino R. (2008) Iron and Nickel isotopic ratios in presolar SiC grains. *The Astrophysical Journal* **689**, 622-645.

Marty B., Zimmermann L., Burnard P. G., Wieler R., Heber V. S., Burnett D. L., Wiens R. C., and Bochsler P. (2010) Nitrogen isotopes in the recent solar wind from the analysis of Genesis targets: Evidence for large scale isotope heterogeneity in the early solar system. *Geochimica et Cosmochimica Acta* **74**, 340-355.

Melis C., Gielen C., Chen C. H., Rhee J. H., Song I., Zuckerman B. (2010) Shocks and a giant planet in the disk orbiting BP Piscium? *The Astrophysical Journal* **724**, 470-479.

Messenger S. (2000) Identification of molecular-cloud material in interplanetary dust particles. *Nature* **404**, 968-971.

Messenger S., Keller L. P., Stadermann F. J., Walker R. M., and Zinner E. (2003)

Samples of stars beyond the solar system: Silicate grains in interplanetary

dust. *Science* **300**, 105-108.

Messenger S., Keller L. P., and Lauretta D. S. (2005) Supernova olivine from cometary dust. *Science* **309**, 737-741.

Messenger S., Nakamura-Messenger K., and Keller L. P. (2008) ^{15}N-rich Organic Globules in a Cluster IDP and the Bells CM2 Chondrite. *Lunar and Planetary Science Conference* 39, Abstract #2391.

Min M., Waters L. B. F. M., de Koter A., Hovenier J. W., Keller L. P., and Markwick-Kemper F. (2007) The shape and composition of interstellar silicate grains. *Astronomy and Astrophysics* **462**, 667-676.

Molster F. J., Yamamura I., Waters L. B. F., Nyman L.-Å., Käufl H.-U., de Jong T., and Loup C. (2001a) IRAS 09425-6040: A carbon star surrounded by highly crystalline silicate dust. *Astronomy and Astrophysics* **366**, 923-929.

Molster F. J., Lim T. L., Sylvester R. J., Waters L. B. F. M., Barlow M. J., Beintema D. A., Cohen M., Cox P., and Schmitt B. (2001b) The complete ISO spectrum of NGC 6302. *Astronomy and Astrophysics* **372**, 165-172.

Molster F. J., Waters L. B. F. M., Tielens A. G. G. M., Koike C., and Chihara H. (2002) Crystalline silicate dust around evolved stars. III. A correlations study of crystalline silicate features. *Astronomy and Astrophysics* **382**, 241-255.

Molster F. J. and Waters L. B. F. M. (2003) The mineralogy of interstellar and circumstellar dust. *SPICA Workshop* **609**, 121-170.

Mostefaoui S. and Hoppe P. (2004) Discovery of abundant in situ silicate and spinel grains from Red giant stars in a primitive meteorite. *The Astrophysical Journal* **613**, L149-L152.

Nagahara H.and Ozawa K. (2009) Condensation kinetics of forsterite and metal and chemical fractionation in the proto solar nebula. Lunar and Planetary Science Conference 40, Abstract #2158.

Nagashima K., Sakamoto N., and Yurimoto H. (2005) Destruction of presolar silicates by aqueous alteration observed in Murchison CM2 chondrite. *Lunar and Planetary Science Conference* 36, Abstract #1671.

Nakamura-Messenger K., Messenger S., Keller L. P., Clemett S. J., and Zolensky M. E. (2006) Organic globules in the Tagish Lake meteorite: Remnants of the protosolar disk. *Science* **314**, 1439-1442.

Nguyen A. N. and Zinner E. (2004) Discovery of ancient silicate stardust in a meteorite. *Science* **303**, 1496-1499.

Nguyen A. N., Stadermann F. J., Zinner E., Stroud R. M., Alexander C. M. O'D., and Nittler L. R. (2007) Characterization of presolar silicate and oxide grains in primitive carbonaceous Chondrites. *The Astrophysical Journal* **656**, 1223-1240.

Nguyen A. N., Nittler L. R., Stadermann F. J., Stroud R. M., and Alexander C. M. O'D. (2010a) Coordinated analyses of presolar grains in the Allan Hills 77307 and Queen Elizabeth Range 99177 meteorites. *The Astrophysical Journal* **719**, 166-189.

Nguyen A. N., Keller L. P., Rahman Z., and Messenger S. (2010b) Microstructure of a supernova silicate grain. *Meteoritics and Planetary Science Supplement* 45, A5423.

Niyogi S. G. and Speck A. K. (2010) A Temporal study of O-rich pulsating variable AGB Star, T Cep: Investigation on dust formation, mineralogy and morphology of Dust Grains. *American Astronomical Society Meeting* 42, Abstract #215.

Nittler L. R., Alexander C. M. O'D., Gao X., Walker R. M., and Zinner E. (1994) Interstellar oxide grains from the Tieschitz ordinary chondrite. *Nature* **370**, 443-446.

Nittler L. R., Alexander C. M. O'D., Gao X., Walker R. M., and Zinner E. (1997a) Stellar sapphires: the properties and origins of presolar Al_2O_3 in meteorites. *The Astrophysical Journal* **483**, 475-495.

Nittler L. R., Alexander C. M. O'D., Gao X., Walker R. M., and Zinner E. (1997b) Presolar Al_2O_3 grains as probes of stellar nucleosynthesis and galactic chemical evolution. *Nuclear Physics* **A621**, 113c-116c.

Nittler L. R., Alexander C. M. O'D., Gallino R., Hoppe P., Nguyen A. N., Stadermann F. J., and Zinner E. K. (2008) Aluminum-, Calcium- and Titanium-rich oxide stardust in ordinary chondrite meteorites. *The Astrophysical Journal* **682**, 1450-1478.

Nollett K. M., Busso M., and Wasserburg G. J. (2003) Cool bottom processes on the thermally pulsing asymptotic giant branch and the isotopic composition of circumstellar dust grains. *The Astrophysical Journal* **582**, 1036-1058.

Posch Th., Kerschbaum F., Mutschke H., Fabian D., Dorschner J., and Hron J. (1999) On

the origin of the 13 μm feature. A study of ISO-SWS spectra of oxygen-rich AGB stars. *Astronomy and Astrophysics* **352**, 609-618.

Posch Th., Kerschbaum F., Fabian D., Mutschke H., Dorschner J., Tamanai A., and Henning Th. (2003) Infrared properties of solid Titanium Oxides: Exploring potential primary dust condensates. *The Astrophysical Journal Supplement Series* **149**, 437-445.

Rauscher T., Heger A, Hoffman R. D., and Woosley S. E. (2002) Nucleosynthesis in massive stars with improved nuclear and stellar physics. *The Astrophysical Journal* **576**, 323-348.

Rietmeijer F. J. M., Pun A., and Nuth J. A. (2009) Dust formation and evolution in a Ca-Fe-SiO-H_2-O_2 vapour phase condensation experiment and astronomical implications. *Monthly Notices of the Royal Astronomical Society* **396**, 402-408.

Rodgers S. D. and Charnley S. B. (2008) Nitrogen superfractionation in dense cloud cores. *Monthly Notices of the Royal Astronomical Society Letters* **385**, L48-L52.

Sandford, S. A., Bernstein, M. P., and Dworkin, J. P. (2001) Assessment of the interstellar proceses leading to deuterium enrichment in meteoritic organics. *Meteoritics and Planetary Science* **36**, 1117-1133.

Scott E. R. D. and Jones R. H. (1990) Disentangling nebular and asteroidal features of CO3 carbonaceous chondrite meteorites. *Geochimica et Cosmochimica Acta* **54**, 2485-2502.

Scott E. R. D. and Krot A. N. (2005) Thermal processing of silicate dust in the solar nebula: Clues from primitive chondrite matrices. *The Astrophysical Journal* **623**, 571-578.

Sears D. W. G., Batchelor J. D., Lu J., and Keck B. D. (1991) Metamorphism of CO and CO-like chondrites and comparisons with type 3 ordinary chondrites. *Proceedings of NIPR Symposium on Antarctic Meteorites* 4, 319-343.

Sloan G. C., Levan P. D., and Little-Marenin I. R. (1996) Sources of the 13 micron feature associated with oxygen-rich circumstellar dust. *The Astrophysical Journal* **463**, 310-319.

Sloan G. C. and Price S. D. (1998) The infrared spectral classification of oxygen-rich dust shells. *The Astrophysical Journal Supplement Series* **119**, 141-158.

Sloan G. C., Kraemer K. E., Goebel J. H., and Price S. D. (2003) Guilt by association: The 13 micron dust emission feature and its correlation to other gas and dust features. *The Astrophysical Journal* **594**, 483.

Speck A. K., Barlow M. J., Sylvester R. J., and Hofmeister A. M. (2000) Dust features in the 10-μm infrared spectra of oxygen-rich evolved stars. *Astronomy and Astrophysics Supplement Series* **146**, 437-464.

Stadermann F. J., Walker R. M., and Zinner E. (1989) Ion microprobe measurements of nitrogen and carbon isotopic variations in individual IDPs. *Meteoritics* **24**, 327.

Stadermann F. J., Croat T. K., Bernatowicz T. J., Amari S., Messenger S., Walker R. M.,

and Zinner E. (2005) Supernova graphite in the NanoSIMS: Carbon, oxygen and titanium isotopic compositions of a spherule and its TiC sub-components. *Geochimica et Cosmochimica Acta* **69**, 177-188.

Stadermann F. J., Floss C., Bose M., and Lea A. S. (2009) The use of Auger spectroscopy for the in situ elemental characterization of sub-micrometer presolar grains. *Meteoritics and Planetary Science* **44**, 1033-1049.

Starrfield S., Gehrz R. D., and Truran J. W. (1997) Dust formation and nucleosynthesis in the nova outburst. In: Astrophysical implications of the laboratory study of presolar materials. *AIP Conference Proceedings* **402**, 203-234.

Stroud R. M., Nguyen A. N., Alexander C. M. O'D., Nittler L. R., and Stadermann F. J. (2008) Transmission electron microscopy of in situ presolar silicates in Alan Hills 77307. *Meteoritics and Planetary Science Supplement* 43, A148.

Terzieva R. and Herbst E. (2000) The possibility of nitrogen isotopic fractionation in interstellar clouds. *Monthly Notices of the Royal Astronomical Society* **317**, 563-568.

Tielens A. G. G. M., Waters L. B. F. M., Molster F. J., and Justtanont K. (1998) Circumstellar silicate mineralogy. *Astrophysics and Space Science* **255**, 415-426.

Todini P. and Ferrara A. (2008) Dust formation in primordial type II supernovae. *Monthly Notices of the Royal Astronomical Society* **325**, 726-736.

Vollmer C., Hoppe P., Brenker F. E., and Holzapfel C. (2007) Stellar $MgSiO_3$ perovskite: A shock-transformed stardust silicate found in a meteorite. *The Astrophysical*

Journal **666**, L49-L52.

Vollmer C., Hoppe P., and Brenker F. E. (2008) Si isotopic compositions of presolar silicate grains from red giant stars and supernovae. *The Astrophysical Journal* **684**, 611-617.

Vollmer C., Hoppe P., Stadermann F. J., Floss C., and Brenker F. E. (2009a) NanoSIMS analysis and Auger electron spectroscopy of silicate and oxide stardust from the carbonaceous chondrite Acfer 094. *Geochimica et Cosmochimica Acta* **73**, 7127-7149.

Vollmer C., Brenker F. E., Hoppe P., and Stroud R. M. (2009b) Direct laboratory analysis of silicate stardust from red giant stars. *The Astrophysical Journal* **700**, 774-782.

Vollmer C. and Hoppe P. (2010) First Fe isotopic measurement of a highly ^{17}O-enriched stardust. *Lunar and Planetary Science Conference* 41, Abstract #1200.

Wasserburg G. J., Boothroyd A. I., and Sackmann I. J. (1995) Deep circulation in red giant stars: a solution to the carbon and oxygen isotope puzzles? *The Astrophysical Journal* **447**, L37-L40.

Waters L. B. F. M., Molster F. J., de Jong T., Beintema D. A., Waelkens C., A. C. A. Boogert, Boxhoorn D. R. et al. (1996) Mineralogy of oxygen-rich dust shells. *Astronomy and Astrophysics* **315**, L361-L364.

Weisberg M. K. and Prinz M. (1998) Sahara 97096: A highly primitive EH3 chondrite

with layered sulfide-metal-rich chondrules. *Lunar and Planetary Science Conference* 24, Abstract #1741.

Woosley S. E. and Weaver T. A. (1995) The evolution and explosion of massive stars. II. Explosive hydrodynamics and nucleosynthesis. *The Astrophysical Journal Supplement* **101**, 181-235.

Zega T. J., Nittler L. R., Busemann H., Hoppe P., and Stroud R. M. (2007) Coordinated isotopic and mineralogic analyses of planetary materials enabled by in situ lift-out with a focused ion beam scanning electron microscope. *Meteoritics and Planetary Science* **42**, 1373-1386.

Zega T. J., Alexander C. M. O'D., Busemann H., Nittler L. R., Hoppe P., Stroud R. M., and Young A. F. (2010) Mineral associations and character of isotopically anomalous organic material in the Tagish lake carbonaceous chondrite. *Geochimica et Cosmochimica Acta* **74**, 5966-5984.

Zhao X., Stadermann F. J., Floss C., Bose M., and Lin Y. (2010a) Characterization of presolar grains from the carbonaceous chondrite Ningqiang. *Lunar and Planetary Science Conference* 41, Abstract #1431.

Zinner E., Amari S., Guiness R., Nguyen A. N., Stadermann F. J., Walker R. M., and Lewis R. S. (2003) Presolar spinel grains from the Murray and Murchison carbonaceous chondrites. *Geochimica et Cosmochimica Acta* **67**, 5083-5095.

Zinner E., Amari S., Guinness R., Jennings C., Mertz A. F., Nguyen A. N., Gallino R.,

Hoppe P., Lugaro M., Nittler L. R., and Lewis R. S. (2007a) NanoSIMS isotopic analysis of small presolar grains: Search for Si_3N_4 grains from AGB stars, and Al and Ti isotopic compositions of rare presolar SiC grains. *Geochimica et Cosmochimica Acta* **71**, 4786-4813.

Zinner E. (2007b) Presolar Grains. In: Treatise on Geochemistry Update 1 (eds. H. D. Holland and K. K. Turekian; vol. ed. A. M. Davis). Elsevier Ltd., Oxford, Online update only. Vol. 1.02 pp. 1-33.

CHAPTER 6

FUTURE WORK

My research work discussed in chapters 3, 4, and 5 has resulted in the identification and characterization of a large inventory of presolar silicate grains. This laboratory study has been possible due to the advent of powerful instrumentation, such as the NanoSIMS and the Auger Nanoprobe. A few outstanding questions in cosmochemistry that are closely associated with presolar silicate grain research are enumerated below.

6.1. Nucleosynthesis

Multi-element isotopic analyses of individual presolar silicate grains are the first step towards understanding the origins of the grains via different nucleosynthetic channels. Numerous isotopic measurements are needed because isotopes of more than three elements are relatively hard to measure in the *same* silicate grain. This is due to the small sizes (< 300 nm) of most silicate grains.

Isotopic dilution is a major concern for measurements of sub-micrometer grains (e.g., Nguyen et al. 2007). It occurs because the presolar silicate grains are surrounded by solar system silicate grains, and the size of the primary ion beam that is used to acquire data is comparable to or larger than the size of the presolar grains. This is particularly true for the O^- primary beam, which is at least about 200 nm in size. However, recently Nguyen et al. (2010) have come up with a solution to this problem. According to this novel method, grains surrounding the presolar silicate grains are sputtered away, and as a result the isotopic dilution problem is mitigated during subsequent isotopic measurements. This

method can be extremely useful in acquiring measurements of isotopes in the NanoSIMS that require an O^- beam, e.g., Mg and Fe isotopes.

Our quest to learn more about the nucleosynthetic processes had led to the development of new, innovative techniques to acquire additional information from the *same* presolar grains. An example is Resonance Ionization Mass Spectrometry (RIMS) used in our area of research, which is capable of acquiring isotopic compositions of heavy elements such as Mo and Ba. The main advantage of the RIMS instrument over secondary ion mass spectrometers is the complete elimination of isobaric interferences (Savina et al. 2003a). This is possible because tunable lasers only ionize atoms of a given element. Resonance Ionization Mass Spectrometry has been successfully applied to acquire the isotopic compositions of s-process elements such as Ba in individual SiC grains (e.g., Savina et al. 2003b, 2004), and can also be applied to study presolar silicate grains. Such a study can provide a clearer picture of stellar evolution for the following reason: It has been well established now that Red Giant stars and Asymptotic Giant Branch stars are O-rich and begin to evolve into C-rich stars, after the commencement of repeated third dredge-up (TDU) episodes. Silicate and oxide grains form during the O-rich phase of a star, while the carbonaceous grains form when C > O. Therefore, measurement of the isotopes of heavy elements in silicate (and oxide) grains will tell us the initial isotopic abundances of the heavy elements, possibly prior to TDU episodes. For example, large anomalies are predicted in ^{58}Fe (Davis et al. 2009); measurement of this isotope of Fe in numerous silicate and carbonaceous grains will allow us to constrain and compare the initial isotopic ratio of the parent stars before they experienced TDU episodes.

Comparison of the initial abundance of s-process elements in stars to the subsequent changes by TDU episodes may allow us to explore more deeply the processes occurring in the interior of an evolved star. Predicted isotopic compositions of s-process elements based on the nucleosynthetic models have been compared to the measured grain data in a small number of cases (e.g., Savina 2003b; Barzyk et al. 2006). Production of s-process nuclides occurs in the H-He intershell in low-mass AGB stars, via the ^{13}C and ^{22}Ne neutron sources. Furthermore, changes in the composition of the s-process nuclides with a change in metallicity are also predicted. For example, large ^{87}Sr depletions (of ~350‰) and $\delta^{88}Sr$ excesses are predicted to occur as the metallicity of the star goes from solar value i.e., 0.02 to 1/6th the solar value (e.g., Davis et al. 2003). Similarly, Davis et al. (2003) predicts that at low metallicity large $^{91,92,96}Zr$ excesses should occur. Therefore, measurements of s-process elements in presolar oxides and the comparison to carbonaceous phases may allow us to understand the evolution of a star from an O-rich phase to a C-rich phase.

6.2. Stellar Environment

Microstructural analyses of a small pool of silicate grains show that many are polycrystalline aggregates of small 50–100 nm sub-grains (e.g., Vollmer et al. 2009a; chapter 5). Transmission electron microscopy has been done to date on very few (~15) silicate grains and many more studies are required. In addition, the aggregates exhibit the same O isotopic compositions but show chemical and structural inhomogeneities (e.g., Vollmer et al. 2009b). These internal inhomogeneities most likely reflect differing growth conditions in a stellar environment; the specific conditions under which such inhomogeneities occur need to be investigated. In fact, various lines of evidence show

that thermodynamic equilibrium is not maintained in stellar outflows and therefore kinetic models of grain nucleation, growth, and survival may be required to explain the microstructures observed in silicate grains (e.g., Gail 2003). Similar studies on presolar graphite grains have been done where microstructural data was used to constrain the circumstellar condensation temperature and pressure ranges (e.g., Bernatowicz et al. 1996).

6.3. Galactic Chemical Evolution

The idea that the isotopic compositions of dust grains evolve over time has been speculated for a long time. Alexander and Nittler (1999) demonstrated that isotopes of Si and Ti bear signatures of the original composition of the parent stars and s-process nucleosynthesis in stars. However, the contribution of s-process nucleosynthesis in Si and Ti is small. Therefore, these elements primarily retain information about the initial compositions of the parent stars. Information about the O-rich parent stars can be gathered from the acquisition of Si and Ti isotopic data from presolar silicate grains. Furthermore, comparing the Ti and Si isotopic compositions of silicates with oxide and carbonaceous phases may elucidate the role of the various processes that occur during the conversion from O-rich to C-rich stars. In order to understand the kind of differences that might be expected, the case for Ti isotopes is stated here. Among the five isotopes of Ti, only ^{50}Ti is predicted to show a large excess relative to ^{48}Ti following third dredge-up. Titanium-50 anomalies observed in a limited set of presolar oxide grains are small or absent (Nittler et al. 2008). The stellar sources of ^{50}Ti excesses are low-mass O-rich AGB stars in which material from the inner He shell has not been dredged up (Nittler et al. 2008). On the other hand, SiC Z grains that exhibit $^{12}C/^{13}C < 100$ and large $^{30}Si/^{28}Si$

ratios show ^{50}Ti excesses; the neutrons from the ^{13}C source have affected the ^{50}Ti/^{48}Ti isotopic ratio in SiC grains (Zinner et al. 2007). These data provide information about the mass of the ^{13}C pocket and the AGB star as well as the initial isotopic ratios of the grains' parent stars prior to AGB nucleosynthesis. Therefore, Si and Ti isotopic measurements on many silicate and oxide grains are required.

6.4. Distribution and Processing of Presolar Dust

Prior to solar system formation, the material from different stars was strewn in the solar nebula. The initial distributions of the presolar material are under a lot of conjecture. We have observed that the distribution of presolar grains within the matrix of primitive meteorites is not always uniform within the areas analyzed (e.g., Floss and Stadermann 2009). The distribution of presolar silicate grains identified *in situ* in meteorites may reflect both the way in which our solar system sampled material from other stars or give us clues to the redistribution of the presolar material in the solar nebula through nebular mixing or outflow activities. The presolar grain distribution is also affected by secondary alteration processes that may have occurred either in the nebula and/or in the parent bodies; certain areas on the meteoritic matrices may be more altered than the others.

Silicates are a less resilient phase than presolar SiC and yet they have survived the numerous destructive conditions around stars, in the interstellar medium, and subsequently in the solar nebula. Presolar grains have been preserved in different classes of meteorites to different degrees. In spite of all the extensive processing mechanisms in play, most presolar silicate grains are largely intact with no shattering visible on their surfaces. However, chemical compositions of grains can be altered by sputtering in the

interstellar medium (ISM). For example, Si and Mg can be preferentially removed from the silicate grains (Jones 2000) and can result in more Fe-rich silicate grains. In addition, irradiation in the ISM can transform olivine into pyroxene grains (Demyk et al. 2001). A comparison of the presolar dust in a large inventory of meteorites belonging to different classes can provide information about the variations in the presolar grain abundances in different parts of the solar nebula where the meteorite parent bodies formed and evolved. Studying meteorites belonging to different petrographic types will also elucidate the role of secondary processing in the parent body. Presolar silicate grain surveys in all classes of meteorites are therefore needed.

On a completely different note, the abundance of presolar silicate grains is much higher in IDPs (Floss et al. 2006; Busemann et al. 2009) than in meteorites (Nguyen et al. 2007, 2010; Floss and Stadermann 2009; Vollmer et al. 2009b). Comets that reside in the outer solar system are the likely parent bodies of interplanetary dust particles (IDPs). Although, the total area measured in IDPs so far is much smaller than in meteorites, the possibility that early solar system processes primarily affected stellar material in the inner solar system (e.g., Williams et al. 1985; Rubin et al. 2007) may be the reason for the high abundance of silicate grains in IDPs. Assuming that the distribution of presolar silicate grains was homogeneous, the abundances in IDPs are higher than those even in the least equilibrated meteorites (Floss and Stadermann 2009). Identification and characterization of silicate grains in IDPs is required to check if the distribution of presolar materials in comets is different than in meteorites.

Both silicates and organic matter are present in the matrices of meteorites, and therefore, understanding the temperature ranges that organic material can withstand or the

degree of aqueous alteration at those temperatures can provide us additional clues as to how presolar silicate grains may have been affected. Laboratory experiments that look at how water and heat affect silicate grains grains need to be conducted. Optical constants from a wide range of amorphous and crystalline silicate materials are also needed to constrain the dust species that are indicated by astronomical spectra.

6.5. Conclusions

More than two decades after presolar grains were first discovered, we are still asking questions about how they formed and survived the hostile conditions they encountered prior and subsequent to their incorporation into meteorites. We hope to address at least some of these aforementioned questions in the future, in order to have a complete picture of the life history of presolar materials in different classes of meteorites.

References

Alexander C. M. O'D. and Nittler L. R. (1999) The galactic evolution of Si, Ti and O isotopic ratios. *The Astrophysical Journal* **519**, 222-235.

Barzyk J. G., Savina M. R., Davis A. M., Gallino R., Pellin M. J., Lewis R. S., Amari S., and Clayton R. N. (2006) Multi-element isotopic analysis of single presolar SiC grains. *New Astronomy Reviews* **50**, 587-590.

Bernatowicz T. J., Cowsik R., Gibbons P. C., Lodders K., Fegley B., Jr., Amari S., and Lewis R. S. (1996) Constraints on stellar grain formation from presolar graphite in the Murchison meteorite. *The Astrophysical Journal* **472**, 760-782.

Busemann H., Nguyen A. N., Cody G. D., Hoppe P., Kilcoyne A. L. D., Stroud R. M., Zega T. J., Nittler L. R. (2009) Ultra-primitive interplanetary dust particles from the

comet 26P/Grigg-Skjellerup dust stream collection. *Earth and Planetary Science Letters* 288, 44-57.

Davis A. M., Gallino R., Straniero O., Domínguez I., and Lugaro M. (2003) Heavy Element Nucleosynthesis in Low Metallicity, Low Mass AGB Stars. *Lunar and Planetary Science Conference* 33, Abstract #2043.

Davis A. M., Gallino R., Cristallo S., and Straniero O. (2009) Asymptotic Giant Branch Stars and Their Influence on the Isotopic Compositions of the Transition Elements. *Lunar and Planetary Science Conference* 40, Abstract #5402.

Demyk K., Carrez Ph., Leroux H., Cordier P. Jones A. P., Borg J., Quirico E., Raynal P. I., and d'Hendecourt L. (2001) Structural and chemical alteration of crystalline olivine under low energy He^+ irradiation. *Astronomy and Astrophysics* **368**, L38-L41.

Floss C., Stadermann F. J., Bradley J. P., Dai Z. R., Bajt S., Graham G., and Lea A. S. (2006) Identification of isotopically primitive interplanetary dust particles: a NanoSIMS isotopic imaging study. *Geochimica et Cosmochimica Acta* **70**, 2371-2399.

Floss C. and Stadermann F. J. (2009) Auger Nanoprobe analysis of presolar ferromagnesian silicate grains from primitive CR chondrites QUE 99177 and MET 00426. *Geochimica et Cosmochimica Acta* **73**, 2415-2440.

Gail H.-P. (2003) Formation and evolution of minerals. In: Astromineralogy (ed. T. Henning). Springer-Verlag, Berlin, pp. 55-120.

Jones A. P. (2000) Depletion patterns and dust evolution in the interstellar medium. *Journal of Geophysical Research* **105**, 10257-10268.

Nguyen A. N., Stadermann F. J., Zinner E., Stroud R. M., Alexander C. M. O'D., and

Nittler L. R. (2007) Characterization of presolar silicate and oxide grains in primitive carbonaceous chondrites. *The Astrophysical Journal* **656**, 1223-1240.

Nguyen A. N., Messenger S., Ito M., and Rahman Z. (2010) Mg isotopic measurement of FIB-isolated presolar silicate grains. *Lunar and Planetary Science Conference* 41, Abstract #2413.

Nittler L. R., Alexander C. M. O'D., Gallino R., Hoppe P., Nguyen A. N., Stadermann F. J., and Zinner E. K. (2008) Aluminum-, calcium- and titanium-rich oxide stardust in ordinary chondrite meteorites. *The Astrophysical Journal* **686**, 1524-1524.

Rubin A. E., J. M. Trigo-Rodríguez, H. Huber, and J. T. Wasson (2007) Progressive aqueous alteration of CM carbonaceous chondrites. *Geochimica et Cosmochimica Acta* **71**, 2361-2382.

Savina M. R., Pellin M. J., Tripa C. E., Veryovkin I. V., Calaway W. F., and Davis A. M. (2003a) Analyzing individual presolar grains with CHARISMA. *Geochimica et Cosmochimica Acta* **67**, 3215-3225.

Savina M. R., Davis A. M., Tripa C. E., Pellin M. J., Clayton R. N., Lewis R. S., Amari S., Gallino R., and Lugaro M (2003b) Barium isotopes in individual presolar silicon carbide grains from the Murchison meteorite. *Geochimica et Cosmochimica Acta* **67**, 3201-3214.

Savina M. R., Davis A. M., Tripa C. E., Pellin M. J., Gallino R., Lewis R. S., and Amari S. (2004) Extinct technetium in silicon carbide stardust grains: Implications for stellar nucleosynthesis. *Science* **303**, 649-652.

Vollmer C., Brenker F. E., Hoppe P., and Stroud R. M. (2009a) Direct laboratory analysis of silicate stardust from Red Giant stars. *The Astrophysical Journal* **700**, 774-782.

Vollmer C., Hoppe P., Stadermann F. J., Floss C., and Brenker F. E. (2009b) NanoSIMS analysis and Auger electron microscopy of silicate and oxide stardust from the carbonaceous chondrite Acfer 094. *Geochimica et Cosmochimica Acta* **73**, 7127-7149.

Williams C. V., Rubin A. E., Keil K., and San M. A. (1985) Petrology of the Cangas de Onis and Nulles regolith breccias: Implications for parent body history. *Meteoritics* **20**, 331-345.

Zinner E., Amari S., Guinness R., Jennings C., Mertz A. F., Nguyen A. N., Gallino R., Hoppe P., Lugaro M., Nittler L. R., and Lewis R. S. (2007) NanoSIMS isotopic analysis of small presolar grains: Search for Si_3N_4 grains from AGB stars and Al and Ti isotopic compositions of rare presolar SiC grains. *Geochimica et Cosmochimica Acta* **71**, 4786-4813.

Appendix

Table A2.1(a): Electron probe data for olivine standards from Hofmeister and Pitman (2007)

	Fosterite Alice Springs Meteorite	**Olivine Susimaki Finland**	**Olivine Kiglapait Labrador***
SiO_2	37.24	35.31	35.61
TiO_2	-	-	-
Al_2O_3	-	-	-
Cr_2O_3	-	-	-
Fe_2O_3	-	1.70	-
FeO	16.92	36.91	37.66
MnO	-	0.53	-
MgO	43.88	25.55	26.68
CaO	1.26	-	0.07
Na_2O	-	-	-
K_2O	-	-	-
Total	99.30	100.00	100.02
Empirical formula	Fo_{82}	Fo_{54}	$Fo_{14}Te_2$

Table A2.1 (b): Electron probe data for pyroxene standards from Hofmeister and Pitman (2007)

	Hedenbergite Iona island Rockland NY	**Pyroxene Burgess Ontario**	**Augite Vesuvius Italy**	**Fassaite Helena MT**	**Diopside Dekalb NY**	**Dymek Ortho-pyroxene**
SiO_2	48	49.22	46.49	41.36	56.03	56.46
TiO_2	-	0.43	1.28	0.76	0.02	0.08
Al_2O_3	0.5	5.9	7.37	15.75	0.37	3.2
Cr_2O_3	-	0.01	0.02	-	0.08	0.02
Fe_2O_3	2	-	-	6.1	-	-
FeO	23	2.39	7.76	0.24	1.02	4.96
MnO	1	0.04	0.15	0.03	0.03	0.03
MgO	2	15.37	12.36	10.34	17.66	35.42
CaO	21	25.65	22.90	25.27	25.97	0.1
Na_2O	-	-	0.30	0.06	0.41	0.01
K_2O	-	0.01	-	0.03	-	-
Total	97.5	99.02	98.63	99.94	101.59	100.28
Empirical formula	$Dp_{13}Hd_{87}$	$En_{44}Fs_4Wo_{52}$	$En_{37}Fs_{13}Wo_{50}$	$En_{33}Fs_{10}Wo_{57}$	$Dp_{97}Hd_3$	

Note: Composition of Olivine Kiglapait Labrador* listed here was obtained using the Scanning Electron Microscope because the sample was found to be contaminated, subsequent to Auger Nanoprobe analysis.

Table A2.2: Sensitivity Factors for Quantification of Auger Spectra (Stadermann et al. 2009)

Element	Auger Transition	Energy (eV)	Sensitivity factor	Uncertainty (% rel.)
O	KLL	510	0.194	3.6
Mg	KLL	1188	0.234	9.4
Al	KLL	1396	0.160	24.9
Si	KLL	1621	0.121	11.0
Ca	LMM	297	0.626	10.8
Fe	LMM	654	0.150	11.2

Table A3.1: Oxygen and Silicon Isotopic Ratios and Grain Sizes of Presolar Silicate and Oxide Grains in Acfer 094

Grain	Size (nm^2)	$^{17}O/^{16}O$ ($\times10^{-4}$)	$^{18}O/^{16}O$ ($\times10^{-3}$)	$\delta^{29}Si$ (‰)	$\delta^{30}Si$ (‰)	Group[†]
Pyroxene-like silicates						
42Ff11O18	340×240	3.76±0.22	2.42±0.05	32±45	-22±55	4
42Ff25O	200×140	6.60±0.34	1.40±0.05	...	...	1
42Fs13	300×200	4.84±0.23	1.21±0.04	...	...	1
42Ft13	180×160	6.20±0.24	1.59±0.04	...	...	1
42Ft14_I	310×150	5.35±0.24	1.98±0.05	...	...	1
42Ft24	290×200	5.63±0.40	2.01±0.08	...	...	1
34C-7*	190×190	8.14±0.53	1.23±0.06	...	...	1
42C-7*	190×155	8.80±0.46	1.76±0.06	...	...	1
42Fe8O18*	220×160	5.68±0.51	1.30±0.07	...	...	1
42Ff2*	200×200	4.92±0.37	2.00±0.07	...	...	1
42Ff12*	330×200	8.51±0.49	2.03±0.07	...	...	1
42Fv114_I*	400×300	7.99±0.16	1.22±0.02	...	...	1
Olivine-like silicates						
42Fc3	290×120	6.16±0.51	1.99±0.09	…	…	1
42Fs8	120×100	7.42±0.05	1.98±0.03	...	...	1
42Fw3	200×120	6.29±0.25	1.85±0.04	...	...	1
42B-11*	150×150	3.61±0.48	2.77±0.13	4±32	28±38	4
42Ft21*	140×100	5.84±0.37	1.95±0.07	…	…	1
42Fu5*	270×180	5.63±0.36	1.60±0.06	…	…	1

Table A3.1 cont'd.

Grain	Size (nm^2)	$^{17}O/^{16}O$ ($\times10^{-4}$)	$^{18}O/^{16}O$ ($\times10^{-3}$)	$\delta^{29}Si$ (‰)	$\delta^{30}Si$ (‰)	Group[†]
Intermediate silicates						
34C-5	190×270	7.38±0.45	1.68±0.07	…	…	1
42B-1	150×190	8.94±0.47	1.09±0.05	...	...	1
42F-11	230×230	8.07±1.21	2.39±0.22	...	...	1
42Fb2	160×120	6.32±0.36	2.06±0.06	...	...	1
42Fd6	320×160	6.65±0.79	1.84±0.13	...	...	1
42Fe2	200×180	5.96±0.38	2.12±0.07	...	...	1
42Fe5O17	140×140	7.13±0.47	2.01±0.07	...	...	1
42Fe8O17	240×90	27.01±0.95	2.38±0.08	...	...	1
42Fe13	200×140	11.31±0.46	1.96±0.06	...	...	1
42Ff3	250×80	4.97±0.51	1.16±0.07	...	...	1
42Ff5	200×140	4.28±0.27	2.44±0.06	48±46	-10±53	4
42Ff10	200×200	9.39±0.85	1.96±0.12	…	…	1
42Fv115	210×170	4.86±0.21	1.90±0.04	…	…	1
42Fv125_I	300×300	5.27±0.19	2.09±0.04	…	…	1
42Fv125_II	90×60	5.15±0.17	1.97±0.03	…	…	1
42Fw9	310×280	5.16±0.27	1.54±0.05	…	…	1

Table A3.1 cont'd.

Grain	Size (nm^2)	$^{17}O/^{16}O$ ($\times10^{-4}$)	$^{18}O/^{16}O$ ($\times10^{-3}$)	$\delta^{29}Si$ (‰)	$\delta^{30}Si$ (‰)	Group†
Other silicates						
34A-4	390×310	4.15±1.17	3.16±0.34	16±22	64±26	4
34A-6	230×190	5.85±0.33	1.43±0.05	…	…	1
42C-5	230×315	8.82±0.91	1.99±0.13	…	…	1
42F-13	150×150	31.83±1.11	1.68±0.08	…	…	1
42Fe14	220×180	5.73±0.26	1.83±0.04	…	…	1
42Ff16	320×160	5.40±0.29	1.82±0.05	…	…	1
42Fs4_I	360×160	6.40±0.21	1.75±0.03	…	…	1
42Fs4_II	280×210	5.84±0.24	1.97±0.05	…	…	1
42Fu7	400×280	7.92±0.30	1.91±0.05	…	…	1
42Fv113	220×210	5.48±0.30	1.70±0.05	…	…	1
Oxides						
34C-6	150×190	7.39±0.49	2.03±0.08	…	…	1
42Fb3	190×90	6.04±0.44	1.56±0.07	…	…	1
42Ff26	270×120	7.31±0.42	1.98±0.06	…	…	1
42Fs6	200×120	7.09±0.27	1.34±0.04	…	…	1

Notes: † Classification into groups based on Nittler et al. (1997). Errors are 1σ.

Table A3.2: Elemental Compositions of Presolar Silicate and Oxide grains in Acfer 094 along with Mg+Fe(+Ca)/Si ratio and mg#

Grain	Si (at.%)	Al (at.%)	Fe (at.%)	Mg (at.%)	Ca (at.%)	O (at.%)	Ti (at.%)	Mg+Fe(+Ca)/ Si	mg#
Pyroxene-like silicates									
42Ff11O18	21.7±2.4	…	21.5±2.4	…	…	56.8±2.0	…	1.0±0.2	0
42Ff25O	22.2±2.4	…	14.3±1.6	7.6±0.7	…	55.9±2.0	…	1.0±0.1	35
42Fs13	20.3±2.2	…	...	20.8±2.0	…	58.9±2.1	…	1.0±0.1	10
42Ft13	19.1±2.1	…	13.0±1.5	8.7±0.8	…	59.2±2.1	…	1.1±0.2	40
42Ft14_I	17.6±1.9	…	15.9±1.8	5.7±0.5	…	60.8±2.2	…	1.2±0.2	27
42Ft24	22.9±2.5	…	16.3±1.8	6.1±0.6	…	54.7±2.0	…	1.0±0.1	27
34C-7*	26.7±2.9	…	7.9±0.9	17.4±1.6	…	48.0±1.7	…	0.9±0.1	69
42C-7*	30.5±3.4	…	22.1±2.5	12.5±1.2	…	34.9±1.3	…	1.1±0.2	36
42Fe8O18*	24.8±2.7	…	11.9±1.3	14.8±1.4	…	48.5±1.7	…	1.1±0.1	55
42Ff2*	22.9±2.5	…	24.9±2.8	…	…	52.2±1.9	…	1.1±0.2	0
42Ff12*	24.9±2.7	…	13.6±1.5	8.5±0.8	…	53.1±1.9	…	0.9±0.1	38
42Fv114_I*	27.8±3.1	…	14.0±1.6	6.3±0.6	4.5±0.5	47.4±1.7	…	0.9±0.1	31
Olivine-like silicates									
42Fc3	14.3±1.6	...	24.8±2.8	6.1±0.6	...	54.8±2.0	...	2.2±0.3	20
42Fs8	15.5±1.7	...	22.0±2.5	8.2±0.8	...	54.4±2.0	...	1.9±0.3	27
42Fw3	13.7±1.5	...	…	27.0±2.5	...	59.3±2.1	...	2.0±0.3	100
42B-11*	22.0±2.4	...	37.8±4.2	14.0±1.3	...	26.2±0.9	...	2.3±0.3	27
42Ft21*	16.6±1.8	...	28.6±3.2	6.1±0.6	...	48.7±1.8	...	2.1±0.3	17
42Fu5*	19.9±2.2	...	24.2±2.7	10.9±1.0	...	44.9±1.6	...	1.8±0.2	31

Table A3.2 cont'd.

Grain	Si (at.%)	Al (at.%)	Fe (at.%)	Mg (at.%)	Ca (at.%)	O (at.%)	Ti (at.%)	Mg+Fe(+Ca)/ Si	mg#
Intermediate silicates									
34C-5	23.8±2.6	...	17.9±2.0	7.4±0.7	5.7±0.6	45.3±1.6	...	1.3±0.2	29
42B-1	23.3±2.6	...	15.4±1.7	16.8±1.6	...	44.5±1.6	...	1.4±0.2	52
42F-11	25.1±2.8	...	29.0±3.2	10.2±1.0	...	35.7±1.3	...	1.6±0.2	26
42Fb2	17.1±1.9	...	24.2±2.7	5.1±0.5	...	53.6±1.9	...	1.7±0.2	17
42Fd6	20.6±2.3	...	21.0±2.4	8.2±0.8	...	50.2±1.8	...	1.4±0.2	28
42Fe2	20.0±2.2	...	19.7±2.2	9.2±0.9	...	51.2±1.8	...	1.4±0.2	32
42Fe5O17	18.8±2.1	...	15.4±1.7	10.7±1.0	1.8±0.2	53.4±1.9	...	1.5±0.2	41
42Fe8O17	18.1±2.0	...	20.5±2.3	6.7±0.6	...	54.7±2.0	...	1.5±0.2	25
42Fe13	17.6±1.9	...	15.7±1.8	13.5±1.3	...	53.2±1.9	...	1.7±0.2	46
42Ff3	17.8±2.0	...	16.9±1.9	8.1±0.8	4.5±0.5	52.7±1.9	...	1.7±0.2	32
42Ff5	16.9±1.9	...	23.4±2.6	…	…	59.6±2.1	...	1.4±0.2	0
42Ff10	20.8±2.3	...	29.8±3.3	…	…	49.4±1.8	...	1.4±0.2	0
42Fv115	18.2±2.0	...	22.2±2.5	…	2.5±0.3	57.2±2.1	...	1.4±0.2	0
42Fv125_I	18.5±2.0	...	19.7±2.2	8.5±0.8	…	53.4±1.9	...	1.5±0.2	30
42Fv125_II	18.9±2.1	...	22.9±2.6	4.5±0.4	…	53.7±1.9	...	1.4±0.2	16
42Fw9	18.4±2.0	...	9.7±1.1	18.0±1.7	…	54.0±1.9	...	1.5±0.2	65

Table A3.2 cont'd.

Grain	Si (at.%)	Al (at.%)	Fe (at.%)	Mg (at.%)	Ca (at.%)	O (at.%)	Ti (at.%)	Mg+Fe(+Ca)/ Si	mg #
Other silicates									
34A-4	12.3±1.3	7.6±1.9	26.2±2.9	7.5±0.7	1.5±0.2	44.9±1.6	…	2.9±0.4	22
34A-6	5.7±0.6	23.2±5.8	16.1±1.8	8.7±0.8	1.2±0.1	45.2±1.6	…	4.6±0.6	35
42C-5	18.1±2.0	…	47.1±5.3	11.3±1.1	…	23.5±0.8	…	3.2±0.5	19
42F-13	5.9±0.6	22.8±5.7	19.4±2.2	4.6±0.4	2.1±0.2	45.3±1.6	…	4.4±0.6	19
42Fe14	29.7±3.3	…	9.3±1.0	6.0±0.6	…	54.9±2.0	…	0.5±0.1	39
42Ff16	10.3±1.1	7.5±1.9	28.3±3.2	3.2±0.3	1.6±0.2	49.1±1.8	…	3.2±0.5	10
42Fs4_I	26.5±2.9	…	11.3±1.3	4.8±0.5	…	57.3±2.1	…	0.6±0.1	30
42Fs4_II	27.0±3.0	…	16.0±1.8	…	…	57.0±2.1	…	0.6±0.1	0
42Fu7	22.7±2.5	…	9.4±1.0	6.1±0.6	3.5±0.4	58.3±2.1	…	0.8±0.1	40
42Fv113	18.8±2.1	19.7±4.9	14.4±1.6	…	…	47.0±1.7	…	0.8±0.1	0
Oxides									
34C-6	…	22.9±5.7	27.0±3.0	8.0±0.8	…	42.2±1.5	…	…	23
42Fb3	…	22.3±5.6	…	13.8±1.3	…	63.9±2.3	…	…	100
42Ff26	…	…	…	…	…	65.8±2.4	34.3±3.4 …	…	…
42Fs6	…	22.7±5.6	13.2±1.5	8.7±0.8	…	55.4±2.0		…	40

Notes: mg# = Mg/(Fe+Mg)×100; Errors are 1σ.

Table A3.3: Mass Boundaries of the Zones and Range of Mass Fraction

Zone	Mass Range ($M_\odot$)	Mix Fraction Range (%)	
		All 5 zones	3 zones
H envelope	4.23–12.61	92.0–99.0	92.0–98.0
He/C	3.05–3.80	1.0–1.9	0.6–3.4
O/C	2.63–3.05	0.8–2.0	0.6–2.7
O/Ne	2.19–2.63		
O/Si	1.92–2.19		

Table A4.1: Oxygen Isotopic Compositions of the Silicate and Oxide Stardust Grains in SAH 97096 and SAH 97159

Grains in	**O-Isotopic ratios**	
SAH 97096	**$^{17}O/^{16}O$ ($\times10^{-4}$)**	**$^{18}O/^{16}O$ ($\times10^{-3}$)**
E5-112	5.8±0.4	1.87±0.08
B2-7	133±1	1.43±0.04
B2-1	3.9±0.2	2.20±0.04
E20-33	6.0±0.6	1.95±0.10
E20-36-tp	7.1±0.9	2.19±0.16
E20-36-bm	6.5±0.7	2.03±0.11
B2-10†	3.9±0.2	2.19±0.04
E20-34†	7.1±0.9	1.77±0.14
SAH 97159	**$^{17}O/^{16}O$ ($\times10^{-4}$)**	**$^{18}O/^{16}O$ ($\times10^{-3}$)**
3_1	4.8±0.2	2.01±0.01
3_4	7.1±0.3	1.47±0.02
3_7	5.6±0.2	1.96±0.01
B-8-1	14.5±0.2	1.64±0.02
B-8-2	6.6±0.2	1.90±0.01
D-1	6.6±0.2	1.98±0.01
D-6	5.5±0.2	1.71±0.01
E-4-2	13.5±0.6	1.87±0.05

Notes: Grains gone after NanoSIMS measurements are marked by †. Errors are 1σ.

Table A5.1: Oxygen Isotopic Compositions of the Presolar Silicate and Oxide Grains in ALHA77307

Grain Name	$^{18}O/^{16}O$ ($\times10^{-3}$)	$^{17}O/^{16}O$ ($\times10^{-4}$)	group	Size (nm^2)
133	0.84±0.01	7.51±0.14	2	560×520
5b-7	1.85±0.03	4.48±0.12	1	360×320
10-4-tp	1.93±0.05	7.84±0.30	1	320×160
11-1-lt	2.05±0.05	12.1±0.4	1	160×160
11-1-rt	2.03±0.03	5.46±0.16	1	320×280
15-5-bm	1.97±0.03	4.70±0.17	1	250×150
18-6	1.97±0.04	4.78±0.17	1	170×170
18-7	1.70±0.03	5.81±0.16	1	320×240
54-1	1.69±0.03	6.12±0.18	1	130×130
48-bm	2.10±0.02	5.27±0.13	1	280×160
1310	1.58±0.02	5.96±0.15	1	330×230
5b-8	2.19±0.03	3.91±0.11	4	480×120
63	2.06±0.03	5.09±0.14	1	320×240
8a-4-bm	1.90±0.04	6.15±0.20	1	400×320
10-4-O18	2.95±0.04	4.45±0.17	4	280×200
114	1.81±0.04	5.01±0.18	1	320×120
116	2.06±0.05	7.27±0.29	1	600×240
12-4	1.84±0.04	9.64±0.28	1	400×240
128	2.19±0.04	3.86±0.15	4	300×300
17b-2	1.85±0.04	5.52±0.23	1	280×160
51-6-O17	1.93±0.04	5.35±0.18	1	270×130
52-15	1.69±0.05	11.2±0.4	1	400×400
53-5	1.99±0.04	4.98±0.18	1	230×200
53-11	1.91±0.04	4.68±0.17	1	300×150
54-9	3.01±0.04	3.55±0.15	4	300×240
111-O	0.92±0.01	8.97±0.16	2	100×100
112	1.68±0.02	5.32±0.11	1	400×320
1-24	2.04±0.03	6.39±0.15	1	320×240
132	1.91±0.03	5.02±0.16	1	400×200
146	1.57±0.02	3.65±0.11	3	520×240
178	2.04±0.04	6.62±0.23	1	160×80
2131	1.93±0.02	7.02±0.15	1	370×320
21422	1.93±0.03	5.77±0.18	1	240×200
2-1425-O2	1.99±0.02	6.19±0.14	1	560×320
32	1.72±0.02	5.25±0.16	1	280×200
42	1.96±0.02	4.91±0.13	1	320×240
44-O	1.61±0.02	7.04±0.18	1	200×200
48-tp	2.04±0.03	5.04±0.15	1	360×280
410	1.78±0.02	4.63±0.14	1	250×230

Table A5.1 cont'd.

Grain Name	$^{18}O/^{16}O$ ($\times10^{-3}$)	$^{17}O/^{16}O$ ($\times10^{-4}$)	Group	Size (nm^2)
7d-2	1.74±0.03	4.89±0.17	1	400×200
8a-3-O17	1.87±0.03	5.60±0.17	1	280×200
107	2.02±0.04	4.87±0.18	1	240×120
113	2.01±0.04	7.29±0.22	1	200×160
13-4	2.00±0.04	5.91±0.19	1	250×150
15-5-tp	1.92±0.04	6.16±0.20	1	200×180
51-7	1.76±0.03	4.98±0.14	1	180×100
51-9	1.89±0.04	12.8±0.35	1	530×250
53-4	2.04±0.04	5.35±0.19	1	160×140
131	1.99±0.03	5.81±0.15	1	250×180
163	1.13±0.02	89.3±0.6	extreme1	320×200
1710	1.86±0.03	4.91±0.18	1	400×240
44-O17	1.99±0.02	5.64±0.15	1	280×240
8a-3-O	0.92±0.02	6.55±0.19	2	480×200
8a-4-tp	2.02±0.04	5.19±0.17	1	360×120
105	1.94±0.04	5.71±0.20	1	160×120
121	1.60±0.03	6.06±0.17	1	280×200
127	1.60±0.03	5.93±0.17	1	400×400
13-5	1.76±0.04	6.15±0.23	1	320×280
51-6-O	1.71±0.03	5.19±0.17	1	320×150
52-8	1.88±0.04	4.74±0.21	1	200×190
53-6	2.02±0.03	5.33±0.16	1	200×100
54-5	1.90±0.03	5.30±0.18	1	200×120
52-4-O17	1.88±0.03	6.5±0.2	1	160×120
10-4-bm	1.61±0.05	10.5±0.36	1	360×280
2132	1.93±0.02	5.89±0.12	1	280×160
21420	1.99±0.03	8.41±0.18	1	140×50
2-1425-O1	2.59±0.03	3.69±0.11	4	380×200
19-1	1.35±0.03	6.41±0.18	1	120×120
16a-3	2.00±0.03	5.06±0.12	1	350×300
33	1.93±0.03	4.65±0.13	1	440×160
52-4-O	1.45±0.04	6.16±0.27	1	210×210
45	2.76±0.03	5.09±0.16	4	320×120
31	1.71±0.04	7.80±0.28	1	320×200
21412	1.49±0.02	6.38±0.14	1	200×140
54-7	2.15±0.02	4.06±0.94	4	180×150
51-1	1.98±0.04	8.16±0.26	1	380×340

Table A5.1 cont'd.

Grain Name	$^{18}O/^{16}O$ ($\times10^{-3}$)	$^{17}O/^{16}O$ ($\times10^{-4}$)	Group	Size (nm^2)
51-8	1.64±0.03	9.51±0.19	1	570×570
55b-4	1.18±0.02	7.58±0.18	2	420×420
172 ¶	1.92±0.03	5.4±0.2	1	200×160
2122-O ¶	2.09±0.03	5.7±0.2	1	160×160
2147 ¶	1.99±0.03	6.04±0.17	1	160×160
8a-1 ¶	2.03±0.05	6.94±0.29	1	160×120
13-1 ¶	2.01±0.04	5.08±0.19	1	200×200
16a-2-lt ¶	1.96±0.02	5.21±0.11	1	200×200
19c-1 ¶	1.97±0.03	5.4±0.2	1	200×200
52-11 ¶	1.50±0.03	6.09±0.17	1	275×235
55b-2 ¶	0.58±0.03	5.9±0.2	2	160×160
55b-3 ¶	2.01±0.05	5.79±0.27	1	160×160

Notes: Grains marked with ¶ were gone before they could be characterized in the Auger Nanoprobe. "na" means not applicable because the grains were sputtered away. Errors are 1σ.

Table A5.2a: Elemental Compositions of the Presolar Silicate Grains in ALHA77307

Grain Name	Ca at.%	O at.%	Fe at.%	Mg at.%	Al at.%	Si at.%	mg#	(Fe+Mg+Ca)/Si	cation/O	O/Si
Pyroxene								**1**	**0.67**	**3**
Pyroxene-like										
133	...	63.1±2.3	...	18.5±1.7	...	18.4±2.0	100	1.0±0.1	0.58±0.05	3.4±0.4
5b-7 *	1.9±0.2	52.4±1.9	13.9±1.6	5.6±0.5	5.8±1.4	20.4±2.2	29	1.0±0.1	0.9±0.1	2.6±0.3
10-4-tp *	...	55.1±2.0	16.6±1.9	5.3±0.5	...	23.0±2.5	24	1.0±0.1	0.8±0.1	2.4±0.3
11-1-lt *	...	54.7±2.0	12.3±1.4	8.7±0.8	7.3±1.8	17.0±1.9	41	1.2±0.2	0.8±0.1	3.2±0.4
11-1-rt *	...	52.7±1.9	12.7±1.4	9.7±0.9	...	24.9±2.7	43	0.9±0.1	0.9±0.1	2.1±0.2
15-5-bm *	...	54.9±2.0	11.5±1.3	9.8±0.9	6.0±1.5	17.8±2.0	46	1.2±0.2	0.8±0.1	3.1±0.4
18-6	...	59.8±2.2	13.6±1.5	8.2±0.8	...	18.4±2.0	38	1.2±0.2	0.7±0.1	3.3±0.4
18-7 *	...	54.8±2.0	11.4±1.3	10.9±1.0	...	22.9±2.5	49	1.0±0.1	0.8±0.1	2.4±0.3
54-1 *	4.9±0.5	54.6±2.0	11.8±1.3	6.3±0.6	...	22.4±2.5	35	1.0±0.1	0.8±0.1	2.4±0.3
48-bm *	...	53.9±1.9	14.2±1.6	7.6±0.7	5.8±1.4	18.5±2.0	35	1.2±0.2	0.9±0.1	2.9±0.3

Table A5.2a cont'd.

Grain Name	Ca at.%	O at.%	Fe at.%	Mg at.%	Al at.%	Si at.%	mg#	(Fe+Mg+Ca)/Si	cation/O	O/Si
Olivine								**2**	**0.75**	**4**
Olivine-like										
1310 *	...	53.4±1.9	16.3±1.8	13.9±1.3	...	16.4±1.8	46	1.8±0.2	0.9±0.1	3.3±0.4
5b-8	...	59.2±2.1	20.8±2.3	6.3±0.6	...	13.6±1.5	23	2.0±0.3	0.7±0.1	4.4±0.5
63	...	55.0±2.0	14.7±1.6	15.9±1.5	...	14.4±1.6	52	2.1±0.3	0.8±0.1	3.8±0.4
8a-4-bm *	...	62.6±2.3	...	25.5±2.4	...	11.9±1.3	100	2.1±0.3	0.60±0.05	5.3±0.6
10-4-O18	...	55.1±2.0	12.9±1.4	16.7±1.6	...	15.3±1.7	56	1.9±0.3	0.8±0.1	3.6±0.4
114 *	...	49.9±1.8	20.6±2.3	13.1±1.2	...	16.3±1.8	39	2.1±0.3	1.0±0.1	3.1±0.4
116	...	55.0±2.0	25.8±2.9	4.5±0.4	...	14.7±1.6	15	2.1±0.3	0.8±0.1	3.7±0.4
12-4 *	...	49.7±1.8	21.1±2.4	13.5±1.3	...	15.6±1.7	39	2.2±0.3	1.0±0.1	3.2±0.4
128	...	56.6±2.0	13.8±1.5	15.1±1.4	...	14.6±1.6	52	2.0±0.3	0.8±0.1	3.9±0.4
17b-2	...	57.7±2.1	15.3±1.7	11.9±1.1	...	15.0±1.7	44	1.8±0.2	0.7±0.1	3.8±0.4
51-6-O17 *	...	52.2±1.9	10.3±1.2	21.5±2.0	...	16.0±1.8	68	2.0±0.3	0.9±0.1	3.3±0.4
52-15	...	55.8±2.0	...	29.8±2.8	...	14.4±1.6	100	2.1±0.3	0.8±0.1	3.9±0.4
53-5 *	...	52.1±1.9	16.8±1.9	16.5±1.6	...	14.6±1.6	50	2.3±0.3	0.9±0.1	3.6±0.4
53-11	...	56.8±2.0	13.3±1.5	16.7±1.6	...	13.3±1.5	56	2.3±0.3	0.8±0.1	4.3±0.5
54-9 *	...	53.2±1.9	11.6±1.3	18.6±1.7	...	16.6±1.8	62	1.8±0.2	0.9±0.1	3.2±0.4

Table A5.2a cont'd.

Grain Name	Ca at.%	O at.%	Fe at.%	Mg at.%	Al at.%	Si at.%	mg#	(Fe+Mg+Ca)/Si	cation/O	O/Si
Intermediate										
111-O	...	55.2±2.0	16.9±1.9	7.2±0.7	6.4±1.6	14.3±1.6	30	1.7±0.2	0.8±0.1	3.9±0.4
112	...	57.3±2.1	11.0±1.2	14.7±1.4	...	17.1±1.9	57	1.5±0.2	0.7±0.1	3.4±0.4
1-24	...	55.9±2.0	16.6±1.9	11.1±1.0	...	16.4±1.8	40	1.7±0.2	0.8±0.1	3.4±0.4
132	...	57.8±2.1	13.4±1.5	11.7±1.1	...	17.1±1.9	47	1.5±0.2	0.7±0.1	3.4±0.4
146	...	56.5±2.0	10.6±1.2	14.9±1.4	...	18.0±2.0	58	1.4±0.2	0.8±0.1	3.1±0.4
178	1.0±0.1	54.6±2.0	12.6±1.4	9.9±0.9	5.3±1.3	16.6±1.8	44	1.4±0.2	0.8±0.1	3.3±0.4
2131	...	59.3±2.1	12.1±1.4	11.2±1.1	...	17.3±1.9	48	1.3±0.2	0.69±0.05	3.4±0.4
21422	...	59.8±2.2	20.2±2.3	4.5±0.4	...	15.5±1.7	18	1.6±0.2	0.7±0.1	3.9±0.4
2-1425-O2	...	57.2±2.1	25.1±2.8	...	...	17.7±1.9	0	1.4±0.2	0.7±0.1	3.2±0.4
32	1.3±0.1	59.1±2.1	9.2±1.0	14.6±1.4	...	15.8±1.7	61	1.6±0.2	0.69±0.05	3.7±0.4
42	...	60.7±2.2	20.7±2.3	4.2±0.4	...	14.5±1.6	17	1.7±0.2	0.6±0.1	4.2±0.5
44-O	1.0±0.1	57.9±2.1	8.5±1.0	14.6±1.4	...	17.9±2.0	63	1.3±0.2	0.7±0.1	3.2±0.4
48-tp	...	58.7±2.1	14.2±1.6	9.9±0.9	...	17.2±1.9	41	1.4±0.2	0.7±0.1	3.4±0.4
410	1.2±0.1	57.1±2.1	20.6±2.3	5.0±0.5	...	16.0±1.8	20	1.7±0.2	0.7±0.1	3.6±0.4
7d-2	...	56.9±2.0	15.0±1.7	10.8±1.0	...	17.3±1.9	42	1.5±0.2	0.8±0.1	3.3±0.4
8a-3-O17	...	55.0±2.0	17.7±2.0	10.3±1.0	...	17.0±1.9	37	1.6±0.2	0.8±0.1	3.2±0.4
107	...	50.1±1.8	17.1±1.9	14.2±1.3	...	18.6±2.0	45	1.7±0.2	1.0±0.1	2.7±0.3
113	...	51.7±1.9	12.3±1.4	11.7±1.1	5.4±1.3	19.0±2.1	49	1.3±0.2	0.9±0.1	2.7±0.3
13-4	...	50.3±1.8	17.4±1.9	14.0±1.3	...	18.2±2.0	45	1.7±0.2	1.0±0.1	2.8±0.3
15-5-tp	2.7±0.3	54.9±2.0	10.0±1.1	8.8±0.8	8.5±2.1	15.2±1.7	47	1.4±0.2	0.8±0.1	3.6±0.4
51-7	...	57.2±2.1	7.5±0.8	16.9±1.6	...	18.4±2.0	69	1.3±0.2	0.7±0.1	3.1±0.4
51-9	...	55.1±2.0	...	25.8±2.4	...	19.1±2.1	100	1.4±0.2	0.8±0.1	2.9±0.3
53-4	...	63.2±2.3	13.3±1.5	8.4±0.8	...	15.1±1.7	39	1.4±0.2	0.58±0.04	4.2±0.5

Table A5.2a cont'd.

Grain Name	Ca at.%	O at.%	Fe at.%	Mg at.%	Al at.%	Si at.%	mg#	(Fe+Mg+Ca)/Si	cation/O	O/Si
Others										
131	...	62.8±2.3	...	15.3±1.4	...	21.8±2.4	100	0.7±0.1	0.59±0.05	2.9±0.3
163	...	62.0±2.2	9.2±1.0	6.3±0.6	...	22.6±2.5	41	0.7±0.1	0.61±0.05	2.7±0.3
1710	...	62.9±2.3	...	14.4±1.4	...	22.7±2.5	100	0.6±0.1	0.59±0.05	2.8±0.3
105	2.1±0.2	59.7±2.1	8.0±0.9	...	9.3±2.3	20.8±2.3	0	0.5±0.1	0.7±0.1	2.9±0.3
13-5	...	60.6±2.2	...	15.6±1.5	...	23.8±2.6	100	0.7±0.1	0.7±0.1	2.5±0.3
2-1425-O1	...	55.8±2.0	18.7±2.1	...	...	25.4±2.8	0	0.7±0.1	0.8±0.1	2.2±0.3
19-1	3.4±0.4	61.0±2.2	...	11.0±1.0	...	24.6±2.7	100	0.6±0.1	0.6±0.1	2.5±0.3
16a-3	...	53.6±1.9	8.8±1.0	6.8±0.6	6.4±1.6	24.3±2.7	44	0.6±0.1	0.9±0.1	2.2±0.3
44-O17	...	51.4±1.9	21.1±2.4	13.8±1.3	...	13.7±1.5	40	2.5±0.3	0.9±0.1	3.8±0.4
8a-3-O	1.1±0.1	56.5±2.0	10.6±1.2	19.2±1.8	...	12.6±1.4	64	2.5±0.3	0.8±0.1	4.5±0.5
8a-4-tp	...	62.8±2.3	17.8±2.0	8.6±0.8	...	10.8±1.2	33	2.4±0.3	0.59±0.04	5.8±0.7
121	...	54.7±2.0	14.2±1.6	17.7±1.7	...	13.4±1.5	55	2.4±0.3	0.8±0.1	4.1±0.5
127	...	55.9±2.0	16.4±1.8	16.0±1.5	...	11.6±1.3	49	2.8±0.4	0.8±0.1	4.8±0.6
51-6-O	...	55.3±2.0	16.3±1.8	17.5±1.6	...	10.9±1.2	52	3.1±0.4	0.8±0.1	5.1±0.6
52-8	...	52.2±1.9	19.5±2.2	14.7±1.4	...	13.6±1.5	43	2.5±0.3	0.9±0.1	3.8±0.4
53-6	...	51.6±1.9	19.5±2.2	17.6±1.7	...	11.4±1.3	47	3.3±0.4	0.9±0.1	4.5±0.5
54-5	3.5±0.4	58.1±2.1	14.0±1.6	11.3±1.1	...	13.0±1.4	45	2.2±0.3	0.72±0.05	4.5±0.5
52-4-O17	...	44.9±1.6	20.4±2.3	9.9±0.9	8.2±2.0	16.5±1.8	33	1.8±0.3	1.2±0.1	2.7±0.3
Si-poor										
33	...	51.1±1.8	30.1±3.4	5.0±0.5	9.3±2.3	4.5±0.5	14	7.8±1.1	1.0±0.1	11.4±1.3

Notes: Grains marked with * in Table 5.2(a) do not have O in stoichiometric proportions (see text). Errors are 1σ. mg# is defined as Mg/(Fe+Mg)*100.

Table A5.2b: Elemental Compositions of the Presolar Oxide and Composite Grains in ALHA77307

Grain Name	Ca at.%	O at.%	Fe at.%	Mg at.%	Al at.%	Si at.%	mg#	(Fe+Mg+Ca)/Si	cation/O	O/Si
Silica										
10-4-bm	...	65.4±2.4	...	...	...	34.6±3.8	...	...	0.5±0.1	...
2132	...	69.1±2.5	...	...	...	30.9±3.4	...	...	0.4±0.1	...
21420	...	69.1±2.5	...	...	...	30.9±3.4	...	...	0.4±0.1	...
Al-oxides										
52-4-O	...	65.4±2.4	...	...	34.6±8.6	...	...	...	0.5±0.1	...
45	...	75.0±2.7	...	...	25.0±6.2	...	...	...	0.4±0.1	...
31	...	74.4±2.7	...	...	25.6±6.4	...	...	...	0.4±0.1	...
Fe-oxides										
21412	...	55.6±2.0	44.4±5.0	...	...	...	...	...	0.8±0.1	...
54-7	...	66.7±2.4	33.3±3.7	...	...	...	...	...	0.5±0.1	...
Composite grains										
51-1(tp)	...	44.7±1.6	27.5±3.1	13±1.2	...	14.8±1.6	32	2.7±0.4	1.2±0.1	3.0±0.3
51-1(bm)	...	50.5±1.8	18.2±2.0	15.0±1.4	...	16.3±1.8	33	2.0±0.3	1.0±0.1	3.1±0.4
51-8 (lt)	3.9±0.4	57.4±2.1	8.4±0.9	8.8±0.8	...	21.5±2.4	51	1.0±0.1	0.7±0.1	2.7±0.3
51-8 (rt)	...	53.8±1.9	15.2±1.7	11.9±1.1	...	19.1±2.1	44	1.4±0.2	0.9±0.1	2.8±0.3
MgO										
55b-4	...	49.2±1.8	...	50.8±4.8	...	...	...	...	1.0±0.1	...

Notes: Grains marked with * in Table 5.2(a) do not have O in stoichiometric proportions (see text). Errors are 1σ. mg# is defined as Mg/(Fe+Mg)*100.

Table A5.3: Carbon and N Isotopic Compositions, C^-/Si^- Ratios, and Sizes of SiC and Carbonaceous Grains in ALHA77307

Grain Name	$^{12}C/^{13}C$	$^{14}N/^{15}N$	$\delta^{13}C/^{12}C$ ‰	$\delta^{15}N/^{14}N$ ‰	Phase (Type/elements)	$^{12}C^-/^{28}Si^-$ ion ratio	Sizes (nm^2)
1211	28.6±0.7	...	2110±25	...	SiC (MS)*	na	200×200
139	48.2±1.6	...	845±35	...	SiC (MS)*	na	200×200
146	105.5±2.2	...	-155±20	...		na	200×160
172	43.2±0.8	...	1060±20	...	SiC (MS)*	na	430×350
2136	60.8±2.4	...	465±40	...	SiC (MS)*	na	160×160
2141	50.2±0.8	...	775±20	...	SiC (MS)*	na	235×235
2148	57.5±1.2	...	550±20	...	SiC (MS)*	na	235×235
21414	110.5±1.9	...	-194±20	...		na	275×200
21418	21.1±0.1	...	3220±6	...	SiC (MS)	na	420×290
21419	105.7±1.8	...	-160±15	...		na	235×235
2142	71.6±2.6	...	240±40	...	SiC (MS)*	na	160×120
51	114.8±4.6	...	-225±40	...		na	235×160
5a1	54.8±0.5	...	625±10	...	SiC(MS)	na	500×400
5b4	52.5±0.9	...	695±20	...	SiC (MS)*	na	350×275
8a1	34.8±0.5	...	1560±15	...	SiC (MS)*	na	350×315
106	4.28±0.04	...	19750±10	...	SiC (A+B)*	na	390×390
111lt	53.7±0.8	...	655±15	...	SiC (MS)	na	430×400
111rt	18.2±0.5	...	3880±35	...	SiC (MS)*	na	200×160
136	11.6±0.2	...	6695±15	...	SiC (MS)*	na	470×390
151	57.8±1.0	...	540±20	...	SiC (MS)	na	110×110
52-17	37.0±2.4	...	1410±75	...	SiC (MS)	na	125×125
53-9	13.5±0.5	...	5620±40	...	SiC (MS)	na	110×90
B2	111.0±3.7	273.4±23.3	-200±35	-5±93	SiC (Y)	1.7	200×170
D2	63.7±1.4	401.0±23.2	400±30	-322±60	SiC (MS)	1.1	260×240
D4	55.2±1.9	244.7±19.1	610±55	111±85	SiC (MS)	1.3	140×110
E1	51.5±1.0	413.8±34.7	730±35	-343±88	SiC (MS)	1.1	230×170
G2-lt	74.7±2.0	810.5±70.7	190±30	-664±90	SiC (MS)	0.8	310×140

Table A5.3 cont'd.

Grain Name	$^{12}C/^{13}C$	$^{14}N/^{15}N$	$\delta^{13}C/^{12}C$ ‰	$\delta^{15}N/^{14}N$ ‰	Phase (Type/Elements present)	$^{12}C^{-}/^{28}Si^{-}$ ion ratio	Sizes (nm^2)
G2-tp	64.5±1.2	517.5±57.2	380±25	-474±117	SiC (MS)	0.8	390×270
G7	20.3±0.8	403.1±86.1	3390±160	-325±244	SiC (MS)	0.5	510×280
D1††	85.3±0.6	187.1±3.4	45±10	454±19	C, O, S	25	580×360
D6	87.3±1.7	139.2±6.4	20±20	954±50	O, C, Mg, Si	3	220×200
D8	88.9±0.8	135.8±2.8	1±10	1003±21	C, O, Fe, S	36	480×460
E2	89.2±0.8	179.1±4.5	-2±10	519±26	C, O	11	460×290
E4-lt	86.0±0.7	174.1±3.1	35±10	563±18	C, O	30	420×380
E4-rt	88.1±0.6	173.7±4.4	10±5	566±26	O, C, Fe	20	660×330
E7-bm	88.9±0.9	192.9±10.1	1±10	410±56	C, O	62	800×400
E7-tp††	83.2±1.0	188.7±10.8	70±10	442±62	C, O	38	380×300
E7-lt††	88.3±1.9	181.4±7.8	7±20	499±46	C, O, Fe, S	12	200×160
E7-rt	90.3±2.3	187.8±12.9	-15±25	448±75	O, C, Fe, Si, Mg	6	140×80
E9-lt	89.0±1.7	178.6±9.2	0±20	523±56	C, O, Al, Fe	9	260×180
E9-rt	88.4±0.9	193.0±4.6	7±11	409±24	C, O	8	290×290
E9-tp	85.5±1.9	172.8±6.8	40±15	574±34	O, C, Fe, S	16	430×200
F1-17	81.8±1.0	138.4±3.5	90±15	965±27	O, C, Si, Mg	4	375×290
F1-19	86.6±2.9	182.7±8.8	30±35	488±52	C, O, S, Fe	4	300×140
G2-rt	84.9±1.1	165.3±5.4	50±15	646±34	O, Si, C, Mg, Fe	4	230×140
G2-me	87.7±1.6	120.1±3.4	15±20	1266±30	O, C, Fe, Si, S	6	200×120
G3-tp	94.5±3.1	164.7±10.3	-50±35	652±69	O, C, Fe, S	3	300×280
G3-rt	84.5±3.2	137.5±13.7	55±40	979±120	O, C, Fe, Si	2	290×290
G3-bm	84.7±2.2	171.7±9.2	50±30	584±58	O, C, Fe, Mg, Si	3	270×200
G4	89.2±2.2	155.5±6.8	-2±25	749±47	O, C, Fe, Ni (grain + coating)	2	Grain~960×960

Table A5.3 cont'd.

Grain Name	$^{12}C/^{13}C$	$^{14}N/^{15}N$	$\delta^{13}C/^{12}C$ ‰	$\delta^{15}N/^{14}N$ ‰	Phase (Type/Elements present)	$^{12}C^-/^{28}Si^-$ ion ratio	Sizes (nm^2)
G7	93.3±3.9	164.7±10.2	-45±45	652±68	O, C, Fe	2	210×130
G9-tp	85.5±1.9	172.8±6.8	40±20	574±42	O, C, Si, Fe, Mg, S	2	870×430
G9-bm	89.3±1.8	180.0±9.4	-3±20	511±56	O, C, Fe, Si, Mg	3	850×550
G10-tp	85.7±1.1	180.6±9.1	40±15	506±54	O, C, Fe, Si	9	540×290
G10-bm	90.7±3.2	180.1±11.7	-20±35	510±71	O, C, Fe, Si, Mg	1	230×110
G11	83.7±2.0	170.5±11.4	65±25	595±74	O, C, Mg, Si, Fe, S	4	710×570
G12	88.2±0.4	176.0±3.9	10±5	545±23	C, O	65	800×430

Notes: The SiC grains are classified into known types (e.g., Zinner 2007); MS stands for mainstream grains. The symbol * identifies those that were classified into different SiC types on the basis of isotopic data alone. Grains identified during C and O ion imaging have "na" written in the field 'C^-/Si^- elemental ratio'. Grains that are nanoglobule candidates are shown with ††. The 1σ error for the C^-/Si^- ratios ranges from 0.01–0.5. The elements present in the carbonaceous grains are listed in the order of increasing abundance.